NASDA 宇宙開発事業団

CRL

International Space Station (ISS)
Japanese Experiment Module - Exposed Facility (JEM-EF)
Superconducting Submillimerter-Wave Limb-Emission Sounder (SMILES)

JEM/SMILES Mission Plan

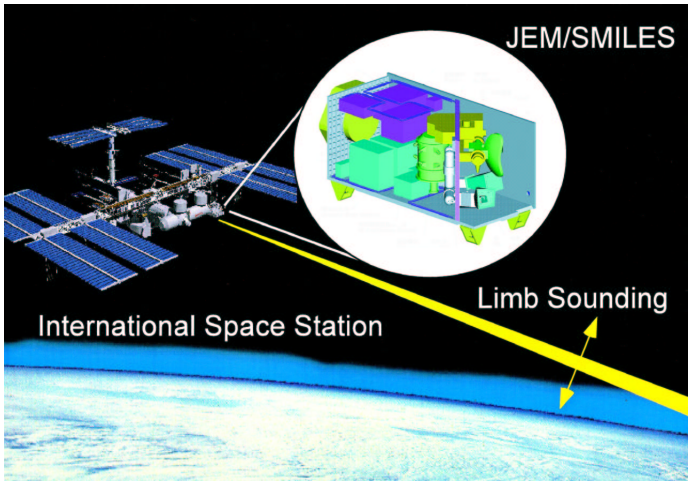

きぼう

Version 2.1
November 15, 2002

SMILES Science Team
SMILES Mission Team

PREFACE to Version 2

In almost two years since the first version was issued, SMILES has seen significant progress in designs of mission instruments and investigations on data analysis. What we expected on SMILES capability has been getting reality through detailed designs and testing results of engineering models. Estimation of data accuracy is also improved by carrying out retrieval simulations, part of which has been conducted in a multi-national collaboration. Scientific discussions have been more focused on potential advantages of SMILES data. This version of SMILES Mission Plan is issued to cover those progresses. Nevertheless, we admit the contents remain short of full satisfaction. Any critical comments will be invaluable for us to make our ways toward the launching of SMILES.

Further information about the SMILES mission including the updated version of this document can be found at the following URL.

`http://smiles.tksc.nasda.go.jp/indexe.shtml`

November 15, 2002

Masato Shiotani
Leader, SMILES Science Team
Kyoto University

Harunobu Masuko
Principal Investigator, SMILES Mission Team
National Space Development Agency
Communications Research Laboratory

PREFACE to Version 1

A proposal of Superconducting Submillimeter-wave Limb-emission Sounder (SMILES) was approved in April 1997 as an experiment on the JEM Exposed Facility. The SMILES experiment has twofold mission objectives: to demonstrate new technology of submillimeter-wave sensor for sounding the middle atmosphere, and to provide scientists with global data of trace gases that are deeply connected to the ozone depletion. The SMILES mission team, which was formed as a joint collaborative group between the National Space Development Agency of Japan (NASDA) and Communications Research Laboratory (CRL), has been concentrating on the technical development of critical components and the design of the whole SMILES system. Although there still remain several unresolved technical problems, the SMILES system is taking shape and seems promising for the mission objectives.

Meanwhile, Japanese researchers in the field of atmospheric sciences have been collaborating with the mission team on critical discussions concerning the mission capabilities for maximizing scientific returns. The discussion has been performed in a working group, the SMILES Science Team, under the Committee for Earth Observation Systems, Earth Science and Technology Forum. This report is a summary of the discussion, which clarifies the fundamental requirements on the SMILES mission, specifically from the scientific viewpoints. Now we believe that SMILES could be a powerful probe for atmospheric researches, if these requirements are met.

We hope this report is read by many people including atmospheric scientists worldwide. Any critical comments on the contents of this report will be appreciated. We will continue our efforts for improving the SMILES instrumental specifications and maximizing the scientific outputs of this challenging mission.

Further information about the SMILES mission including the updated version of this document can be found at the following location.

`http://smiles.tksc.nasda.go.jp/indexe.shtml`

The activity is sponsored by Earth Science & Technology Organization (ESTO) under a research contract with NASDA.

February 19, 2001

Masato Shiotani
Leader, SMILES Science Team
Committee for Earth Observation Systems
Earth Science and Technology Forum

Harunobu Masuko
Principal Investigator, SMILES Mission Team
National Space Development Agency
Communications Research Laboratory

Contents

List of Figures

clearpage

List of Tables

Contributors to the JEM/SMILES Mission Plan

Name	E-mail	Affiliation	Chapter*
Amano, Takayoshi	amano@mito.ipc.ibaraki.ac.jp	Ibaraki Univ.	4
Bühler, Stefan	sbuehler@uni-bremen.de	IUP	4
Habara, Hideta	habara@mtg.biglobe.ne.jp	TKSC, Ibaraki Univ.	4
Inatani, Junji	inatani.junji@nasda.go.jp	TKSC	**3**
Kasai, Yasuko	ykasai@crl.go.jp	CRL	2, **4**
Manabe, Takeshi	manabe@crl.go.jp	CRL	3
Masuko, Harunobu	masuko@crl.go.jp	CRL	**1**
Miura, Takeshi	miura.takeshi@nasda.go.jp	TKSC	3
Nagahama, Tomoo	nagahama@a.phys.nagoya-u.ac.jp	Nagoya Univ.	2
Nishibori, Toshiyuki	nishibori.toshiyuki@nasda.go.jp	TKSC	3
Ochiai, Satoshi	ochiai@crl.go.jp	CRL	3, 4
Ozeki, Hiroyuki	ozeki.hiroyuki@nasda.go.jp	TKSC	2, 3
Shibasaki, Kazuo	sibasaki@eorc.nasda.go.jp	EORC	**6**
Shiotani, Masato	shiotani@kurasc.kyoto-u.ac.jp	Kyoto Univ.	**2**
Shirai, Tomoko	shirai@eorc.nasda.go.jp	EORC	2
Suzuki, Makoto	suzuki@eorc.nasda.go.jp	EORC	**5**
Takahashi, Chikako	takahashi.c@fip.co.jp	FIP	4
Takahashi, Kenshi	kent@stelab.nagoya-u.ac.jp	STEL	2
Tsujimaru, Sho	sho@eorc.nasda.go.jp	EORC	4
Verdes, Carmen	cverdes@uni-bremen.de	IUP	4

* Boldface indicates the editor of the chapter.

CRL : Communications Research Laboratory
Koganei, Tokyo 184-8795, Japan

TKSC : National Space Development Agency of Japan
Tsukuba Space Center
Tsukuba 305-8505, Japan

EORC : National Space Development Agency of Japan
Earth Observation Research Center
Harumi, Chuo-ku, Tokyo 104-6023, Japan

STEL : Solar-Terrestrial Environment Laboratory
Nagoya University
Honohara, Toyokawa 442-8507, Japan

FIP : Fujitsu FIP Corporation
Aomi, Tokyo 135-1612, Japan

Kyoto Univ. : Kyoto University
RASC, Gokasho, Uji, Kyoto 611-0011, Japan

Ibaraki Univ. : Ibaraki University
Bunkyo, Mito 310-8512, Japan

Nagoya Univ. : Nagoya University
Furo-cho, Chikusa-ku, Nagoya 464-8601, Japan

IUP : Institute of Environmental Physiks
University of Bremen, FB1
PO Box 330440
28334 Bremen, Germany

1 Executive Summary

This chapter outlines the mission plan of the Superconducting Submillimeter-wave Limb-emission Sounder (SMILES), which is to be accommodated by the Exposed Facility (EF) of the Japanese Experiment Module (JEM) on the International Space Station (ISS). The JEM/SMILES mission was approved in 1997, and is currently under development jointly by the Communications Research Laboratory (CRL) and National Space Development Agency of Japan (NASDA).

1.1 Introduction

Trace gases such as ClO, BrO, HO_2 have been depleting ozone in the stratospheric. The origins of such trace gases are human-made chlorofluorocarbons (CFCs), halogen-containing substances, methane, and others. Figure 1.1 shows the north-south variations of the ozone depletion between 1979 and 1997 [*World Meteorological Organization*, 1998]. After the Montreal Protocol [*United Nations Environmental Programme*, 1987] and its amendments, the total combined abundance of ozone-depleting compounds in the lower atmosphere peaked around 1994, which is now slowly declining. The combined abundance of the stratospheric chlorine and bromine was expected to peak before the year 2000, as shown in Figure 1.2 [*World Meteorological Organization*, 1998]. Its decrease is indispensable for recovery of the ozone layer. A WMO report [*World Meteorological Organization*, 1998] says, even if there were to be an immediate stop to all emissions of human-made ozone-depleting substances, including those currently in use, stratospheric halogen loading would not return to the 1980 levels by 2033. Therefore, it is needed to continuously monitor the stratospheric chlorine and bromine for analyses of the ozone trend.

The ozone changes will affect the Earth's climate, and changes in climate and meteoro-

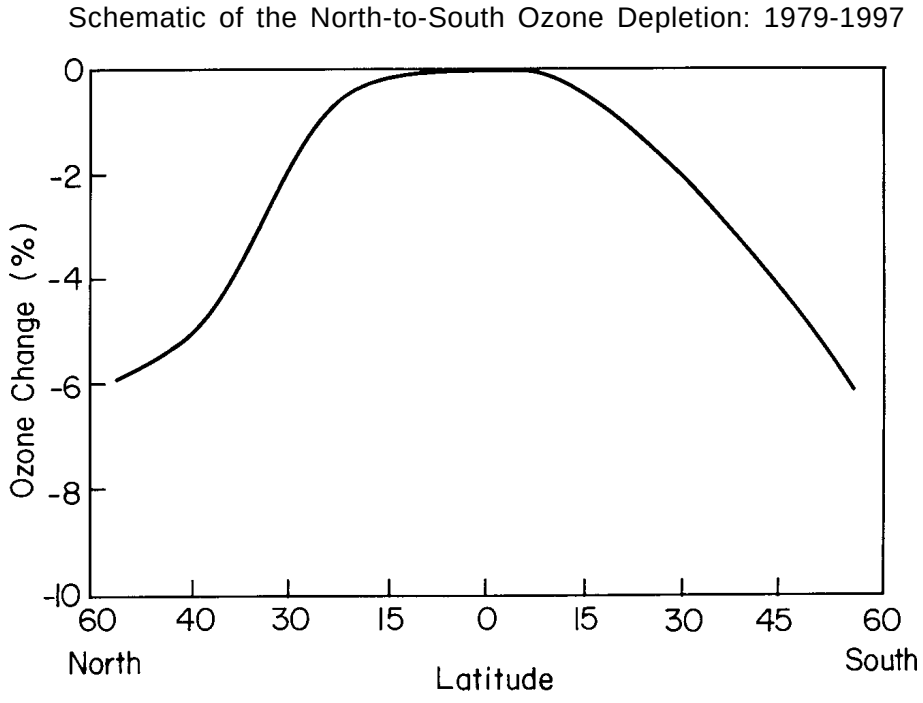

Figure 1.1 Schematic of the north to south ozone depletion from 1979 to 1997[*World Meteorological Organization*, 1998].

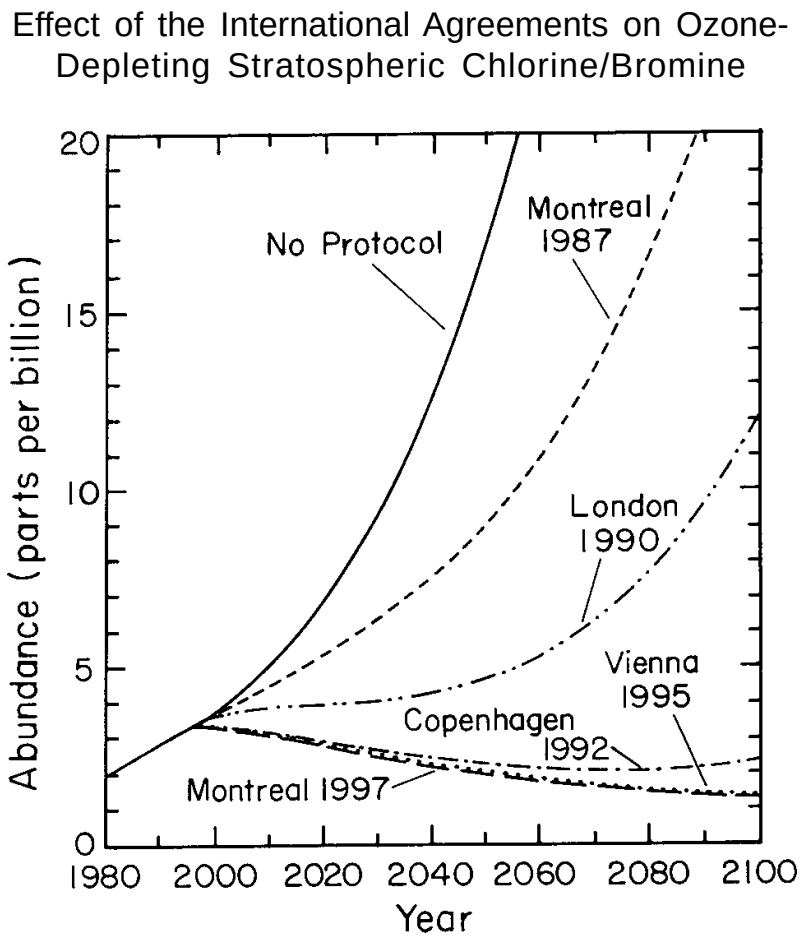

Figure 1.2 Prediction of combined abundance of stratospheric chlorine and bromine, which is based on each protocol and amendment [*World Meteorological Organization*, 1998].

logical conditions will affect the ozone depletion, because they share a number of common physical and chemical processes [*World Meteorological Organization*, 1998]. Stratospheric ozone losses have caused a cooling of the lower stratosphere and a global negative radiative forcing to the climate system. The future behavior of ozone also will be affected by changing abundances of methane (CH_4), nitrous oxide (N_2O), water vapor (H_2O), and sulfate aerosol. Understanding of the relationships between the ozone trend and climate change is connected to chemical processes within trace gases and their coupling with dynamic processes.

This situation requires three-dimensional and simultaneous measurements of ozone and trace gases in the stratosphere and upper troposphere. Also important is global accurate data with high resolutions in time and location. Submillimeter limb-emission sounding from space will have several advantages of meeting these requirements [*Waters*, 1993]. Figure 1.3 schematically shows the method of limb-emission sounding. Many species among trace gases have spectral emissions in submillimeter ranges. The heterodyne spectroscopy has a high spectral resolution that is needed for precise retrieval of trace gases. Emission measurements, which are independent of sunlight in any region, are preferable for complete global observations and essential for understanding diurnal cycles of chemical processes. The limb-emission sounding also has another advantage of reasonable

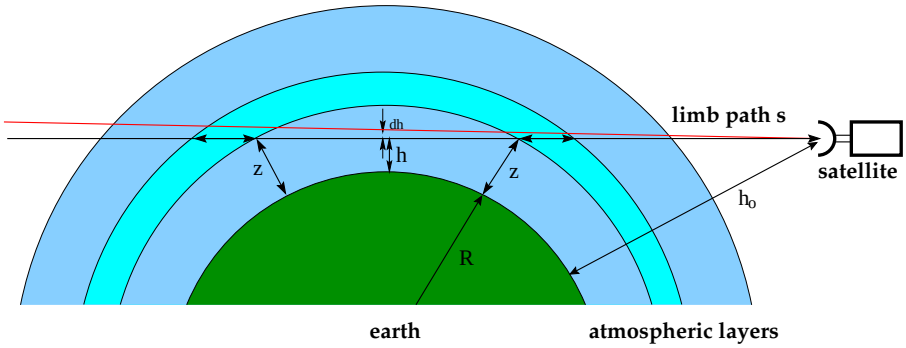

Figure 1.3 The method of limb-emission sounding from the ISS.

altitude resolution. Since a mechanically scanning antenna is used to sweep the limb atmosphere vertically, the altitude resolution is basically determined by the beam size at the atmosphere. Furthermore, submillimeter molecular emissions are less dependent on atmospheric temperatures, and no aerosols will affect submillimeter measurements, which also makes the submillimeter observations preferable.

On the other hand, recent progress in submillimeter receiver technology has enabled us to drastically improve the quality of limb-emission sounding data. A 4 K-cooled superconductive mixer receiver will detect molecular spectra with an order-of-magnitude higher signal-to-noise ratio than the conventional ambient-temperature semiconductor receiver. This improvement is essential to produce global distribution maps of trace gases, whose emissions are generally weak because of thermal excitation at ambient temperatures of the atmosphere. Submillimeter waves around the wavelength of 0.5 mm or less are profitable for observing various trace gases up to high altitudes with reasonable signal-to-noise ratios. For simultaneous observations of a dozen of trace gases as well as atmospheric temperatures and pressures, we need a receiver with a wide instantaneous bandwidth, and a wide-band radio spectrometer with high frequency resolution. Single-sideband (SSB) observation with the submillimeter mixer is preferable for producing reliable quantitative data.

In a bid to demonstrate new submillimeter technology in space and to conduct limb-emission sounding for a group of trace gases, the CRL and NASDA, with a technical support of the National Astronomical Observatory (NAO), submitted an experiment proposal of Superconducting Submillimeter-wave Limb-emission Sounder (SMILES), in response to the announcement of opportunity (AO) for the use of the Exposed Facility (EF) of the ISS-JEM. The proposal was accepted in March 1997, and the instrumental development started from the fiscal year 1998 under the permission of the Space Development Board of Japan.

For full understanding of atmospheric environment, more comprehensive and simultaneous measurements of chemical and physical processes are needed for a wide range of the atmosphere. For this purpose, an atmospheric chemistry and dynamics mission, ATMOS-C, has been proposed in Japan [*ATMOS-C1 Team*, 1997]. An extended version of SMILES with several bands from 300 GHz to 2.5 THz to measure ClO, BrO, H_2O, OH, atmospheric temperature, etc. is a candidate sensor proposed for ATMOS-C. JEM/SMILES is therefore regarded as a pre-phase experiment to ensure the feasibility of ATMOS-C/SMILES.

1.2 Atmospheric Submillimeter Observations from Space

The first of millimeter-wave limb-emission sounding from space was made by the Microwave Limb Sounder (MLS) on the Upper Atmosphere Research Satellite (UARS), which was launched in September 1991 by NASA [*Waters*, 1993]. UARS-MLS was developed by the Jet Propulsion Laboratory (JPL), in collaboration with the Rutherford Appleton Laboratory, Heriot-Watt University, and Edinburgh University in the United Kingdom. The UARS-MLS instrument carries ambient-temperature double-sideband radiometers operating at 63 GHz, 183 GHz, and 205 GHz, which enable simultaneous observations of the atmospheric temperatures, pressures (about 30–60 km), H_2O (about 15–85 km), O_3 (about 15–80 km), and ClO (about 15–45 km) in the stratosphere. UARS-MLS is still in operation. The system noise temperature for the 205 GHz band is 990 K (double sideband), which provides zonal mean measurements of ClO profiles with a sensitivity of about 0.1 ppbv and each limb-scan measurement of ClO with a sensitivity of 0.5 ppbv. Sensitivities to O_3 and H_2O in the middle stratosphere are a few percent in each limb scan. The UARS-MLS observations have produced a variety of atmospheric researches until today [*Waters et al.*, 1999], such as findings of the correlations between ozone losses and ClO enhancement in polar regions.

The Max-Planck Institute for Aeronomy, University of Bern, and Naval Research Laboratory conducted three short-period observations in March 1992, August 1993, and November 1994 with the Millimeter-wave Atmospheric Sounder (MAS) on the Atmospheric Laboratory for Applications and Science (ATLAS) mission. The frequency bands used for ATLAS/MAS are almost the same as those of UARS-MLS.

The Swedish Space Corporation (SSC) has launched an aeronomy-and-astronomy joint mission, Odin, in February 2001, in collaboration with France, Finland, and Canada. The objectives in aeronomy are to measure the height profiles of trace species in the stratosphere and mesosphere. The Odin millimeter and submillimeter limb-emission sounder is operated at 119 GHz for temperatures and pressures, at 495 GHz for H_2O and HNO_3, and at 561 GHz for H_2O isotope, NO, N_2O, NO_2, H_2O_2, ClO, CO, and HO_2. The radiometers use single-sideband (SSB) Schottky-diode mixers that are cooled to 50-80 K by a closed-cycle Stirling refrigerator. The noise temperatures (SSB) of the receiver are around 500 K at 119 GHz, and 2,000 K for the submillimeter ranges.

NASA is to launch the Earth Observing System (EOS) Chemistry, now called "Aura", as a follow-on mission of UARS in 2004. EOS-Aura has a sun-synchronous orbit with a height of 705 km. It will carry an improved version of UARS-MLS [*Waters*, 1999]. An intense objective of Aura-MLS is to measure the upper-troposphere (UT) and lower-stratosphere (LS) for global change monitoring. It will observe submillimeter transitions for chemical studies of the stratosphere. The Aura-MLS adopts ambient-temperature double-sideband mixers operational at 118 GHz for temperatures and pressures, at 190 GHz for H_2O and HNO_3, at 240 GHz for ozone and CO, at 640 GHz for ClO, HCl, BrO, HO_2, and N_2O, and at 2.5 THz for OH. The antenna scans the atmosphere from 2 km to 60 km. The size of the primary reflector is the same as that of UARS-MLS (except 2.5 GHz), which provides a vertical resolution of 1.5 km in the 640 GHz band.

Other new proposals of submillimeter limb-emission sounder are discussed also in ESA and European countries. Future missions will obviously utilize submillimeter waves that enable simultaneous observations of many trace species. In particular, high sensitivity will be essential for those missions to clarify trends of trace gases in mid-latitudes and to detect dynamical features of the atmosphere. It requires further developments toward more extended submillimeter measurements technology, including superconductive receivers of high sensitivity, and wide-band spectrometers of high resolution.

1.3 Objectives of the JEM/SMILES Mission

The JEM/SMILES mission has both engineering and scientific objectives as follows. While technical developments for SMILES are a challenging task that we believe will open new possibilities for future missions, emphasis is also put on scientific productivity of SMILES in atmospheric researches.

1.3.1 Demonstration of New Technology for Submillimeter-wave Limb-emission Sounder

JEM/SMILES will demonstrate the effectiveness of a highly sensitive instrument for submillimeter limb-emission sounding. Its high sensitivity is attributed to a low noise receiver with superconductor-insulator-superconductor (SIS) mixers operating in cryogenically cooled conditions (at 4.5 K). In order to realize a compact SIS receiver in space without a huge and massive storage tank of liquid helium, we have developed a mechanical 4 K cooler. Neither a superconductivity sensor nor a 4 K mechanical cooler has ever been flown in space until today. This is the most critical technology of the SMILES experiment. However, that is not all we need. Several other key techniques are needed, such as a high-precision antenna, submillimeter optics, submillimeter signal source, cryogenically cooled IF amplifier, and acousto-optic spectrometer, for all of which we have quite limited precedents of space use. The SMILES mission has an engineering objective to establish these key techniques toward a high-sensitivity submillimeter limb-emission sounder. The engineering usefulness will not be limited within applications to atmospheric sciences. They also will be utilized for future space science missions.

1.3.2 Demonstration of High-quality Data for Atmospheric Trace Gases

High sensitivity with the SMILES observation data will drastically reduce the errors in atmospheric volume mixing ratios retrieved for various molecular species. Figure 1.4 summarizes the result of simulation studies described in Chapter 4. With respect to ozone and HCl, the single-scan data that is available in every 53 seconds will be sufficient to retrieve their mixing ratios with errors significantly less than 5 percent (ozone) or 10 percent (HCl) at any latitudes. As for ClO, which is the most important ozone destruction species, the retrieval error levels estimated with the single-scan data are less than 30 percent at low and middle latitudes, and less than 10 percent for the ClO enhancement in the lower stratosphere at high latitudes.

For other less abundant species such as CH_3CN, HOCl, HO_2, HNO_3, and BrO, scientific data will be obtained from a half-day zonal mean for a 5-degree width in latitude, which is produced with 30 pieces of single-scan data. The retrieval errors estimated with such zonal mean are less than 10 percent for CH_3CN at low latitudes, and for HOCl globally. The error levels will be less than 30 percent for HO_2 in the equator and for HNO_3 at middle and high latitudes. Those for BrO remain at 50 percent levels at any latitudes, which however will be improved with observation data that is averaged over a longer period.

A new aspect of the SMILES data is the capability to measure ozone isotopes including ^{18}OOO and ^{17}OOO. For these two species, the retrieval errors are estimated to be less than 3 percent with respect to a model profile of their abundance based on the isotopic ratio of oxygen atoms in the ocean water.

1.3.3 Delivery of Useful Database for Atmospheric Researches

The third objective is to demonstrate scientific values of SMILES sensitive measurements by shedding new light on chemical processes and regional interactions, particularly in

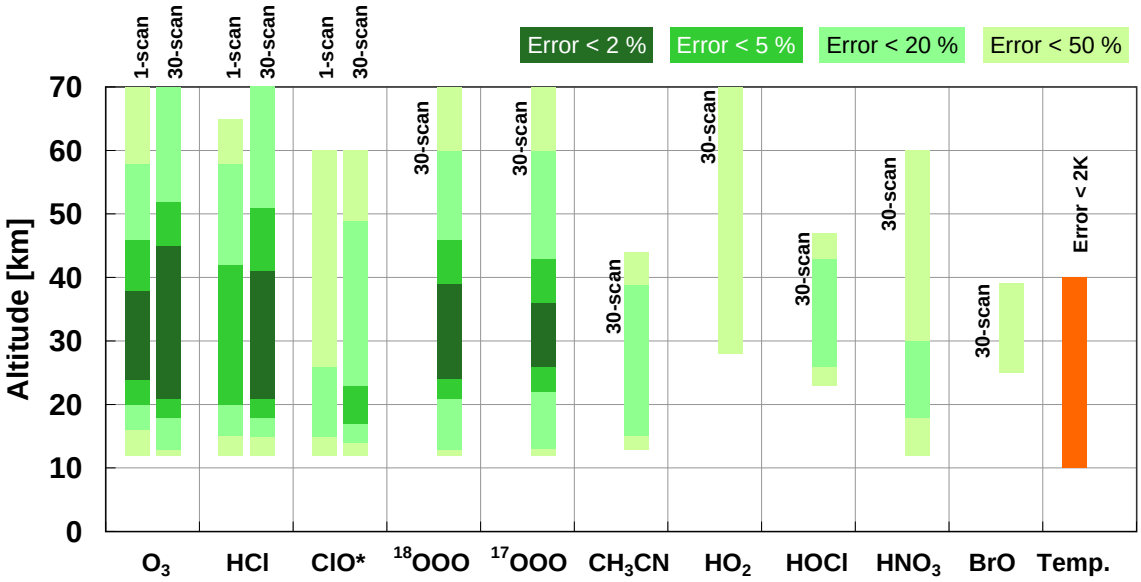

Figure 1.4 Altitude coverage of the JEM/SMILES data estimated from preliminary results of simulation studies assuming 0°N standard profile for each molecular species except for ClO for which the standard profile for polar region is assumed. Refer to Chapter 4 for more details.

the equatorial and in the northern high-latitude regions. SMILES data will enable us to investigate the chlorine and bromine chemistry and the HOx chemistry around the polar vortex region and over the equatorial and mid-latitude regions. The SMILES mission also provides a database for ozone variations in time and position around the upper troposphere and lower stratosphere (UT/LS). SMILES' wide-band and high-resolution spectroscopic data also enables us to investigate the isotopic compositions of ozone. The enrichment of rare isotopes in altitude distribution is reported and expected to reflect some unknown atmospheric processes. Chapter 2 will describe SMILES scientific objectives in detail.

1.4 Overview of the JEM/SMILES Mission

1.4.1 The ISS, JEM, and Measurement Coverage of SMILES

Figures 1.5 and 1.6 show the configurations of the ISS and JEM, respectively. JEM is attached to the front side of the ISS. Scientific experiments will be conducted both in the Pressurized Module (PM) and on the Exposed Facility (EF). JEM-EF has 10 interface ports to accept experiment payloads, four of which are on the front side of the ISS. The use of the interface ports is shared between Japan and the United States. The AO to which the SMILES proposal was submitted was for the first use of four Japanese interface ports. Maximum envelope specified for a JEM-EF experiment unit is 0.8 m (W) × 1.0 m (H) × 1.85 m (L). Maximum allowable mass is 500 kg. Services such as electricity, liquid coolant, and data communications including the Ethernet are to be supplied through the EF interface ports.

The ISS has a circular orbit with an inclination angle of 51.6°. Most scientific experiments will be conducted while the ISS is in the inertial flight condition to meet microgravity requirements. It results in a steady decrease in altitude, and re-boosting is needed periodically. The optimum operational altitude of the ISS and the re-boosting period depends

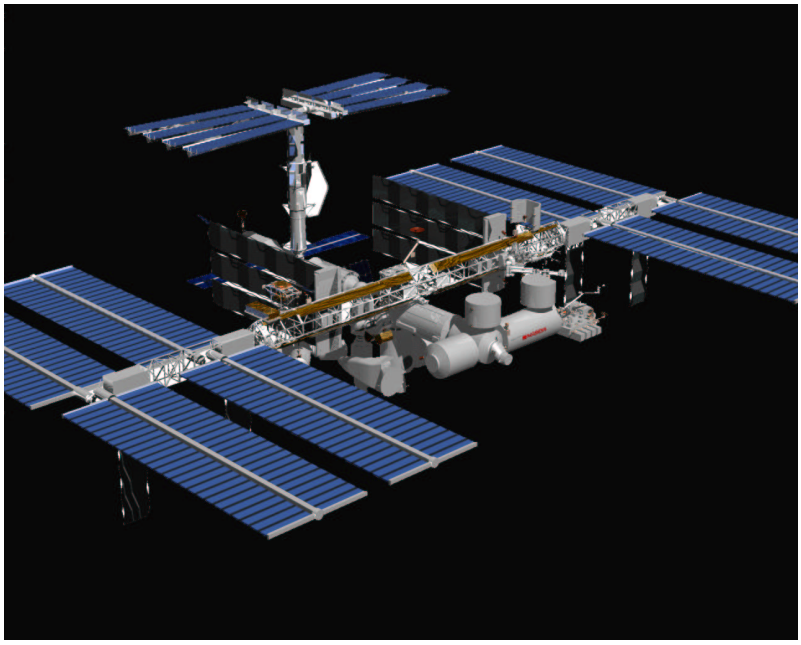

Figure 1.5 Artistic view of the International Space Station (ISS).

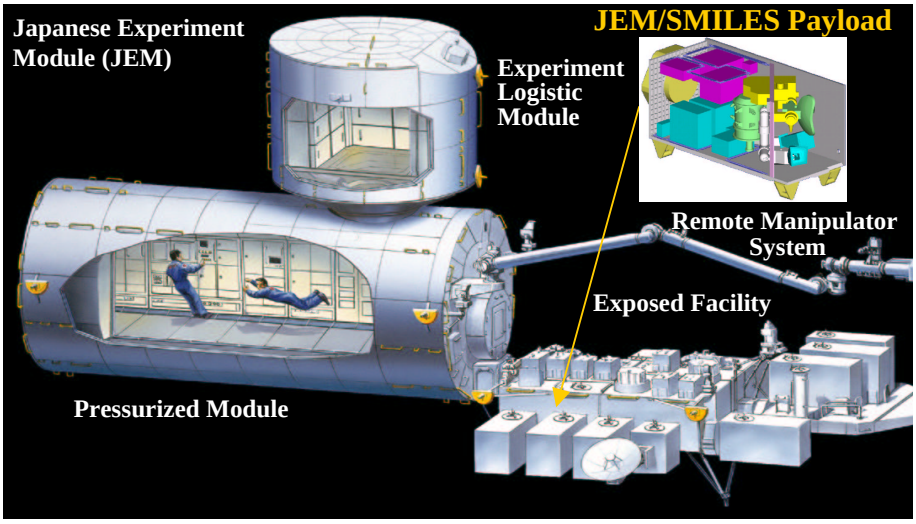

Figure 1.6 Japanese Experiment Module (JEM) and Exposed Facility (EF).

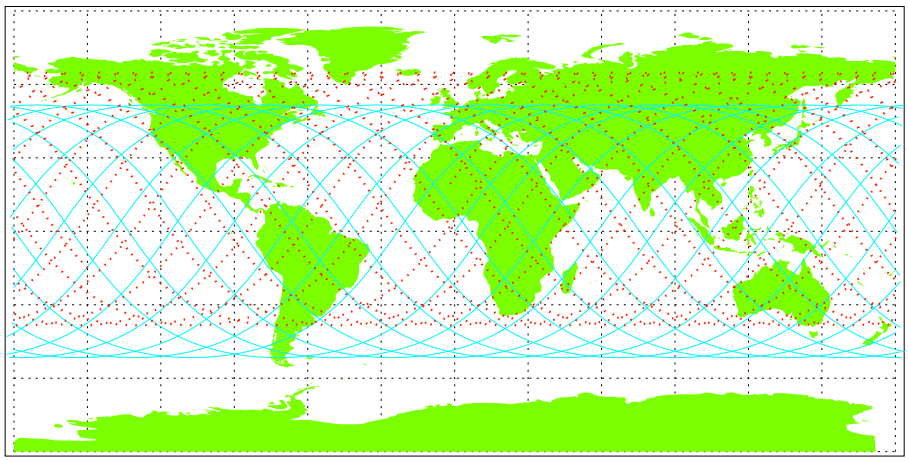

Figure 1.7 World map of orbit and measurement positions of JEM/SMILES.

on the solar activity, which affects the Earth atmosphere.

With respect to the attitude of the ISS, a set of Control Moment Gyros (CMG) will work to keep the ISS in the Torque Equilibrium Attitude (TEA). No thrusters are operated while the ISS is in the microgravity mode. Maximum range of operational attitude, which is defined by deviations from the Local-Vertical-Local-Horizontal (LVLH) attitude, is specified as $-20°$ to $+15°$ in pitch, and within $\pm 15°$ both in yaw and roll. Changes in the operational attitude during the orbital period of 93 minutes can be approximated by sinusoidal oscillations with amplitude less than $2°$ (peak-to-peak) in each axis [*Treder*, 1999].

For limb-emission sounding, variations in yaw are not critical, but those in pitch and roll have to be canceled by adjusting the initial angle of the antenna scanning. The initial angle will be calculated on the ground and commanded to SMILES, based on the predicted attitude of the ISS (and of SMILES). The ISS attitude estimation accuracy is described as $0.5°$ (3σ) at the ISS navigation base, and $3.0°$ (3σ) at attached payloads (see Table 3.6). These are knowledge errors in determination of absolute attitude. With its own Star Tracker (STT) in SMILES, we will be able to predict the SMILES attitude with the accuracy of $0.5°$ (3σ). This error corresponds to about 20 km at the atmosphere (for the ISS altitude of 407 km). Therefore, the mechanical adjustment of the initial angle is not sufficient to ensure the antenna to scan an exact height range of the atmosphere. Current design of the antenna scan pattern (see Section 3.2.1) includes a margin of +35 km, and -30 km to ensure observations for 10 km to 60 km.

Another critical issue is stability of the ISS attitude while a single scan is performed in 53 s. The attitude change rate is specified as $\pm 0.002°\mathrm{s}^{-1}$. This corresponds to a deviation of around $0.1°$ in a single scan, which is the same size as the half-power beam-width of the antenna. There is no hardware to compensate this deviation on board, although the STT measures it every second. Some necessary compensation should be done in data processing on the ground.

In order to measure high-latitude regions, the antenna beam is tilted $45°$ left from the direction of orbital motion. This design enables SMILES to observe latitudes from $38°$S to $65°$N (for cases when yaw attitude is nominal). Figure 1.7 shows measurement positions along the ISS orbit. In this case, however, the antenna beam is interfered with a rotating solar paddle of the ISS in every orbit. The latitude of observation points where

Table 1.1 Objective trace gases and their observation frequencies considered for JEM/SMILES. Local frequency is taken at 637.32 GHz.

Species	624.32 -625.52 GHz Band-A	625.12 - 626.32 GHz Band-B	649.12 - 650.32 GHz Band-C
O_3	625.37	625.37	-
ClO	-	-	649.45
HCl	624.98 (^{37}Cl)	625.92 (^{35}Cl)	-
HOCl	625.07	-	-
^{81}BrO	624.77	-	650.18
HO_2	-	-	649.70
H_2O_2	625.04	-	-
HNO_3	624.48, 624.78	-	650.28
SO_2	624.89	625.84, 626.17	649.24
CH_3CN	624.8	-	-

Mode-1: Band-A and Band-B
Mode-2: Band-A and Band-C
Mode-3: Band-B and Band-C

the interference occurs moves according to the solar angle. Average unobservable duration at each local time and position is estimated to be less than 10 %.

1.4.2 Objective Species and Measurement Frequency

Many of important stratospheric trace species, such as ozone, ClO, HCl, HOCl, BrO, HO_2, O_3-isotopes, have emission spectra in a submillimeter region around 640 GHz, and the atmospheric opacity is comparatively lower around this region. On the other hand, a millimeter region around 300 GHz is better for measurements of ozone, water vapor, and oxygen in the lower stratosphere (LS) and upper troposphere (UT), because of lower opacity in the millimeter region. But high sensitivity is not critical for detection of these abundant gases. Therefore, we have prioritized the submillimeter measurements of stratospheric trace gases for the SMILES mission. Table 1.1 shows trace gases observed in the 640 GHz region, which is divided into three frequency bands. Two bands are located in the lower sideband (Band-A and Band-B) and the other is in the upper-sideband (Band-C) in respect of a single submillimeter local oscillator fixed at 637.32 GHz. Both sidebands are detected separately by means of a single sideband (SSB) filter. Two of the three bands are selected at a time and delivered to the Acousto-optic Spectrometer (AOS). The first IF is selected to be 11–13 GHz. The IF instantaneous bandwidth is much narrower than that required to completely involve all of important species in the 640 GHz region. This is unavoidable for protecting the IF band against strong environmental electromagnetic fields that are anticipated in the ISS and JEM.

Figure 1.8 shows the arrangements we have made for SMILES observation bands. There are some disadvantages in this frequency design. For example, we cannot include an N_2O emission line at 652.83 GHz within our measurement band due to the restricted IF bandwidth mentioned above. In addition, no suitable emission lines for measuring water vapor are available around 640 GHz. Since water vapor measurements in the LS/UT region are particularly important in the tropics, we are investigating the possibility of estimating

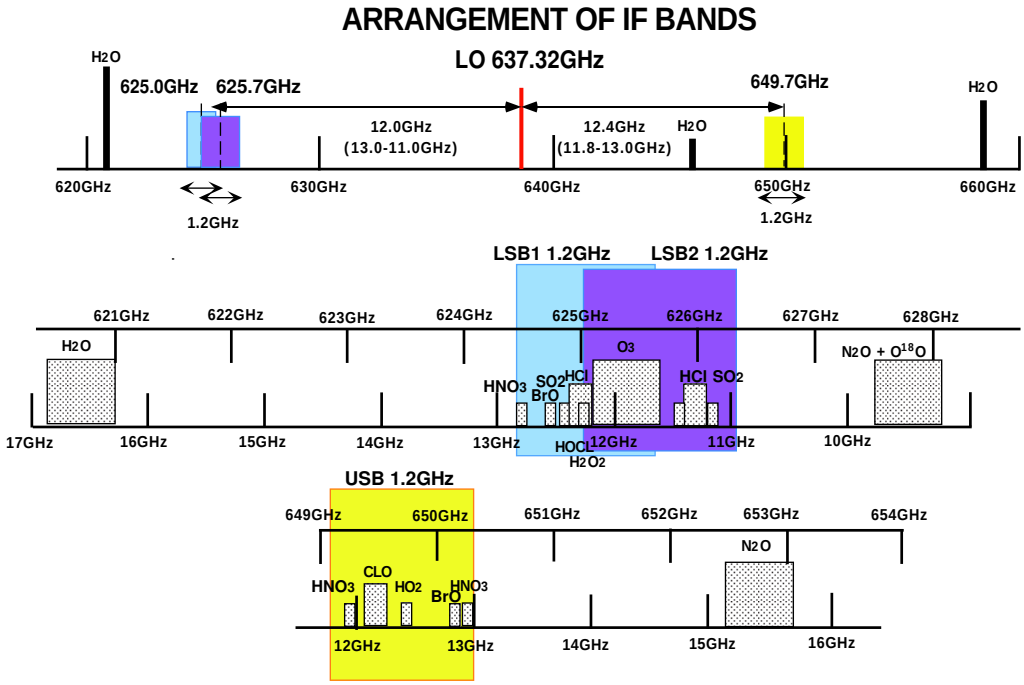

Figure 1.8 Arrangement of IF bands.

water vapor by means of continuum emissions around 640 GHz. Furthermore, no suitable oxygen-molecule line is available in the SMILES measurement band, which is usually used for measuring atmospheric temperatures and pressures. Nonetheless, our simulation has shown that the temperatures and pressures could be derived from the retrieval process of measured species (see Chapter 4 in detail).

1.4.3 SMILES Payload

The SMILES payload is composed of the Submillimeter Antenna (ANT), Submillimeter Receiver (SRX), IF Amplification Section (IFA), Radio Spectrometer (AOS), Star Tracker (STT), Data Processing and Control Section (DPC), and Payload Bus (BUS).

The ANT is an offset Cassegrain antenna with an elliptical reflector of 40 cm x 20 cm, which gives an elliptical beam with a half-power beam-width (HPBW) of 0.08° in elevation and 0.17° in azimuth. The antenna scans the atmosphere vertically at the rate of 0.1125°s^{-1}, and the atmospheric signals are accumulated within the AOS in every consecutive 0.5 s. This gives a sampling interval of 0.056° (corresponding to 2.1-4.1 km at the tangent point). The effective vertical resolution to the atmospheric layer is calculated as 0.096° (corresponding to 3.5-4.1 km), which includes the effects of the antenna running in 0.5 s and the broader horizontal response of the antenna. Surface accuracy of the main reflector is designed to be 15 μm, which gives the beam efficiency larger than 90 % for a 2.5-times HPBW area.

The SRX is composed of the Ambient Temperature Optics (AOPT), Cryo-electronics Unit (CRE), Ambient Temperature Amplifiers (AAMP), Helium Gas Compressors (HECP), Submillimeter LO Controller (SLOC), CRE Control Electronics (CREC), and Stirling & JT Drive Electronics (SJTD). The AOPT combines quasi-optically the submillimeter signals from the antenna and local oscillator (LO), while terminating the image band to the

2.7 K cosmic microwave background. Sideband separation, higher than 20 dB, is made by a new-type of Martin-Puplett interferometer. The submillimeter LO is generated by a frequency tripler and doubler associated with a phase-locked Gunn-diode oscillator operated at 106.22 GHz. A quasi-optical circular polarizer, which is composed of a mirror and wire-grid, is integrated in the AOPT to reduce spectral baseline ripples due to standing waves.

The CRE includes two SIS mixers and four IF amplifiers. The SIS mixers are based on Nb/AlOx/Nb devices and equipped with a corrugated feed horn. They are integrated into a block of submillimeter optics cooled at 4.5 K. Two SIS mixers, by detecting perpendicular polarizations each other, observe the upper sideband and lower sideband separately. Cryogenically cooled IF amplifiers are based on high-electron-mobility transistor (HEMT) devices. Two of them are put at 20 K stage, and another two at 100 K stage. They are operated at 11–13 GHz with a noise temperature of about 15 K (for amplifiers cooled to 20 K) and 40 K (for amplifiers cooled to 100 K). The noise temperature of the whole SMILES system is mainly determined by the performance of the SRX. The noise temperature of the SRX is estimated around 500 K for single sideband measurements.

The SIS mixers and IF amplifiers are cooled by a 4 K mechanical cooler, which is composed of a two-stage Stirling cycle and Joule-Thomson cooler. The former has a cooling capacity of 1 W at 100 K, and 200 mW at 20 K. The latter has a capacity of 20 mW at 4.5 K. The total power consumption is about 300 W, including a conversion loss in the power supply. The total mass of the cooler is 90 kg, including the cryostat,

Table 1.2 Major design parameters of the SMILES payload.

RF Frequency (LSB)	624.32 - 626.32 GHz
RF Frequency (USB)	649.12 - 650.32 GHz
System Noise Temperature	Less than 700 K (SSB)
Integration Time	0.5 sec for each observation point
Input Signal Intensity	0–300 K in brightness temperature
Spectral Resolution	1.8 MHz (FWHM)
Spectral Coverage	1,200 MHz × 2
Antenna Aperture	0.4 m (vertical) × 0.2 m (horizontal)
Effective Antenna Beam-width	0.096° (HPBW, elevation)
Instrumental Height Resolution	3.5 km – 4.1 km (nominal)
Instrumental Error in Tangent Height	0.76 km (rms, bias) 0.34 km (rms, random)
Sensitivity in Brightness Temperature (for each scan)	about 0.7 K (rms) for $T_b < 20$ K about 1.0 K (rms) for $T_b > 20$ K
Accuracy in Brightness Temperature (for each scan)	about 1 K (rms) for $T_b < 20$ K about 3% (rms) for $T_b > 20$ K
Data Rate	Less than 200 kbps
Measurement Height	$10 - 60$ km
Observation Latitudes	65°N - 38°S (nominal)
Mission Life	1 year
Power Consumption	about 800 W including payload bus
Payload Weight	less than 500 kg
Payload Size	0.8 m (W) × 1 m (H) × 1.85 m (L)

helium gas compressors, and power supply. The cryostat, which includes three different temperature stages (4.5 K, 20 K, and 100 K), cold-head of the two-stage Stirling cycle, heat exchangers for the Joule-Thomson cooler, and sophisticated structures for thermal isolation, is designed to be about 500 mm long and 350 mm in diameter.

The submillimeter signal of the atmosphere in Band-A, Band-B, and Band-C is converted to the first IF at 11–13 GHz. It is further down-converted to the second IF at 1.55–2.75 GHz, and delivered to the Radio Spectrometer (AOS). The AOS has two units of signal analyzers; each has a frequency coverage of 1.2 GHz over 1500 channels. The spectral resolution is 1.8 MHz (FWHM) while the channel separation is about 0.8 MHz/channel.

SMILES observation data combined with housekeeping and attitude information are continuously transmitted via satellite link with a data rate of about 200 kbps. The total power consumption and mass, including all components of the payload bus, are estimated to be about 800 W and less than 500 kg, respectively. Table 1.2 shows major design parameters of the SMILES payload.

1.4.4 Data Processing and Distribution

SMILES raw data including atmospheric spectra and housekeeping items are transmitted to the Tsukuba Space Center (TKSC), NASDA, via the Data Relay and Test Satellite (DRTS), a Japanese relay satellite. At first, the raw data are edited to generate Level_0 data, which are packed into units each corresponding to a certain portion of an orbit. The data will be checked for overlaps and losses, and necessary flags will be added. The quantity of Level_0 data is estimated to be 2 GB/day. Secondly, the Level_0 data will be converted to Level_1 data, which comprise engineering values, spectral temperatures, calibration data, and measurement parameters including estimated tangent heights and positions. The size of Level_1 data will be 4 GB/day. In the third step, the height profiles of volume mixing ratios are generated along the orbital trajectory for all target gases, which are processed from the Level_1 data and ancillary information by means of a retrieval algorithm. This product is called Level_2 data, and the size will be 94 MB/day or 23.5 GB/year for an operation rate of 70 %. All of the first data processing will be made at NASDA/TKSC within the experimental period. The data is transmitted to the Communications Research Laboratory (CRL), the Earth Observation Research Center (EORC) of NASDA, and the University of Bremen, a partner of the JEM/SMILES project. These three cooperative institutions will respectively produce Level_3 data: averaging over a gridded area of latitude and longitude in every week or month; collocation with other measurements such as EOS-Aura; combination with model-derived temperatures and pressures; combination with assimilation study data set. After the SMILES operation is completed, all of the data will be archived in the CRL, and reprocessing will be made if necessary. Figure 1.9 shows the SMILES data transmission, processing and distribution. Users in prior registration can access the data provided at the institution's site via electronic lines. The data stored in CD-ROMs will be distributed to all users on request.

1.4.5 Calibration and Validation

In-orbit calibrations will be made for the intensity and frequency of submillimeter signals in every scan of the atmosphere. The atmospheric intensity is calibrated by comparison with reference data for "hot load" and "cold sky". For this purpose a carefully designed "hot load" is used, which can be regarded as a perfect submillimeter blackbody. Potential frequency shift of AOS is measured also in every scan with a reference signal delivered from a well-stabilized comb generator. This frequency calibration gives a real relation between

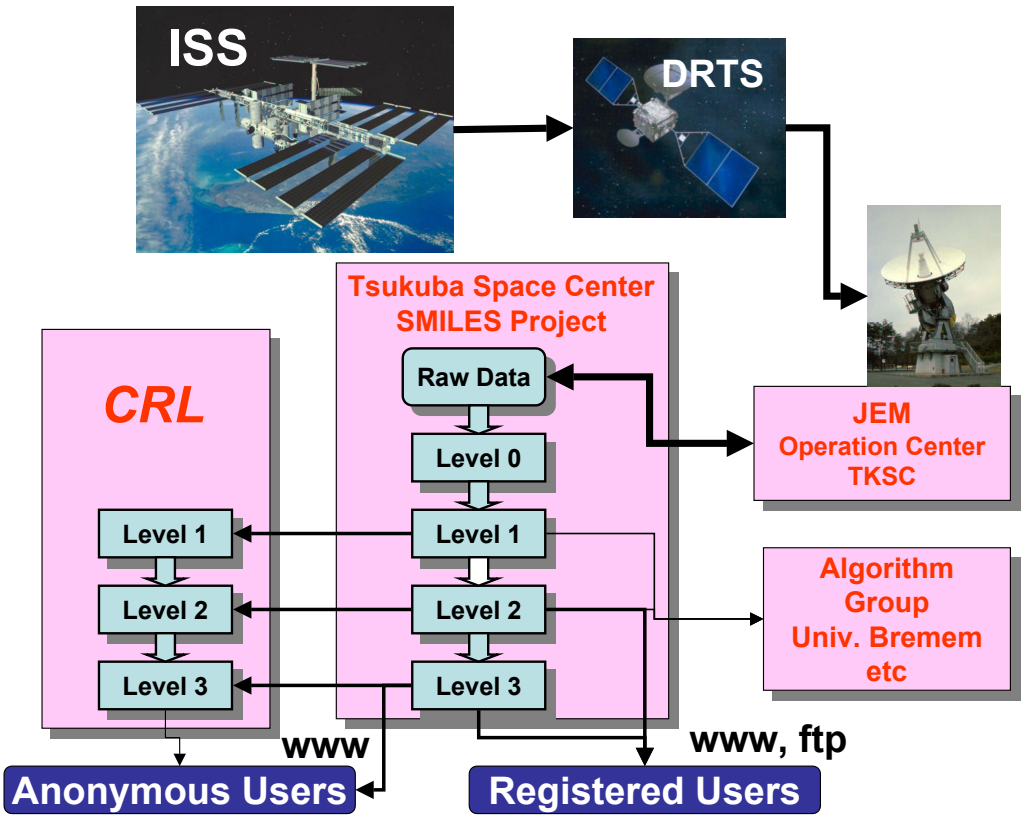

Figure 1.9 JEM/SMILES data transmission, processing and distribution.

the channel number of AOS and frequency. However, these are minimum processes to establish the accuracy of SMILES observation data. There remain several other factors to affect the absolute accuracy of retrieved quantities for each species, including optimization of detail processes in retrieval algorithm. Cross-calibration with other satellite data, such as EOS-Aura-MLS, is therefore very important. Furthermore, scientist groups supported by NASDA and the CRL would contribute to validation studies for the SMILES data. Validation studies will be made mainly by correlative measurements from the ground, balloons, aircraft, and satellites.

- Ground-based observations will be made at existing sites including; Fairbanks in Alaska (CRL, University of Alaska), Tsukuba (National Institute for Environmental Studies: NIES), Rikubetsu (NIES, Solar-Terrestrial Environment Laboratory of Nagoya University), and Indonesia (NASDA, Japanese universities) . Observations will be conducted with ozonesondes, lidars, Fourier Transform spectrometers, and short millimeter-wave radiometers. Measurements by international networks, such as NDSC stations, will also be valuable.

- Field campaign experiments will be planned in a high-latitude area and in an equatorial area, by synthesizing ground-based sensors, sondes, balloon-borne sensors, and airborne sensors. The CRL is developing a balloon-borne submillimeter limb-emission sounder, and the University of Bremen is operating an airborne submillimeter sounder.

- Cross-validation with other satellite sensors, such as EOS-Aura, will also be considered.

1.4.6 Data Retrieval Method

Rodgers' optimal estimation method [*Rodgers*, 1976; *Rodgers*, 1990] will be adopted as a retrieval algorithm of SMILES data. In applying the method to SMILES, there are the following items to be considered.

- Elimination of background emissions due to thermal emissions and the sidelobe response of the antenna.
- Elimination of effects of residual standing waves.
- Compensation for potential attitude irregular variations.
- Estimation of accurate tangent height.
- Nonlinear effect on the radiation transfer of abundant species.

In order to estimate measurement errors for target species, and to find what factors are critical to them, the CRL have conducted simulation studies since 1999. The simulator consists of three parts, i.e. Forward Model I, Forward Model II, and Inversion Model. The Forward Model I gives the antenna temperature by calculating the radiative transfer formula with assumed atmospheric conditions and antenna response pattern. The Forward Model II simulates the output signal of the system, using the antenna temperature calculated by the Forward Model I, and including the effects of system noise temperature, optical losses, standing waves, image bands, AOS response function, calibration, digitization, etc. After the Level_0-to-Level_1 simulation processing, the Inversion Model retrieves height profiles based on Rodgers' optimal estimation method. The simulator enables us to estimate the measurement capability of SMILES, the degree of errors caused by various conditions of the atmosphere and instrument, and the speed of data processing. The simulator is also useful in developing and checking the data retrieval algorithm. It also can be used to estimate post-flight calibrations and validations.

The University of Bremen has also developed its own retrieval algorithm and conducted thorough comparisons with the CRL simulator. The comparisons have shown the two systems are generally consistent with minor differences to be improved. Furthermore, the University of Bremen has proposed the feasibility to retrieve atmospheric temperatures and pressures successfully from SMILES data. The details are described in Chapter 4.

Accurate spectroscopic information, such as frequency, spectral intensity, pressure broadening parameters, and their temperature dependence, is essential for decreasing errors in the retrieval processing. A spectral catalogue published by the Jet Propulsion Laboratory (JPL) [*Pickett et al.*, 1992] gives the parameters. However, as far as submillimeter transitions are concerned, the accuracy of those parameters is not experimentally established yet. The exact values of the parameters are to be measured by laboratory experiments. This is also indispensable part of the SMILES project, and dedicated experiments are being conducted at the Ibaraki University and Fukui University.

1.5 Development Schedule and Operation Plan

JEM/SMILES is to be carried to the ISS in 2007 aboard the H-II Transfer Vehicle (HTV) that is launched by a boost-up version of H-IIA rocket from the NASDA launch site in the Tanegashima Island, Japan. Figure 1.10 shows the schedule of the SMILES development

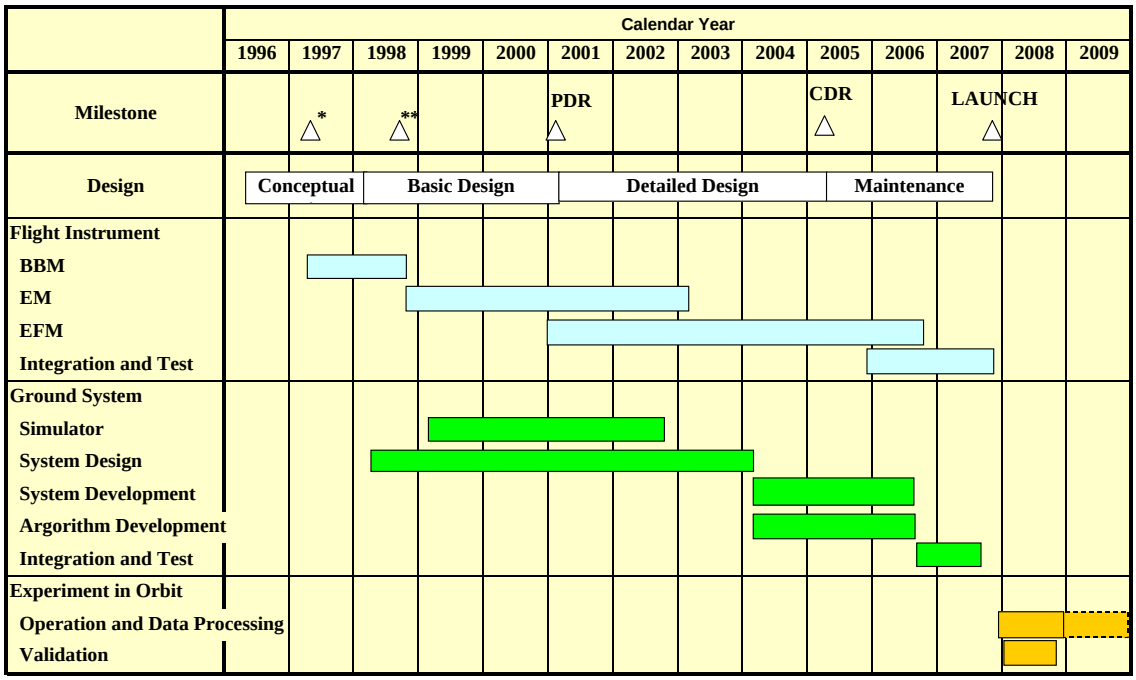

Figure 1.10 Schedule of JEM/SMILES.

and experiment. In order to shorten development period and to decrease cost, simpler and effective ways have been pursued in all areas of the project: such as the EFM approach in which some parts of the engineering model (EM) be used as the flight model (FM) after refurbishing. Although instrumental development is generally making progress in line with the schedule, the actual launch of SMILES is dependent on many programmatic issues including the future plans of the ISS, JEM, and HTV.

The official mission duration of SMILES is one year in space. However, if the next mission is not ready and SMILES is still good enough to continue its operation, there could be a chance to extend the mission beyond one year. SMILES should be operational continuously during the whole mission period except for the initial phase of mission check-out. But in reality, we foresee several cases that may hamper continuous observations. The ISS altitude decreases gradually during its inertial flight, and the ISS is re-boosted periodically. In this case, the usual stability of the ISS attitude is not guaranteed. Secondly, the ISS attitude will change largely while the Space Shuttle is moored at the ISS, which makes the SMILES antenna look at beyond the limb atmosphere. Thirdly, some restrictions could be imposed on SMILES concerning available amount of resources from the ISS or JEM, specifically in electricity and data communications. This also could affect normal observations of SMILES.

1.6 Mission Organization

The National Space Development Agency of Japan (NASDA) and Communications Research Laboratory (CRL) are main organizations cooperatively responsible for the overall SMILES experiment. The Space Utilization Research Program (SURP) and Space Utilization Research Center (SURC), both in NASDA/TKSC, and the CRL are responsible for the payload development and flight operation of SMILES. The Earth Observation

Table 1.3 JEM/SMILES Project Key Personnel.

PERSONNEL	AFFILIATION	RESPONSIBILITY
Masuko, Harunobu masuko@crl.go.jp	CRL, NASDA	Principal Investigator
Inatani, Junji inatani.junji@nasda.go.jp	NASDA/TKSC	Hardware development
Satoh, Ryouta satoh.ryouta@nasda.go.jp	NASDA/TKSC	Project management
Manabe, Takeshi manabe@crl.go.jp	CRL	Hardware development
Suzuki, Makoto suzuki@eorc.nasda.go.jp	NASDA/EORC	Ground system development
Shiotani, Masato shiotani@kurasc.kyoto-u.ac.jp	Kyoto University	Chief scientist
Shibasaki, Kazuo sibasaki@eorc.nasda.go.jp	NASDA, Kokugakuin University	Validation program
Klaus Künzi kunzi@physik.uni-bremen.de	University of Bremen	Scientific cooperation
Amano, Takayoshi amano@mito.ipc.ibaraki.ac.jp	Ibaraki University	Spectroscopic measurements

Research Center (EORC) and Earth Observation Program Department (EOPD), both in NASDA, share development of the ground system, data processing, and distribution of the Level_1, Level_2, and Level_3 data, with the CRL and NASDA/TKSC. They also support science teams for validation and data analysis. The CRL also conducts development of the ground system, data processing, and distribution of another type of Level_3 data, in addition to archiving of the whole SMILES products. The CRL also participates in the validation activities. In addition, the Nobeyama Radio Observatory (NRO), in the National Astronomy Observatory of Japan (NAO) technically supports the development of the SIS mixers. The Ibaraki University supports the project by laboratory measurements of spectroscopic parameters. The University of Bremen, in Germany, is an international collaborator participating in simulation studies, algorithm development, validation studies, and science. The University of Bern, in Switzerland, is collaborating with the CRL to develop the submillimeter optics for the SMILES receiver. Table 1.3lists the key personnel of the SMILES project.

References

ATMOS-C1 Team, ATMOS-C1 Mission Proposal, *Earth Observation Committee/Earth Science & Technology Forum* (forum@hq.esto.or.jp), *Earth Science and Technology Organization (ESTO)* 97OA1-D003A, 1997.

Pickett, H., R. Poynter, and E. Cohen, *Submillimeter, Millimeter and Microwave Spectral Line Catalog: Revision 3,* Tech. Rep. 80-23, Jet Propulsion Laboratory, California Institute of Technology, Pasadena, CA, USA, 1992.

Rodgers, C. D., Retrieval of atmospheric temperature and composition from remote measurements of thermal radiation, *Rev. Geophys. and Space. Phys.,14*, 609-624, 1976.

Rodgers, C. D., Charactrization and error analysis of profiles retrieved from remote sensing measurements, *J. Geophys. Res., 95* (D5), 5587-5595, 1990.

Treder, A. J., Space Station GN&C Overview for Payloads, *Space Technology and Application International Forum*, 1999.

United Nations Environmental Programme, *The 1987 Montreal Protocol on Substances That Deplete the Ozone Layer*, 1987.

Waters, J. W., Microwave Limb Sounding, in *Atmospheric Remote Sensing by Microwave Radiometry*, edited by M. A. Janssen, John Wiley and Sons, Inc., 383-496, 1993.

Waters, J. W., W. G. Read, L. Froidenvaux, R. F. Jarnot, R. E. Cofield, D. A. Flower, G. K. Lau, H. M. Pickett, M. L. Santee, D. L. Wu, M. A. Boyles, J. R. Burke, R. R. Lay, M. S. Loo, N. J. Livesey, T. A. Lungu, G. L. Manney, L. L. Nakamura, V. S. Perun, B. P. Ridenoure, Z. Sippony, P. H. Siegel, R. P. Thurstans, R. S. Harwood, H. C. Pumphery, and M. J. Filipiak, The UARS and EOS Microwave Limb Sounder (MLS) Experiments, *J. Atmospheric Science, 56* (2), 194-218, 1999.

Waters, J. W., An Overview of the EOS MLS Experiment, *JPL D-15475*, Version 1.1, (http://mls.jpl.nasa.gov/), October 1999.

World Meteorological Organization (WMO), Scientific Assessment of Ozone Depletion: 1998, *Global Ozone Research and Monitoring Project* – Report No. 44, 1998.

2 Scientific Objectives

2.1 Summary

One of the most unique characteristics of the JEM/SMILES observation is its high sensitivity in detecting atmospheric limb emission of the submillimeter wave range. Molecular species to be observed by JEM/SMILES are: normal O_3, isotope O_3, ClO, HCl, HOCl, BrO, HO_2, H_2O_2 and HNO_3 (See Section 4.2.4). Thus, the JEM/SMILES mission is distinguished as that focusing on the detailed halogen chemistry related to ozone destruction. Spatial coverage is near global, but there is no observational chance at polar latitudes (See Section 3.2.2). In spite of this limitation, we expect high possibility to make measurements within the elongated polar vortex in the northern hemisphere. Vertical resolution is supposed to be about 3 km. Detectable range for each of the molecular species with height will be discussed in detail in Section 4.

In view of the above-mentioned status, we focus on the following scientific targets for the JEM/SMILES mission.

- Variation and its impact of radical species
- Isotopic composition of ozone

JEM/SMILES will make measurements on several radical species crucial to the ozone chemistry. Some of them have never be seen by any other satellite measurements, and the JEM/SMILES mission will be the first to detect them such as BrO. It would be very interesting to see the space-time variations in the polar vortex and even in the background situation. Overall observations of these radical species will provide us further insight into the ozone chemistry in the middle atmosphere.

Another possible scientific objective using the JEM/SMILES data is on the isotopic composition of ozone. Unusually high enrichment in most of the heavy ozone isotopomers has been puzzling problem and we still don't have a clear answer for this. The JEM/SMILES observation will provide us important findings to work out the puzzle of ozone isotope anomaly.

In the following, the background and detailed description for the JEM/SMILES scientific targets will be discussed.

2.2 Background

The earth system consisting of the atmosphere, the ocean, and the biosphere has been affected by natural and artificial perturbations. Resulting changes in the earth system become obvious in several places and in several parameters. Among those the middle atmosphere is one of the good places to sense such changes, since it has been known that there are some sensitive atmospheric parameters and minor species. In recent years we have found several important trends in the middle atmosphere, and now we need the synthetic understanding of these variations to project the future state of the earth system.

After the discovery of the Antarctic ozone hole in the mid 1980s, numerous observations from the ground, aircraft and satellites have been conducted to clarify the mechanism. One of the characteristic features is that the ozone hole is a typical phenomenon in the southern hemisphere where the polar vortex is stronger and the resulting temperature is colder than the northern hemisphere. However, in the 1990s, it has been reported that the late-winter ozone amounts in the Arctic have decreased significantly [*Newman et al.*, 1997].

Surrounding the Arctic ozone depletion, a decrease of lower stratospheric ozone at mid latitudes in the northern hemisphere has been noticed recently. In *WMO Scientific*

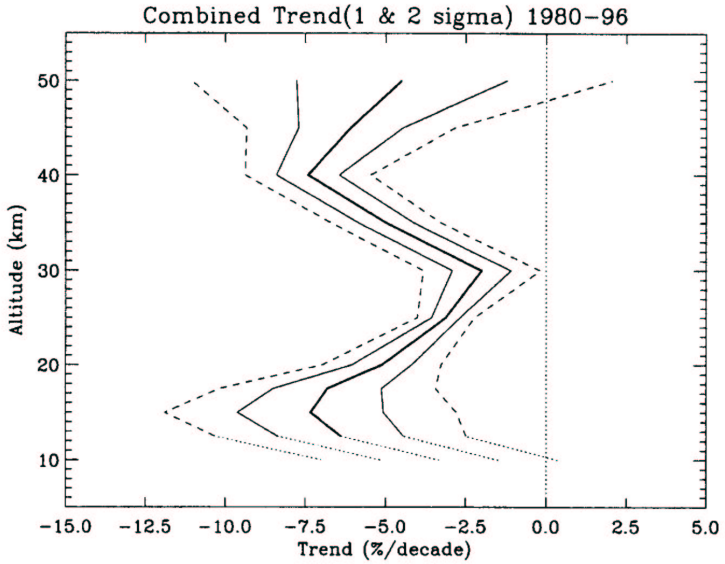

Figure 2.1 Estimate of the mean trend using all four measurement systems at northern mid-latitudes (heavy solid line). Combined uncertainties are also shown as 1 σ (light solid line) and 2 σ (dashed line) (After [*WMO*, 1999]]).

Assessment of Ozone Depletion [1999, vertical distribution of the mean trend in the northern mid latitude is presented (Figure 2.1). This figure shows the lower stratospheric trend with 7.5 % decrease for decade, in addition to the upper stratospheric trend which is driven by the accumulation of anthropogenic chlorine. The lower stratospheric trend is also supposed to be contributed by the increased chlorine and bromine loading. However, the quantitative understanding about this mid latitude decrease is still uncertain. At the same time a cooling trend in the lower stratosphere has been observed. It is supposed to be due to the ozone decrease in the lower stratosphere [*WMO*, 1999]. The cooling trend may also contribute to the decreasing trend in ozone, but quantitative argument is not satisfactory yet.

One of the most highlighted trends in the stratosphere is an increasing one in water vapor, though it is not directly related to the anthropogenic perturbation (*SPARC Assessment of Upper Tropospheric and Stratospheric Water Vapor* [2000]). The observations show that water vapor has increased at a rate of about 1 %/year (Figure 2.2). This increase may be attributed to an increase in methane entering the stratosphere, because water vapor in the stratosphere is produced by the methane oxidation. The increase in methane, however, is found to be far below what we expect from the observational increase in water vapor. Another idea to explain the water vapor trend is a control by the equatorial tropopause temperature, which can affect the concentration of water vapor entering the stratosphere, but this does not seem the case because the observations show the cooling trend in the equatorial tropopause temperature. Thus the mechanism of the water vapor trend has not been explained yet. Dvortsov and Solomon [2001] conducted a model calculation by taking account of the water vapor increase. They found that it can contribute to the cooling trend in temperature from the radiative aspect of water vapor and to the decreasing trend in ozone from the chemical role of it.

Associated with the mid latitude ozone depletion, the lower stratospheric ozone is sensitive to the volcanic aerosols. The Mt. Pinatubo eruption is a good natural experiment

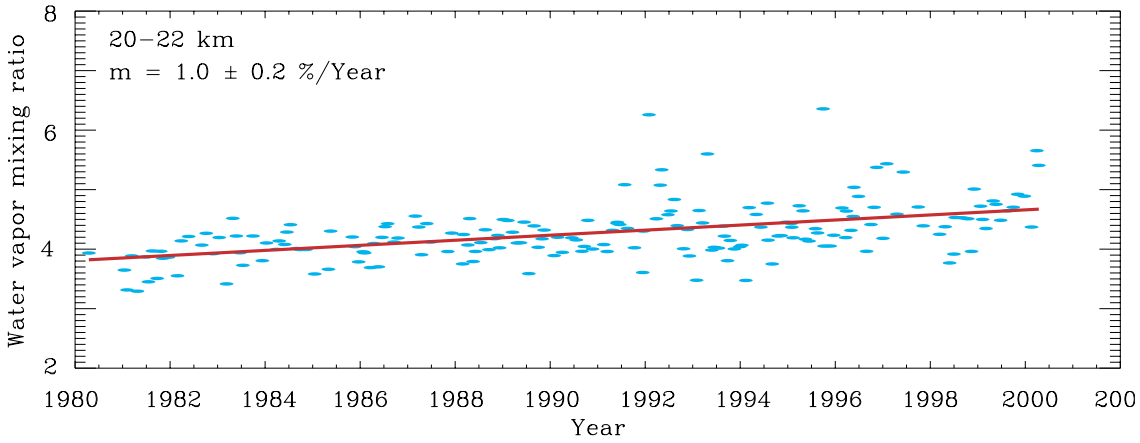

Figure 2.2 Time series of 20- 22 km layer averaged water vapor mixing ratio over Boulder. (After [*SPARC*, 2000]).

to learn its effect on the atmospheric dynamics and chemistry. After the eruption of Mt. Pinatubo in June 1991, significant total ozone decrease was observed. The eruption could modify the thermal structure of the atmosphere, then the general circulation, through the radiative effect. At the same time the increase of sulfuric aerosols may promote the heterogeneous chemistry around the tropopause region. Figure 2.3 shows a result from the two dimensional model with or without temperature variations and the aerosol effects

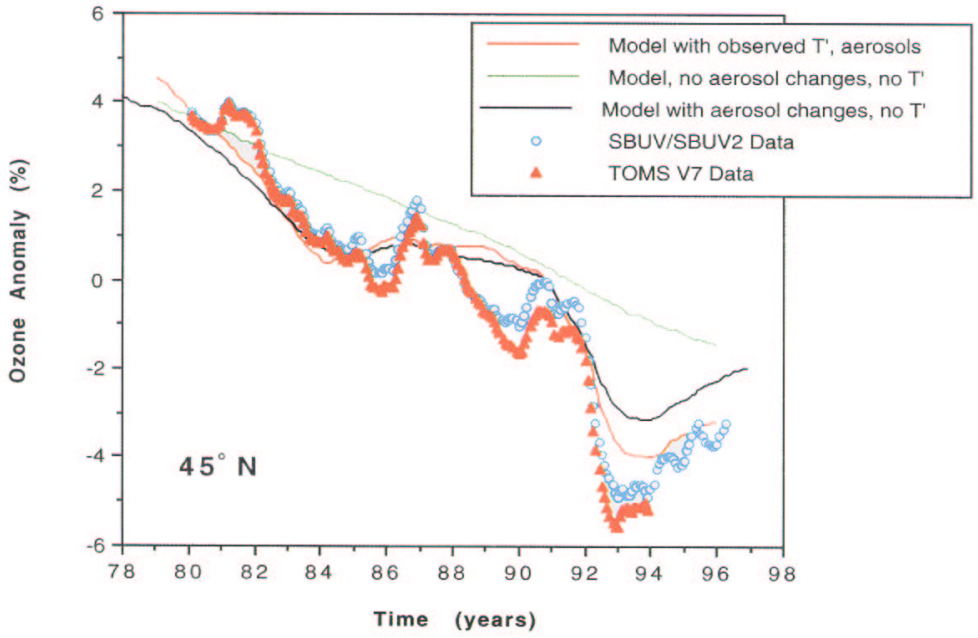

Figure 2.3 Observed and calculated total ozone anomalies from 1979 to 1997 at 45°N. (From [*Solomon et al.*, 1997].)

[*Solomon et al.*, 1997]. This suggests that chemical effects owing to the aerosol loading play a significant role in perturbing the ozone anomalies.

From a dynamical point of view, understanding the meridional circulation in the stratosphere is also very important. Most long-live trace species are emitted in the troposphere as natural or anthropogenic perturbations. These are transported into the stratosphere and are deformed there. Methane is oxidized in the upper stratosphere and produces water vapor which is an important minor species to affect radiative balance of the atmosphere. CFCs are also destructed in the upper stratosphere, resulting in the production of chlorine species which affect the ozone layer especially in the lower stratosphere polar region during the spring time. Therefore, investigation of the atmospheric meridional circulation is a key issue to know temporal and spatial distributions of the minor species and their effects on the atmosphere.

Particularly the upper troposphere and lower stratosphere (UT/LS) is an important region for the dynamical processes such as transport and mixing, because the photochemical time scale of ozone in UT/LS is comparable or longer than that of the dynamical time scale. Of course the chemical processes such as heterogeneous reactions on PSCs are crucial to understand the ozone distribution and variation in the lower stratosphere in association with the ozone depletion. It has recently been recognized that the meridional circulation around UT/LS should be understood from the global view of dynamics (Figure 2.4). *Holton et al.* [1995] presented an idea that the upward motion at equatorial

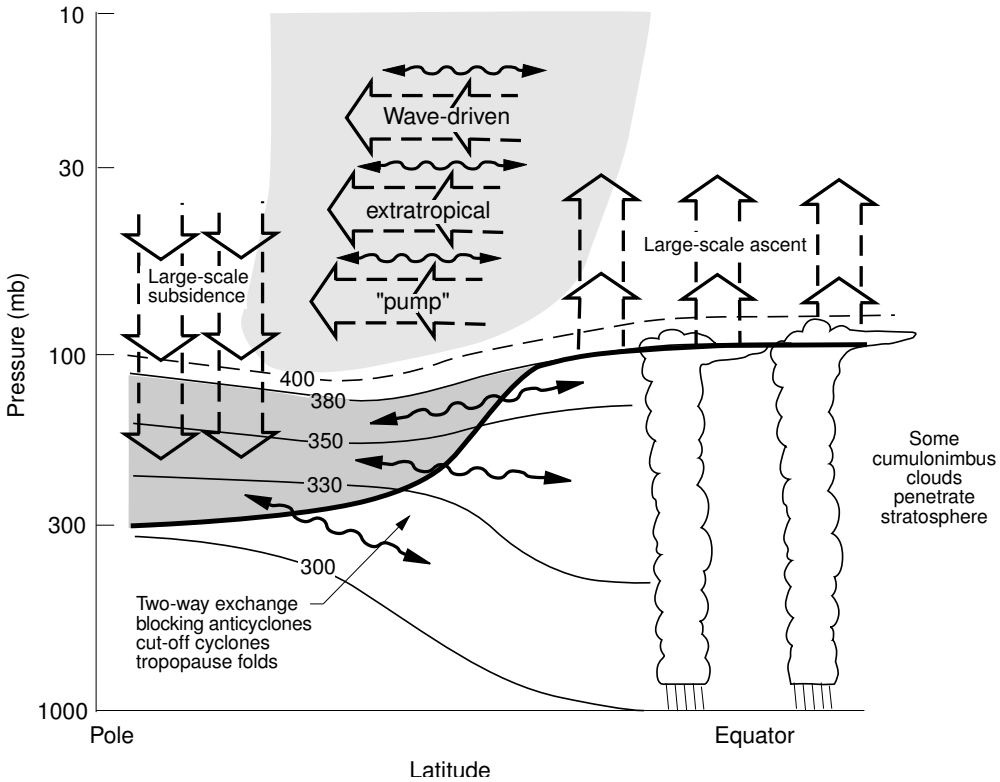

Figure 2.4 Dynamical aspects of stratosphere-troposphere exchange. The tropopause is shown by the thick line. Thin lines are isentropic or constant potential temperature surfaces labeled in kelvins. In detail, see *Holton et al.* [1995]

.

latitudes and the downward motion at mid- and high latitudes in the lower stratosphere are mainly driven by planetary wave induced torque. The meridional circulation is controlled by the strength of wave driving in the both hemispheres as the season goes by. At equatorial latitudes a modulation of the meridional circulation produces changes in the tropopause properties such as the tropopause height and the tropopause temperature. The manifestation of these combination is a recent finding of the so-called tape recorder signal in water vapor over the equator [*Mote et al.*, 1996].

All these factors affecting the earth's atmosphere system are closely connected with each other, but our recognition on these processes has just started; we don't know detailed inter-relation between the trends. We need comprehensive understanding of these variations to construct reliable models for the future earth system.

2.3 Radical Species in the Stratosphere

2.3.1 Introduction

Recently it has been widely recognized that ozone abundance in the lower stratosphere has crucially decreased. The Antarctic ozone hole has been observed since 1980's, the Arctic ozone depletion is another one over the past decade, and the mid latitude decrease trend in the northern lower stratosphere is slowly but certainly emerging. Current observational evidences and their understandings are summarized in detail in *WMO Scientific Assessment of Ozone Depletion* [1999]. What we have learned about the scenario of the ozone depletion is that the chlorine chemistry is crucial even in the lower stratosphere when the chemical processes such as heterogeneous reactions on PSCs occur.

One of the most successful results from the satellite was brought by the Microwave Limb Sounder (MLS) onboard the Upper Atmosphere Research Satellite (UARS). The MLS measurements provided the first global maps of stratospheric ClO, which should be observed when ozone is destructed by reactive chlorine chemistry. Figure 2.5 shows such enhancement of ClO and low abundance of O_3 even in the northern hemisphere of the lower stratosphere.

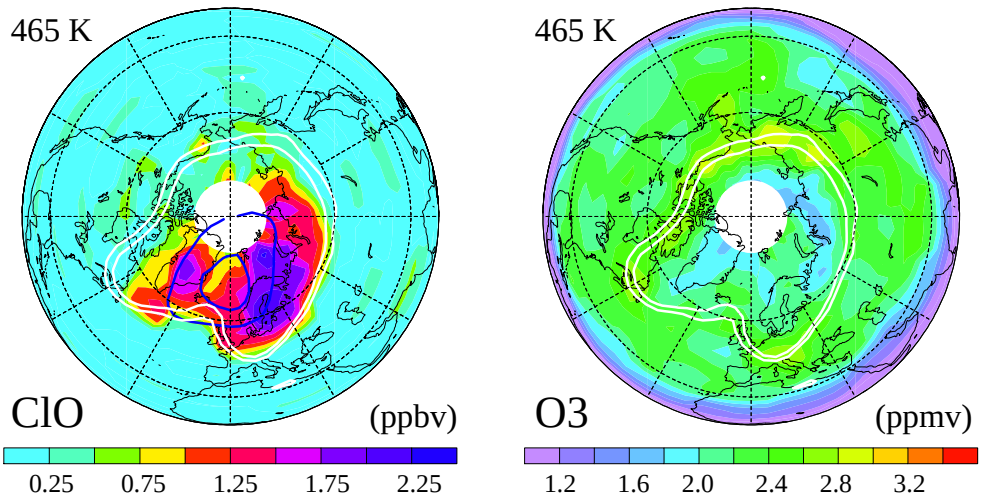

Figure 2.5 UARS MLS measurements of ClO and O_3 for February 20, 1996 for the northern hemisphere (After *Manney et al.* [1996]).

The decrease of ozone in the upper stratosphere has also been noticed on the basis of recent satellite observations (e.g. Figure 2.1). This decreasing trend is also understood in terms of the accumulation of anthropogenic chlorine. Especially in the upper stratosphere not only ClO_x cycle, but also NO_x, BrO_x and HO_x cycles become very important.

Here we will briefly see such reactions in association with the ozone destruction processes.

2.3.2 Chlorine and Bromine Chemistry

Over the Earth's lifetime, natural processes have regulated the balance of ozone in the stratosphere. In the past two decades, however, human production of halogen-containing compounds, such as chlorofluoro-carbons (CFCs), has brought an additional force to destroy ozone. Once in the stratosphere, the CFC molecules break up due to UV radiation and release their chlorine atoms. The free chlorine atoms then react with ozone molecules taking one oxygen atom to form chlorine monoxide as shown in Eq. (2.1).

$$\begin{aligned} Cl + O_3 &\rightarrow ClO + O_2 \\ ClO + O &\rightarrow Cl + O_2 \\ net \quad O + O_3 &\rightarrow O_2 + O_2 \end{aligned} \tag{2.1}$$

The reaction cycle happens over and over again as called catalytic reaction, allowing a single atom of chlorine to destroy many of ozone. Fortunately, chlorine atoms do not remain in the stratosphere forever. When a free chlorine atom reacts with gases such as methane (CH_4), it produces molecule such as hydrogen chloride (HCl). This Chlorine cycle is illustrated in Figure 2.6 (right).

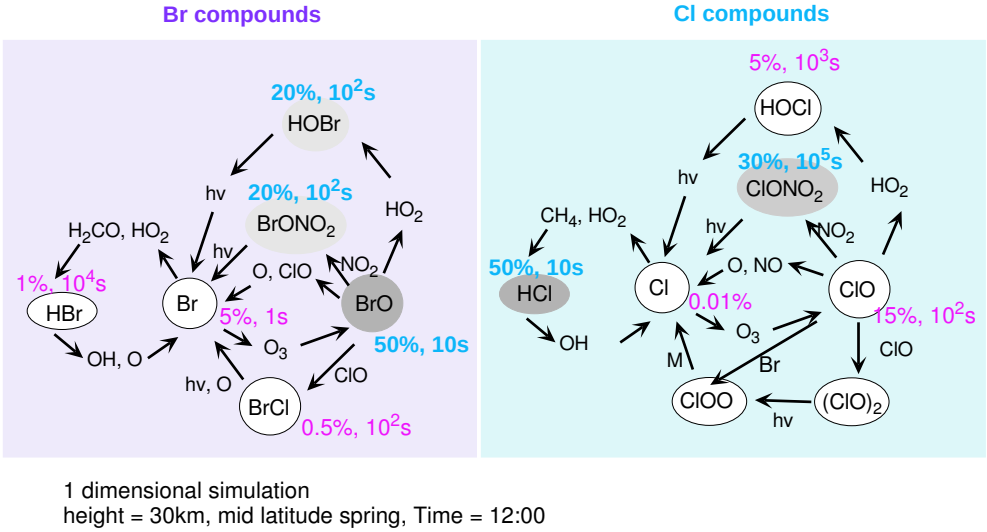

Figure 2.6 Ozone depletion reaction (% and lifetime) (After *Lary* [1996, 1997]).

Bromine-related chemistry in the stratosphere has become an important issue since the halons and methyl bromide have been suspected as ozone-depleting substances more powerful than the CFCs. Bromine is estimated to be about 50 times more efficient than Cl in destroying stratospheric ozone on a per-atom basis. Methyl bromide, which represents

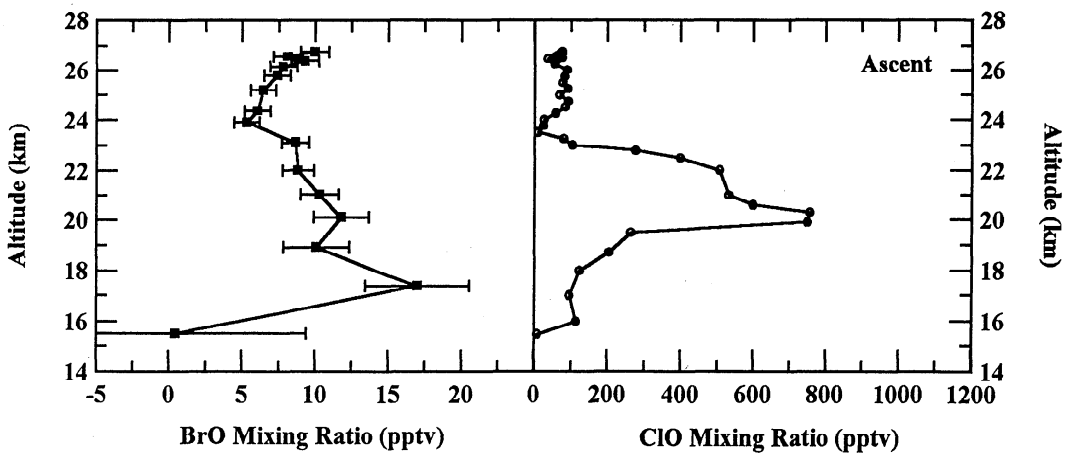

Figure 2.7 Profile of BrO mixing ratios (left panel); ClO mixing ratios from *Pierson et al.* [1997] (After [*McKinney et al.*, 1997]).

the major source of bromine in the stratosphere, is used as an agricultural fumigant, and is an interesting compound in the context of stratospheric ozone depletion because it has significant natural sources and also has a very short lifetime in the troposphere.

Br photo-chemistry is believed to be basically similar to that of Cl, but the lifetime of radicals and reservoirs is completely different from that of Cl. In the Br chemistry, HBr and $BrONO_2$ do not work as reservoirs, as shown in Figure 2.6. In contrast to chlorine species, there have been few measurements of bromine compounds in the stratosphere. No observation has been reported for the thermal emission in the frequency region of the infrared and sub-millimeter. Almost the only in situ observation of BrO in the stratosphere is plotted in Figure 2.7 [*McKinney et al.*, 1997].

2.3.3 HO_x Chemistry

Reactions of HO_x family (OH, HO_2, H_2O_2) are also considered to play an important role in the whole stratosphere. In spite of the fundamental importance of HO_x family, the observational data remains one of the poorest in the atmosphere. Global measurements of the latitudinal, seasonal, and diurnal variation in the HO_x family and related species, ClO_x, BrO_x, H_2O, CH_4, H_2 and O_3 are needed to address this deficiency. The JEM/SMILES observation will enable us to obtain the global data for HO_2, H_2O_2, HOCl, HOBr, ClO, BrO and O_3. Figure 2.8 summarizes ozone loss mechanism by the HO_x catalytic cycle, and we will see details in the following.

(a) *HO_x reactions destroying the odd oxygens*

The odd oxygen, O and O_3, are destructed by the activated hydrogen through a variety of catalytic cycles. In Figure 2.8, the reactions destroying the odd hydrogen in a direct manner are represented by the straight blue line. Water vapor molecule can be transformed into two OH radicals via the reaction of water vapor with the first electronically excited oxygen atom.

$$H_2O + O(^1D) \quad \rightarrow \quad 2OH$$

OH radical reacts with O_3 to form HO_2, and HO_2 radical reacts with O to produce OH

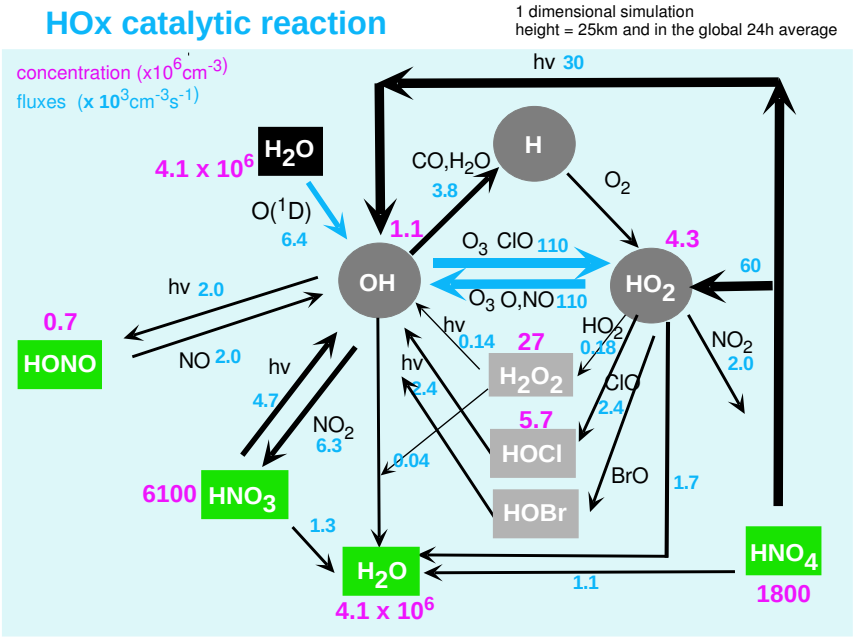

Figure 2.8 Gas phase reaction of HO_x in the stratosphere (Based on *Brasseur* [2000]).

radical. The sum of reactions is written as follows.

$$\begin{aligned} OH + O_3 &\rightarrow HO_2 + O_2 \\ HO_2 + O &\rightarrow OH + O_2 \\ net \quad O + O_3 &\rightarrow O_2 + O_2 \end{aligned} \tag{2.2}$$

It should be noticed that the net effect of the reactions is simply a conversion of two odd oxygens into two O_2 molecules.

(b) *Reservoir molecules*

The reservoir molecules are able to remove HO_x through catalytic reactions. In Figure 2.8, reservoir molecules are written by using green letters (i.e., H_2O, HNO_3, and HNO_4). These molecules are produced by the reaction such as,

$$\begin{aligned} OH + HO_2 &\rightarrow H_2O + O_2 \\ OH + NO_2 + M &\rightarrow HNO_3 + M \\ HO_2 + NO_2 + M &\rightarrow HNO_4 + M \end{aligned}$$

As these reservoir molecules are stable chemical compounds and have very long lifetimes, they are transported into the troposphere. They have an important role of removing HO_x from the stratosphere altogether.

(c) *Reactions in the upper stratosphere*

In the upper stratosphere, where O atoms are relatively plentiful, the HO_x catalytic cycle outlined above is fairly effective. Two other reactions are also important in the upper stratosphere. The first one involves a free H (hydrogen) atom as an intermediate compound. This reaction is described in the upper part of Figure 2.8. Two O atoms are

converted into a single diatomic oxygen molecule.

$$\begin{aligned} H + O_2 + M &\rightarrow HO_2 + M \\ HO_2 + O &\rightarrow OH + O_2 \\ OH + O &\rightarrow H + O_2 \\ net \quad 2O &\rightarrow O_2 \end{aligned} \tag{2.3}$$

The second reaction involves the loss of two odd oxygens. The two odd oxygens are converted into two diatomic oxygen molecules.

$$\begin{aligned} OH + O_3 &\rightarrow HO_2 + O_2 \\ HO_2 + O &\rightarrow OH + O_2 \\ net \quad O_3 + O &\rightarrow 2O_2 \end{aligned} \tag{2.4}$$

(d) *Reactions in the lower stratosphere*

The HO_x cycles interacting with the chlorine or bromine cycles are important in the lower stratosphere. This is the most complicated one of the catalytic cycles, but yields the similar catalytic destruction of odd oxygen as we have seen so far. In these reactions, X can be either chlorine or bromine:

$$\begin{aligned} XO + HO_2 &\rightarrow HOX + O_2 \\ HOX + h\nu &\rightarrow OH + X \\ OH + O_3 &\rightarrow HO_2 + O_2 \\ X + O_3 &\rightarrow XO + O_2 \\ net \quad 2O_3 &\rightarrow 3O_2 \end{aligned} \tag{2.5}$$

These two cycles are shown in the lower part of Figure 2.8.

2.3.4 Targets

JEM/SMILES will make measurements on several radical species crucial to the ozone chemistry. Some of them have never seen by any other satellite measurements in the stratosphere, and the JEM/SMILES mission will be the first to detect them such as BrO. Especially in the lower stratosphere it would be very interesting to see the space-time variations of these species. Though there is a limitation of latitudinal coverage of the JEM/SMILES observations, we expect high possibility to make measurements within the elongated polar vortex in the northern hemisphere. Also we hope JEM/SMILES has a capability to observe such species even in the background situation.

The upper stratosphere is another interesting field to investigate from the viewpoint of the ozone budget. By the use of the JEM/SMILES data we may try to estimate the decreasing trend of ozone affected by the anthropogenic chlorine and bromine loading. As to the HO_x reaction cycle, for example, the volume mixing ratios of HO_2 and H_2O_2 become large in the upper stratosphere and the mesosphere. This region is still unknown considering the distribution of HO_x species.

2.4 Observation of Ozone Isotopes

2.4.1 Introduction

A problem in molecular and atmospheric physics has puzzled scientists for almost two decades: the unusually high enrichments in most of the heavy isotopomers of ozone have

been observed in the troposphere and stratosphere [*Thiemens*, 1999]. In general, by combining the observed isotopic compositions with knowledge of the rates and isotope effect of each of the process producing and removing a given molecule in a system, one should be able to validate them with each other. Alternatively, if the isotopic composition and either the isotope specific production or loss rates are known, the other may be inferred from the available observations using a simple model on the basis of the corresponding chemistry of the molecule. Despite the extensive laboratory studies and atmospheric observations have been made, a convincing physical explanation of the processes to result in the heavy ozone isotope enrichment is still missing.

The oxygen isotope distribution in the Earth's atmosphere is well defined. The three stable isotopes have the following abundance: $^{16}O = 0.9976$, $^{17}O = 0.00037$, and $^{18}O = 0.00204$. Besides the dominant form of ozone, $^{48}O_3$, the isotopomers produced by single replacement of ^{16}O to ^{17}O or ^{18}O are of any significance in the atmosphere, namely $^{49}O_3$ and $^{50}O_3$, respectively. The abundance ratios of these isotopomers are statistically calculated to be 900 and 163 for $^{48}O_3/^{49}O_3$ and $^{48}O_3/^{50}O_3$, respectively. The degree of the ozone isotope enrichment is defined as $\delta^M O = ({}^M R_{obs}/{}^M R_{std} - 1) \times 1000$ [‰], where ${}^M R_{obs}$ is the observed abundance ratio of the heavy isotopomer with mass number M, and ${}^M R_{std}$ is the standard ratio described above [*Kaye*, 1987]. Isotope fractionation in chemical reaction is usually explained in terms of its mass-dependence. For example, the isotope ratios in a three-isotope system are an approximate linear function of the differences in the reciprocal masses of the isotopic species. In the case of ozone isotopes, mass-dependent fractionation is given by $\delta^{17}O \approx 0.5\delta^{18}O$. Thus, 2 ‰ enrichment in ^{18}O is accompanied by 1 ‰ fractionation of ^{17}O. The "mass-independent isotopic compositions," or simply "isotope anomaly" are now known to be pervasive in a range of atmospheric molecules, including O_3, CO_2, N_2O and sulfate aerosols, which awaits for thorough understanding of the mechanism.

2.4.2 Atmospheric Observations and Laboratory and Theoretical Studies

The first observational evidence of the ozone isotope anomaly was found during a balloon flight using an in-situ airborne mass spectrometer (AMS) in 1981 [*Mauersberger*, 1981]. Their study showed the stratospheric ozone is greatly enriched in $^{50}O_3$, as high as $\delta \approx 400$ ‰ at 32 km, with approximately equal $\delta^{17}O$ and $\delta^{18}O$ enrichments. Hereafter, heavy isotope enrichments in stratospheric ozone have been confirmed by various techniques as reviewed by *Johnson et al.* [2000] (Figure 2.9). The first ground-based FT-IR measurements were made in 1985 and could discriminate between the two isotopomers of $^{50}O_3$ while mass spectrometric measurements cannot. The higher column enrichment in asymmetric isotopomer of $^{18}O^{16}O^{16}O$ than symmetric one $^{16}O^{18}O^{16}O$ was observed. The Atmospheric Trace Molecule Spectroscopy (ATMOS) Grille Spectrometer has flown four times on the Space Shuttle since 1985. The zonal mean profiles of $^{18}O^{16}O^{16}O$ and $^{16}O^{18}O^{16}O$ retrieved showed no statistically significant variation with latitude, altitude, or time. The FIRS-2 FTIR spectrometer also made measurements during seven balloon flights, which took place between 1989 and 1997.

The extent of the enrichments observed are in good agreement except that AMS measurements showed systematically larger enrichments in ^{18}O compared to cryogenic sampling (CS), ATOMS, and FIRS results. Meanwhile, observed variation of the enrichments with latitude, altitude, or time are not consistent with each other where the statistically significant variability was seen in AMS and CS measurements while it was not seen in spectroscopic observations. One possible explanation of the discrepancy is that the small variability may not be detected with the limited precision of the remote sensing mea-

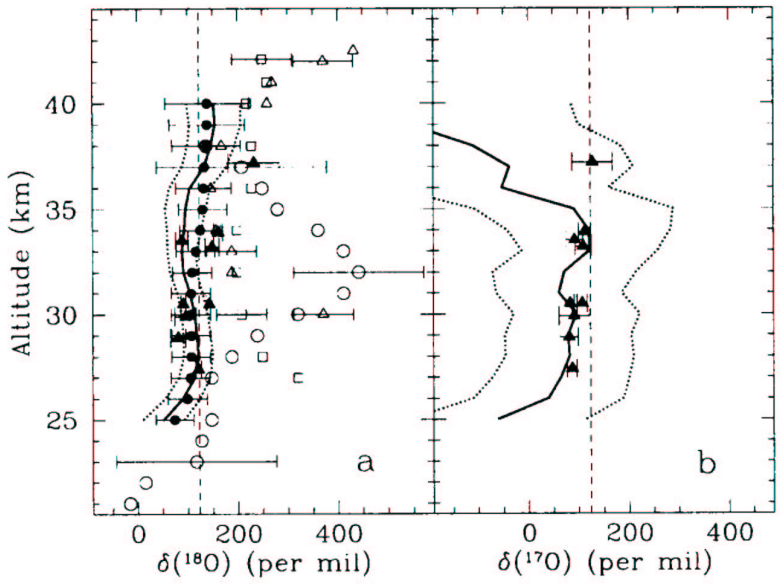

Figure 2.9 Comparison of published results of measurements of heavy ozone enrichment. (a) Enrichment for $^{50}O_3$. Enrichment for $^{49}O_3$. (From *Johnson et al.* [2000]).

surements. Very recently, *Mauersberger et al.* [2001] have made a critical review for the stratospheric ozone isotope data, whose samples were cryogenically collected in the past. They concluded that the data indicated $^{50}O_3$ enrichment ranging from 70 to 90 ‰ in the middle stratosphere, in which the enrichments were in good agreement with results from laboratory studies, and suggested to abandon several measurements showing very high enrichments due to unidentified measurement errors.

Since pioneering work of atmospheric observations by *Mauersberger* [1981], the dedicated laboratory experiments have emerged to explain the ozone isotope anomaly occurred in the stratosphere. The relative recombination rate coefficients for ozone production from various combinations of atomic and molecular oxygen isotopes have been evaluated through mass spectrometric and tunable diode laser spectroscopic experiments [for example *Mauersberger et al.*, 1999]. Those studies suggest that, for example, the rate coefficient of the recombination $^{16}O + ^{18}O^{18}O$ is about 50 % larger than that of the standard $^{48}O_3$ formation. Such laboratory data have been applied to model the enrichments of symmetric and asymmetric $^{50}O_3$ and $^{49}O_3$ in the stratosphere [*Johnson et al,* 2000]. Laboratory experiments also motivated quantum chemical treatment of the kinetic isotope effects in the recombination processes [*Gao and Marcus*, 2001].

2.4.3 Targets

The inability to account for the stratospheric ozone isotope anomaly and variability represents a significant inadequacy in our understanding of the chemical transformation and/or transport of stratospheric and tropospheric ozone. The magnitude of the heavy isotope enrichment at times far exceeds that expected on the basis of laboratory measurements and theoretical studies as shown in Figure 2.9. Further improvement of precision, spatial and temporal coverage of the measurement are required to get a firm picture of the enrichments in stratospheric $^{50}O_3$ and $^{49}O_3$, which will provide vital information for the

sound understanding of the mechanism of the isotopic fractionation. Global and quantitative measurements may elucidate hitherto unobserved chemical processes related to the heavy isotope enrichment of ozone, by making a comparison with the experimental and theoretical studies. The JEM/SMILES observations will cover polar, mid latitude and tropical region (from 38°S to 65°N) in the latitude range between 10 and 60 km with all 5 isotopes of mono-substituted ozone; $^{16}O^{16}O^{16}O$, $^{16}O^{18}O^{16}O$, $^{18}O^{16}O^{16}O$, $^{16}O^{17}O^{16}O$, and $^{17}O^{16}O^{16}O$. The first simultaneous observation of ozone isotopic species reduces systematic errors due to the difference of the observational methods as previously. We propose that the new tool JEM/SMILES observation will provide us important findings to work out the puzzle of ozone isotope anomaly

It is worth while commenting that ozone molecule is believed to be the principal source of mass-independent fractionation in other atmospheric molecules and its anomaly can transfer to other species either through direct reaction or via reaction with the ozone photolysis products. For example, precise measurements of the ozone isotopomer distributions are crucial to investigate the oxygen isotope distributions of stratospheric and mesospheric CO_2 by means of a photochemical model calculation [*Barth and Zahn*, 1997]. This is because the CO_2 isotope anomaly is thought to be related to the ozone isotope anomaly through the reaction of CO_2 with $O(^1D)$ generated via UV photolysis of ozone. More recently a photochemical equilibrium model for short-lived radical species such as ClO, HO_x, and NO_x, has been constructed to calculate their amounts of mass-independent fractionations under mid-latitude conditions [*Lyons*, 2001]. Thus the JEM/SMILES observations of ozone isotopomer would also be incorporated in the studies of isotope anomalies of other atmospheric species.

References

Barth, V. and A. Zahn, Oxygen isotope composition of carbon dioxide in the middle atmosphere, *J. Geophys. Res.*, *102*, 12995–13007, 1997.

Brasseur, G. P., Lecture talk on *The Chemistry of Atmospheric Ozone*, at Hokkaido University, Sapporo, Japan, July, 2000.

Dvortsov, V. L., and S. Solomon, Response of the stratospheric temperatures and ozone to past and future increases in stratospheric humidity, *J. Geophis. Res.*, *106*, 7505–7514, 2001.

Gao, Y. Q. and R. A. Marcus, On the theory of the strange and unconventional isotopic effects in ozone formation *J. Chem. Phys.*, *116*, 137–154, 2002.

Holton, J. R., P. H. Haynes, M. E. McIntyre, A. R. Duglass, R. B. Rood, and L. Pfister, Stratosphere-troposphere exchange, *Rev. Geophys.*, *33*, 403–439, 1995.

Johnson, D. G., K. W. Jucks, W. A. Traub, and K. V. Chance, Isotopic composition of stratospheric ozone, *J. Geophys. Res.*, *105*, 9025–9031, 2000.

Kaye, J. A., Mechanisms and observations for isotope fractionation of molecular species in planetary atmosphere, *Rev. Geophys.*, *25*, 1609–1658, 1987.

Lary, D. J., Gas phase atmospheric bromine photochemistry, *J. Geophys. Res.*, *101*, 1505–1516, 1996.

Lary, D. J., Catalytic destruction of stratospheric ozone, *J. Geophys. Res.*, *102*, 21515–21526, 1997.

Lyons, J. R., Transfer of mass-independent fractionation in ozone to other oxygen-containg radicals in the atmosphere, *Geophys. Res. Lett.* , *28*, 3231–3234, 2001.

Manney, G. L., M. L. Santee, L. Froidevaux, J. W. Waters, and R. W. Zurek, Polar vortex conditions during the 1995–96 Arctic winter: Meteorology and MLS ozone. *Geophys. Res. Lett.*, *23*, 3203–3206, 1996.

Mauersberger, K., Measurement of heavy ozone in the stratosphere, *Geophys. Res. Lett.*, *8*, 935–937, 1981.

Mauersberger, K., B. Erbacher, D. Krankowsky, J. Gunther, and R. Nickel, Ozone isotope enrichment: Isotopomer-specific rate coefficients, *Science*, *283*, 370–372, 1999.

Mauersberger, K., P. Laemmerzahl, and D. Krankowsky, Stratospheric ozone isotope enrichments

– revisited, *Geophys. Res. Lett.* , *28*, 3155–3158, 2001.

McKinney, K. A., J. M. Pierson, and D. W. Toohey, A wintertime in situ profile of BrO between 17 and 27 km in the Arctic vortex. *Geophys. Res. Lett.*, *24*, 853–856, 1997.

Mote, P. W., K. H. Rosenlof, M. E. McIntyre, E. S. Carr, J. C. Gille, J. R. Holton, J. S. Kinnersley, J. M. Pumphrey, J. M. Russell III, and J. W. Waters, An atmospheric tape recorder: The imprint of tropical tropopause temperatures on stratospheric water vapor, *J. Geophys. Res.*, *101*, 3989–4006, 1996.

Newman, P. A., J. F. Gleason, R. D. McPeters, and R. S. Stolarski, Anomalously low ozone over the Arctic, *Geophys. Res. Lett.*, *24*, 2689–2692, 1997.

Pierson, J. M., K. A. McKinney, D. W. Toohey, A. Engel, and P. A. Newman, In situ balloon measurement and modeling studies of ClO in the Arctic Vortex, *J. Atm. Chem.*, 1997.

Solomon, S., S. Borrowmann, R. R. Garcia, R. Portmann, L. Thomason, L. R. Poole, D. Winker, and M. P. McCormick, Heterogeneous chlorine chemistry in tropopause region. *J. Geophys. Res.*, *102*, 21411–21429, 1997.

SPRC, SPARC Assessment of Upper Tropospheric and Stratospheric Water Vapor, *SPARC Report No. 2*, Ed. by D. Kley, J. M. Russell, and C. Phillips, WCCRP No 113, WMO/TD-No 1043, December 2000.

Thiemens, M. H., Mass-independent isotope effects in planetary atmospheres and the early solar system *Science*, *283*, 341–345, 1999.

WMO (World Meteorological Organization), Scientific Assessment of Ozone Depletion: 1994, Global Ozone Research and Monitoring Project – Report No. 44, Geneva, 1999.

Yung, Yuk L., W. B. Demore, and Joseph P. Pinto, Isotope exchange between carbon dioxide and ozone via O(^{1}D) in the stratosphere, *Geohpys. Res. Lett.*, *18*, 13–16, 1991.

3 Instrumental Capabilities

3.1 Introduction

3.1.1 ISS and JEM

3.1.1.1 Overall Structure

The Japanese Experiment Module (JEM), also known by a Japanese nickname *Kibo*, is the segment of ISS developed by the National Space Development Agency (NASDA) of Japan for supporting research and development experiments in the ISS orbit. The JEM consists of manned Pressurized Module (PM), Experiment Logistic Module-Pressurized Section (ELM-PS), and Exposed Facility (EF). The JEM Exposed Facility (EF), an unpressurized pallet structure exposed to the space environments, will be located just outside of the JEM Pressurized Module (PM) placed at the ram-port side of the ISS. The SMILES payload will be attached to the ram side of the JEM-EF at the location EFU #1 or EFU #3 as shown in Figure 3.1 and Figure 3.2.

3.1.1.2 Orbit and Attitude

The ISS will be in a nearly circular orbit at a nominal altitude of approximately 400 km with an inclination of 51.6 degrees to the equator, and will usually maintain a torque equilibrium attitude (TEA) during the microgravity mode of its operation. It is predicted that the ISS altitude will vary between 350 km and 460 km. In order to keep this altitude range, the ISS will be periodically reboosted approximately every 10 to 45 days by using onboard thrusters. During this Reboost Mode, the ISS attitude will be yaw-maneuvered by 180 degrees.

The ISS flight attitude (orientation relative to the plane of its orbit) is referenced to local-vertical/local-horizontal (LVLH) axes fixed with respect to the ISS's near-circular orbit [*NASA*, 1999]. The torque equilibrium attitude (TEA), which balances the average external torque disturbances such as aerodynamic torque and gravity gradient, will vary around the local-vertical/local-horizontal (LVLH) coordinate as shown in Figure 3.1. The x-axis points along the orbital velocity vector (the ram direction) and the z-axis points radially toward the Earth's center (or toward the nadir direction.) The ISS attitude variation will never exceed ± 15 degrees in roll and yaw angles and $+15$ and -20 degrees in pitch angle from the nominal LVLH attitude. The detailed descriptions of the orbit and attitude variations will be found in 3.2.5.

3.1.1.3 ISS Operational Modes

The ISS will be operated according to a number of specific modes of operation, each of which has a specified set of conditions and capabilities. Currently defined operation modes include Standard mode, Reboost mode, Microgravity mode, Survival mode, Proximity-Operations mode, Assured-Safe-Crew-Return mode, and External-Operations mode. Although most modes support research payload operations at some level, there are some modes for which payloads operations may be sharply curtailed or discontinued. Microgravity and Standard modes are the primary modes of operation during which full support for research payload will be provided. During Microgravity mode the ISS must be operated so as to meet a stringent set of requirements for its microgravity environment maintaining

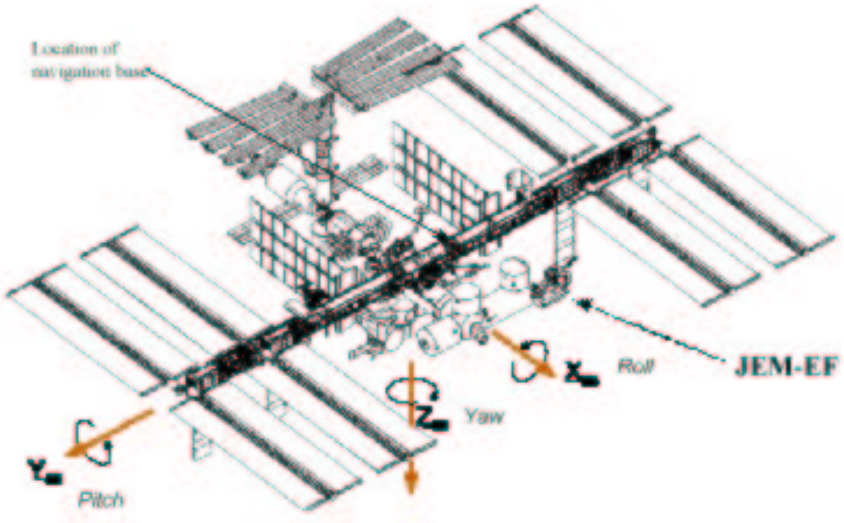

Figure 3.1 Space Station reference coordinate system. The x-axis points along the orbital velocity vector (the ram direction), the z-axis points radially toward the Earth's center (or toward the nadir direction).

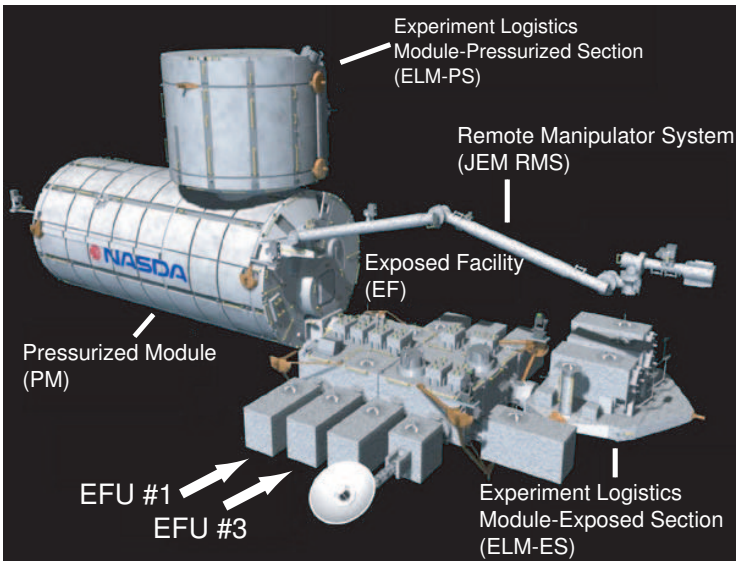

Figure 3.2 Configuration of Japanese Experiment Module (JEM). SMILES will be attached at the location EFU #1 or EFU #3

its attitude by non-propulsion means. Standard mode is similar to Microgravity mode except that microgravity environment will not be guaranteed.

In Reboost mode, drastic variations of altitude and attitude due to maneuvering will be expected. A periodic reboosting of the ISS will be carried out approximately every 10 to 45 days as described in 3.1.1.2. During Survival mode which will be invoked for the case of contingency, support and commanding for research payload are precluded. In these two

modes of operation, atmospheric observation by SMILES cannot be carried out.

In the remaining three modes of operation, Proximity-Operations, Assured-Safe-Crew-Return, and External-Operations, it is still not certain to what extent the SMILES atmospheric observations can be properly performed.

3.1.1.4 Data Link between JEM/SMILES and ground facility

Three types of data communications links are provided by the ISS for onboard data communications [*NASA*, 1999]: 1) a MIL-STD-1553B Payload Bus, 2) an IEEE 802.3 Ethernet, and 3) a fiber-optic High-Rate Data Link (HRDL). Among them, SMILES will employ the Payload Bus #2 for commanding and transmission of health-and-status (H&S) and house-keeping (HK) data of instruments, and the Ethernet for transmission of observation data as well as the instrument HK data.

There are two data links either through the U.S. Tracking and Data Relay Satellite System (TDRSS) or through the Japanese Data Relay Test Satellite System (DRTSS) are available for command uplink and data downlink between the ISS and the ground facilities at Tsukuba Space Center (TKSC) [*NASDA*, 1998]. Considering the resource allocation among International Partners for the TDRSS link, SMILES will only use the Japanese DRTSS link for which NASDA is allocated 50 % of link capacity. Although two DRTSs (DRTS-W and DRTS-E) are planned, only one DRTS (DRTS-W) will be available at the time of SMILES launch. Since the DRTS is an geostationary satellite, the DRTS link is secured only for a limited percentage of time during which it is visible from the ISS. During the loss-of-sight period referred to as Zone of Exclusion (ZOE), downlink data will be temporally stored in the High Rate Data Recorder (HRDR) with a capacity of 20 Gbits of the Interorbit Communication System (ICS) of JEM. Currently, downlink data rate available to SMILES is estimated to be 200 kbps at the most.

3.1.2 SMILES Payload

3.1.2.1 Payload Configuration

SMILES payload instrument consists of a number of sections as listed in Table 3.1. Figure 3.3 shows a block-diagram of SMILES payload instrument. The Submillimeter Antenna (ANT), Submillimeter Receiver (SRX), Intermediate Frequency Amplification Section (IFA), and Radio Spectrometer (AOS) comprises the main part of the payload. The Star Tracker (STT) has a function of detection and calibration of the SMILES payload attitude.

The SMILES is equipped with a heterodyne superconductor-insulator-superconductor (SIS) receiver to be operated in the 625/650-GHz band as a limb-emission sounding radiometer. The SMILES has a mechanically scanning elliptical offset-Cassegrain antenna with diameters of 40 cm × 20 cm to achieve an altitude resolution of about 3.5—4.1 km at the tangential altitude ranging from upper troposphere (10 km) to lower mesosphere (60 km) from the orbit of the ISS. The atmospheric limb emission collected by the ANT is directed to the SRX, where the received submillimeter-wave signal is combined with a reference signal (637.32 GHz) from a submillimeter-wave local oscillator (SLO), and is directed to SIS mixers through quasioptics consisting of focusing mirrors, wire-grids, and a sideband filter. Two SIS mixers, one of which for upper sideband (USB: 649.12 GHz – 650.32 GHz) and the other for lower sideband (LSB: 624.32 GHz – 626.32 GHz), are operated for simultaneously down-converting both sidebands into the intermediate frequency

Table 3.1 Configuration of SMILES Payload.

Section	Subsystem Components
Submillimeter Antenna (ANT)	Antenna Reflectors (REF)
	Antenna Mounting Structure (MNT)
	Beam Transfer Section (TRN)
	Cold-sky Terminator (CST)
	Antenna Drive Electronics (ADE)
	Calibration Hot Load (CHL)
Submillimeter Receiver (SRX)	Ambient Temperature Optics (AOPT)
	Cryo-electronics Unit (CRE)
	Ambient Temperature Amplifiers (AAMP)
	Helium Gas Compressors (HECP)
	Submillimeter LO Controller (SLOC)
	CRE Control Electronics (CREC)
	Stirling & JT Drive Electronics (SJTD)
IF Amplification Section (IFA)	
Radio Spectrometer (AOS)	AOS Analyzer Unit (AU)
	AOS Control & Video Unit (CVU)
Star Tracker (STT)	STT Camera Units (CAM)
	STT Camera Controller (CAMC)
Data Processing and Control Section (DPC)	
Payload Bus (BUS)	Electric Power System (EPS)
	Mainframe Structure (MFS)
	JEM Interface Mechanism (JIF)
	Thermal Control System (TCS)

(IF) band ranging between 11 GHz and 13 GHz. The IF signals are further down-converted and amplified in the IFA, and then analyzed by two acousto-optical spectrometers in the AOS. Further details of the functions of each subsystem will be described in the following sections.

3.1.2.2 Dimension, Mass, Power, and Data Rate

Figure 3.1.2.1 shows an external view of the SMILES payload. The envelope of the SMILES payload mainframe structure has a dimension of 1.85 m $\times$ 1 m $\times$ 0.8 m. The total mass of the payload is less than 500 kg. The electrical power consumption of the payload is less than 900 W for normal operation.

As a data communications interface for commanding and telemetry, SMILES will use the MIL-STD-1553B Payload Bus #2 and the IEEE 802.3 Ethernet. Commands from the ground and the ancillary data such as the reference time data are transmitted to the DPC through the Payload Bus #2 via the JEM Control Processor (JCP) and the Payload Data Handling Unit (PDH) and are distributed to SMILES subsystems [*NASDA*, 1998].

The Health and Status (H&S) data and the experimental data of the subsystem instruments are collected by the DPC and are downlinked to the ground through the 1553B Payload Bus #2 via the PDH and the JCP. The instrument experimental data are down-

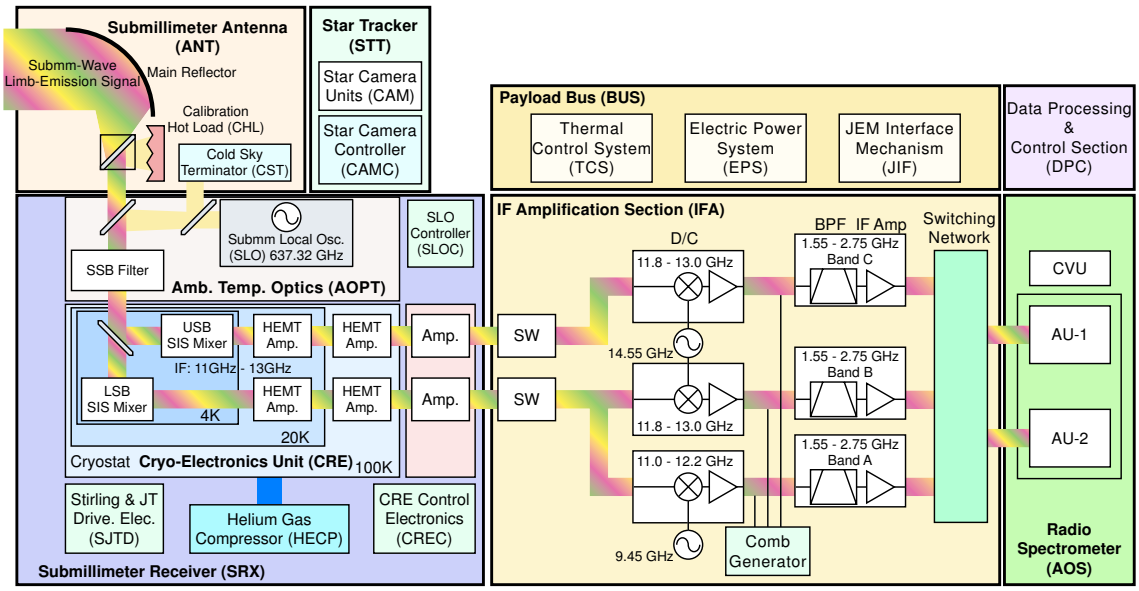

Figure 3.3 Block diagram of JEM/SMILES payload.

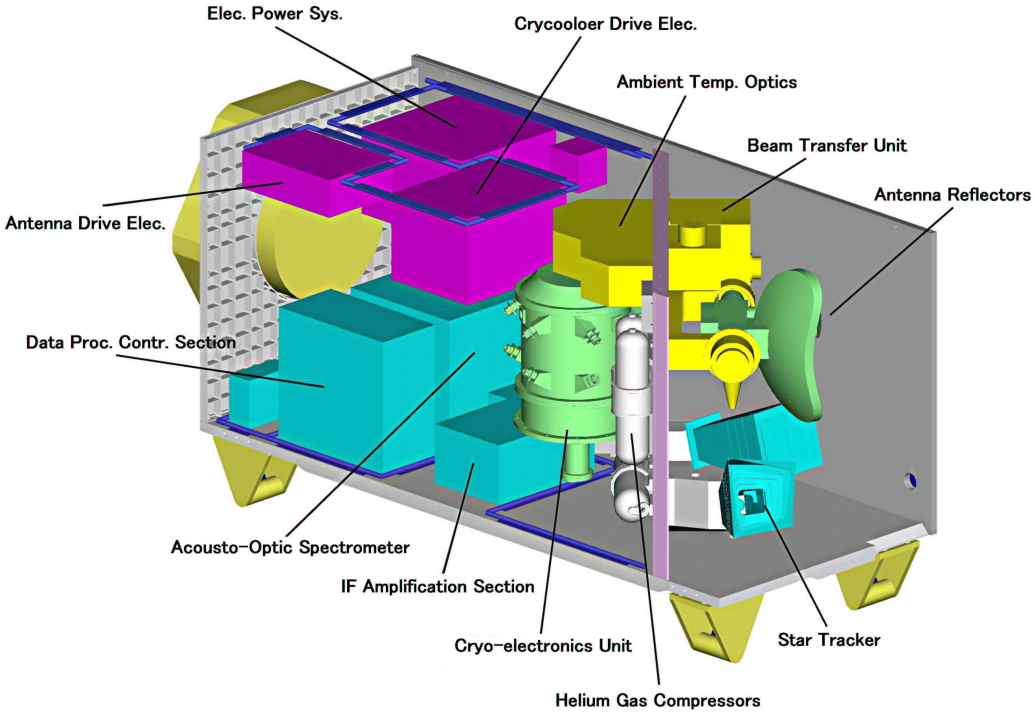

Figure 3.4 External view of the SMILES payload.

linked through the Ethernet along with the atmospheric observation data yielded by the AOS. The downlink 1553B data rate is estimated to be about 18 kbps which includes the H&S data of about 90 bps. The downlink Ethernet data rate is estimated to be less than

200 kbps.

3.1.2.3 Launching and Installation to JEM

SMILES will be launched around in 2007 by a Japanese H-IIA rocket from Tanegashima Space Center of NASDA in Japan. The SMILES payload will be transported to the orbit of the ISS by H-II Transfer Vehicle (HTV) and attached either to the JEM-EF Unit (EFU) #1 or #3. According to the current plan, on-orbit experiment mission period is scheduled to be one year. If there is no succeeding mission payload that takes place of the EFU position occupied by SMILES, the mission period of SMILES may be prolonged as long as the payload instruments are alive.

After the completion of its on-orbit mission, SMILES will be detached from the JEM-EF and thrown away into the atmosphere by HTV.

3.1.3 Mission Instruments

Mission instruments whose functions and performances are decisive to SMILES experiments comprise a submillimeter antenna, submillimeter receiver, intermediate frequency (IF) amplification section, radio spectrometer, star tracker, and data processing and control section. The following sections will give explanations and basic requirements for those instruments.

3.1.3.1 Submillimeter Antenna (ANT)

SMILES needs a submillimeter antenna that has a reasonable size and high degree of accuracy. Large mirror is preferable from the viewpoint of achieving a higher spatial resolution, particularly in the vertical direction. A kind of trade-off is, however, unavoidable over the spatial resolution and a given envelope for JEM payloads. Our choice is an elliptical mirror with dimensions of 40 cm in vertical direction and 20 cm in horizontal. The mirror is not so large, but it must be highly accurate in shape for generating a high-quality beam at submillimeter wavelengths. One important figure of merit is the beam efficiency, which represents how much radiation is collected in the main beam in comparison with inevitable sidelobe contributions. We regard a reasonable target for the beam efficiency is 90 % for the antenna alone, which means the efficiency in the case the antenna is illuminated by an ideal feed, and 85 % for the whole integrated SMILES system. In addition to these radio (optical) qualities, we need mechanical accuracies to determine the beam direction while the antenna is continuously driven along the atmosphere scan path. Since the vertical beam size is 0.09° (HPBW), the angular accuracy of the antenna driving mechanism must be better than 0.01°. The basic requirements on the antenna performance are summarized in Table 3.2.

3.1.3.2 Submillimeter Receiver (SRX)

A superconducting low-noise receiver is a key instrument of SMILES experiment. With SIS mixers associated with cryogenically cooled HEMT amplifiers, it will reduce receiver noise by a factor of 20 in comparison with the conventional semiconductor diode-mixer receiver. The SMILES receiver noise temperature will be about 500 K (SSB). Two SIS mixers, which are pumped by a single submillimeter LO source, will receive the atmospheric signal in the upper sideband (USB) and lower sideband (LSB) separately: one for 649.12—650.32 GHz, and the other for 624.32—626.32 GHz. The LO frequency will be stabilized to 10^{-7} by

Table 3.2 Requirements for SMILES-ANT

Items	Requirements
Observation frequency	624.32 — 650.32 GHz
Main reflector aperture size	400 mm (El) × 200 mm (Az)
Main beam width	0.09° (El) × 0.18° (Az)
Main beam efficiency	Higher than 90 %
Reflection loss	Higher than 50 dB
Elevation angle range	−40° to +5°
Elevation angle control accuracy	±0.01°

means of a phase-locked loop. A quasi-optical sideband filter, based on a modified Martin-Puplett interferometer, makes each SIS mixer sensitive to the atmospheric emissions only in one sideband, with suppression of more than 15 dB over the other sideband. A 4-Kelvin class mechanical cooler is another key component of SMILES. A combined system of a two-stage Stirling cooler and Joule-Thomson circuit will cool SIS mixers and their associated optics to 4.5 K, first HEMT amplifiers to 20 K and second HEMT amplifiers to 100 K. All the cooled components are contained in a cryostat that is thermally isolated from the ambient temperatures. The coolers are continuously operated with pressurized He gas supplied by compressors. The cooler lifetime will be determined by either residual mechanical abrasion or He gas deterioration due to outgassing. Current estimate of life is one year or longer. Basic requirements on the submillimeter receiver are summarized in Table 3.3.

Table 3.3 Requirements for SMILES-SRX

Items	Requirements
Input Frequency	624.32—626.32 GHz (channel-T)
	649.12—650.32 GHz (channel-R)
Image Rejection Ratio	More than 15 dB
LO Frequency	637.32 GHz
LO Frequency Accuracy	±64 kHz
LO Phase Noise	Lower than −75 dBc/Hz (offset 1 MHz)
Output Frequency	11.00—13.00 GHz (channel-T)
	11.80—13.00 GHz (channel-R)
Gain Linearity	±1% or less
Gain Variation	$3\%_{p-p}$ or less in 1 minute
Receiver Noise Temperature	500 K or less

3.1.3.3 IF Amplification Section (IFA)

IFA has functions of frequency down conversion and signal transmission from SRX to AOS. Since SMILES has three RF observation bands (Band-A and Band-B in LSB, and Band-C in USB), and two AOS units, it makes simultaneous observations only for two bands among three. So IFA should have functions of flexible combinations among these inputs and outputs, which is required from operational points of view as well as to prepare a kind of redundancy for reliability. IFA also contains functions of adjusting the output

power level and of generating reference signals, a comb generator, for calibrating the AOS frequency drift. The basic requirements are given in Table 3.4.

Table 3.4 Requirements for SMILES-IFA

Items	Requirements
Input Frequency	11.00—13.00 GHz (Band-A & B)
	11.80—13.00 GHz (Band-C)
Output Frequency	1.55—2.75 GHz
LO Frequency Drift	100 kHz or less
Gain Ripple	2.0 dB_{p-p} or less in a signal band
Gain Variation	0.04 $dB_{p-p}deg^{-1}$ or less
Comb Generator Frequency Step	100 MHz
Comb Generator Frequency Drift	17 kHz or less

3.1.3.4 Radio Spectrometer (AOS)

SMILES adopts the acousto-optical spectrometer (AOS) for analyzing the atmospheric signal and detecting its power spectrum. AOS will have two analyzing units, each of which has a frequency coverage of 1.55—2.75 GHz with a resolution of 1.8 MHz (FWHM) and each power spectrum is obtained with a CCD array of 1728 channels. The CCD data is digitized, accumulated and sent to DPC in every 1 sec. The basic requirements are given in Table 3.5.

Table 3.5 Requirements for SMILES-AOS

Items	Requirements
Input Frequency	1.55—2.75 GHz
Frequency Resolution	1.8 MHz or less (FWHM)
CCD: Number of Channels	1728 channels / each CCD
CCD: Channel Separation	0.8 MHz or less
Noise Dynamic Range	9 dB or more (for 10 % additional noise)
A/D Conversion Accuracy	12 bits
A/D Differential Nonlinearity	$\pm 1/2$ LSB or less
Data Accumulation	500 ms
Output Data Length	16 bits
Output Data Rate	108 kbps

3.1.3.5 Star Tracker (STT)

Since the ISS or JEM attitude is assumed to be unstable, SMILES will be equipped with two STT cameras to determine its real time attitude. Each camera will work unless the sun comes within an angular distance of 30°. STT will determine the attitude of the SMILES mainframe structure with respect to the stellar inertia coordinate. It is then converted to the attitude with respect to the coordinate fixed to the Earth to calculate the position of the tangential point of the SMILES beam. The basic requirements for STT are listed in Table 3.6.

Table 3.6 Requirements for SMILES-STT

Items	Requirements
Stellar Detection Limit	6.5 mag.
Attitude Determination Accuracy	0.003° (rms) for pitch, yaw
	0.03° for roll
	±0.03° for bias component
Attitude Refresh Period	0.96 s
Allowable Attitude Change Rate	$0.6°s^{-1}$
Solar Avoidance Angle	30° (separation from the STT axis)
Field of View	$18.4° \times 13.4°$
Reference Stellar Catalogue	Hipparcos Catalogue

3.1.3.6 Data Processing and Control Section (DPC)

DPC will have the following functions:

- to control the antenna scan, which is to be synchronized with IFA, AOS and STT,
- to acquire observation data from AOS and STT,
- to acquire telemetry data from almost all components of SMILES,
- to send necessary commands to SMILES components,
- to have data interfaces with ISS/JEM.

3.2 Field of View (FOV)

3.2.1 Altitude Scanning of the Antenna

3.2.1.1 Scanning Profile

The antenna scanning profile of SMILES is shown in Figure 3.5. Although the altitude and attitude of the ISS (and also SMILES) will vary during a mission life, a scanning profile of the antenna can be defined in terms of the relative elevation angles. A repetition period of the antenna scan is designed to be 53 seconds, the first 29.5 seconds of which are allocated to observations toward limb directions. The rest of the scan period is dedicated to calibrations for the system gain and the AOS frequency. The former is done firstly by directing the main reflector to a reference sky, at the altitude higher than 160 km, and secondly by inserting a calibration hot load (CHL) into the antenna submillimeter optics. A switching mirror is used for this operation. Frequency scale of the AOS is calibrated with a set of carrier signals injected into the IF band. The antenna scanning and the data accumulation in the AOS have to be synchronized by a SYNC pulse provided from the SMILES Data Processing and Control Section (DPC) with the accuracy of 1 ms.

3.2.1.2 Range of Tangent Point Altitude

The height of tangent point for a line-of-sight depends on the antenna elevation angle as well as the altitude and attitude of the ISS/SMILES. Precise direction of the submillimeter beam will be determined with a reference to the Star Tracker (STT) data in the Level-1 data processing on the ground. In orbit, however, the prediction errors and fluctuations of

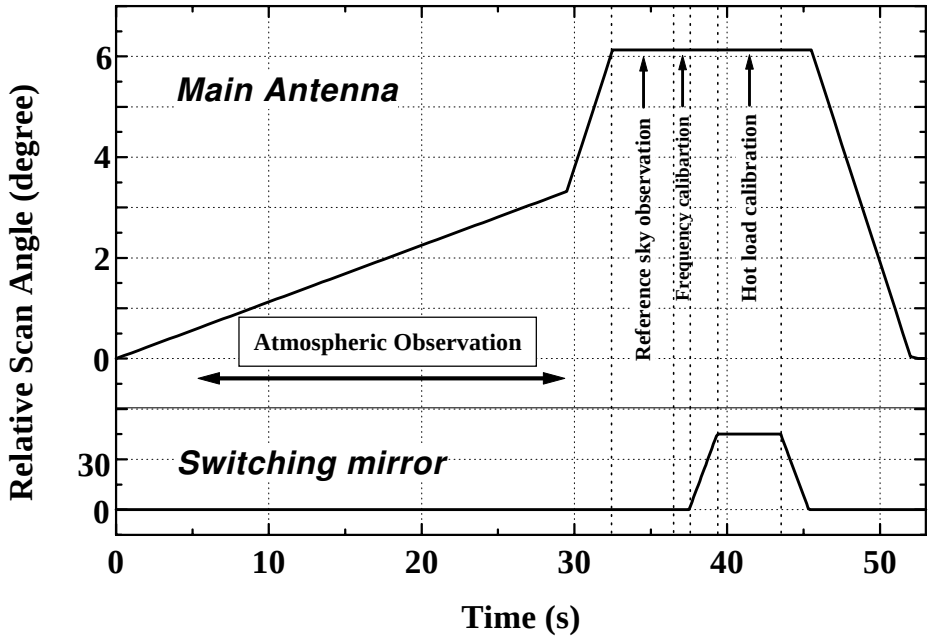

Figure 3.5 Antenna scanning pattern of SMILES with the associated operation of a switching mirror for radiometric calibration.

the ISS attitude will bring a large uncertainty in the tangent point altitude. For simplicity of the system, we have designed the ascending phase wide enough to cover the altitude range of 10 to 60 km with a sufficient margin. Initial tangent point altitude of every scan is settled to a nominal value of −35 km on the basis of predicted information of the ISS orbit and attitude. An expected range of real observational altitudes is listed in Table 3.7 for several representative altitudes and attitudes of the ISS.

3.2.1.3 Spatial Sampling Rate and Altitude Resolution

During atmospheric observations in the scanning period, the antenna ascends at a stepping rate of 12 Hz with a unit angle of 0.009375°. The emissions from the limb-atmosphere are accumulated, or averaged, for 500 ms to generate a unit output data. Strictly speaking, six different emissions originating from six consecutive altitudes contribute to each spectrum data. The effective beam-size for such output spectrum is calculated to be 0.096° in HPBW. Both the beam size and sampling interval, expressed in altitude at the tangent point, depend on the altitude and attitude of the ISS. They also vary along the antenna scan, because the distance between the tangent point and the ISS decreases as we go to the higher tangent point altitude. Figures 3.7 and 3.8 shows how the beam size and sampling interval will change while the antenna is ascending in a single scan.

Table 3.7 Expected range of tangent point altitudes for several ISS conditions.

Roll (deg.)	Pitch (deg.)	Yaw (deg.)	ISS Altitude (km)	Obs. Range (km)	Reference Sky (km)
0	0	0	350	−35 - 84	168
0	0	0	400	−35 - 92.5	184
0	0	0	460	−35 - 102	201
*1 0.5	−8.8	−2.0	350	−35 - 83	167
*1 0.5	−8.8	−2.0	400	−35 - 91.5	182
*1 0.5	−8.8	−2.0	460	−35 - 101	200
*2 −15	−20	−15	350	−35 - 82.5	166
*2 −15	−20	−15	400	−35 - 91	181
*2 −15	−20	−15	460	−35 - 100	198
*3 15	15	15	350	−35 - 83.5	167
*3 15	15	15	400	−35 - 92	183
*3 15	15	15	460	−35 - 101	200

*1: Expected ISS attitude after FLT 15A (Rev.D) SMILES will be installed around this event. *2 and *3 : The worst case of the ISS attitude.

3.2.1.4 Reference-sky Calibration

Onboard calibration of the radiometric gain will be done with two noise references at submillimeter wavelengths; the hot-load (CHL) that is virtually a black-body at the ambient temperature, and the reference sky that can be regarded as the microwave cosmic background. The two references are measured by the SMILES receiver in every antenna scan. The reference sky is measured with the main reflector of the antenna that is set at 6.13° upward with respect to its initial position. As far as the initial antenna position is adjusted in every scan at the nominal altitude of −35 km, which is to be programmed based on the prediction of the ISS altitude and attitude, the real height of the reference sky will be higher than 160 km. Since SMILES observes at around 640 GHz, the brightness temperature, which usually expressed in the Rayleigh-Jeans temperature, of the cosmic background is virtually zero Kelvin.

For the hot load calibration, a switching mirror is inserted into the antenna optics for the SMILES receiver to view the CHL. The physical temperature of the CHL is measured with the accuracy of 0.1° every 10 seconds. Since the reflectivity of the CHL is well suppressed to −55 dB or less, its brightness temperature is also accurate. In the scan period of 53 seconds, we allocate 4 seconds each to the hot load and reference sky calibrations. This method makes the increase of spectral noise, which is attributed to the subtraction between the atmospheric and the reference sky data, to be less than 10 %.

3.2.1.5 Continuity of Observations

Once SMILES is launched and attached to the JEM-EF Unit, the first several weeks will be reserved for initial checkout of the instruments. During this period, electrical performance of the radiometer is optimized and the antenna pointing accuracy is established. During a mission life, several engineering tests will be scheduled to confirm operating conditions of the instruments. In addition to the engineering tests, several factors can prevent continuous observations:

1. Acute attitude changes of the ISS
   Among the ISS operational modes, Microgravity Mode is only suitable for limb sounding from the viewpoint of attitude stability. More than 30 successive days in one time and more than 180 days in total per year are planned to be in Microgravity Mode after completion of the ISS construction. During the construction phase of the ISS, the length of this mode will be shortened due to more flights accessing to the ISS. Observations can be continued during Standard Mode, if attitude changes are found not severe. Dynamical analysis of the SMILES attitude is still in progress.

2. Poor environmental conditions on the ISS
   RF electromagnetic fields radiated from transmitters on the ISS may deteriorate the quality of the observed spectra. Of course, in its current design, the SMILES instruments are well shielded against such harmful radiations by means of completely enclosed panels. The submillimeter receiver is also protected by the cryostat. In spite of that, some interference may remain on the observed spectra in the worst cases. The increase of the background pressure around the JEM also may limit normal operation of SMILES, because we have to protect cryogenically cooled components from contamination. This situation can occur in the events such as water dump from the Space Shuttle orbiter, the ISS boosting by a propulsion module, or ventilation from the pressurized module of the JEM.

3. Limitations on the ISS resources
   The ISS is a multi-purpose facility that accommodates many experiments in the same period. SMILES will be provided from the ISS-JEM with resources such as electric power, coolant, and means of data communications. When a large amount of electric power is needed for some other experiment on board, SMILES may be requested to reduce its power consumption. It is however impossible for SMILES to continue atmospheric observations with a reduced level of power consumption. On the other hand, heavy traffic in the ISS data link system may force SMILES to reduce its data generation. This also means that SMILES has to be dormant.

3.2.1.6 Effects of Atmospheric Refraction

So far the effects of refraction due to Earth's atmosphere on the limb-sounding field-of-view are ignored. For submillimeter-waves propagated in the actual Earth's atmosphere, the propagation path is deviated from the geometrical straight line due to refraction caused by vertical gradient of the refractive index which depends on the atmospheric pressure, temperature, and humidity.

Figure 3.6 shows the effects of refractive bending on the limb-sounding line-of-sight paths for two typical reference atmospheres, i.e., low-latitude annual and high-latitude-winter atmospheres[1]. It is found in Figure 3.6 that the refractive bending of the path gives rise to an appreciable deviation from the geometrically calculated one for the paths with tangent points below 20 km.

A significant deviation are found for the actual atmosphere below 15 km in tangent point altitude compared with the case of no refraction (Fig. 3.6). However, variations among different models of atmospheres, which representing seasonal changes, are almost negligible for altitudes above 2 km [*Manabe*, 2000]. The simple exponential model [*International Telecommunication Union*, 1997], in which the atmospheric refractivity n is given

[1]Further detailed discussions on the effects of atmospheric refraction on JEM/SMILES limb-sounding and their dependence on atmospheric models and on radiowave frequency, etc., are found elsewhere [*Manabe*, 1999; *Manabe*, 2000].

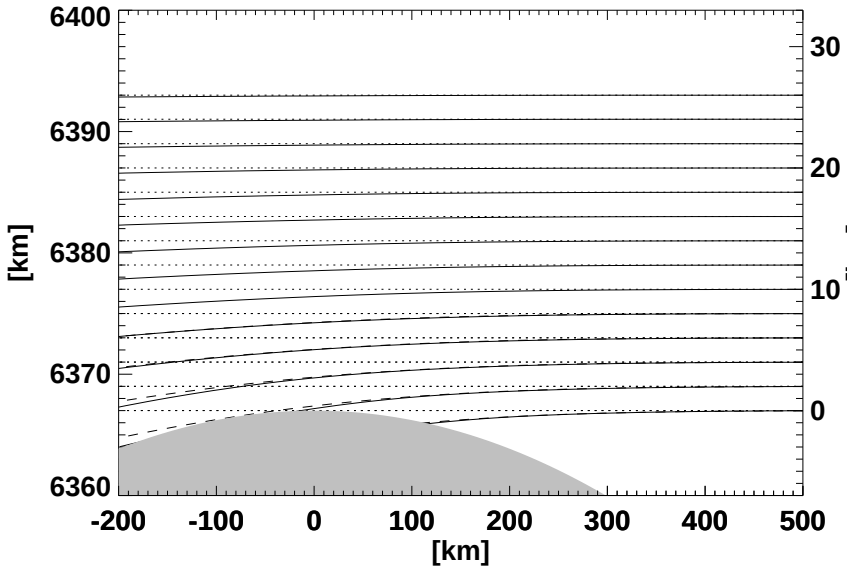

Figure 3.6 Effects of atmospheric refraction on limb-sounding line-of-sight paths for geometrical tangent height without refraction of every 2 km from 0 km to 26 km. Solid and dashed curves are calculated for the low-latitude-annual and high-latitude-winter reference atmospheres [*Manabe*, 2000; *International Telecommunication Union*, 1997], respectively, while the dotted line represents the geometrical ray without refraction. Although the ordinate is exaggerated about 10 times as the abscissa, geometrical rays without refraction are represented by straight lines. For the sake of clarity, nominal tangent points for refraction-free rays are aligned on $x = 0$ km. The SMILES orbital altitude is assumed to be 400 km.

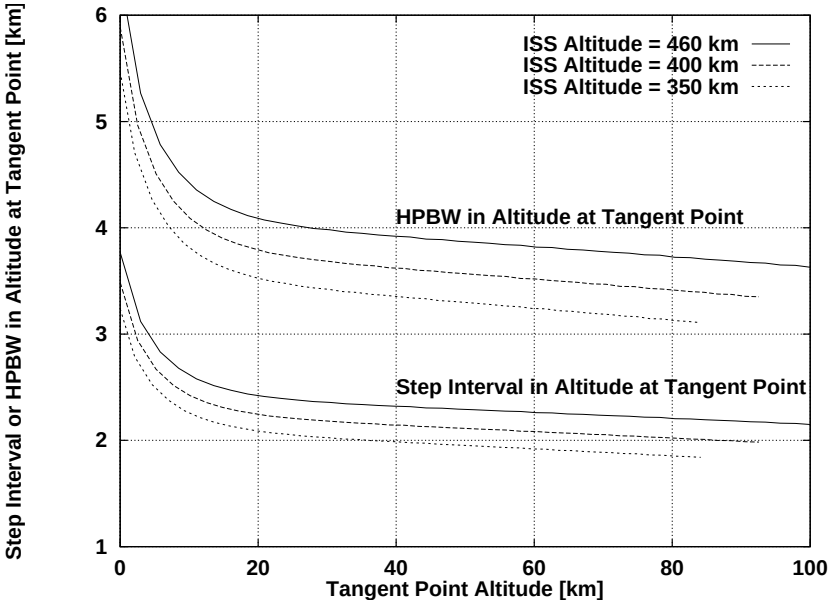

Figure 3.7 Antenna scanning step interval and vertical half-power beamwidth (HPBW) at tangent point for exponential model atmosphere for ISS orbital altitudes of 350 km, 400 km, and 460 km

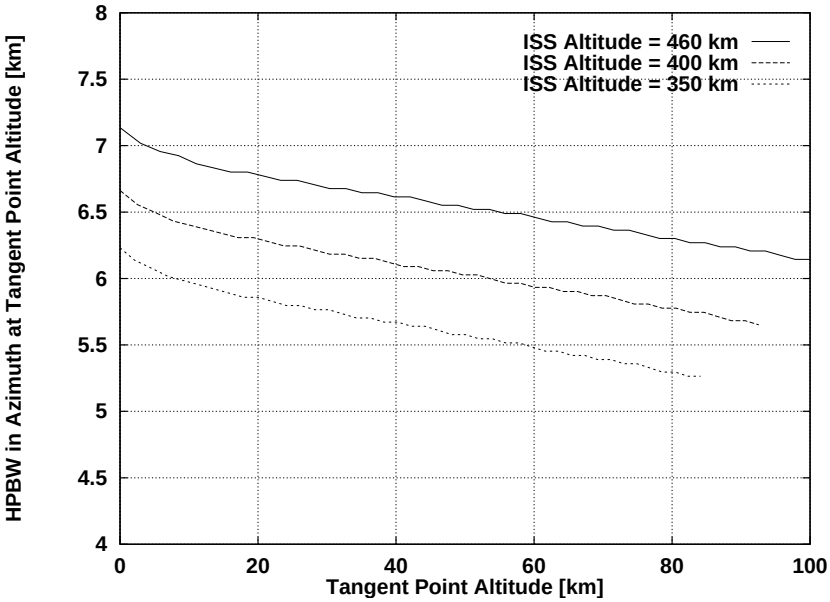

Figure 3.8 Horizontal half-power beamwidth (HPBW) at tangent point for exponential model atmosphere for ISS orbital altitudes of 350 km, 400 km, and 460 km

by a simple exponential function of altitude h [km] as

$$n(h) = 1 + 315 \times 10^{-6} \exp(-h/7.35), \tag{3.1}$$

is found to be a good approximation to a wide range of actual atmosphere.

As a result of the refractive bending of the limb-sounding path, the spatial resolution defined by the antenna beamwidth at the tangent point becomes slightly worse than is expected by ignoring atmospheric refraction. Figures 3.7 and 3.8 show the effects of atmospheric refraction on the spatial resolution at the tangent point calculated for the cases of ISS orbital altitude of 350 km, 400 km, and 460 km by assuming the exponential reference atmosphere whose altitude profile of atmospheric refractivity is given by Eq. (3.1) and the spherical Earth with a radius of 6378.136 km.

3.2.2 Global Coverage

3.2.2.1 Global Coverage of Atmospheric Limb Scanning

Since the ISS orbit is a circular orbit with an inclination of 51.6° to the equator, the highest latitude reached by the ISS orbit is 52° in north and south. In order to extend the latitudinal coverage to the north polar region where the ozone depletion is significant, the field-of-view of the SMILES antenna is deflected 45° to ram port side from the ISS orbital plane. SMILES limb-sounding observation with this field-of-view deflection provides a latitudinal coverage 65° N to 38° S on each orbit.

In Figure 3.9, red segments depict the ground projections of the tangent points for the altitude of 10 km to 60 km in the antenna scanning scheme described in 3.2.1. The associated one-day orbit, shown by a blue curve, is assumed to start from the ascending node in the prime meridian. Each red segment corresponds each limb scan from 10 km to 60 km in altitude. In this calculation, it is assumed that the Earth is spherical with a radius of 6378 km, the ISS travels at a speed of 7.669 km/s in a circular orbit with an

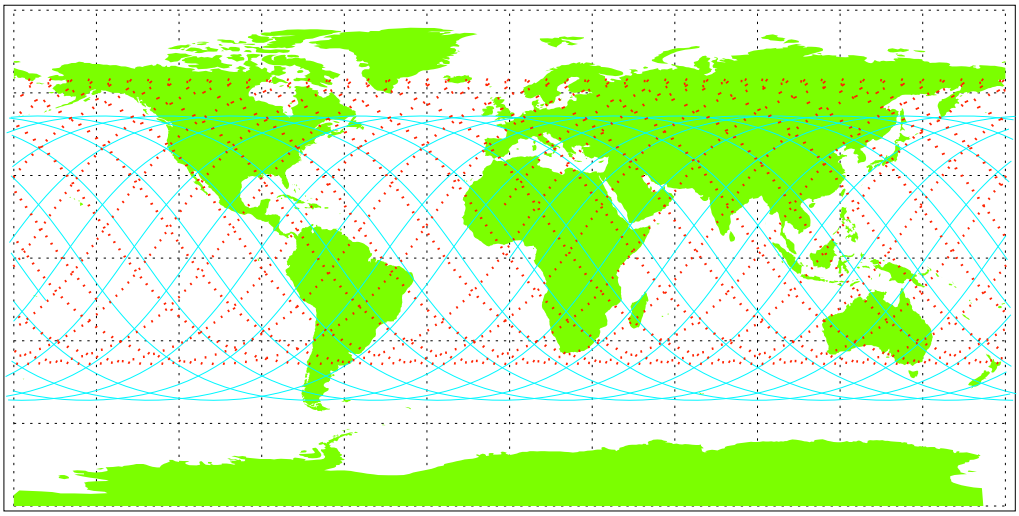

Figure 3.9 The SMILES observation tangent-point coverage (red dots) for an ISS one-day orbit starting from the ascending node corresponding to the prime meridian (blue curve). Only the tangent points within the altitude range between 10 km and 60 km are plotted. The earth is assumed to be spherical with a radius of 6378.136 km. The ISS orbital altitude is assumed to be 400 km. (Cylindrical equidistant projection)

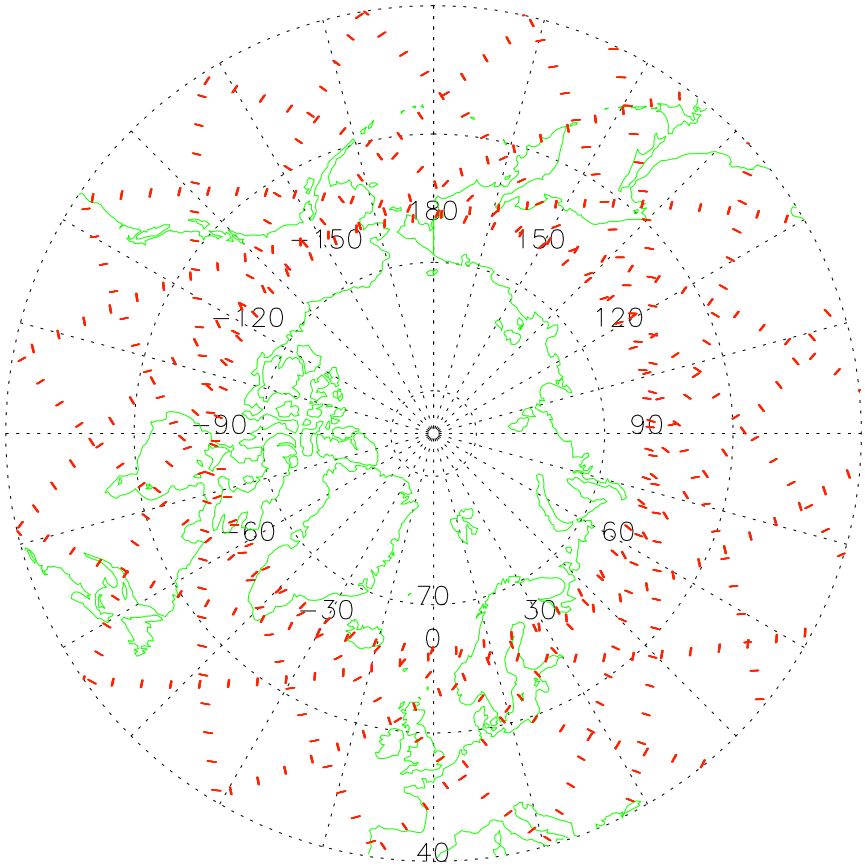

Figure 3.10 The SMILES observation tangent-points coverage (red dots) viewed from the north. (Azimuthal equidistant projection)

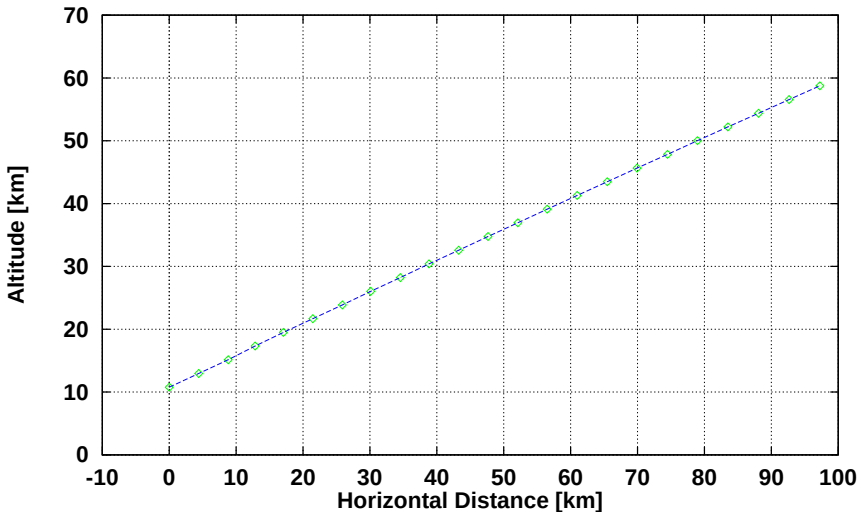

Figure 3.11 Trajectory of tangent points in a vertical plane for single limb scanning.

orbital altitude of 400 km. An along-track separation of about 360 km between adjacent limb scans, which corresponds to about 105 limb scans per orbit, can be achieved by the SMILES antenna scanning scheme described in 3.2.1. Figure 3.10 shows the coverage of the SMILES observation tangent points around the Arctic Circle. It is found in Figure 3.10 that the limb sounding by SMILES samples most densely the northern high latitude region around the 65° N parallel of latitude around which the polar vortex may appear.

Figure 3.11 shows the trajectory of the tangent points in the vertical plane for a limb scanning from 10 km to 60 km. For each limb scanning, the tangent point travels about 100 km in horizontal direction as its altitude increases from 10 km to 60 km[2]

3.2.2.2 Horizontal Resolution

In the retrieval of scientific parameters, the atmosphere should be assumed to be homogeneously stratified, i.e., the atmospheric properties depend only on the altitude. In Figure 3.12, the area where the horizontal homogeneity should be assumed is depicted by a right blue triangle for a single limb scan from 10 km to 60 km. The size of this triangle area is considered to be a measure of the horizontal resolution for single limb scanning. The base of this triangular area is about 1550 km irrespective of the ISS orbital position while its altitude varies within a range between 50 km and 57 km depending on the ISS longitude.

3.2.2.3 Effects of ISS Attitude and Altitude on Global Coverage

So far the attitude of ISS is assumed to be in the nominal LVLH attitude ignoring attitude variation. If the attitude variation of ±15° in yaw angle is taken into account, the latitudinal coverage should be between 68°N and 35°S for a −15° yaw deviation, and between 61°N and 42°S for a +15° yaw deviation (the yaw angle of the ISS is defined

[2]It should be noted that the effects of atmospheric refraction is ignored here. If the effects of atmospheric refraction are taken into account, horizontal extent of the tangent points for a shingle limb scanning becomes appreciably longer than 100 km. See http://www.crl.go.jp/ck/ck321/smiles/refrac/refrac.html, and http://www.crl.go.jp/ck/ck321/smiles/refrac/refrac.pdf.

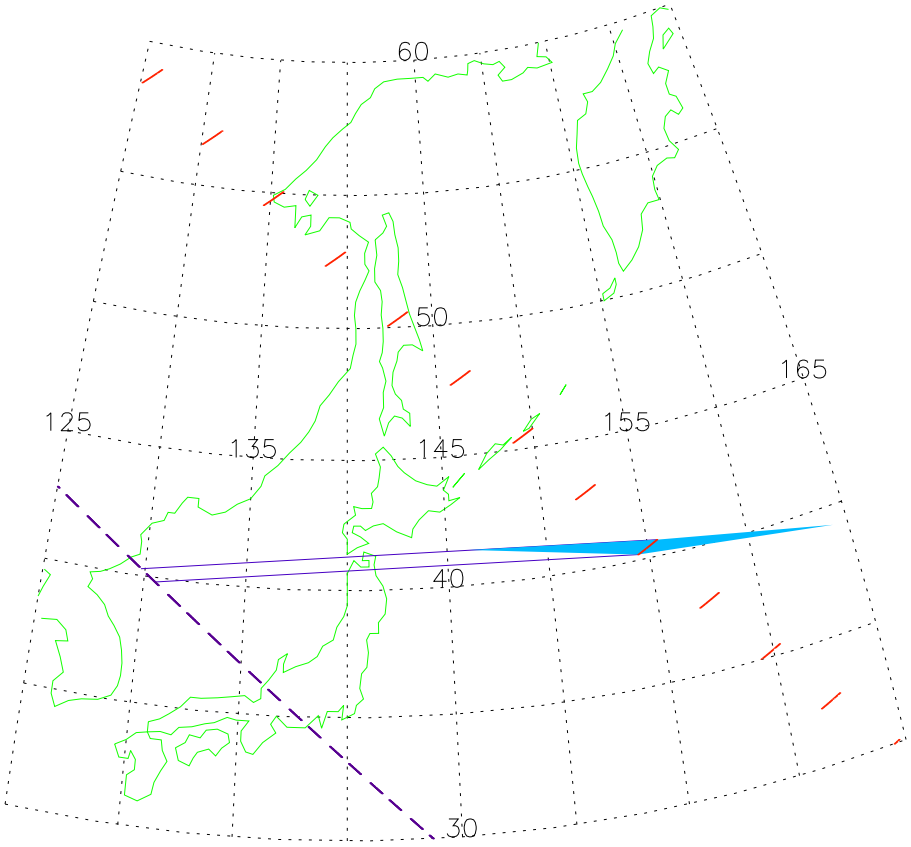

Figure 3.12 The horizontal resolution of SMILES observation depicted by a blue triangle defined as the area where the horizontal homogeneity should be assumed for limb sounding. Red segments are the ground projection of the trajectory of tangent points within a range between 10 km and 60 km. Broken line is a sub-orbital track of the ISS.

in Fig. 3.1) The effects of pitch and roll variations are trivial since the range of antenna elevation scanning has some margin for short-term small variations as described in 3.2.1.2 and can be offset for long-term large variations.

If the ISS altitude is within a range between 350 km and 460 km, its variation has smaller effects on the latitudinal coverage than the yaw variation. Highest latitudes covered by SMILES limb observations are summarized in Table 3.8 for several different combinations of the ISS altitude and yaw deviation. The highest latitude is defined here as the one reached by the 10-km altitude tangent point by SMILES limb observation.

Table 3.8 Highest latitudes sampled by SMILES limb scanning. Highest latitudes are defined as the highest latitude of the tangent point for altitude of 10 km reached by SMILES limb scanning

(a) Northern Hemisphere

	+15°	0°	−15°
460 km	61.9°N	66.2°N	69.6°N
400 km	61.2°N	65.3°N	68.4°N
350 km	60.6°N	64.4°N	67.4°N

(b) Southern Hemisphere

	+15°	0°	−15°
460 km	41.3°S	37.0°S	33.6°S
400 km	42.0°S	37.8°S	34.8°S
350 km	42.6°S	38.8°S	35.8°S

3.2.3 Interference with FOV

3.2.3.1 Interference by the Sun

Since the ISS orbit is sun-asynchronous, the incidence of solar radiation can be from any direction except that of the Earth. SMILES does not have an azimuthal drive of the main reflector, so that its main beam inevitably makes an occasional encounter with the sun. In that case, the SMILES receiver will suffer from about 10 times larger signal than the normal operation. SMILES will use a switching mirror to protect critical devices such as the Radio Spectrometer (AOS). Besides the main reflector, SMILES has the Cold-sky Terminator (CST) that sees the zenith. The CST is used as a low-temperature submillimeter-wave source for the image sideband of SIS mixers, so that the signal from the CST is always fed to the SMILES receiver on almost equal weight of intensity with the signal from the main reflector. Coaxial switches, denoted as 'sw' in Fig. 3.3, in the IF Amplification Section (IFA) will be turned off while solar radiation interferes with the CST beam.

The Data Processing and Control Section (DPC) will control these switching operations, following a programmed sequence. Because of the uncertainty of the ISS attitude, the duration of the switch-off mode must be longer than that expected only from the antenna beam-width. The frequency of interference by the sun in the main beam and the CST beam depends on the ISS orbit, season, latitude, and local time. The sun hits the main beam in the morning of a particular season depending on the latitude, while the sun comes to the zenith when the ISS flies over low latitudes around its local noon.

In Figure 3.13, the local times of the SMILES observation points are plotted with green dots in the latitude range of 0 - 10°N, 30 - 40°N, and 50 - 60°N. In this figure, red crosses show where the sun comes within ±2° from the line-of-sight of the main beam. The solar interference with the main beam occurs around 6 o'clock of local time in the season near equinox. In the same figure, the interference with the CST beam is shown with orange boxes. The points where the sun comes within ±3° from the ISS zenith are marked. This interference occurs at the local noon occasionally. Refer the caption of the figure for assumptions used in this calculation.

3.2.3.2 Interference by the Solar Paddle

While SMILES has an ability of dense observation in Arctic region, its main beam is occasionally interfered by the ISS solar paddles. The SMILES main beam views 45° north from the ISS orbital plane. The huge photovoltaic arrays, which rotate around the axis of the ISS main truss, will intersect the SMILES main beam twice an orbital rotation of the ISS (Figure 3.14). Blue circles in Fig. 3.13 plot the points where the photovoltaic arrays come within ±0.1° from the SMILES main beam. Averaged probabilities of the interference are 1.2%, 0.8%, and 0.5% in the latitude range of 0 - 10°N, 30 - 40°N, and 50 - 60°N, respectively. If we assume the main beam is interfered when the photovoltaic arrays come within ±1°, the probabilities increase. The probabilities of the occurrence of interference are shown in Fig. 3.15 for three different types of interferences described above. Local times when the interferences occur are unevenly distributed, in particular local noons have the higher probabilities of the interference as shown in Fig. 3.15.

3.2.4 Antenna Response Pattern

SMILES has a mechanically-scanning offset-Cassegrain antenna of 400 mm × 200 mm in diameter, which is designed to generate an elliptical beam with an altitude resolution of around 3.2-4.4 km at tangent altitudes ranging from 10 km to 60 km, while keeping the physical size small enough to be compatible with the payload envelope. The Half-power

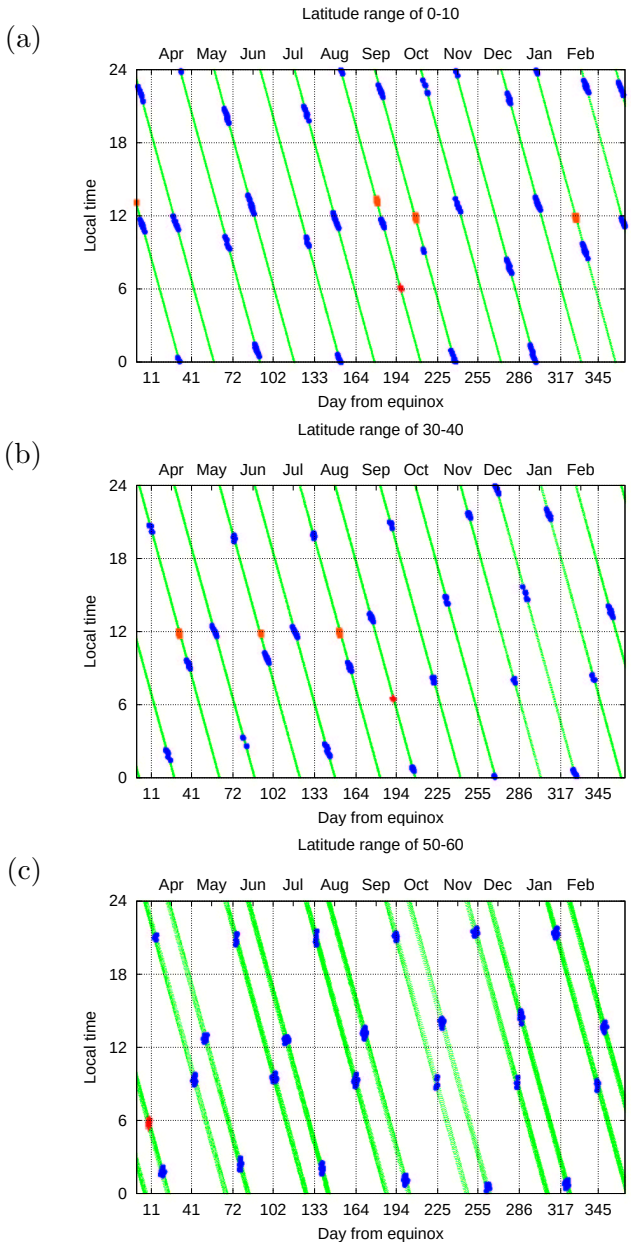

Figure 3.13 The local time of the SMILES measurements. The local times are shown (green dots) with respect to the day from the vernal equinox. The SMILES single scan is assumed to last 53 seconds. Green dots are replaced with other marks when one of the measurements in the scan has the solar interference with the main beam (red vertical crosses), or the CST beam (orange boxes), or the solar paddle interference with the main beam (blue circles). Three latitudinal zones are calculated; (a) 0 - 10°N, (b) 30 - 40°N, and (c) 50 - 60°N. Assumptions are; a circular orbit of the ISS, a spherical earth, the ISS decreasing altitude from 400 km to 386 km, a simple rotation of the ISS solar paddle pointing toward the sun, and the SMILES location of EFU #3 on JEM-EF. It is judged to be interfered when the interior angle between the sun and the main beam, the sun and the CST beam, and the nearest point of the solar paddles and the main beam are lower than 2°, 3°, and 0.1°, respectively.

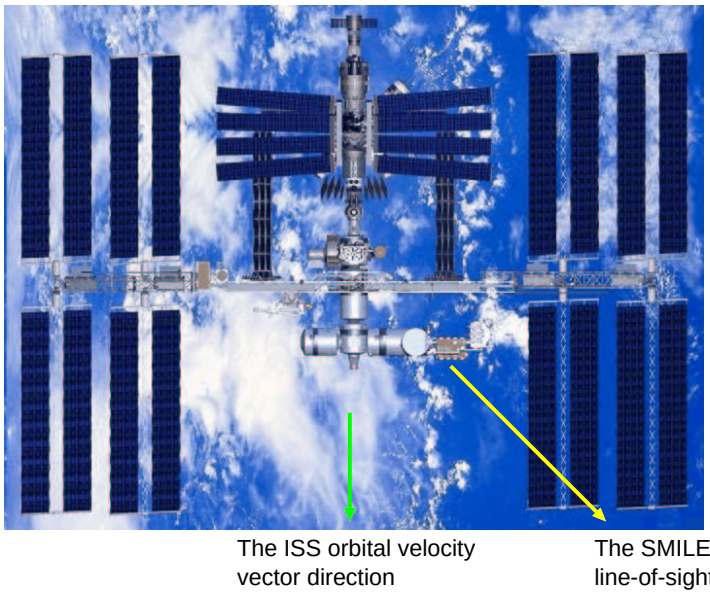

Figure 3.14 Top view of the ISS. The rotating solar paddle will occasionally intercept the SMILES main beam (yellow arrow).

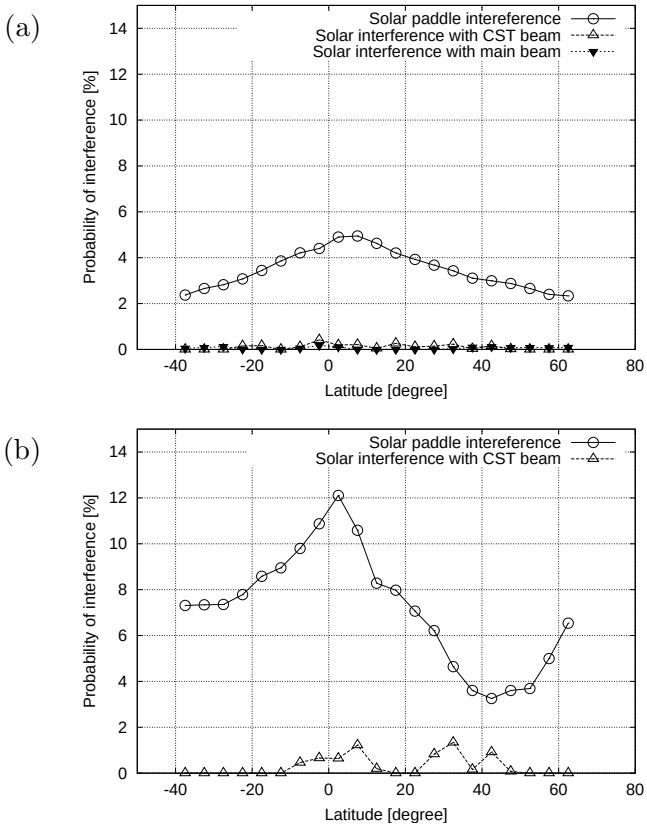

Figure 3.15 The probability of the interference versus latitude. Plotted are the ratios of the numbers of scan which include interfered measurements by the sun with the main beam (filled triangles) or with the CST beam (open triangles) or by the solar paddle with the main beam (circles) to the total number of scan. The ratios are calculated from (a) whole one year scans and (b) one year scans corresponding to local times between 9:00 and 13:00.

Table 3.9 Antenna Specification. * Frequency: 637.32 GHz. FOV beam efficiency is defined as the relative radiated power involved within a 2.5-time HPBW area.

Item	Characteristic
Antenna shape	Elliptical-beam offset Cassegrain
Aperture diameters	400 mm × 200 mm
Main reflector material	Aluminum with a sandblast treatment
Surface roughness of reflectors	5 μm rms
Surface accuracy of reflectors	15 μm rms
Aperture edge-level	-20 dB*
Beam width (HPBW$_{Az}$)	0.173°*
Beam width (HPBW$_{El}$)	0.083°*
FOV beam efficiency	Higher than 90 %*

specification of the SMILES antenna is summarized in Table 3.9.

A calculated near-axis response pattern of the SMILES antenna is shown in Figure 3.16 (designed by MELCO). The surface shape of the main- and sub-reflectors has been op-

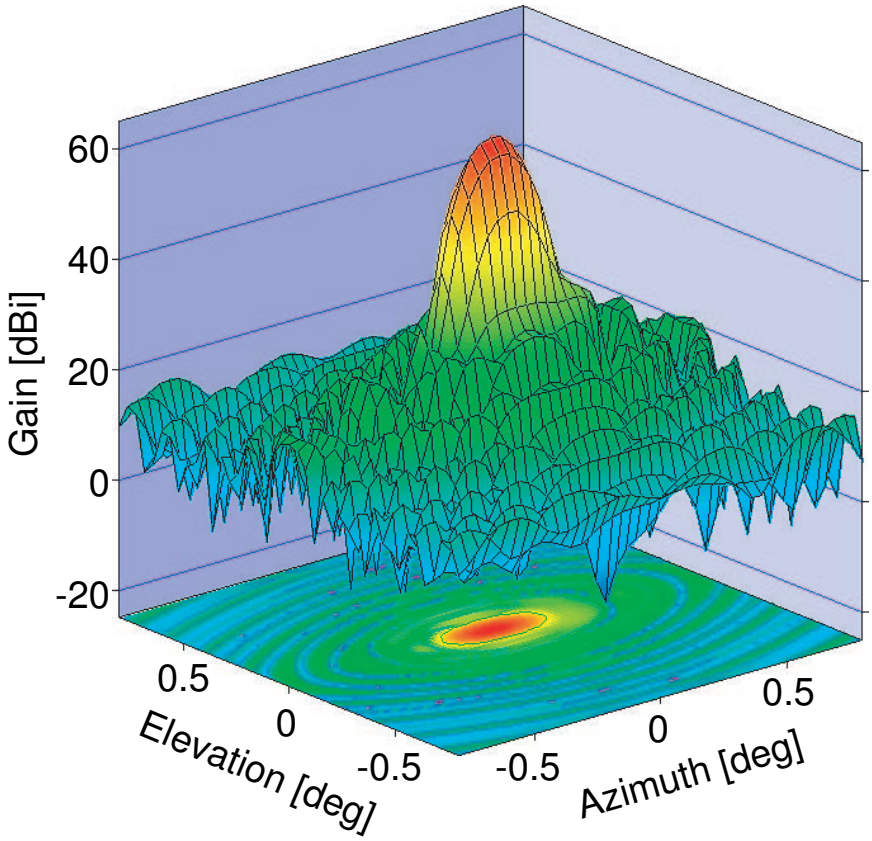

Figure 3.16 Calculated near-axis antenna response pattern.
(designed by MELCO)

timized for achieving low sidelobe levels and high beam efficiency. Such quality of the submillimeter beam is essential to reduce additional noise contributions from the earth and the SMILES payload itself. The actual response pattern of the antenna will be evaluated with a near-field phase-retrieval measurement on the ground.

3.2.4.1 Response Pattern Model

In order to evaluate the effect of the antenna response pattern on atmospheric limb scanning, we introduce an approximate response pattern model. An antenna response function is described as $P(Az, El)$.

The model is defined in four regions and consists of three functions as shown in Figure 3.17. Region A is an area to define the FOV beam efficiency. Region B represents a main beam area. Region A is within region B. A response pattern in regions A and B (P_{main}) is approximated by a gaussian function as following:

$$P_{\mathrm{main}}(Az, El) = 10 \log \left(a_0 + a_1 \exp \left(-\frac{1}{2} \left(\left(\frac{Az}{a_2} \right)^2 + \left(\frac{El}{a_3} \right)^2 \right) \right) \right) \ [\mathrm{dB}] \tag{3.2}$$

where Az and El is the azimuth and elevation angles in a coordinate fixed on the main reflector. Region C describes an error pattern area. In region C, a response pattern (P_{error})

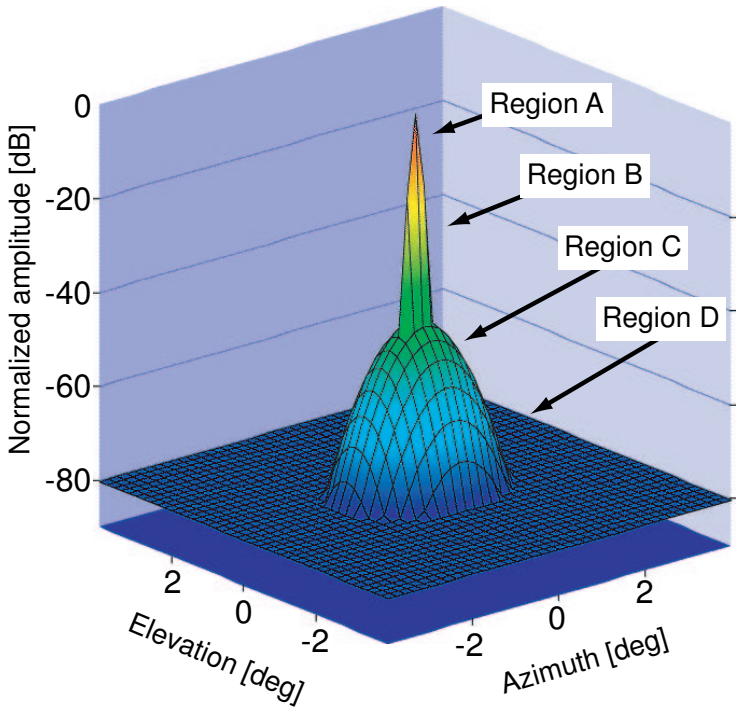

Figure 3.17 Approximate response pattern. Region A is an area to define the FOV beam efficiency. Region B represents the main beam area. The response pattern in region B is approximated by a gaussian function. Region C describes an error pattern area. The response pattern in region C is described by second order polynomials of azimuth and elevation angles in decibel values. Region D is a wide angle pattern area. Its response function is described by a constant.

Table 3.10 Response pattern model coefficients for several cases in FOV beam efficiency. Coefficients $a_0 \sim a_3$ and $b_1 \sim b_5$ are common for all cases. Coefficients b_0 and c_0 in each case are different.

(a) Common coefficients

a_0	a_1	a_2	a_3	
-9.2377 $\times 10^{-5}$	1.0026	7.1774 $\times 10^{-2}$	3.4227 $\times 10^{-2}$	
b_1	b_2	b_3	b_4	b_5
0.92124	-0.23690	-11.084	-0.45984	-18.485

(b) Different coefficients

FOV beam efficiency	96 %	90 %	85 %	80 %
b_0	-44.210	-29.042	-26.021	-24.133
c_0	-80.242	-79.963	-79.535	-79.254

is described by second order polynomials of azimuth and elevation angles as

$$P_{\text{error}}(Az, El) = b_0 + b_1 \times Az + b_2 \times El + b_3 \times Az^2 + b_4 \times Az \times El + b_5 \times El^2 \text{ [dB]}. \quad (3.3)$$

Region D is a wide angle pattern area. Its response function (P_{wide}) is described by a constant as following:

$$P_{\text{wide}}(Az, El) = c_0(= \text{constant}) \text{ [dB]}. \quad (3.4)$$

Then, the response function is determined by a maximum value among the three functions as

$$P(Az, El) = \max[P_{\text{main}}(Az, El), P_{\text{error}}(Az, El), P_{\text{wide}}]. \quad (3.5)$$

The FOV efficiency for the ideal response pattern is 96.1 %. However, the real FOV efficiency may deteriorate due to several causes, such as thermal distortion and mechanical misalignment. It is considered that these factors cause a decrease of main beam gain and an increase of power level in the error pattern region. Following this assumption, the model coefficients are determined. We find model coefficients for four cases in FOV efficiency as shown in Table 3.10.

3.2.4.2 Effective Response Pattern for Atmospheric Limb Scanning

The antenna response pattern is usually expressed with a radiation characteristic in a certain cut plane such as Az=0. For the atmospheric limb scanning, however, an effective response pattern in the height direction is more important. Since the atmosphere is well stratified, the vertical response pattern $P_{vert}(El)$ is obtained from the following equation:

$$P_{vert}(El) = \int_{Az_-}^{Az_+} P(Az, El) \cos(El) d(Az), \quad (3.6)$$

where $P(Az, El)$, Az_+, and Az_- represent the antenna response function, and the azimuth boundary angles of the FOV. Based on the actual extent of the open window for the antenna, we assume that Az_+ and Az_- is +99° and -5°, respectively. As previously mentioned in 3.2.1.3, atmospheric emissions from six consecutive tangent point altitudes

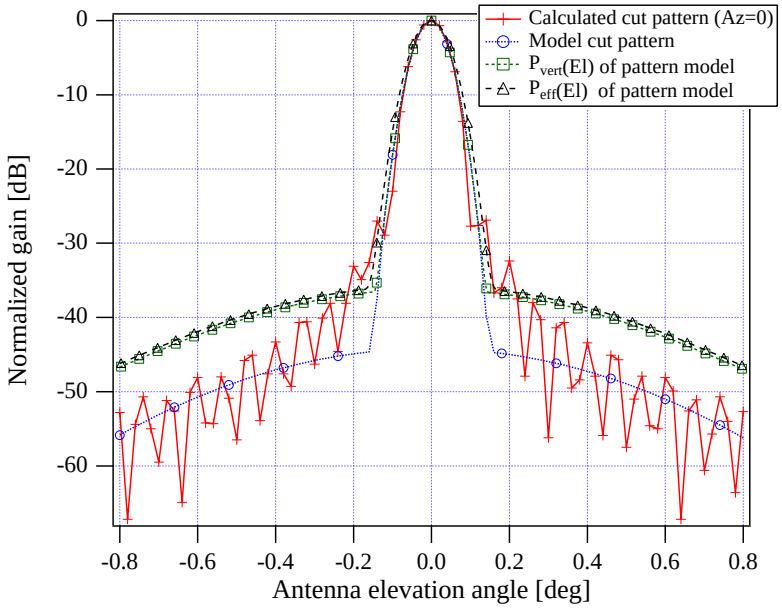

Figure 3.18 Effective antenna response pattern.

will be collected and integrated in each unit of the output data. Therefore, the effective response pattern $P_{eff}(El)$ is calculated by averaging $P_{vert}(El)$ for six consecutive altitudes as the following:

$$P_{eff}(El) = \frac{1}{6}\sum_{j=0}^{j=5} P_{vert}(El + (j - 2.5)\Delta El), \tag{3.7}$$

where ΔEl is a unit stepping angle of the SMILES antenna, 0.009375°, which is driven by the Antenna Drive Electronics (ADE).

Figure 3.18 shows the vertical and the effective antenna responses for the pattern model in comparison with cut-responses at $Az = 0$ for the designed pattern and the model pattern.

All patterns are normalized by each antenna gain. The result shows the sidelobe levels of the vertical and the effective antenna response pattern are approximately 9 dB higher than those of the cut response pattern. It means that SMILES has a higher sensitivity to the atmospheric emissions at adjacent altitudes than expected simply from the vertical cut response pattern.

The HPBW of the vertical response pattern is similar to that of the cut response pattern of the model. They are 0.080°. The effective beam size is 0.090° in HPBW, which is 12 % larger than that for the cut response pattern of the model.

3.2.4.3 Beam Efficiency

In the SMILES antenna specification, the FOV beam efficiency is defined by the ratio of the power radiated into an elliptical cone with a flare-angle of 2.5-time HPBW to the total power radiated by a feed horn. The feed horn adopted for SMILES is a so-called "back-to-back horn," which is placed at the interface point between the SMILES antenna and the Ambient Temperature Optics (AOPT). It is a circular corrugated waveguide with

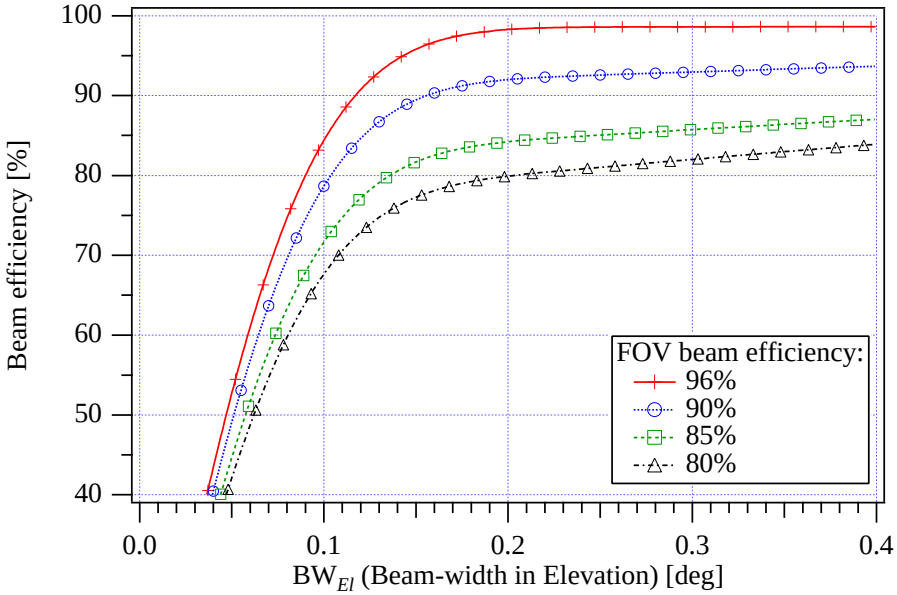

Figure 3.19 Beam efficiency.

a taper in one end, which will feed the antenna. This optical approach is adopted to make electro-magnetic shielding for the sensitive submillimeter receiver against high-level artificial electric fields anticipated on the ISS. To understand the relationship between the beam efficiency and a degradation of the beam quality, we have calculated a beam efficiency as a function of a beam width in the elevation angle, BW_{El}. Such function is defined by

$$\eta_{beam}(\mathrm{BW}_{El}) = \frac{\int_{-\mathrm{BW}_{El}/2}^{\mathrm{BW}_{El}/2} P_{vert}(El)d(El)}{P_{total}}, \tag{3.8}$$

where P_{total} is the total power and BW_{El} is the full extent of the elevation angle to define the beam efficiency.

The calculated results are shown in Figure 3.19. We have assumed that the FOV beam efficiencies are 96 %, 90 %, 85 %, and 80 %. A decrease in the FOV beam efficiency represents a decrease in the main beam power level and the increase in a error pattern power level. When the FOV beam efficiency is higher than 90 %, the beam efficiency will approximately saturate around the definition area of the FOV beam efficiency, which is the 2.5 times as wide as the HPBW_{El}.

We will discuss the effect of the FOV beam efficiency on the brightness temperature in detail in 3.3.5.

3.2.5 ISS Orbit and Attitude Variations

3.2.5.1 Orbit

The ISS is in a nearly circular orbit with an altitude of 350 – 460 km and an inclination of 51.6° to the equator. Major characteristics of the orbit are listed in Table 3.11 [*NASA*, 2000]. The orbit will decay due to atmospheric drag on the ISS, which is enlarged with its

low altitude and large cross section. The lower limit of the ISS altitude, for its existence in orbit, is taken as 278 km. The operational altitude must be kept higher than 350 km, where the orbital decay takes 180 days to reach the lower limit. Periodic boosting by using onboard thrusters will be carried out to maintain the ISS altitude within 350 – 460 km. The orbit control accuracy is specified as 305 m (3σ) in terms of the semi-major axis. The orbit determination accuracy is 305 m (3σ) for the semi-major axis, and 914 m (3σ) for the position vector. The ISS orbit prediction data will be found on the NASA website at http://spaceflight.nasa.gov/realdata/sightings/SSapplications/Post/JavaSSOP/orbit/ISS/SVPOST.html, and orbit determination data will be provided from the NORAD data website at http://celestrak.com/NORAD/elements/.

Table 3.11 Characteristics of the ISS Orbit

Parameters	Characteristics
Nominal Orbit	Altitude : 407 km Inclination : 51.6°
Range of Operational Altitude	350 km to 460 km
Orbit Control Accuracy	Semi-major axis : 305 m (3σ)
Orbit Determination Accuracy (Knowledge Accuracy)	Semi-major axis : 305 m (3σ) Position vector : 914 m (3σ)
Orbit Prediction Accuracy	TBD

Table 3.12 ISS Orbital Elements

Prediction Data			
Website	Coordinates	Description	Notes
NASA	M50 cartesian	position, velocity	M50 : Inertial mean of year 1950 frame of reference
	M50 keplerian	6 orbital elements	
	M50 cartesian	position, velocity	J2000 : Inertial mean of year 2000 frame of reference
	J2000 cartesian	position, velocity	
	Keplerian	TLE (5 orbital elements, mean mortion)	TLE : Two-lines elements
	Keplerian	AMSAT (5 orbital elements, mean mortion)	
Determination Data			
NORAD	Keplerian	NORAD TLE (5 orbital elements, mean mortion)	

3.2.5.2 Attitude Control

The ISS will fly in the so-called "Local Vertical Local Horizontal (LVLH)" attitude. This means that the ISS attitude is nominally fixed in a reference coordinate that is defined

by a local horizontal plane and a local vertical direction (nadir). Since the ISS attitude is affected by perturbation torque due to aerodynamic drag and gravity gradient, it is controlled by a set of onboard Control Moment Gyros (CMGs) to maintain the Torque Equilibrium Attitude (TEA). Major characteristics of the ISS attitude are shown in Table 3.13 [*NASA*, 2000; *Treder*, 1999]. Absolute tilt angles are allowed up to $\pm 15^\circ$ in roll and yaw, and $-20/+15^\circ$ in pitch. These angles depend on the mass characteristics of the whole ISS and atmospheric changes due to the solar activity. Its stability during a cycle period of orbit is specified to be within 3.5° per axis, and the rate of attitude change is within $\pm 0.002^\circ$/sec per axis. This attitude change rate is formally applied to the pressurized modules during microgravity operations. During a unit scan of the SMILES antenna, which lasts 53 seconds, the track of the scanning beam can deviate from an ideal straight ascending line by about the same size as its HPBW. We have to determine the real track with a help of the star tracker that is equipped in SMILES.

Table 3.13 Characteristics of the ISS Attitude (TEA:Torque Equilibrium Attitude)

Parameters	Characteristics
Nominal Attitude	LVLH attitude
Range of Operational Attitude	Roll, Yaw : $+15^\circ$ to -15° Pitch : $+15^\circ$ to -20°
Attitude Control Accuracy	$\pm 5^\circ$ per axis (compared with the commanded values)
	$\pm 3.5^\circ$ per axis (controlling to TEA)
Attitude Change Rate	Within $\pm$ 0.002°/sec per axis (during microgravity operations, in pressurized labs)
Attitude Estimation Accuracy	0.5° per axis (3σ) 0.01°/sec per axis (3σ)
(Knowledge Accuracy)	(at the NASA navigation base) 3.0° per axis (3σ) (at attached payload)
Attitude Prediction Accuracy	TBD
Continuous Period in the TEA	30 days

3.2.6 Tangent Height Calibration

3.2.6.1 Calibration Scheme

By comparing observed stellar images with an installed star catalog, the Star Tracker (STT) will calculate the orientation of the mechanical framework of the STT camera in the heliocentric inertial equatorial reference coordinate system (HCS) which is an inertial coordinate system with its origin located at the sun and its equatorial plane in the earth orbital plane. The STT on SMILES provides the output in the quaternion representation. It is a method to express a rigid-body rotation by means of the direction cosines (e_1, e_2, e_3) of an axis and a rotation (Φ) around the axis. Four parameters of the quaternion is

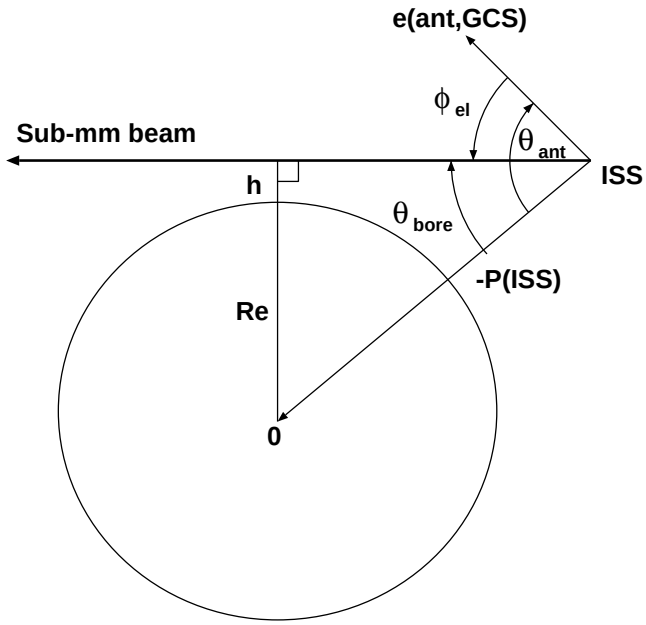

Figure 3.20 Geometrical definition of tangent-point altitude

defined as

$$q_1 \equiv e_1 \sin\frac{\Phi}{2}, \tag{3.9}$$

$$q_2 \equiv e_2 \sin\frac{\Phi}{2}, \tag{3.10}$$

$$q_3 \equiv e_3 \sin\frac{\Phi}{2}, \tag{3.11}$$

$$q_4 \equiv \cos\frac{\Phi}{2}. \tag{3.12}$$

With these four parameters, we can express any rigid-body rotation by the following matrix.

$$\boldsymbol{M}[\boldsymbol{q}] = \begin{bmatrix} q_1^2 - q_2^2 - q_3^2 + q_4^2 & 2(q_1q_2 + q_3q_4) & 2(q_1q_3 - q_2q_4) \\ 2(q_1q_2 - q_3q_4) & -q_1^2 + q_2^2 - q_3^2 + q_4^2 & 2(q_2q_3 + q_1q_4) \\ 2(q_1q_3 + q_2q_4) & 2(q_2q_3 - q_1q_4) & -q_1^2 - q_2^2 + q_3^2 + q_4^2 \end{bmatrix}. \tag{3.13}$$

If a unit vector in the STT-based coordinate is represented by $\boldsymbol{e}(stt)$, the direction of the antenna mounting basis (a reference direction corresponding to the antenna elevation angle of 0°) that is evaluated in the geodetic coordinate system (GCS), which is an earth-based coordinate with its origin at the earth center and its equatorial plane in the earth equator, $\boldsymbol{e}(ant, GCS)$, is calculated by

$$\boldsymbol{e}(ant, GCS) = \boldsymbol{M_2} \cdot \boldsymbol{M_1} \cdot \boldsymbol{K}(ant, stt) \cdot \boldsymbol{e}(stt), \tag{3.14}$$

where $\boldsymbol{M_1}$ and $\boldsymbol{M_2}$ are coordinate transformation matrices to express the conversion from the STT-based coordinate to the heliocentric inertial equatorial coordinate system (HCS), and that from the HCS to the GCS, respectively. The matrix elements of $\boldsymbol{M_1}$ are expressed with the quaternion components of the STT outputs. Matrix $\boldsymbol{K}(ant, stt)$ denotes a vector

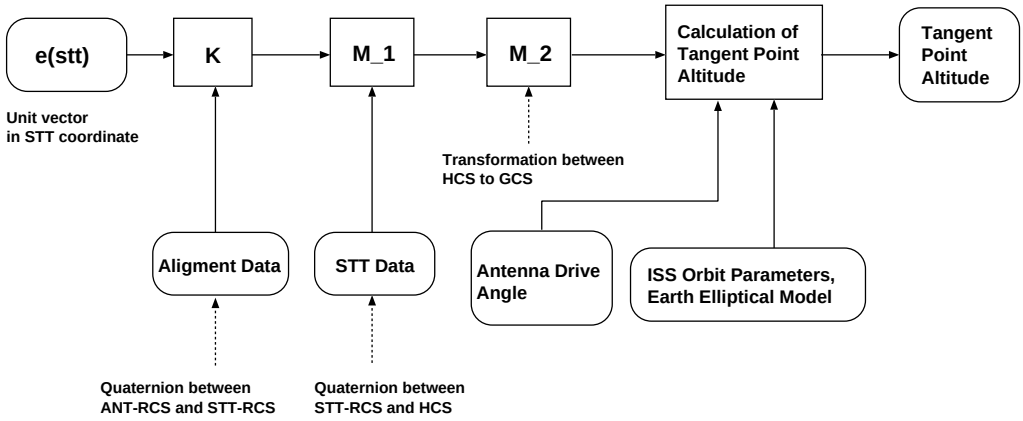

Figure 3.21 Flow chart of STT data analysis

rotation from the unit vector of the STT-based coordinate to the axis of the antenna-mounting basis. Matrix $\boldsymbol{M_2}$ includes transformation in time system. A difference between the UT1 and UTC should be taken into account (UT1 represents the rotation of the earth while UTC are determined on the base of atomic time).

The tangent-point altitude for the limb-sounding observations is derived from $\boldsymbol{e}(ant, GCS)$ and information such as the ISS position in orbit, scanning angle of the antenna, and surface model of the Earth. The STT is mechanically fixed to the antenna-mounting basis, while the main reflector of the antenna will rotate around the elevation angle (ϕ_{el}). If the ISS position is determined with a position vector $\boldsymbol{P}(ISS)$ in the GCS, the angle between the line-of-sight of the antenna (mechanical axis) and $\boldsymbol{P}(ISS)$ is calculated as

$$\theta_{bore} = \arccos\left[\frac{-\boldsymbol{P}(ISS)\boldsymbol{e}(ant, GCS)}{\mid \boldsymbol{P}(ISS) \mid}\right] - \phi_{el}. \tag{3.15}$$

The tangent-point altitude is given by

$$h = \mid \boldsymbol{P}(ISS) \mid \sin\theta_{bore} - R_e, \tag{3.16}$$

where R_e represent the Earth radius at the tangent point.

3.2.6.2 Calibration Accuracy

Several factors that affect the accuracy of tangent point height are listed in Table 3.14. They include errors both in the attitudes of the SMILES antenna and in the ISS orbital altitude. Among the attitudinal errors are the squint of the submillimeter beam from the mechanical axis of the antenna reflector, offset angle in the driving mechanism of the antenna, thermal bending of the antenna structure with respect to the STT, alignment errors between the antenna and STT, measurement errors in the STT, and errors due to imperfect time synchronization between the ISS and STT. On the other hand, errors in the ISS orbit determination will affect the knowledge of tangent point height. Expected error values for those factors are given in two columns for bias and random errors. Bias error means its effect is applied in common to all of the data acquired in a unit scan of the antenna (in 53 sec). The relative altitude distance between any two points is not affected by the bias errors. But random error occurs independently for each point. While

the current estimation of those error values are very tentative, we expect that the beam squint will be the largest factor in bias errors. It should be calibrated in orbit by means of observing a reference object such as the moon. The overall altitudinal error without the beam squint is estimated about 0.76 km in bias error, and 0.34 km in random error (both in 1σ).

Table 3.14 Residual Errors in the tangent height after calibration with the STT data

Error Factors	Bias Error@1σ		Random error@1σ	
Attitudinal Errors:				
Sub-mm beam offset from the REF axis	0.13°	5.02 km	–	–
Mechanical driving errors of REF	0.007°	0.27 km	0.007°	0.27 km
Thermal bending of REF against STT	0.003°	0.12 km	–	–
Mechanical alignment of REF against STT	0.007°	0.27 km	–	–
STT measurement errors	0.007°	0.27 km	0.0015°	0.06 km
Time synchronization errors	0.20 sec	0.50 km	0.07 sec	0.18 km
Altitudinal Error:				
Determination errors of the ISS position	–	0.3 km	–	0.1 km
Overall(rss) with the beam offset		5.07 km		0.34 km
Overall(rss) without the beam offset		0.76 km		0.34 km

REF means the main and sub reflectors of the antenna. STT is the Star Tracker. Altitudinal sensitivity to the attitude error is 38.6 km/deg, and that to the error in time is 2.52 km/sec for the nominal orbital height of 400 km.

3.3 Spectral Regions and Sensitivity

3.3.1 Observation Frequency Bands

Three observation frequency bands have been selected in line with the SMILES scientific objectives toward chlorine-related processes in the stratosphere. Most important molecular transitions included in these bands are 649.45 GHz (ClO), 625.92 GHz ($H^{35}Cl$) and 624.98 GHz ($H^{37}Cl$), as well as 625.37 GHz and others for O_3. This selection is a result of optimization between scientific targets and instrumental restrictions, such as the number of SIS mixers and down-converters. The first intermediate frequency (IF) is determined to avoid potential interference by high-level electromagnetic fields in the ISS environments. A spectral range around 650 GHz and the other around 625 GHz are simultaneously observed in the upper sideband (USB) and lower sideband (LSB), respectively, of the submillimeter mixing with a single local oscillator (LO) at 637.32 GHz. In Figures 3.22-3.24, expected emission profiles are calculated based on a standard model of the atmosphere (Rutherford Appleton Laboratory). The brightness temperature and line-width of the atmospheric emissions are widely varied, depending on the tangent altitude of the observing line-of-sight. Frequency coverage is 624.32 - 625.52 GHz in Band-A, 625.12 – 626.32 GHz in Band-B, and 649.12 – 650.32 GHz in Band-C. As SMILES has only two units of spectrometers, only two among these three bands are observed at a time. Nevertheless, Band-A and Band-B are partially overlapped to keep observations of O_3 at 625.37 GHz being conducted in any cases. HCl lines are observed in both Band-A and Band-B, while they are attributed to different isotopes of chlorine. The natural abundance of ^{35}Cl and ^{37}Cl is 75.78 percents and 24.22 percents respectively. ClO is observed only in Band-C. There are two ^{81}BrO

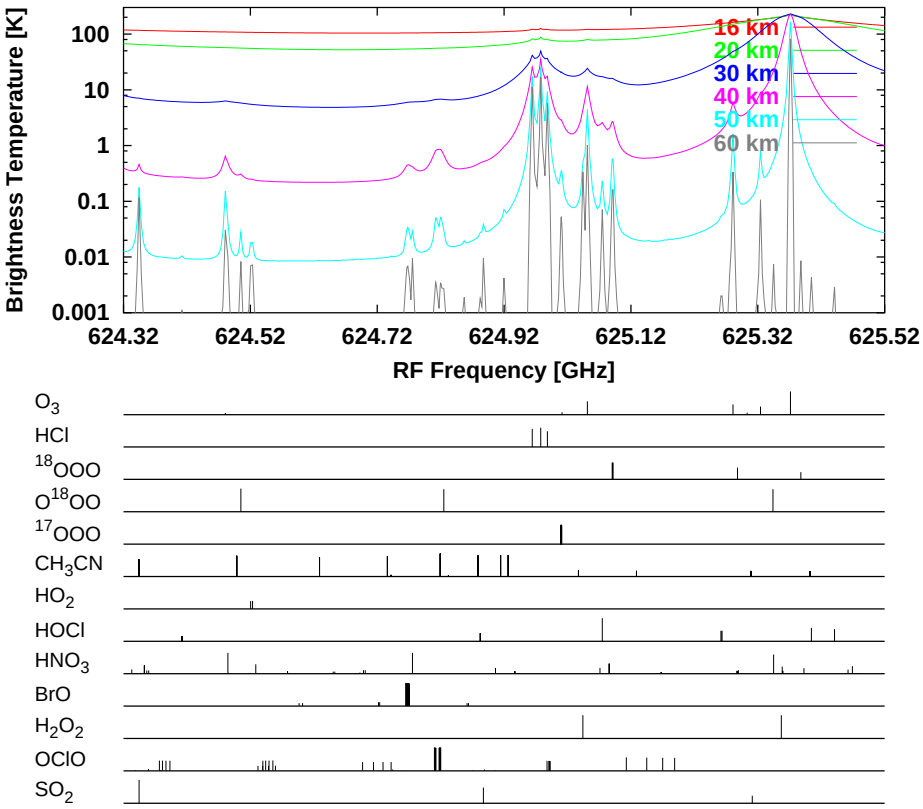

Figure 3.22 Atmospheric emission profiles expected for Band-A.

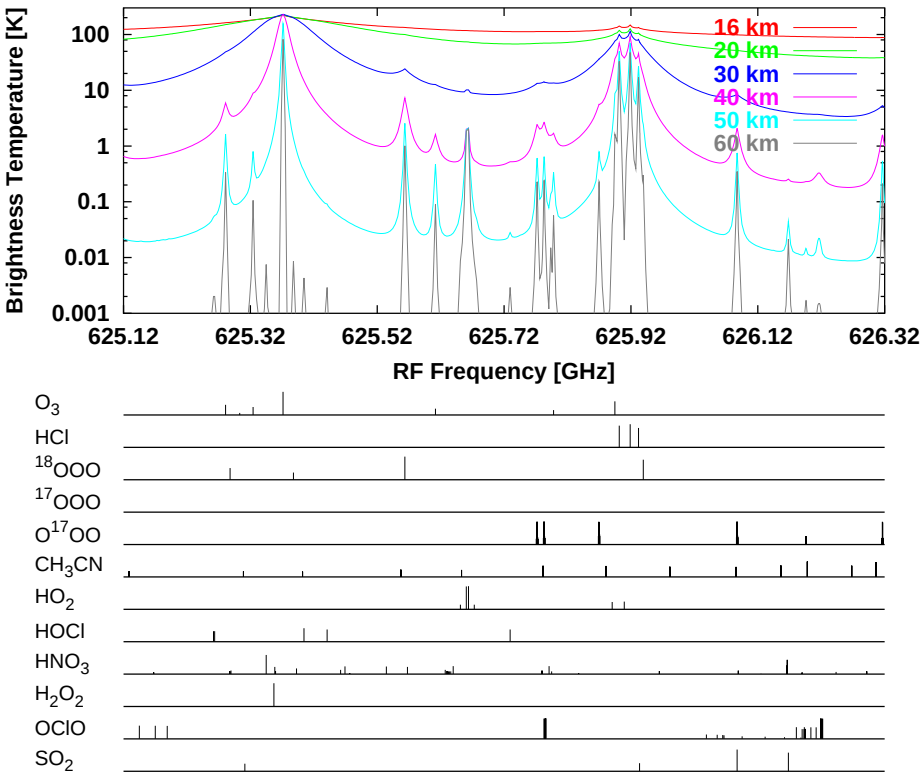

Figure 3.23 Atmospheric emission profiles expected for Band-B.

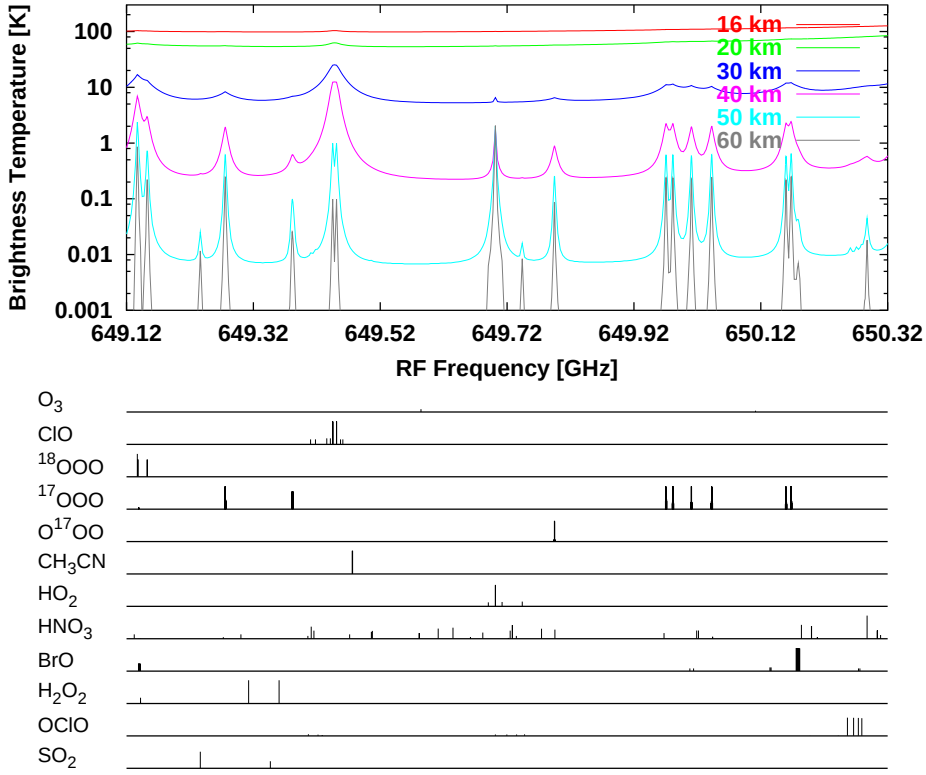

Figure 3.24 Atmospheric emission profiles expected for Band-C.

lines, at 624.77 GHz and 650.18 GHz, included in Band-A and Band-C.

3.3.2 Frequency Down-conversion

3.3.2.1 Intermediate Frequency System

The three submillimeter-wave bands are converted to the first IF by two SIS mixers operated at 4.5 K in a cryostat [*Fujii et al.*, 2000; *Inatani et al.*, 1997]. By means of a quasi-optical single-sideband (SSB) filter, the USB and LSB emissions are separately converted to the first IF, which is 11.8 – 13.0 GHz for the USB and 11.0 – 13.0 GHz for the LSB. Band-A and Band-B are two different portions inside the LSB, while Band-C is in the USB. These are further down-converted to the second IF in 1.55 – 2.75 GHz, and spectral features in each band are analyzed by the Acousto-optic Spectrometer (AOS).

When a microwave mixer is sensitive to both its USB and LSB, the sideband of interest is called a "signal band," and the other undesirable sideband is an "image band." Even with an SSB filter, its performance to reject an image band is not perfect. This situation makes it important to know how the image band is superimposed on the signal band. Figure 3.25 illustrates how the three submillimeter-wave observation bands are converted down to the second IF.

3.3.2.2 Sideband Separation

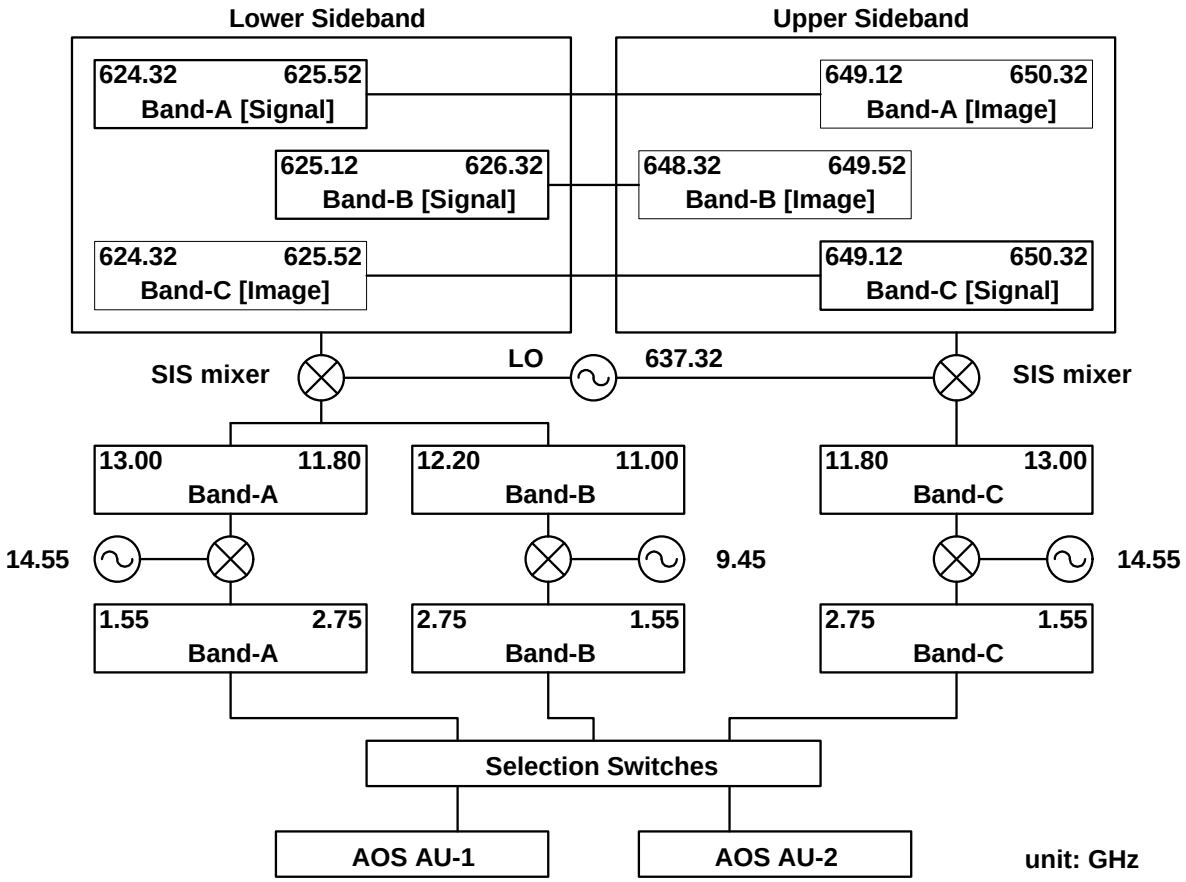

Figure 3.25 Frequency conversion in SMILES: Both signal and image bands are converted to the first IF, while the image is suppressed by an SSB filter. The frequency conversion to the second IF is made completely in a single sideband mode.

Figure 3.26 illustrates the schematic configuration of SSB filtering and local injection in the receiver optics of SMILES. To separate the two sidebands, SMILES is equipped with a quasi-optical SSB filter in its submillimeter optics. The SSB filter, which is a modified Martin-Puplett interferometer [*Inatani et al.*, 1999] newly proposed for SMILES, has the ability to reject the image band by 20 dB or more in the SMILES observation bands. This proposed SSB filter is composed of a pair of frequency-selective polarizers (FSP1 and FSP2) each of which consists of a free-standing wire-grid backed by a flat mirror, and is intended to achieve a function as a dual-beam interferometer equivalent to that of the conventional type Martin-Puplett interferometer (MPI) [*Martin*, 1982].

The functional blockdiagram of the sideband separation in the SMILES submillimeter-wave optics is shown in Figure 3.27. The SIS mixer-1 is well coupled to the antenna (ANT) in the USB, but is not in the LSB. In the LSB, it is coupled to the Cold-sky Terminator (CST), which is a reference port terminated to the 2.7-K cosmic microwave background. Since the CST is free from the atmospheric emissions, this method allows the SIS mixer-1 to selectively down-convert the USB atmospheric emissions into the first IF. In the same way, the SIS mixer-2 down-converts the LSB atmospheric emissions into the first IF. In addition to sideband separation, the SSB filter coupled with the wire-grids RG1 and LG1 has a function of injecting the local signal from the submillimeter-wave local

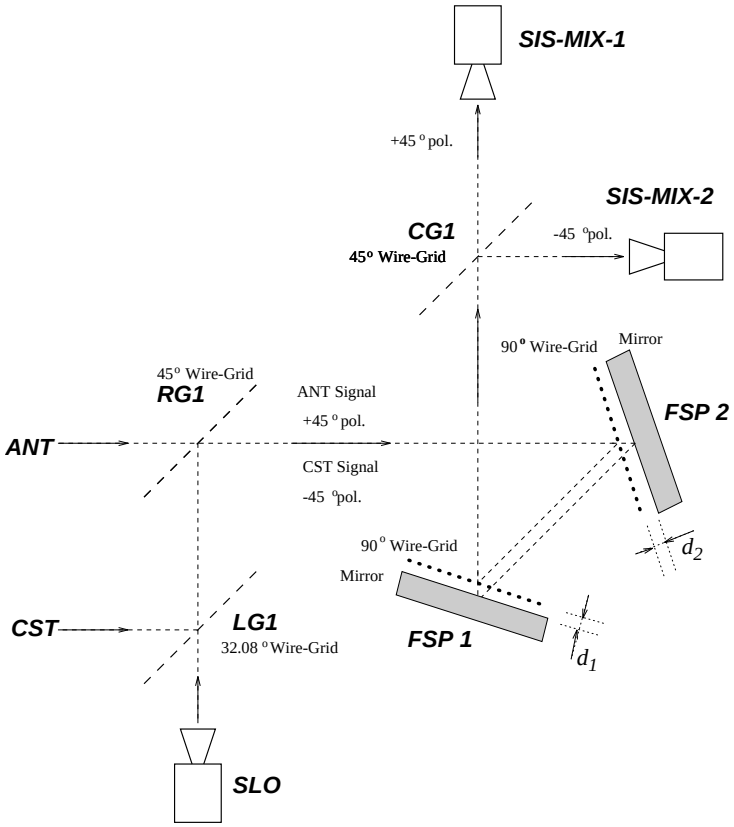

Figure 3.26 Schematic configuration of SSB filtering and local injection in the SMILES receiver optics

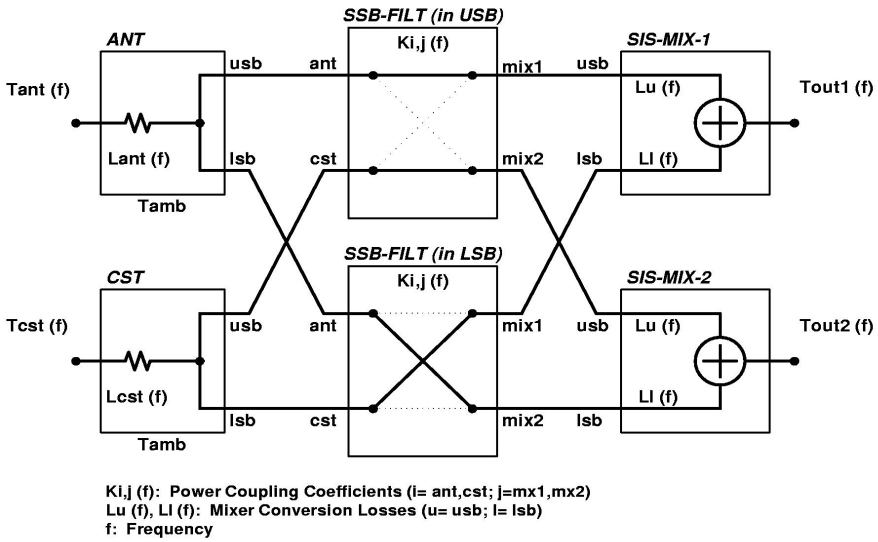

Figure 3.27 The function of the SSB filter in detail. The antenna port is coupled with the mixer-1 in the USB, but with the mixer-2 in the LSB. CST stands for the Cold-sky Terminator, which is free from the atmospheric emissions. Solid lines mean an efficient coupling, and dotted lines a suppressed coupling.

oscillator (SLO) to both LSB (SIS-MIX-1) and USB (SIS-MIX-2) mixers for frequency down-conversion.

The sideband separation characteristics of the modified Martin-Puplett interferometer are determined by the grid-mirror spacings, d_1 and d_2, of two FSPs. In the design of the SMILES submillimeter-wave opticas, a combination of the spacings, $d_1 = 1.545$ mm and $d_2 = 1.572$ mm, is adopted as a reasonable choise by which we can achieve image rejection better than 15 dB both for LSB and USB of SMILES observation bands while keeping the difference in local-signal power couplings to USB and LSB mixers less than 0.5 dB. The pass-band transmission and image rejection characteristics calculated around the SMILES obeservation bands by an exact theory for the two FSP combination are shown by red symbols in Fig. 3.28. Although the exact theoretical calculations are rather involved, the transmission and rejection characteristics around the SMILES observation bands are found to be well approximated by simple functions describing power coupling coefficients for the SIS mixer-i to the ANT port, $K_{i,a}$, and to the CST port, $K_{i,c}$, given by

$$K_{i,j}(f) = \frac{1 + \alpha^2 + 2\alpha \cos(\frac{m\pi f}{f_0})}{4} \qquad (i = 1 \text{ or } 2,\ j = a \text{ or } c). \tag{3.17}$$

A nonlinear least-squares fitting gave an exellent fit of (3.17) to the exact theoretical calculation as shown in Fig. 3.28 with the values of parameters, m, f_0 and α, listed in the

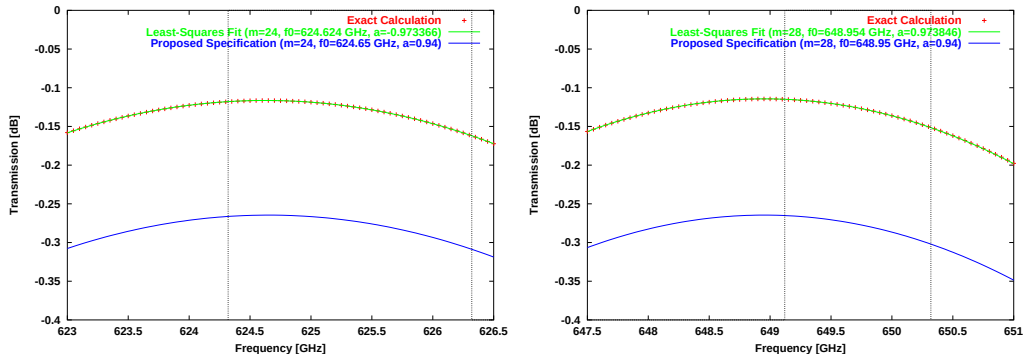

(a) Transmission Characteristics in LSB. (b) Transmission characteristics in USB.

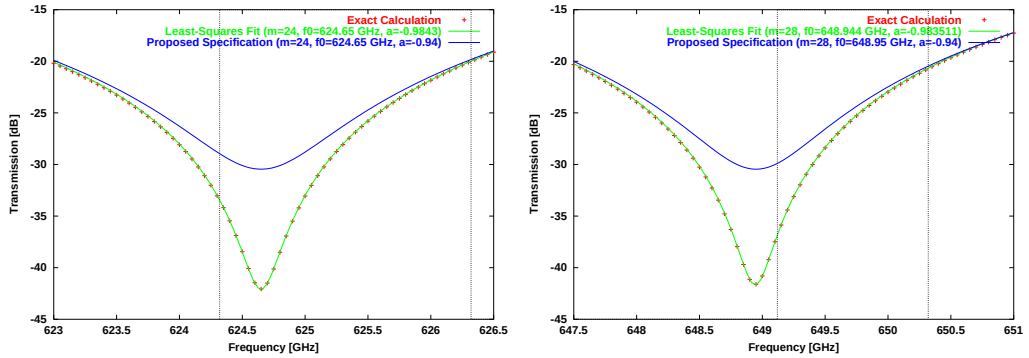

(c) Image rejection characteristics in LSB. (d) Image rejection characteristics in USB.

Figure 3.28 Coupling coefficient K_{ij} for signal transmission and image rejection of the SSB filter designed for SMILES. +: Exact theretical calculation for SSB filter; green curves: least-squares fit to the exact calculation; blue curves: simplified model for SSB characteristics of SMILES optics.

Table 3.15 Model parameters m, α, f_0 of power coupling coefficients K_{ij} for least-squares-fit model of SSB filter and simplified model for SMILES optics

			Least-Squares Fit			Proposed Specification		
Band		$K_{i,j}$	m	f_0	α	m	f_0	α
LSB	Transmission	$K_{1,a}, K_{2,c}$	24	624.624 GHz	0.973366	24	624.65 GHz	0.94
	Rejection	$K_{2,a}, K_{1,c}$	24	624.65 GHz	-0.9843	24	624.65 GHz	-0.94
USB	Transmission	$K_{2,a}, K_{1,c}$	28	648.954 GHz	0.973846	28	648.95 GHz	0.94
	Rejection	$K_{1,a}, K_{2,c}$	28	648.944 GHz	-0.983511	28	648.95 GHz	-0.94

columns labeled as *Least-Squares Fit*. By considering imperfectness of optical components not only in the SSB filter but also in whole optics, we propose to use a more conservative model given by (3.17) with the values of parameters, m, f_0 and α, listed in the columns labeled as *Proposed Specification* in Table 3.15. The power coupling coefficients given by this *Proposed Specification* is also shown in Fig. 3.28

With this *Simple Model*, the effects of the image band on the atmospheric observations are calculated in Figures 3.29 – 3.30. The image contribution suppressed by the SSB filter is superimposed on the signal spectra in the first IF. More precisely, we have to take account of the difference in the SIS mixer conversion losses for the USB and LSB, which could be up to 2 dB depending on particular device of the SIS mixer. But this effect is not included in Figures 3.29 – 3.31.

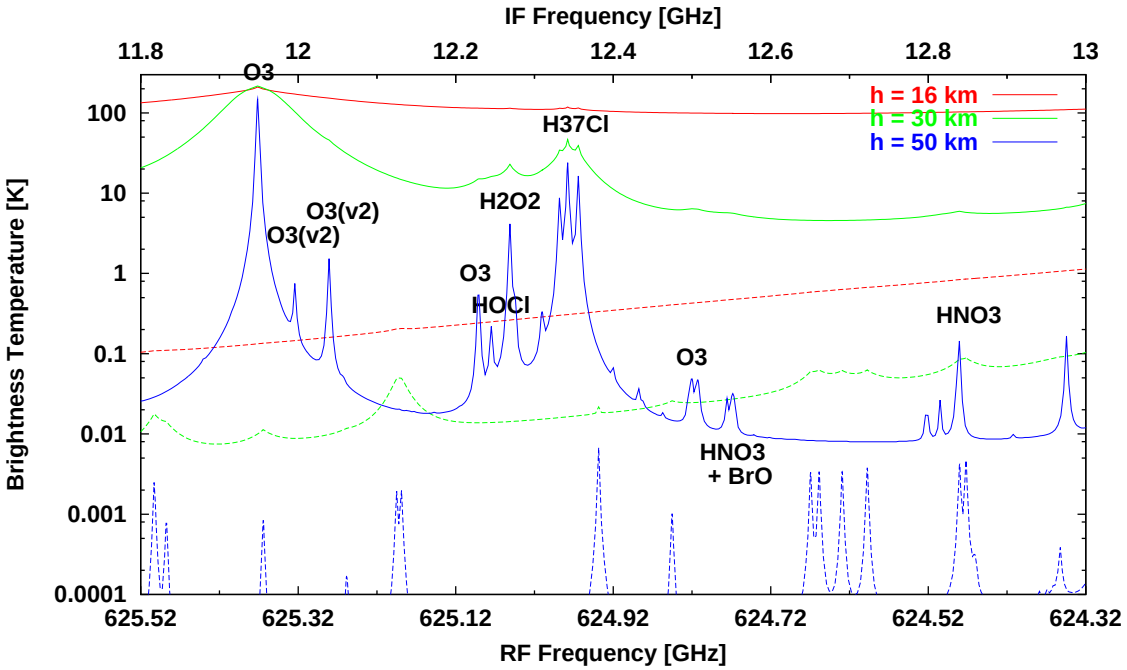

Figure 3.29 The effect of the image contributions in Band-A. Solid curves denote the signal intensities and dashed curves the image contributions.

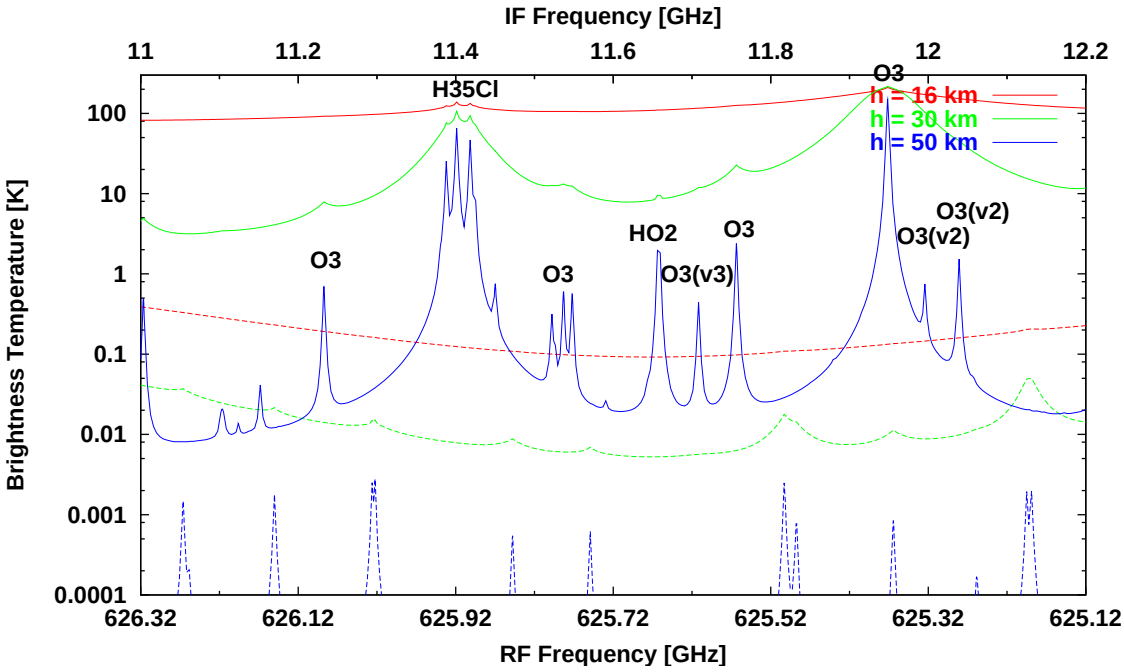

Figure 3.30 The effect of the image contributions in Band-B.

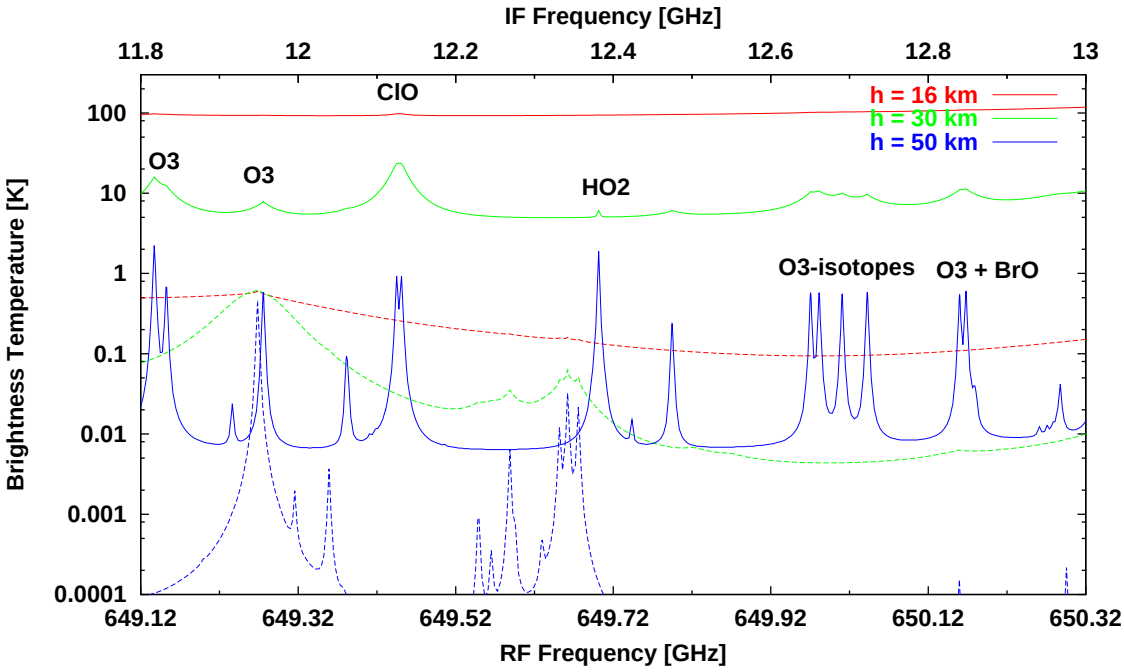

Figure 3.31 The effect of the image contributions in Band-C.

3.3.3 Acousto-optic Spectrometer

3.3.3.1 Frequency Characteristics

Two acousto-optic spectrometers (AOS) give us a powerful means of obtaining spectral images of various chemical species in a required range of altitudes, while constituting the system with a single type of spectrometer (see Figure 3.32). Each AOS has 1500 spectral channels to cover the bandwidth of 1200 MHz. Two units of AOS can be combined by selecting a mode in the IF switching network, which enables us to view a limb spectrum with a 2000-MHz bandwidth over 3000 frequency channels. Channel separation is typically 0.8 MHz, but the channel number is not always linearly related with its corresponding frequency. In addition, the relation can be influenced by the change of the environmental temperature. Some calibration process is needed on board, which is described in the remaining.

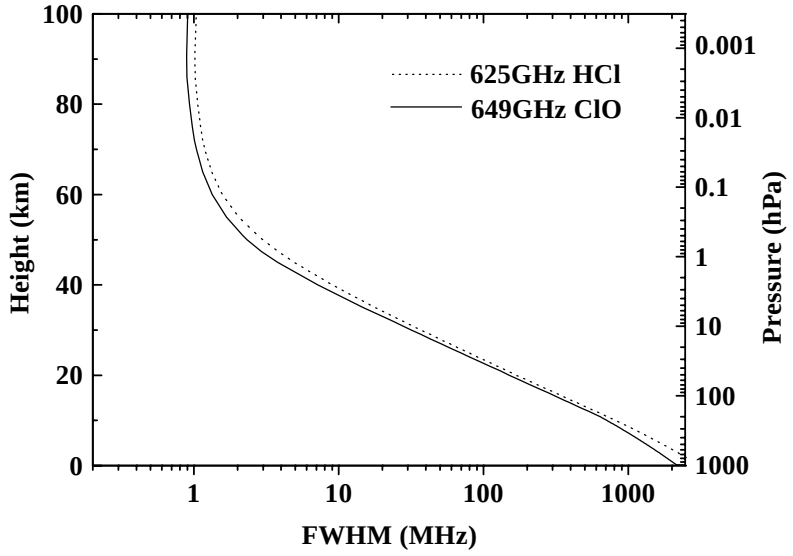

Figure 3.32 Spectral line-width versus atmospheric height with respect to two important lines of the SMILES mission.

Spectrometer's response function is obtained with the input of a carrier signal, the typical shape of which is depicted in Figure 3.33. Any input spectra to the AOS are convoluted with this kind of frequency response function, the full-width at half-maximum (FWHM) of which is often called as "resolution bandwidth" of the AOS. The FWHM for the AOS on SMILES will be 1.4 MHz or less. With this frequency response function, we can estimate the influence of some strong emissions at neighbor frequencies on the emission profile of interest.

On the other hand, when we deal with noise characteristic of the AOS, we should use the noise bandwidth, which represents the width of such an equivalent boxcar filter that gives the same fluctuations on the output spectra. The noise bandwidth for the AOS on SMILES is derived to be 2.5 MHz. With this value, we can estimate the standard deviation of the spectral fluctuations on the AOS output data. Each output spectrum is obtained in every 500 ms. If the system noise temperature is 500 K, the standard deviation for the

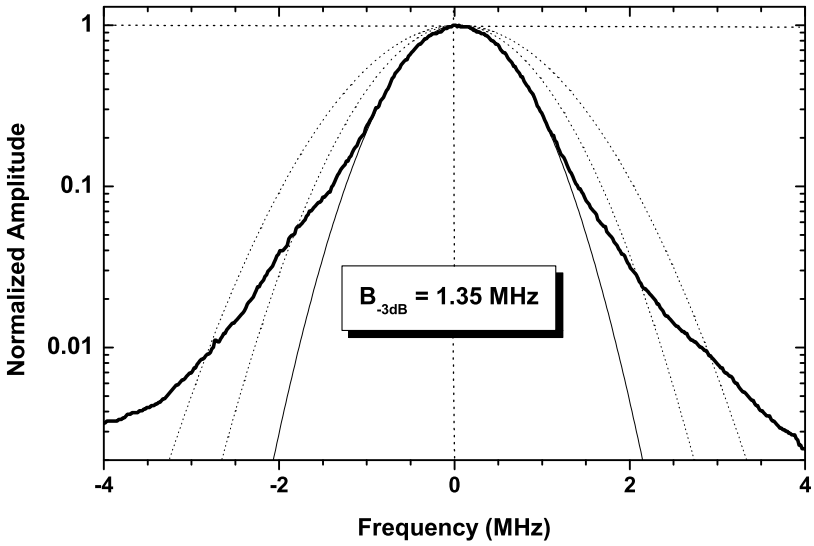

Figure 3.33 Frequency response function of the SMILES/AOS. The typical resolution bandwidth is 1.35 MHz.

snap shot spectrum will be approximately 0.5 K.

3.3.3.2 Frequency Calibration

Frequency calibration of the spectrometer will be accomplished by using a frequency reference with the absolute accuracy of about 10 kHz over the whole mission life. It is installed in the IFA section, generating a series of carrier signals with an interval of 100 MHz. The output of this comb generator will be injected to the AOS once in every scan of the antenna (53 seconds). Peak positions of each picket are derived against channel numbers, and the relation between frequency and channel number will be established by a polynomial fitting. Residuals of such fitting will be typically less than 30 kHz as shown in the Figure 3.34, which gives the error in frequency of the AOS spectra.

3.3.3.3 Noise Dynamic Range

Radio signal is converted to optical one in the AOS, and it is detected by a CCD array. The read-out voltages, or the number of collected charges in each cell of the CCD array, should be proportional to the input RF power levels, but they are usually modified by several additional factors in reality. The variance of the original RF noise at CCD is expressed by the following well-known expression:

$$N_{RF}^2 = \frac{Q^2}{B \cdot t}, \tag{3.18}$$

where Q,B, and t represent the number of collected charges at CCD, noise band-width, and the integration time for collecting charges, respectively. Potential contributors to

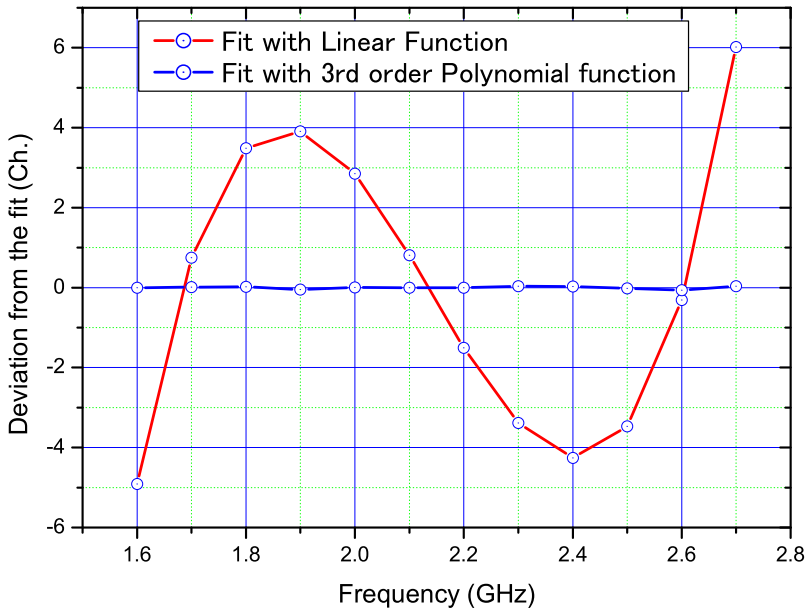

Figure 3.34 Residuals from the frequency fit with comb generator. 1 Ch. corresponds to approximately 0.8 MHz.

additional noise are photon shot noise, CCD dark noise, quantization noise, and detection circuit noise:

$$N_{add}^2 = N_{photon}^2 + N_{CCD}^2 + N_{AD}^2 + N_{Detection-circuit}^2. \tag{3.19}$$

The read-out noise of the AOS is the sum of the RF noise and the additional ones:

$$N_{read-out}^2 = N_{RF}^2 + N_{add}^2. \tag{3.20}$$

The relative weight of the additional noise will increase as the RF power decreases. So if a criterion is settled so that the noise variance ratio $N_{read-out}^2/N_{RF}^2$ to be less than 1.21, then we can define a range of RF power levels, for which the additional noise is less than 10%. We call this the "noise dynamic range" of the AOS. As far as the observed spectra lie within the noise dynamic range, the increase of the system noise due to the AOS can be negligible.

Alternatively, we can calculate an increase of noise at a given signal level. Its coefficient is a function of the signal level, and expressed as $f(D)$, where $D = Q_{sat}/Q$, and

$$T_{sys}^{eff} = T_{sys}^{org} \cdot f(D), \tag{3.21}$$

$f(D)$ can be calculated with the AOS instrumental parameters:

$$f(D) = \sqrt{1 + \frac{B \cdot t}{Q_{sat}} \cdot D + B \cdot t \left(\frac{q_0^2 + q_{eff}^2}{Q_{sat}^2} + \frac{1}{2^{2n} \cdot 12} \right) \cdot D^2}, \tag{3.22}$$

where, q_0, Q_{sat}, n, and q_{eff} are dark current noise, amount of the saturation charge, quantization bit of the A/D converter, and equivalent amount of charge of the detection

circuit noise, respectively. A typical behavior of $f(D)$ is depicted in Figure 3.35. In SMILES/AOS, the noise dynamic range of 9 dB is foreseen for a criterion of additional noise of 10%.

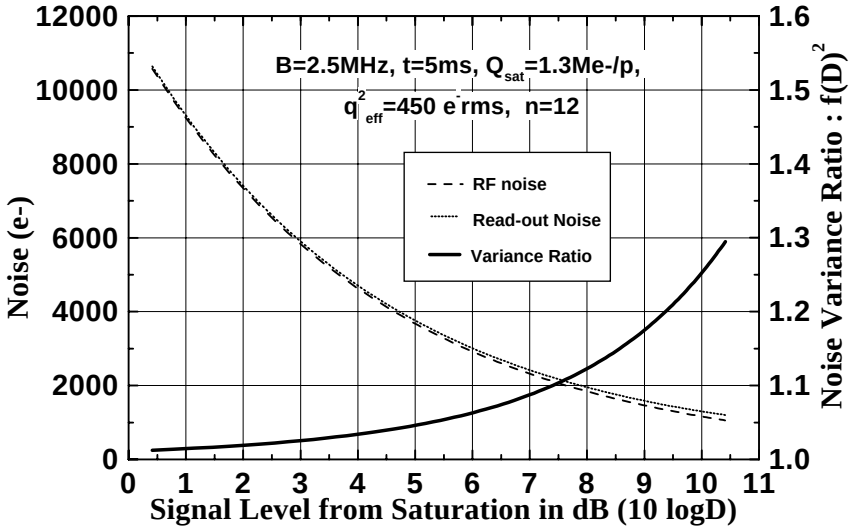

Figure 3.35 RF noise, read-out noise and the variance ratio of them

3.3.3.4 Differential Non-Linearity

Another concern with the AOS in obtaining the limb spectrum is "differential non-linearity (DNL)" of the analog to digital converter, which was first claimed by R. Schieder of the University of Cologne. The DNL is irregularities in the "monotonic character" of the conversion from input analog voltages to digitized values. Noise due to this effect is non-statistical, because it is reproducible if we repeat measurements under the same conditions. It is troublesome that this effect is never visible as far as the signal and the reference are of the same power level, which is usually the case when a long-term integration test is performed in a laboratory. The Allan variance test also can never be an indicator of this effect. For atmospheric observations, however, the input power levels are largely separated between the signal and the reference. This makes it indispensable for us to pay an extra attention to this issue. It is difficult to predict the exact effect of the DNL for the SMILES/AOS, because the characteristics of A/D converters are varied among individual products. Nevertheless, we can simulate the atmospheric observation based on the characteristics of the A/D converter of the same type as planned to be used for the SMILES/AOS.

Figure 3.36 shows the effect of the differential non-linearity on the observed spectra. ΔT denotes the difference between the digitized and the analog values of the brightness temperature. We see that a specific undulation of the spectrum appears, and it remains unchanged even after 60 times of accumulation of the spectrum, which corresponds to a one-day average for a zonal map with a latitudinal interval of 5°. The magnitude of the undulation depends heavily on the temperature of the limb spectrum. If the brightness temperature of the limb spectrum is not so different from the reference sky, this effect is

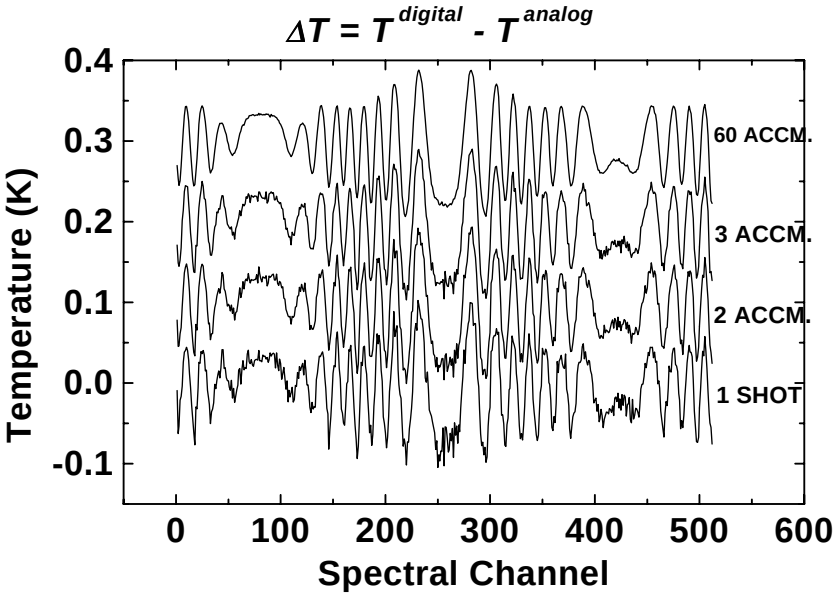

Figure 3.36 Simulated effects of the differential non-linearity on the spectrum for 1 shot, and for 2, 3, and 60 accumulations. The latter three spectra are shifted upward by 0.1, 0.2 and 0.3 K, respectively. The difference in brightness temperature between the limb atmosphere and the reference sky is taken as 20 K, and no gain variation is assumed in each integration period.

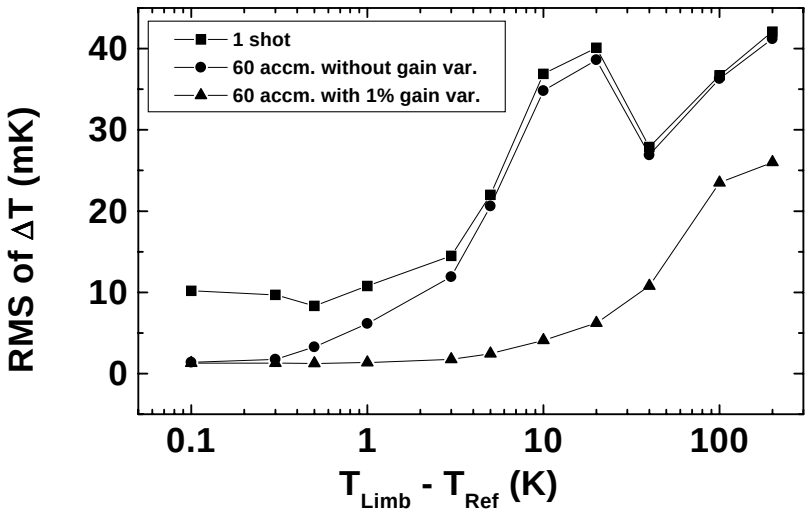

Figure 3.37 Dependence of the DNL effect on the difference of brightness temperature between the limb atmosphere and the reference sky.

much suppressed. On the contrary, the DNL effect cannot be ignored for low altitudes (high brightness temperatures).

Though the DNL is troublesome in measuring the atmospheric spectra, it is found that a small variation of the system gain has a possibility to smooth out this effect efficiently. Figure 3.37 shows the DNL effect against the difference in the input power levels between the two spectra. The lowest plot in the figure depicts an improvement of the sensitivity by including a "random" gain variation of 1% over 60 observational opportunities. This phenomenon will be rationalized by the shift of the "operational point" due to the gain variation. This plot tells us that if a gain variation occurs randomly, the DNL effect will be removed by accumulation. In the real observational conditions, the result will be between the two plots in the figure.

3.3.4 Sensitivity

3.3.4.1 Radiometric Noise

The sensitivity of SMILES to detect molecular emissions is mainly determined by the system noise temperature, T_{sys}, which is expressed by the following equation for the upper sideband observation (see Figure 3.27):

$$\begin{aligned} T^u_{sys} &= \begin{pmatrix} 1 & A^l & C^u & C^l \end{pmatrix} \cdot \begin{pmatrix} T^u_{ant} + T_{amb} \cdot (L_{ant} - 1) \\ T^l_{ant} + T_{amb} \cdot (L_{ant} - 1) \\ T^u_{cst} + T_{amb} \cdot (L_{cst} - 1) \\ T^l_{cst} + T_{amb} \cdot (L_{cst} - 1) \end{pmatrix} \\ &+ T^{dsb}_{rx} \cdot \left(1 + \frac{L_u}{L_l}\right) \cdot \frac{L_{ant}}{K^u_{ant}}, \end{aligned} \tag{3.23}$$

$$A^l = \frac{K^l_{ant}}{K^u_{ant}} \cdot \frac{L_u}{L_l}, \quad C^u = \frac{K^u_{cst}}{K^u_{ant}} \cdot \frac{L_{ant}}{L_{cst}}, \quad C^l = \frac{K^l_{cst}}{K^u_{ant}} \cdot \frac{L_{ant}}{L_{cst}} \cdot \frac{L_u}{L_l}. \tag{3.24}$$

Here T_{ant} and T_{cst} are input power levels to the Submillimeter Antenna (ANT) and Cold-sky Terminator (CST), expressed in brightness temperatures. Superscripts u and l indicate that the quantity is evaluated in the USB and LSB, respectively. T_{amb} is the brightness temperature for a black-body at the ambient temperature. L_{ant} and L_{cst} are propagation losses in the ANT and CST. T^{dsb}_{rx} is the receiver noise temperature evaluated in the double sideband (DSB) mode. This is the most dominant factor of the system noise temperature, and it is mainly determined by the performance of the submillimeter mixer inside the receiver. SMILES adopts cryogenically-cooled superconductive SIS mixers, instead of the conventional semiconductor diode mixers, to drastically reduce the value of T^{dsb}_{rx}. L_u and L_l are mixer conversion losses in the USB and LSB. These values are also much reduced in SIS mixers compared with the diode mixers. K_{ant} and K_{cst} are the mixer's power coupling coefficients with the ANT and CST, which are determined by the performance of the quasi-optical SSB filter. With this T^u_{sys}, the receiver output power corresponding to an input signal ΔT to the antenna is expressed as

$$T^u_{out} = (\Delta T + T^u_{sys}) \cdot \frac{K^u_{ant} G_{if}}{L_{ant} L_u}. \tag{3.25}$$

The minimum detectable temperature (1-sigma) is evaluated by the radiometer equation,

$$T_{rms} = \frac{T_{sys}}{\sqrt{B \cdot \tau}}, \tag{3.26}$$

where B is a detection noise bandwidth and τ is an integration time. T_{sys} of SMILES is about 500 K, for cases where the noise contribution from the atmosphere itself can be neglected. With B=2.5 MHz, τ=0.47 sec, the above equation gives a value of 0.46 K (rms).

3.3.4.2 Gain Stability

The second factor that can affect sensitivity is gain variation of amplifiers in the receiver system. Since the receiver gain is calibrated in every 53 seconds, our concern is variations in this short time scale. They will occur due to changes in the physical temperature of amplifiers. They can be separated into two parts: (1) a change in the relative frequency characteristics of the gain (we call this "gain fluctuation"in this chapter), and (2) a parallel shift of gain levels while the relative frequency characteristics are kept unchanged. The former will affect the sensitivity to spectrum, but the latter will be related only to the absolute calibration accuracy of brightness temperatures. The former amplitude is considered to be much smaller than the latter one. In order that the former fluctuation should not affect the spectral sensitivity, a requirement:

$$\left(\frac{\Delta G}{G}\right)^2 \ll \frac{1}{B\tau}, \tag{3.27}$$

has to be satisfied in the data integration time of τ(0.5 sec in SMILES). This requires the gain fluctuation of this kind be smaller than 0.03 % for the whole SMILES receiver. On the other hand, the gain variation of the second kind has to be less than 1 percent in a period of 53 seconds in order to achieve a 1-percent accuracy in the calibration of brightness temperatures.

3.3.4.3 Standing Waves

The third factor that can deteriorate the actual spectral sensitivity is standing waves in the submillimeter optics. The SMILES observations are performed in three successive steps with three different submillimeter inputs to the receiver: atmospheric emissions at numbers of consecutive tangent altitudes, reference-sky emissions at the altitude of 160 km or higher, and thermal emissions of the Calibration Hot-load (CHL). The AOS output voltages for these steps are described as follows:

$$V_{atm} = G_{sys} \cdot \{T_a(atm) \cdot M_{obs}(atm) + T_{sys}\}, \tag{3.28}$$
$$V_{ref} = G_{sys} \cdot \{T_a(ref) \cdot M_{obs}(ref) + T_{sys}\}, \tag{3.29}$$
$$V_{hot} = G_{sys} \cdot \{T_a(hot) \cdot M_{cal} + T_{sys}\}. \tag{3.30}$$

Here T_a is the antenna temperature evaluated at the input port of the receiver, and T_{sys} is the system noise temperature. G_{sys} is the system gain. $M_{obs}(atm)$, $M_{obs}(ref)$ and M_{cal} are power modulation factors due to standing waves. They are generated by a pair of reflections; one at the input port of the receiver and the other at some point in the submillimeter optics. The power modulation is due to the interference between an original incident wave and an additional one superimposed on it after a return trip along the optical path.

$$M_{obs} = \mid 1 + r_{obs} \cdot \exp(-j \cdot 2kL_{obs}) \mid^2 . \tag{3.31}$$

Here r_{obs} represents the relative strength of the superimposed wave, and L_{obs} is the distance between the two ends of the return trip ($k = 2\pi/\lambda$). On the other hand, the standing waves while the hot-load is observed are described by

$$M_{cal} = \mid 1 + r_{obs} \cdot \exp(-j \cdot 2kL_{obs}) + r_{cal} \cdot \exp(-j \cdot 2kL_{cal}) \mid^2 . \tag{3.32}$$

Here r_{cal} represents the relative strength of a superimposed wave that is returned from the hot-load, and L_{cal} is the distance between the input port of the receiver and the hot-load. The observed antenna temperature is derived from

$$T_a^{obs}(atm) = \frac{V_{atm} - V_{ref}}{V_{hot} - V_{ref}} \cdot \{T_a(hot) - T_a(ref)\} + T_a(ref). \tag{3.33}$$

Since M_{obs} and M_{cal} are frequency-dependent, this observed antenna temperature is also frequency-dependent, which makes a baseline ripple in the frequency spectrum.

There are several factors to determine the amplitude of standing waves. One is a difference (time variation) between $M_{obs}(atm)$ and $M_{obs}(ref)$. This difference can be generated by a thermal change of the physical distance between the two reflecting points in the optics. Keeping such temperature drift as small as 0.5 deg in 53 seconds could minimize this effect. The other factor originates from the insertion of the hot-load itself. The amplitude of this standing wave is mainly determined by the reflectivity of the hot-load. It has to be less than -50 dB to make r_{cal} lower than -60 dB. Recent experiments have demonstrated that the CHL meets such requirement (A.Murk, personal communication). The third factor is the variation of the system gain. Without such variations, the standing waves would decrease for lower atmospheric temperatures. The gain variation, however, makes the subtraction of T_{sys} incomplete in Eq. (3.33), which leaves some level of standing waves even for lower atmospheric temperatures.

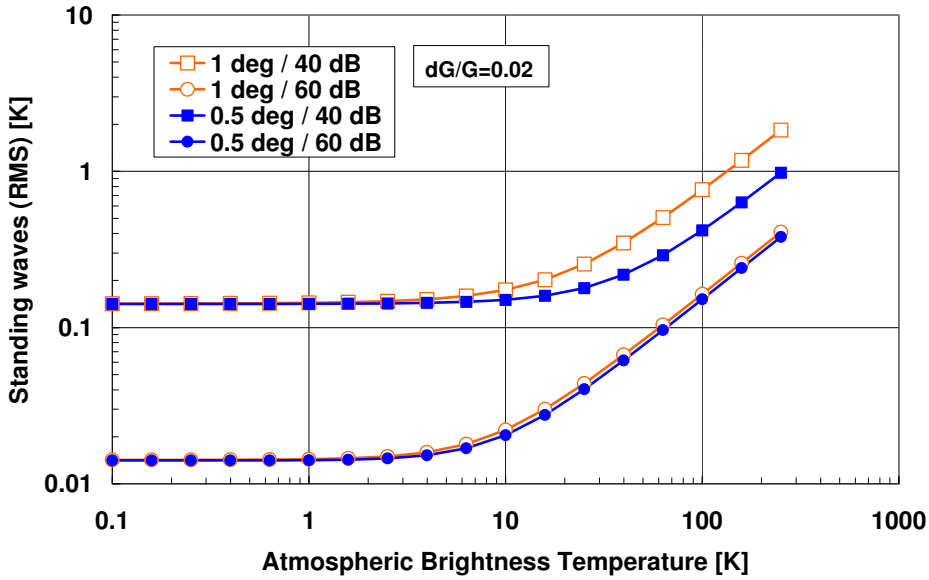

Figure 3.38 Estimated amplitude of standing waves as a function of atmospheric brightness temperature. Two cases for thermal stability in 53 seconds, and two cases for the strength of superimposed waves are calculated. The variation of the system gain is assumed to be 2 percent in 53 seconds.

The estimated amplitudes of standing waves are shown in Fig. 3.38. Two different cases are assumed with respect to thermal stability (1 deg or 0.5 deg in 53 seconds) and the relative level of superimposed waves (-40 dB or -60 dB for r_{obs}). r_{cal} is fixed at -60 dB, and the gain variation is assumed to be 2 percent. When r_{cal} is -60 dB, the amplitude (rms) of spectral ripples is less than 0.5 K for $T_a(atm)$ of 300 K, and linearly decreases for lower atmospheric temperatures, but remains around 0.02 K for temperatures lower than 10 K.

3.3.4.4 Differential Non-linearity of A/D Converter

The fourth factor we have to concern is differential non-linearity (DNL) of the analog-to-digital converter in the AOS. The incremental analog voltage, needed to give a step of smallest digital bit, is not exactly constant over the dynamic range. When a particular feature of this deviation is coupled with the frequency characteristic of the receiver gain, it results in a modulation of the signal spectra. This issue has been discussed in detail in section 3.3.3. With a measured feature of the DNL for the same type of analog-to-digital converter that is to be used for the AOS in SMILES, we have found this effect remains relatively small as shown in 3.41. But we have to keep it in mind that a temporal gain variation of 1 % is assumed there to estimate the DNL effect for the integrated data for a day.

3.3.4.5 Electromagnetic Interference

The fifth factor that could deteriorate the sensitivity of SMILES is electromagnetic interference. All the payloads aboard the International Space Station are requested to be compatible with the electromagnetic conditions specified in the requirement document (SSP-30237) [*NASA*, 1999]. Among categories with respect to the electromagnetic com-

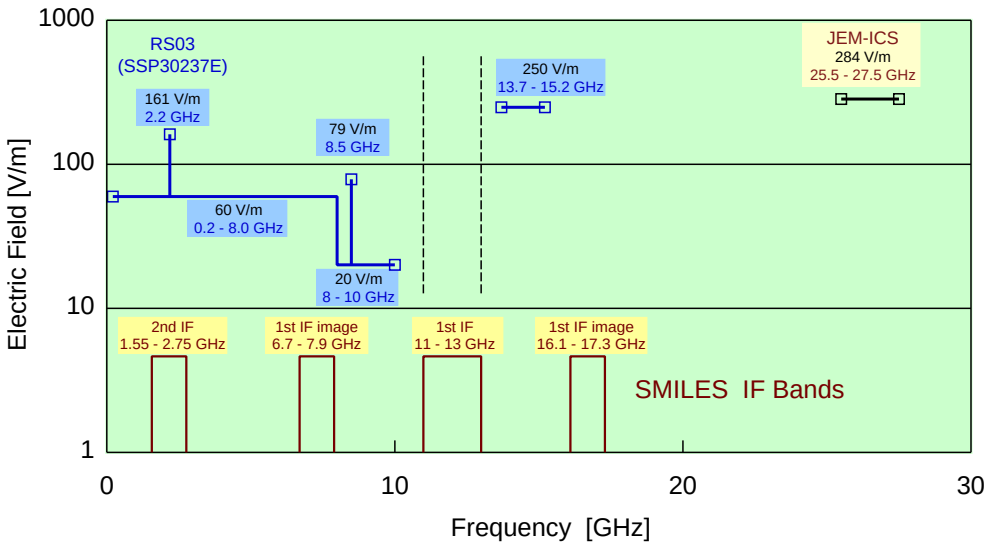

Figure 3.39 ISS environmental field. All the payloads aboard the ISS are requested to be compatible with the electromagnetic conditions specified in the requirement document (SSP-30237) [*NASA*, 1999].

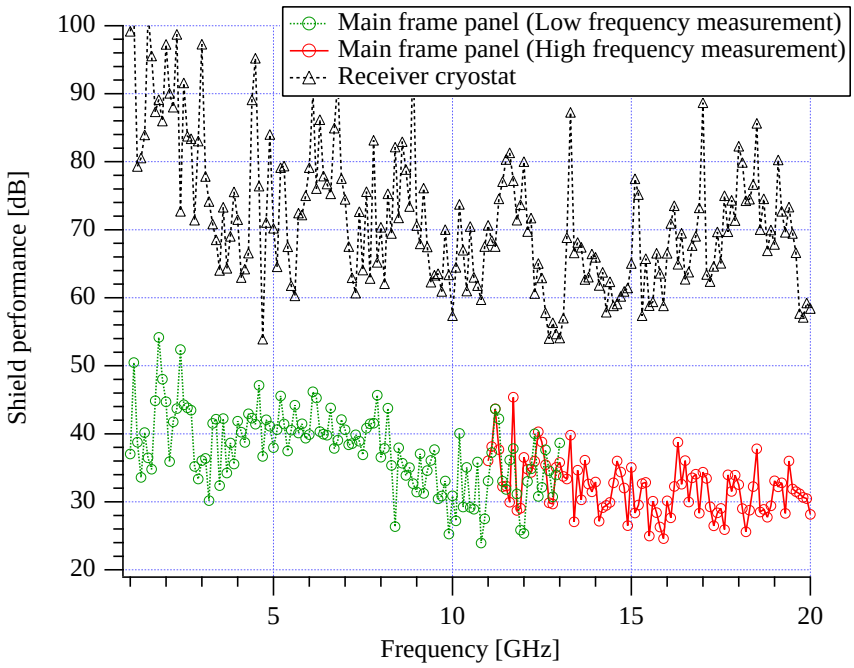

Figure 3.40 Shield performance. Thr measurement result demonstrates that the shielding performance of 20 dB and 50 dB has been achieved for the SMILES' structural model and the engineering model of the cryostat, respectively.

patibility (EMC) specifications, radiated susceptibility (RS) is most critical for SMILES to achieve its designed sensitivity. Figure 3.39 depicts radiated field specification levels as well as SMILES intermediate frequency (IF) band allocations. High electric fields must be anticipated at the SMILES' second IF band and a pair to the image bands according to the specification, while the first IF band (11 - 13 GHz) is not cited. To minimize the interference in such an environments, immunities of RF components shall be improved by paying special attention for their packaging. Our design target is not to observe, or recognize any spurious signal in a 'snap shot' (0.5 sec. integration) spectrum due to the electromagnetic interference. However, the ISS electromagnetic field specification is so harmful for the SMILES instrument to exhibit its full performance by itself. It is therefore essential for the payload instruments of SMILES being completely enclosed with an electromagnetic shield except for the antenna section. In particular, the most sensitive components, such as the SIS mixers and HEMT amplifiers, are to be tightly shielded by the cryostat. Figure 3.40 shows the shielding performance of the SMILES' structural panel and cryostat up to 26.5 GHz, demonstrating that the shielding performance of 20 dB and 50 dB have been achieved for the SMILES' structural model and the engineering model of the cryostat, respectively[*Miura et al.*, 2002; *Seta et al.*, 2002]. The submillimeter-wave signal from the antenna must be introduced to the cryostat without degrading the shielding capability. This will be accomplished by letting the submillimeter-wave beam pass through a small metallic tube (corrugated circular waveguide) that works as a cutoff filter against undesirable microwave field at 27 GHz or less.

Consolidating all the available data concerning the immunity of the instruments against the electromagnetic field radiation as well as the shielding performance so far achieved, we conclude that any spurious will not be observed in a snap shot spectrum under the

specified EMC conditions. As for the first IF frequency region, we estimate the field strength around the SMILES payload must be less than 2 V/m.

This frequency region is not cited in the EMC specification document because no transmitters emitting at this frequency are so far registered. Installation of new RF transmitter on the ISS can be a potential risk to prevent SMILES from appreciating its full sensitivity. Since this shall be approved through the evaluation of the EMC of the existent instruments aboard the ISS, we are requesting a control for 11-13 GHz emissions.

3.3.4.6 Overall Sensitivity

Overall sensitivity of SMILES is calculated in Figure 3.41 with the above factors except for the electromagnetic interference. For a unit data obtained in 53 seconds, the standard deviation of the noise in the spectral profile is expected to be about 0.7 K for brightness temperatures less than 20 K, but it increases gradually for higher temperatures due to standing waves. It will be about 1 K (rms) for brightness temperatures around 200 K, if the actual standing waves in orbit are of the level described above. In data processing on the ground, we will produce latitudinal zone-averaged spectral profiles to find the altitude-latitude relation of each species. The sensitivities of such zonal averaged data, generated by integrating unit data over all longitudes with a width of 5° in latitude, are also estimated for an integration period of 1 day and 1 month. The standard deviations will be reduced to 0.1 K for 1 day, and 0.03 K for 1 month, both for low brightness temperatures. They also increase for higher brightness temperatures due to the standing waves, which are not reduced by averaging unit data. Note that the sensitivity calculated here is for the spectral profiles with a frequency resolution of 2.5 MHz. If another kind of averaging, over several channels of the AOS, is available, the sensitivity will be improved even for a unit data at the price of lower frequency resolution.

3.3.5 Brightness Temperature Calibration

3.3.5.1 Calibration Scheme

If we take into account antenna responses in its wide-angle error pattern and thermal losses at antenna mirrors, the AOS output voltages are expressed by the next equations, corresponding to the three steps of data acquisition in a unit cycle (53 seconds).

$$\begin{pmatrix} V_{atm}/C_{aos}(G_{sys}+\Delta G_{sys}) \\ V_{ref}/C_{aos}G_{sys} \\ V_{hot}/C_{aos}G_{sys} \end{pmatrix} = \begin{pmatrix} T_{atm} & T_{err}+\Delta T_{err} & T_{mir}+\Delta T_{mir} & T_{sys}+\Delta T_{sys} \\ T_{ref} & T_{err} & T_{mir} & T_{sys} \\ T_{hot} & T_{hot} & T_{hot} & T_{sys} \end{pmatrix} \begin{pmatrix} K/L \\ (1-K)/L \\ (L-1)/L \\ 1 \end{pmatrix}. \quad (3.34)$$

It is assumed that some variations occur in G_{sys}, T_{err}, T_{mir} , and T_{sys} in a period between the time of atmospheric observations and that of intensity calibration. The meaning of each parameter is as follows:

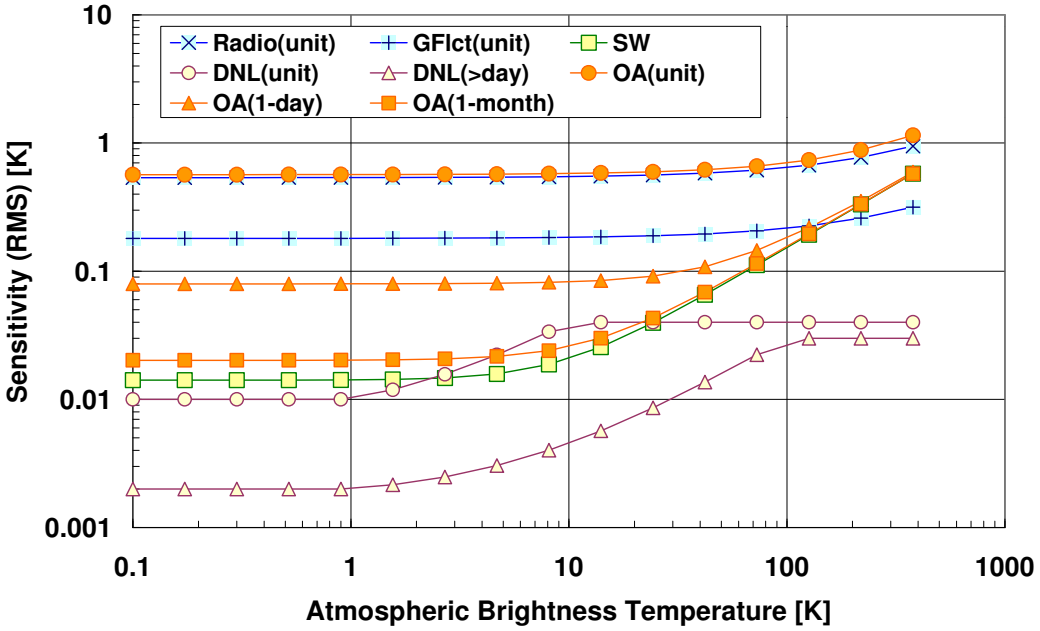

Figure 3.41 Overall Sensitivity: "Radio"; radiometric noise, "GFlct"; gain fluctuation, "SW"; standing waves, "DNL"; differential non-linearity of the analog-to-digital converter, "OA"; overall sensitivity obtained by rss (root-sum-squares). "unit" means the unit data obtained in 53 seconds. Standing waves are not reduced by averaging.

$V_{atm}, V_{ref}, V_{hot}$	;	Output voltages at the AOS corresponding to the atmosphere, reference sky, and hot-load, respectively (the zero-point offset is omitted for simplicity),
C_{aos}	:	Power-to-voltage conversion factor at the AOS,
G_{sys}	:	Total gain of the system that is from the calibrator to the AOS
K	:	Beam efficiency for the FOV defined by a 2.5×HPBW area,
L	:	Thermal losses at the antenna mirrors located before the calibrator,
T_{atm}, T_{ref}	;	Brightness temperatures integrated in the FOV corresponding to the atmosphere and reference sky, respectively,
T_{err}	:	Brightness temperature integrated outside the FOV,
T_{mir}	:	Brightness temperature of the antenna mirrors located before the calibrator, when they are assumed to be a black-body,
T_{hot}	:	Brightness temperature of the Calibration Hot-load (CHL),
T_{sys}	:	System noise temperature (SSB) evaluated at the calibrator.

With three observable voltages, V_{atm}, V_{ref}, and V_{hot}, we obtain an observable quantity, $VCAL$, that is basically free from the particular frequency characteristics in C_{aos}, G_{sys},

and the zero-point offset at the AOS.

$$VCAL = \frac{V_{atm} - V_{ref}}{V_{hot} - V_{ref}}. \tag{3.35}$$

With the measured value of $VCAL$, we obtain the atmospheric brightness temperature T_{atm} that is integrated in the FOV. However, there are several kinds of errors that will affect the derived value of T_{atm}.

At first, let us consider a simple case where no variations occur in G_{sys} , T_{err}, T_{mir}, and T_{sys}. We have

$$VCAL = \frac{T_{atm} - T_{ref}}{(T_{hot} - T_{ref}) + \frac{1-K}{K}(T_{hot} - T_{err}) + \frac{L-1}{K}(T_{hot} - T_{mir})}. \tag{3.36}$$

In this equation, the parameters have their real values at the time of observations. If we know and assume the values of T_{ref}, T_{err}, T_{mir}, T_{hot}, K, and L, then we can derive T_{atm} from this same equation. With these assumed values indicated with an asterisk, we obtain

$$VCAL = \frac{T^{obs}_{atm} - T^{*}_{ref}}{\left(T^{*}_{hot} - T^{*}_{ref}\right) + \frac{1-K^{*}}{K^{*}}(T^{*}_{hot} - T^{*}_{err}) + \frac{L^{*}-1}{K^{*}}(T^{*}_{hot} - T^{*}_{mir})}. \tag{3.37}$$

In this case, knowledge errors for these parameters will limit the accuracy of the derived value of T^{obs}_{atm}. This knowledge error can be evaluated by

$$\Delta T^{knw}_{atm} = T^{obs}_{atm} - T_{atm} = (\kappa - 1) \cdot T_{atm} \tag{3.38}$$

$$\kappa = \frac{T^{*}_{hot} + \frac{1-K^{*}}{K^{*}}(T^{*}_{hot} - T^{*}_{err}) + \frac{L^{*}-1}{K^{*}}(T^{*}_{hot} - T^{*}_{mir})}{T_{hot} + \frac{1-K}{K}(T_{hot} - T_{err}) + \frac{L-1}{K}(T_{hot} - T_{mir})}, \tag{3.39}$$

where T_{ref} and T^{*}_{ref} are assumed to be zero. Actually the antenna looks at the cosmic microwave background for the reference submillimeter input. Since the frequency of 640 GHz is in Wien's region of its 2.7-K spectrum, the brightness temperature expressed in Rayleigh-Jeans approximation is virtually zero.

As a second step, let us consider the effects of time variations of parameters between the time of atmospheric observations and that of intensity calibration. In this case, $VCAL$ is expressed as

$$VCAL = \frac{(T_{atm} - T_{ref}) + \Delta T^{var}_{atm}}{(T_{hot} - T_{ref}) + \frac{1-K}{K} \cdot (T_{hot} - T_{err}) + \frac{L-1}{K} \cdot (T_{hot} - T_{mir})}. \tag{3.40}$$

The error of derived T_{atm} due to variations is evaluated by

$$\Delta T^{var}_{atm} = \frac{1-K}{K} \cdot \Delta T_{err} + \frac{L-1}{K} \cdot \Delta T_{mir} + \frac{L}{K} \cdot \Delta T_{sys} + \frac{L}{K} \cdot \frac{V_{atm}}{C_{aos} G_{sys}} \cdot \frac{\Delta G_{sys}}{G_{sys}}. \tag{3.41}$$

Since the values of K and L are close to unity, and ΔT_{err} and ΔT_{mir} are likely of the order of 10 K, the first two terms should be smaller than the third and fourth terms.

$$\Delta T^{var}_{atm} \approx \Delta T_{sys} + (T_{atm} + T_{sys}) \frac{\Delta G_{sys}}{G_{sys}}. \tag{3.42}$$

This error is therefore the combination of a shift of the baseline in the frequency spectrum and a modification of the observed value of T_{atm}.

The third error factor on the derived T_{atm} is a residual nonlinear behavior of the system gain. The system gain is actually measured in orbit as a ratio of the difference of

two resultant output voltages to the difference of two input power levels: the hot-load and reference sky. The gain non-linearity is defined as a deviation of the actual output voltage from the expected value given by linear interpolation between the two measured points. This effect will be approximated by

$$\Delta T_{atm}^{GNL} = T_{atm} \cdot \frac{\Delta G_{sys}^{GNL}}{G_{sys}}. \tag{3.43}$$

This effect is therefore a modification of the observed value of T_{atm}.

For clarification, T_{atm} is not the real brightness temperature, $T_b(\theta_{atm})$, of the limb atmosphere exactly at a certain tangent altitude, but the one averaged in the FOV with a weighting function expressed by a near-axis response pattern of the antenna, $P(\theta)$.

$$T_{atm} = \frac{\int_{fov} T_b(\theta_{atm} + \theta) \cdot P(\theta) d\theta}{\int_{fov} P(\theta) d\theta}. \tag{3.44}$$

The role of the Level-1 data processing is to derive this averaged brightness temperature that should be as free as possible from system parameters and effects of the wide-angle response pattern. On the other hand, the effect of the near-axis response pattern is strongly coupled with the altitude distribution of the molecular mixing ratio itself, which should be properly resolved in the Level-2 processing.

3.3.5.2 Calibration Accuracy

We estimate the calibration accuracy of T_{atm} in the following. Error factors to be estimated are the knowledge error, gain variation, gain non-linearity, standing waves, differential non-linearity, and radiometer noise. To estimate the effect of knowledge errors quantitatively, let us assume reasonable values and the extent of knowledge errors for the parameters used in Eq. (3.38).

K :	0.92	$\pm$ 0.02	(to be evaluated by the ground measurements)
L :	0.5 dB	$\pm$ 0.2 dB	(to be evaluated by the ground measurements)
T_{err} :	100 K	$\pm$ 30 K	(to be evaluated by the ground measurements)
T_{mir} :	270 K	$\pm$ 10 K	(to be measured in orbit)
T_{hot} :	300 K	$\pm$ 1 K	(to be measured precisely in orbit)

Expected error in the derived value of T_{atm}, calculated by Eq. (3.38), is shown in Figure 3.42 as a function of its assumed value. This error is proportional to the brightness temperature, and its relative value is less than 3 percent (rms). The knowledge error is the largest one among various error factors considered here.

Secondly, the calibration accuracy is affected by temporal variation of the system gain and system noise temperature. It is expressed by Eq. (3.42). If we can remove the effect of the baseline shift (uncertainty) from the original observed data, the calibration error of the brightness temperature will be proportional to its value. In Figure 3.42, it is shown as "GTV", which is about 1 percent (rms) corresponding to the gain variation of $\pm$2 percent in maximum amplitude.

Thirdly, the calibration accuracy is affected by the gain non-linearity. The effect expressed by Eq. (3.43) is depicted as "GNL" in Figure 3.42 for the case of residual non-linearity of $\pm$1 percent in maximum amplitude.

Errors due to other factors such as standing waves, differential non-linearity, and radio noise are also included in Figure 3.42, which are shown a"SW", "DNL", and "Radio". In

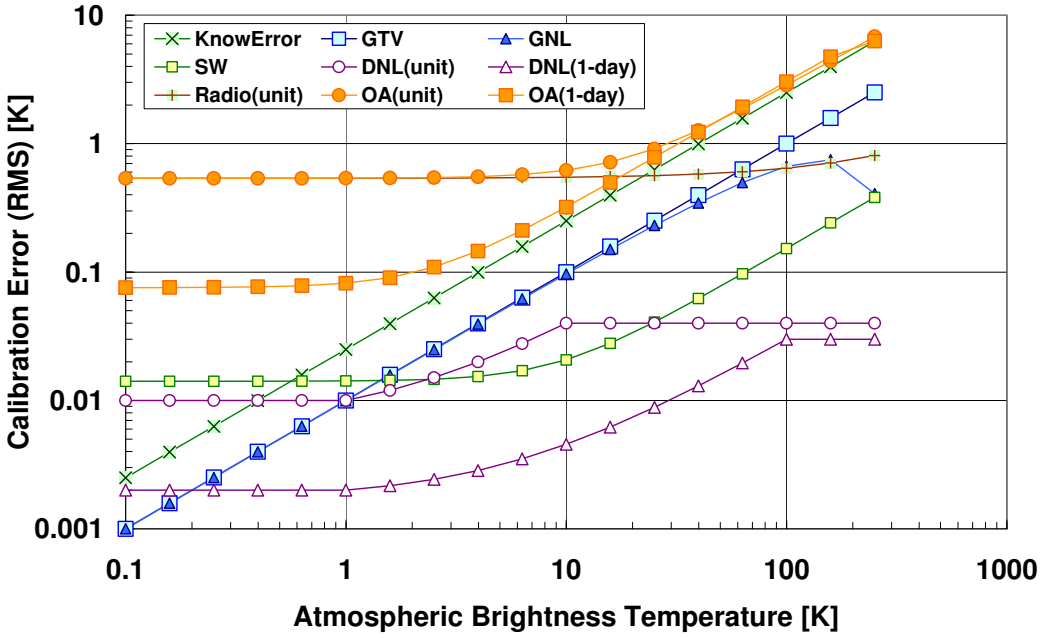

Figure 3.42 Calibration accuracy of the brightness temperature: "KnowError"; knowledge error, "GTV"; time variation of the system gain, "GNL"; non-linearity of the system gain, "SW"; standing waves, "DNL"; differential non-linearity of the analog-to-digital converter of the AOS, "Radio"; radiometer noise, and "OA"; overall error.

conclusion, the overall error is about 0.8 K (rms) for atmospheric brightness temperatures lower than 20 K, and about 3 percent (rms) for higher temperatures. The radiometer noise dominates in lower temperatures, and the knowledge error does in higher temperatures. For the zonal averaged data in 1 day, the overall calibration error will decrease as the radiometer noise decreases for atmospheric temperatures lower than 20 K. But this is also limited by the knowledge error for temperatures between 2 K and 20 K.

We have to keep in mind that Figure 3.42 does not include the uncertainty of the spectral baseline, i.e. the level of zero emissions. As shown in Eq. (3.42), time variations of the system gain and system noise temperature can contribute to a large shift of the baseline. It is difficult to evaluate its amount precisely, but it may reach up to ± 20 K, if both $\Delta T_{sys}/T_{sys}$ and $\Delta G_{sys}/G_{sys}$ are ± 2 percent. This uncertainty of the baseline will not affect the accuracy of the observed emissions with a line-width that is narrow enough compared with the bandwidth (1.2 GHz) of the AOS. However, this uncertainty will limit the capability of SMILES to derive some parameters, such as concentration of water vapor in the atmosphere, from the absolute level of its brightness temperature, because of its flat spectrum.

3.4 Conclusion

Chapter 3 has dealt with instrumental capabilities of SMILES. Emphasis is put on the aspects of those that are directly coupled to the quality of observational data. We have investigated SMILES performances with respect to the field of view as well as the spectral regions and sensitivity. To conclude this chapter, we put two tables for description of SMILES mission instruments (Table 3.16) and for a summary of those capabilities (Table 3.17). Note that some figures in the latter table are still under investigation and subject to future revisions.

Table 3.16 Description of SMILES Mission Instruments

Instruments	Description
Submillimeter Antenna	
Type	Offset Cassegrain antenna shaped for an elliptical beam
Size of main reflector	400 mm (Vertical) × 200 mm (Horizontal)
Azimuth	Fixed to 45-deg north with respect to the ISS forward direction
Elevation	Movable from $-40°$ to $+5°$
Intensity calibration	With an ambient-temperature load and cold sky
Sumillimeter Receiver	
Type	Cryogenically cooled heterodyne receiver
Submillimeter mixer	SIS mixer with Nb/AlOx/Nb junctions operating at 4.5 K
LO source	Gunn diode oscillator and frequency multiplier
First-stage IF amplifier	HEMT amplifier operating at 20 K
Cryogenics	Two-stage Stirling cooler plus Joule-Thomson cooler
Sideband separation	Modified Martin-Puplett interferometer
IF Amplification Section	
Type	Down conversion and amplification
Switching	Switching to control signal flow into AOS units
Reference frequency	Reference CW generation for AOS frequency calibration
AOS	
Type	Radio spectrometer based on acouto-optical interaction
Light deflector	LiNbO3-based Bragg's cell
Laser	Laser diode emitting at 785 nm
Detector	CCD linear array
Star Tracker	
Type	Image mapping and comparison with a star catalogue
Field of view	$18.4° \times 13.4°$
Star catalogue	Hipparcos data containing 12200 stars

Table 3.17 Summary of SMILES Instrumental Capabilities

Parameters	Characteristics
Spatial Coverage	
Tangent-point Height	−10 km to 60 km (minimum)
Latitude	65°N to 38°S (nominal)
Data Sampling Interval	Around 360 km along the orbit
Data Sampling Speed	105 sets of data per orbit
Orbital Period	About 93 minutes
Accuracy of Height Determination	
Bias Error	About 0.76 km (rms)
Random Error	About 0.34 km (rms) [after calibrated for a beam-offset error]
Resolution of Tangent-point Height	
Effective Beam-width (HPBW)	0.096° (3.5-4.1 km in height scale)
Sampling Interval	0.056° (2.1-2.4 km in height scale) [for the ISS altitude of 407 km]
Frequency Coverage	
Band-A	624.32 — 625.52 GHz
Band-B	625.12 — 626.32 GHz
Band-C	649.12 — 650.32 GHz
Major Molecular Species to be Measured(*)	
Band-A	O_3, O_3-isotopes, $H^{37}Cl$, H_2O_2, $HO^{35}Cl$, HNO_3, SO_2, ^{81}BrO
Band-B	O_3, O_3-isotopes, $H^{35}Cl$, HO_2, HNO_3, SO_2, $O^{35}ClO$
Band-C	^{35}ClO, O_3-isotopes, HO_2, HNO_3, SO_2, ^{81}BrO
Sensitivity for Atmospheric Brightness Temp.	
For Unit Data	About 0.7 K (rms) for $T_b < 20$ K
(Acquired in every 0.5 sec)	About 1.0 K (rms) for $T_b = 200$ K
For Daily 5-deg Zonal Avg. Data	About 0.1 K (rms) for $T_b < 20$ K
(Integrated over all longitudes)	About 0.3 K (rms) for $T_b = 200$ K
Accuracy for Atmospheric Brightness Temp.	
For Unit Data	About 1 K (rms) for $T_b < 20$ K
	About 3 % (rms) for $T_b > 20$ K
For Daily 5-deg Zonal Avg. Data	About 0.1 K (rms) for $T_b < 2$ K
	About 3 % (rms) for $T_b > 2$ K
Baseline Uncertainty	Less than ±20 K
Spectrometer Capabilities	
Frequency Resolution (FWHM)	1.8 MHz
Channel Separation	0.8 MHz per channel
Number of Channels	1728 channels per a CCD unit

*Only two bands are operational at a time.

References

Fujii, Y., K. Kikuchi, J. Inatani, Y. Irimajiri, M. Seta, S. Ochiai, T. Manabe, H. Masuko, T. Noguchi, K. Narasaki, S. Tsunematsu, and T. Shirota, Space-borne 640-GHz SIS Receiver Based on 4-K Mechanical Cooler, *UV, Optical, and IR Space Telescope and Instruments, Proceedings of SPIE, 4013,* 90—99, 2000.

Inatani, J., T. Noguchi, S. C. Shi. K. Miyazawa, H. Masuko. S. Ochiai, Y. Irimajiri, M. Kyoya, K. Narasaki, S. Tsunematsu, M. Murakami, and D. Okamoto, A Submillimeter SIS Receiver Cooled by a Compact Stirling-JT Refrigerator, Eighth International Symposium on Space Terahertz Technology, 273—280, 1997.

Inatani, J., S. Ochiai, T. Manabe, M. Seta, R. Wylde, and D. H. Martin, A New Configuration of the Martin-Puplett Interferometer with Low-Reflection, IEEE Seventh International Conference on Terahertz Electronics Proceedings, 260—263, 1999.

International Telecommunication Union, *ITU-R Reccomendations,* Rec. ITU-R 835-2, 1997 P Series-Part I, Geneve, 1997.

Manabe, T., Effects of Atmospheric Refraction on Limb Sounding from JEM/SMILES, available at http://www.crl.go.jp/ck/ck321/smiles/refrac.pdf, 1999.

Manabe, T., Effects of Atmospheric Refraction on Limb Sounding from JEM/SMILES –Part II–, available at http://www.crl.go.jp/ck/ck321/smiles/refrac/refrac.html, 2000.

Miura, T., T. Nishibori, J. Inatani, and JEM/SMILES Mission Team, Measurement of Shield Performance of JEM/SMILES Payload, Proceedings of the 2002 IEICE General Conference, (Communications 1), 396 (B-4-47), 2002 (in Japanese).

Martin, D. H., Polarizing (Martin-Puplett) interferometric spectrometers for the near- and submillimeter spectra, in *Infrared and Millimeter Waves,* vol. 6, K. J. button, Ed. New York: Academic Press, 1982, pp. 65—148.

NASDA, *Introductory Guidebook for JEM Exposed Facility Potential Users,* JBX-98079, National Space Development Agency of Japan, 1998.

NASA, *International Space Station User's Guide Release 2.0,* National Aeronautics and Space Administration, available at http://spaceflight.nasa.gov/station/reference/issug/ISSUG1-11.pdf, http://spaceflight.nasa.gov/station/reference/issug/ISSUG12-34.pdf, http://spaceflight.nasa.gov/station/reference/issug/ISSUG35-50.pdf.

NASA, *Space Station Electromagnetic Emission and Susceptivility Requirements,* SSP 30237, Revision E, September, 1999.

NASA, *System Specification for the International Space Station,* SSP41000R, March 20, 2000.

Ozeki, H., Y. Kasai, S. Ochiai, S. Tsujimaru, J. Inatani, H. Masuko, C. Takahashi, L. Mazuray, and C. Rosolen, Submillimeter-wave Spectroscopic Performance of JEM/SMILES, SPIE Second International Asia-Pacific Symposium on Remote Sensing of the Atmosphere, Environment, and Space, Sendai, Japan, October 9–12, 2000.

Seta, M., T. Miura, T. Manabe, S. Tsunematsu, T. Nishibori, and J Inatani, 'Evaluation of Electromagnetic Shielding Capability of a Spaceborne Cryostat for a Sensitive Receiver,' Proceedings of the 2002 IEICE General Conference, (Communications 1),397 (B-4-48), 2002 (in Japanese).

Treder, A. J., *Space Station GN&C Overview for Payloads, Space Technology and Applications International Forum-1999,* 49-57, 1999.

4 Retrieval– Principle and Method

4.1 Retrieval Algorithm

4.1.1 Principle of Limb Sounding Instruments

Microwave limb sounding instruments obtain remote measurements of atmospheric parameters by observing thermal emission at millimeter and sub-millimeter-wavelength as the instrument field of view (FOV) is scanned through the atmosphere. Limb sounding means that the atmosphere is observed tangentially, as schematically shown in Figure 4.1.

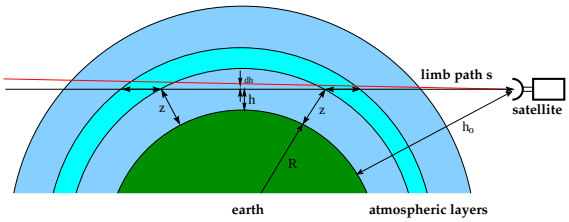

Figure 4.1 Illustration of limb sounding geometry. The satellite is in orbit and looks tangentially through the atmosphere. The beam is lowest at the tangent point at an altitude h.

The intensity detected by satellite observation contains implicit information about the parameters of interest. The extraction of these parameters from the satellite measurement requires knowledge of the radiative transfer in the atmosphere. The radiative transfer equation, introduced by Chandrasekhar [*Chandrasekhar*, 1960], describes the way in which the intensity is affected by extinction and emission of radiation. The intensity, I, is defined as the power of radiation per unit area, per unit solid angle, and per unit frequency interval (measured in $\mathrm{Wm^{-2}sr^{-1}Hz^{-1}}$). In the case of a non-scattering atmosphere (clear sky), for an arbitrary slant path, the intensity I at frequency ν received by an instrument at position $s = 0$ is given by :

$$I(\nu) \quad = \quad I_\infty(\nu)\zeta(\infty,\nu) + \int_0^\infty k(s,\nu)B(\nu,T(s))\zeta(s,\nu)ds \tag{4.1}$$

where k is the total absorption coefficient (the SI unit for k is $\mathrm{m^{-1}}$), ζ is the transmittance, B is the Planck function (which is derived under thermodynamic equilibrium condition), and I_∞ is the intensity at the limit of the atmosphere, which is cosmic background radiation or emission from the ground. The meaning of these quantities is explained below. Equation 4.1 is schematically shown in Figure 4.2.

For a mixture of gases the total absorption coefficient (summed over all the species) is given by:

$$k = \sum_i n_i \sigma_i \tag{4.2}$$

where n_i is the number density of species i (measured in $\mathrm{m^{-3}}$), and σ_i is the absorption cross section (measured in $\mathrm{m^2}$).

The optical depth (or opacity) τ, between an initial point s_0 and a final point s is defined as:

$$\tau(s,\nu) = \int_{s_0}^{s} k(s,\nu)ds \tag{4.3}$$

and the transmittance ζ is defined as:

$$\zeta(s,\nu) = \exp(-\tau(s,\nu)) \tag{4.4}$$

The Planck function describes the intensity which a perfect blackbody at temperature T emits, and is defined as:

$$B(\nu, T) = \frac{2h\nu^3}{c^2(\exp(h\nu/k_B T) - 1)} \tag{4.5}$$

where h is Planck's constant, k_B is Boltzmann's constant, and c is the speed of light. $B(\nu, T)$ has the same units as $I(\nu, T)$, i.e. $\mathrm{Wm^{-2}sr^{-1}Hz^{-1}}$.

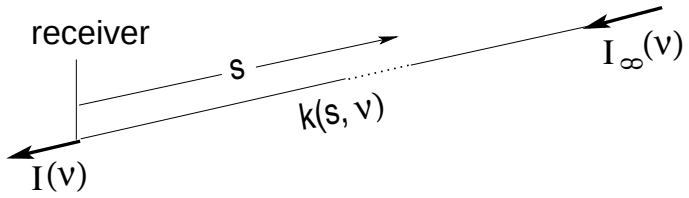

Figure 4.2 Schematic display of the geometry for remote sensing of the atmosphere.

The atmospheric radiative transfer is simulated by a computer model, called forward model $\mathbf{F}$, using a limited number of parameters as input. The calculation of the absorption coefficients (Equation (4.2)) and the integration of the radiative transfer equation (Equation (4.1)) are performed for a single frequency and a pencil beam, respectively, while both the spectrometer channels and antenna pattern are not infinitely narrow. Therefore a convolution between the signal from the atmosphere as a function of frequency and the spectrometer channel shape, and between the signal as a function of viewing direction and the antenna pattern, is required. Thus, the observed signal becomes a vector y, which can be expressed as:

$$\mathsf{y} = \mathbf{F}(\mathsf{x}, \mathsf{b}) + \epsilon \tag{4.6}$$

where (x, b) gives a total description of both the atmospheric and sensor states, and ϵ is the measurement noise. The x vector contains all the parameter to be retrieved, while the vector b contains the model parameters. For a heterodyne instrument, as is the case of the SMILES instrument, the most important sensor parts are the antenna, the mixer, the sideband filter and the spectrometer.

4.1.2 Retrieval Method and Basic Error Estimation

Including the measurement noise $\boldsymbol{\epsilon} = {}^T(\epsilon_1, \epsilon_2, \cdots, \epsilon_m)$, the observation equation is expressed by

$$\mathbf{y} = \mathbf{F}(\mathbf{x}) + \boldsymbol{\epsilon}. \tag{4.7}$$

Here we omit the model parameters appearing in the forward model for simplicity.

In general the forward function $\mathbf{F}$ is nonlinear with respect to the state vector but the linear approximation is expected to be reasonable for most target gases of SMILES. In this assumption, it is natural to expand the forward function around the *a priori* value $\mathbf{x}_a$,

$$\mathbf{y} \approx \mathbf{F}(\mathbf{x}_a) + \mathbf{K}_x(\mathbf{x} - \mathbf{x}_a) + \boldsymbol{\epsilon}, \tag{4.8}$$

$$\mathbf{K}_x = \left.\frac{\partial \mathbf{F}(\mathbf{x})}{\partial \mathbf{x}}\right|_{\mathbf{x}_a}. \tag{4.9}$$

The retrieval method which we adopt is the optimal estimation method [*Rodgers*, 1976]. The optimal linear solution can be given by

$$\hat{\mathbf{x}} = \mathbf{x}_a + \mathbf{D}_y \left[\mathbf{y} - \mathbf{F}(\mathbf{x}_a)\right], \tag{4.10}$$

where the contribution function is

$$\begin{aligned} \mathbf{D}_y &= (\mathbf{K}_x^T \mathbf{S}_\epsilon^{-1} \mathbf{K}_x + \mathbf{S}_a^{-1})^{-1} \mathbf{K}_x^T \mathbf{S}_\epsilon^{-1}, & (4.11)\\ &= \mathbf{S}_a \mathbf{K}_x^T (\mathbf{K}_x \mathbf{S}_a \mathbf{K}_x^T + \mathbf{S}_\epsilon)^{-1}, & (4.12) \end{aligned}$$

and $\mathbf{S}_\epsilon$ and $\mathbf{S}_a$ are the measurement error covariance matrix and the *a priori* error covariance matrix, respectively. It is also possible to express the retrieval in terms of the averaging kernel matrix

$$\mathbf{A} \equiv \frac{\partial \hat{\mathbf{x}}}{\partial \mathbf{x}} = \mathbf{D}_y \mathbf{K}_x, \tag{4.13}$$

as follows:

$$\hat{\mathbf{x}} = (\mathbf{I} - \mathbf{A})\mathbf{x}_a + \mathbf{A}\mathbf{x} + \mathbf{D}_y \boldsymbol{\epsilon}. \tag{4.14}$$

Finally, the retrieval error covariance is given by

$$\begin{aligned} \mathbf{S} &= (\mathbf{A} - \mathbf{I}_n)\mathbf{S}_a(\mathbf{A} - \mathbf{I}_n)^T + \mathbf{D}_y \mathbf{S}_\epsilon \mathbf{D}_y^T, & (4.15)\\ &= (\mathbf{K}_x^T \mathbf{S}_\epsilon^{-1} \mathbf{K}_x + \mathbf{S}_a^{-1})^{-1}. & (4.16) \end{aligned}$$

The comprehensive error analysis including the model parameters is found in the original literature [*Rodgers*, 1990].

4.2 Simulation of Observation Spectra

We have two simulators available for analyses of the SMILES observations. One is SMOCO (SMILES Observation retrieval Code) developed by the CRL, and the other is ARTS (Atmospheric Radiative Transfer Simulator) by the Institute of Remote Sensing, University of Bremen, Germany, and the Chalmers University, Göteborg, Sweden. These simulators are capable to produce emission spectra of the SMILES observations by the use of atmospheric and instrumental knowledge. They can also calculate the weighting functions. These are essential quantities used to expand the observation equation into a linear relation in the optimal estimation method. Since the simulation model is the basis for the correct retrieval of atmospheric species from the limb sounding measurements, we conducted intercomparisons between the two simulation models. SMOCO and ARTS have basically generated the same spectra. The results are also given in this section.

4.2.1 ARTS Forward Model

Forward models consist of either empirically determined relationships or numerical counterparts of the physical relationships needed to describe the radiative transfer and sensor effects. The ARTS is mainly of the latter type, but some parts are more based on empirical investigations, such as the parameterizations of continuum absorption.

The ARTS forward model is separated into two parts: atmospheric part and sensor part. Thus, the state vector x and forward model parameter vector b are expressed as:

$$\mathsf{x} = \begin{pmatrix} \mathsf{x}_r \\ \mathsf{x}_s \end{pmatrix} \tag{4.17}$$

and

$$\mathsf{b} = \begin{pmatrix} \mathsf{b}_r \\ \mathsf{b}_s \end{pmatrix}, \tag{4.18}$$

respectively, where $(\mathsf{x}_r, \mathsf{b}_r)$ refers to the atmospheric part, and $(\mathsf{x}_s, \mathsf{b}_s)$ refers to the sensor part.

4.2.1.1 Atmospheric Part

The first part describes the atmospheric radiative transfer, independent of the sensor characteristics, i.e., for pencil beam (infinite spatial resolution) monochromatic (infinite frequency resolution) signals. The intensity i of the signal received from the atmosphere is expressed by:

$$\mathsf{i} = \mathbf{F}_a(\mathsf{x}_r, \mathsf{b}_r) \tag{4.19}$$

Practically, to calculate i (by solving the radiative transfer equation), the line of sight (LOS) is divided into n equidistant points (distance noted with Δl). The absorption and transmission is assumed to vary linearly between the points. The optical depth τ_i, associated with the step i is calculated as:

$$\tau_i = \frac{\Delta l}{2}\left(k_i + k_{i+1}\right), \quad 1 \leq i < n \tag{4.20}$$

where k_i and k_{i+1} are the absorption coefficients calculated at the i^{th} and $(i+1)^{th}$ LOS points, respectively.

The transmission associated with step i is:

$$\zeta_i = \exp(-\tau_i), \quad 1 \leq i < n \tag{4.21}$$

The absorption coefficients are calculated at the LOS points, from the absorption matrix, calculated on a logarithmic pressure grid, by linear interpolation. The grid for the calculation of the absorption matrix does not necessarily contain the corresponding grid points of the LOS.

The source function S_i is assumed to vary linearly between the LOS points, but for simplicity, a single source function value S_i is assigned to each LOS point, i.e.,:

$$S_i = \frac{S_i + S_{i+1}}{2}, \quad 1 \leq i < n \tag{4.22}$$

The intensity at the point n, i.e. at the end of LOS, is computed using the following iterative expression:

$$\mathsf{i}_{i+1} = \mathsf{i}_i\zeta_i + S_i\left(1 - \zeta_i\right), \quad 1 \leq i < n-1 \tag{4.23}$$

where i_i is the intensity reaching point i. The iteration starts by setting i_1 to the cosmic background radiation.

4.2.1.2 Sensor Part

The second part takes into account the sensor characteristics, such as the measurement vector is given by:

$$\mathsf{y} = \mathbf{F}_s(\mathsf{i}, \mathsf{x}_s, \mathsf{b}_s) + \epsilon_{\mathsf{y}} \tag{4.24}$$

where the i is the vector holding the spectral values of the signal emitted by the atmosphere for a set of considered frequencies, and viewing directions (calculated as described

above). For a heterodyne instrument, as is the case of millimeter/sub-millimeter limb sounding instruments, the most important sensor parts are the antenna, the mixer, the sideband filter and the spectrometer. Therefore, the modeling of the sensor part is either a summation of different frequencies (mixer), or it is a convolution of the spectra as a function of frequency (spectrometer) or as a function of viewing direction (antenna) with the characteristic instrument response functions of concern. Summation and weighting of the spectral components are both linear operations, and thus it is possible to model the effects of the different sensor parts as subsequent matrix multiplications of the monochromatic pencil beam spectrum [*Eriksson*, 2001]:

$$\mathsf{y} = \mathsf{H}_n \cdots \mathsf{H}_2 \mathsf{H}_1 \mathsf{i} + \epsilon_{\mathsf{y}} \tag{4.25}$$

where n is the total number of the considered sensor components, and H_i $(1 \leq i \leq n)$ is the sensor matrix corresponding to the i^{th} component of the sensor. Thus, the sensor model can be implemented as a straightforward matrix multiplication and the measurement vector is given by:

$$\mathsf{y} = \mathsf{H}\mathsf{i} + \epsilon_{\mathsf{y}} \tag{4.26}$$

where $\mathsf{H} = \mathsf{H}_n \cdots \mathsf{H}_2 \mathsf{H}_1$.

The big advantage of this implementation is that the sensor matrix H is constant for a specific instrument, and it can be stored for further calculations.

4.2.1.3 Weighting Function

The separation of the forward model in two parts, the atmospheric part and the sensor part, is very important for the practical calculation of the weighting function. Thus the weighting function, representing the sensitivity of the measurement to the state vector x, can be written as:

$$\mathsf{K}_{\mathsf{x}} = \frac{\partial \mathsf{y}}{\partial \mathsf{x}} = \frac{\partial \mathsf{y}}{\partial \mathsf{i}} \frac{\partial \mathsf{i}}{\partial \mathsf{x}} = \mathsf{H} \frac{\partial \mathsf{i}}{\partial \mathsf{x}} \tag{4.27}$$

Thus the new parts needed to calculate atmospheric weighting functions, are function giving $\partial \mathsf{i}/\partial \mathsf{x}$, where x is the state vector representing a VMR profile, or temperature profile, or spectroscopic data, etc.

The weighting functions can be calculated analytically, or numerically. In ARTS the weighting functions are in general calculated analytically (e.g., for the VMR profiles) but there are some exceptions (e.g., for the atmospheric temperature profile when the hydrostatic equilibrium is assumed, or for the pointing offset) when they are calculated numerically.

4.2.2 SMOCO Forward Model

SMOCO and ARTS share purposes and basic functions. The SMOCO forward model also comprises two components, i.e., atmospheric part and sensor one. These are constructed in principle according to the same method as described for ARTS. Therefore, the following descriptions are focused mainly on aspects characteristic to SMOCO.

4.2.2.1 Atmospheric Part

The atmospheric part of SMOCO calculates molecular absorption coefficients by a line-by-line method, and numerically solves radiative transfer equations for the limb atmosphere. SMOCO has taken emission-line frequencies from the JPL catalog [*Pickett et al.*, http://spec.jpl.nasa.gov/], and parameters for pressure broadening and pressure shifts from

the HITRAN data or other published information. The absorption by water vapor and the continuum emissions are calculated by Liebe's millimeter-wave propagation model (MPM93)[*Liebe*, 1993]. SMOCO takes into account atmospheric refraction when it solves radiative transfer equations. The refraction is significant for lower altitudes as shown in Section 3.2.1.6. SMOCO is capable to deal with an asymmetric atmosphere that has different molecular mixing ratios in farther and nearer regions from the tangent point along the line of sight. This function is effective to improve a horizontal resolution in the direction if needed.

4.2.2.2 Sensor Part

In the sensor part, SMOCO deals with instrumental effects including the antenna radiation pattern, receiver sidebands, Doppler shift of frequency, and AOS frequency response function.

Antenna Radiation Pattern

The antenna will receive radiation signals that come to the aperture in an extended solid angle around the optical axis. Such response is expressed by the antenna radiation pattern, which is modeled in Section 3.2.4 for the SMILES antenna. The signal power received by the antenna is given by a spatial integration of the atmospheric brightness distribution weighted with the antenna radiation pattern. The main beam in the radiation pattern is often described by its half-power beam-width (HPBW). The HPBW of the SMILES antenna will be 0.08° (in elevation) and 0.16° (in azimuth). The spatial integration will cover the main beam and its surrounding area within a diameter of 2.5 times the HPBW. We call this area a field of view (FOV) for SMILES observations. However, we cannot completely neglect the power contribution from the outside of the FOV. The SMILES design assumes that the integration of the antenna radiation pattern within the FOV be higher than 85 % of the whole integration over 4π steradian. SMOCO takes into account these effects when it calculates the signal power received by the antenna.

Receiver Sidebands

Since the submillimeter mixer, including SMILES' SIS mixer, is sensitive to both sidebands, the receiver output is proportional to the combined RF power from the upper sideband (USB) and lower sideband (LSB). This means that the atmospheric emissions in one sideband (signal band) are superimposed on those from the other sideband (image band). However, thanks to a single sideband (SSB) filter, SMILES can suppress the image-band levels lower than 1 percent as shown in Section 3.3.2.2. SMOCO calculates the frequency down-conversion by the submillimeter receiver associated with the SSB filter.

Doppler Shift of Frequency

SMOCO deals with the Doppler shift of frequency caused by the movement of the ISS and the rotation of the Earth. The shift due to the ISS motion is some 10 MHz, depending on yaw deviations in the SMILES attitude. The shift due to the Earth rotation is about 1.5 MHz at most, while the effect is larger when the ISS flies toward the south compared with the case toward the north. Since the direction of the frequency shift for the LSB and USB is opposite in the IF domain, the effect is to be calculated prior to the down conversion in the forward model. Furthermore, the effect has to be properly taken into

account when some daily or weekly averaged data are simulated and used in the retrieval process.

Acousto-Optical Spectrometer (AOS)

First, each channel of the AOS has a Gaussian-like frequency response function as shown in Section 3.3.3.1. By integrating original real spectra with the weighting function, SMOCO simulates the AOS output that is separated in channels. Secondly, since the exact frequency of each channel is sensitive to the environment temperatures, SMILES measures the frequency-channel relation in every 53 seconds with a reference signal onboard. The relation is to be used in the calculation of the AOS output.

4.2.2.3 Weighting Function

The variation in the brightness temperature observed at a tangent height can be expressed by a linear combination of variations in the molecular volume-mixing ratio, pressure, temperature, and the error in the tangent height determination of each observation.

$$\Delta T_A = \int_{z_{min}}^{z_{max}} \left\{ \sum_i K_i \Delta x_i + K_p \Delta(\ln P) + K_T \Delta T \right\} \mathrm{d}z + K_{HT} \Delta z_0. \tag{4.28}$$

Each weighting function is therefore given by

$$K_i = \frac{\partial T_A}{\Delta z \partial x_i}, \quad K_P = \frac{\partial T_A}{\Delta z \partial \ln P}, \quad K_T = \frac{\partial T_A}{\Delta z \partial T}, \quad K_{HT} = \frac{\partial T_A}{\partial z_0}, \tag{4.29}$$

where z_0 is the tangent height of the antenna beam axis. SMOCO evaluates the weighting functions by analytic expressions, but does the tangent height errors from numerical differences,

$$K_{HT} = \frac{T_A(z_0 + \Delta z_0) - T_A(z_0)}{\Delta z_0}. \tag{4.30}$$

4.2.3 Forward Model Intercomparison

An intercomparison was carried out between the results produced by two forward models, SMOCO and ARTS. This concerned both the computation of absorption coefficients and integration of radiative transfer.

The intercomparison calculations were performed using a number of input parameters predefined by the ARTS developers.

Absorption Coefficient Intercomparison

In order to check the model implementation for line absorption calculations, line-by-line calculations were carried out. Absorption coefficients were computed for a large number of frequencies in a variety of spectral ranges where important molecular species have signatures. The considered spectral ranges were about 1 GHz wide, and centered on the set of selected molecular species spectral transitions listed in Table 4.1. A set of spectroscopic parameters for each considered transition was defined by the ARTS developers, including the line center frequency, the line intensity, the lower state energy, and the pressure

species	line center frequency	species	line center frequency
H_2O	22.2 GHz	N_2O	502 GHz
O_3	110.83 GHz	HNO_3	544 GHz
O_2	118.7 GHz	CO	576 GHz
H_2O	183.3 GHz	O_3	625.37 GHz
HCN	354 GHz	HCl	625.9 GHz
ClO	501 GHz	ClO	649.45 GHz

Table 4.1 Selected molecular species transitions for the absorption coefficients intercomparison.

broadening parameters. The provided spectroscopic data was based on the HITRAN catalog [*Rothman et al.*, 1992]. The Voigt lineshape was selected to compute the absorption coefficients. The polynomial coefficients used to compute the partition function, and the isotopic ratio for each isotope of each target species were also provided. In addition to the spectroscopic data, provided were the atmospheric temperature and pressure profile, and the VMR profiles of the selected molecular species.
The spectra of the absorption coefficients were calculated for atmospheric levels ranging from 0 to 60 km, for the full set of considered spectral lines in one run. That means that the possible contributions from the strong lines far away from the watched spectral range are also included.

The results of the intercomparison showed that there is a good agreement between the two models. With a few exceptions for some spectral ranges the relative differences between the models are less than 1%. Here we present only some results for a set of spectral ranges around some transitions mainly of interest for the SMILES study:

- H_2O at 22.23 GHz, a transition of great interest for microwave radiometry.
- O_3 at 625.37 GHz, the transition observed by the SMILES instrument (in Band A and Band B).
- HCl at 625.9 GHz, observed by the SMILES instrument (in Band B).
- ClO at 649.45 GHz, a transition of great interest for microwave radiometry . This emission will also be observed by the SMILES instrument (in Band C).

The two models are very close to each other. In the frequency range around the H_2O line emission a relative difference of less than 0.015% is found (Figure 4.3, lower plot). Similar results are obtained for the spectral range around 625.37 GHz (Figure 4.4, lower plot). In the spectral range around 626.9 GHz (Figure 4.5, lower plot) the relative differences between the two models are about 1%. The differences appear to be caused by the pressure shift, which seems to be not taken into account in the SMOCO model. An offset between the two calculations appear in the spectral range around the ClO transition at 649.45 GHz (Figure 4.6, lower plot). This offset seems to be caused by a baseline due to other line species absorption, as at this altitudes the emission signal from ClO is almost negligible (see Figure 4.6, upper plot).

Radiative Transfer Intercomparison

The intercomparison at the stage presented here aimed to investigate the differences between the models due solely to the numerical solution of the radiative transfer equation. A

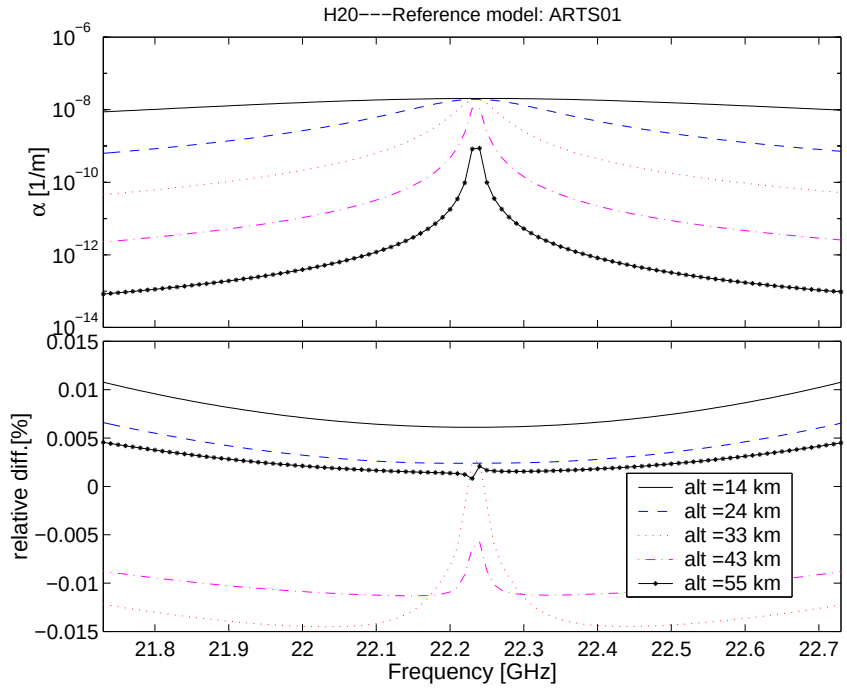

Figure 4.3 Upper: ARTS calculations of the absorption spectra in the frequency range around the H_2O line at 22.23 GHz for different atmospheric levels. Lower: Relative difference between the absorption spectra calculated with the two models SMOCO and ARTS. The ARTS model was taken as a reference model.

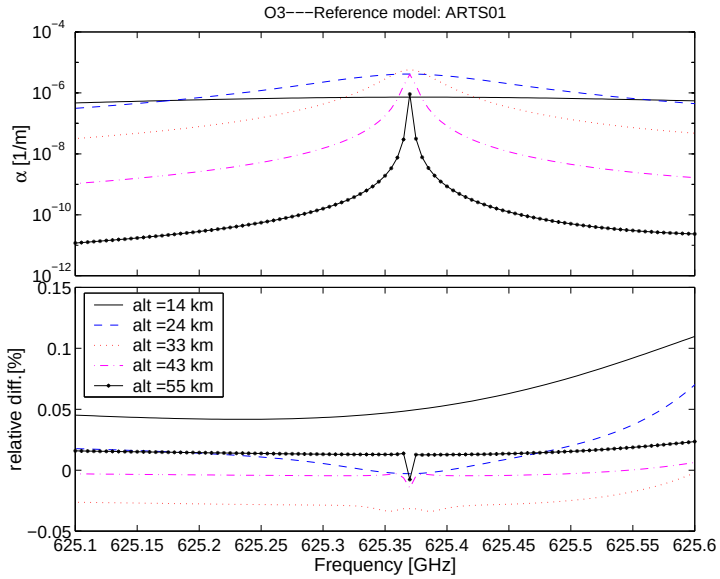

Figure 4.4 Upper: ARTS calculations of the absorption spectra in the frequency range around the O_3 line at 625.37 GHz for different atmospheric levels. Lower: Relative difference between the absorption spectra calculated with the two models SMOCO and ARTS. The ARTS model was taken as a reference model.

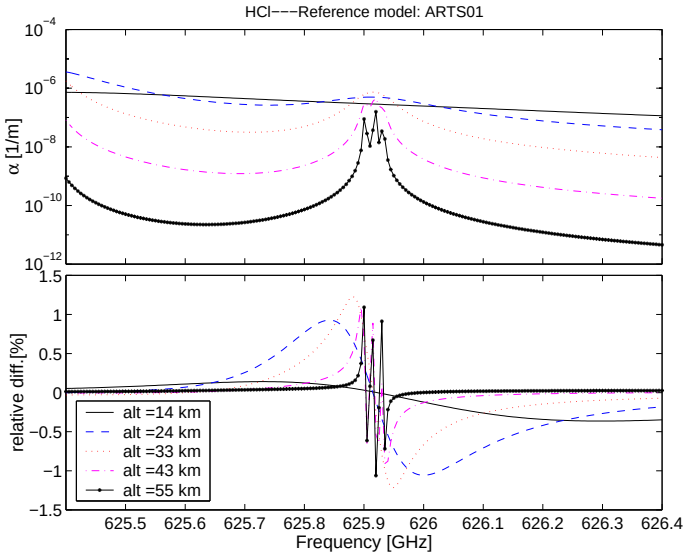

Figure 4.5 Upper: ARTS calculations of the absorption spectra in the frequency range around the HCl line at 625.9 GHz for different atmospheric levels. Lower: Relative difference between the absorption spectra calculated with the two models SMOCO and ARTS. The ARTS model was taken as a reference model.

standard set of absorption coefficient spectra, calculated on a fine vertical grid, was provide by the ARTS developers. These absorption spectra were used the provide the brightness temperature for a set of viewing direction. The other necessary specifications, such as the platform altitude, were also provided. The brightness temperature spectra seen by a limb looking instrument under a set of viewing angle, and the absolute difference between the SMOCO and ARTS calculations are displayed in Figure 4.7. An absolute deviation of about 1 K appears in the line wings (Figure 4.7, lower plot). The deviations in the line center are almost negligible.

4.2.4 Observational Spectra Simulated by SMOCO

JEM/SMILES has three frequency bands: Band-A; 624.32 – 625.52 GHz, Band-B; 625.12 – 626.32 GHz, and Band-C; 649.12 – 650.32 GHz. Figure 4.8 shows an example of the SMILES spectra for the three frequency bands at a tangent height of 40 km. These spectra are expected with an averaging of 30 atmospheric scans in orbit, which correspond to a half-day (12 hour) zonal mean averaged over a 5° latitude-width in the mid-latitude.

In the above simulations SMOCO was used with settings as follows.

- We used an antenna response pattern including wide-angle sidelobes with a beam efficiency of 0.85, which is described in section 3.2.4 of this Mission Plan.
- The ISS altitude is assumed to be its nominal value 407 km.
- The model atmospheres at latitudes of 0°N, 45°N, and 80°N are of the Rutherford Appleton Laboratory, which include molecular concentrations, temperatures, pressures from 0 to 120 km.
- The center frequencies of molecules used in SMOCO are shown in Table 4.2.

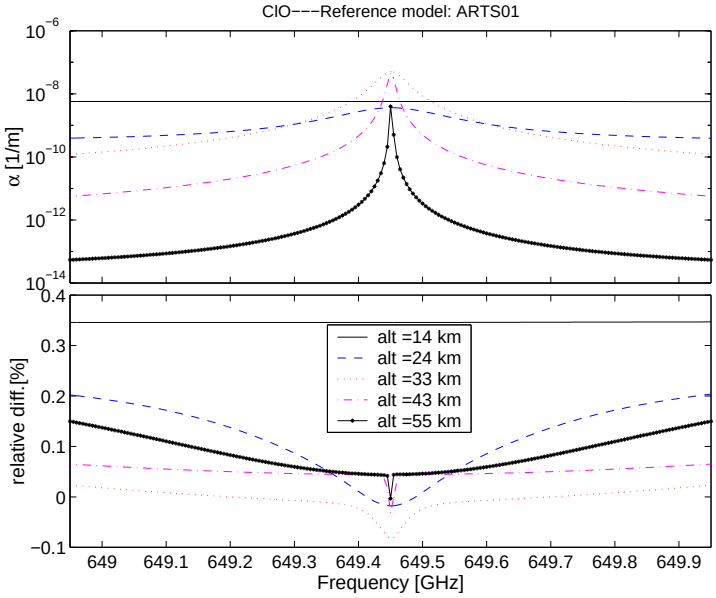

Figure 4.6 Upper: ARTS calculations of the absorption spectra in the frequency range around the ClO line at 649.45 GHz for different atmospheric levels. Lower: Relative difference between the absorption spectra calculated with the two models SMOCO and ARTS. The ARTS model was taken as a reference model.

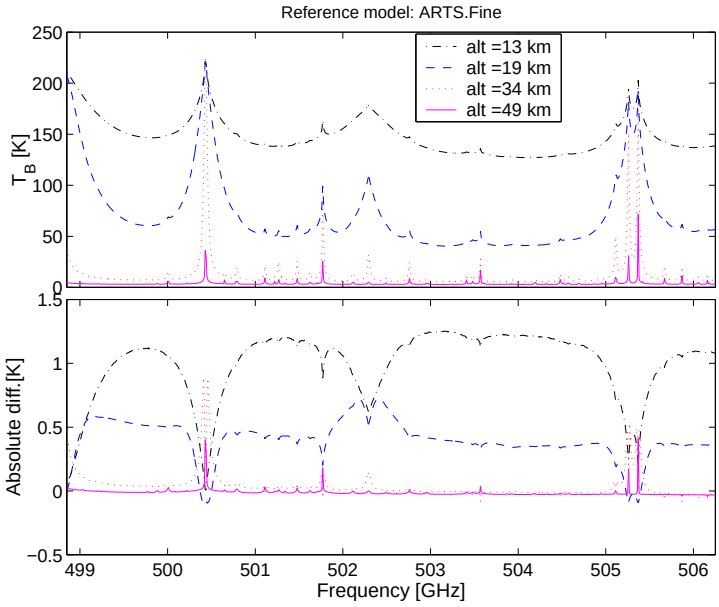

Figure 4.7 Upper: Arts calculations of brightness temperature spectra seen by a limb sounding instrument. Lower: Absolute difference between brightness temperatures calculated with the two models (SMOCO and ARTS) calculation. The ARTS model was taken as a reference model.

Table 4.2 Molecular transition frequencies of JEM/SMILES species.

BAND A (GHz)		*BAND B* (GHz)		*BAND C* (GHz)	
624.32-625.52 GHz		625.12 - 626.32 GHz		649.12 - 650.32 GHz	
HNO_3	624.48				
CH_3CN	624.50				
CH_3CN	624.63				
CH_3CN	624.73	$HO^{81}Br$	625.18		
^{81}BrO	624.77	O_3 (v_2)	625.28	^{18}OOO	649.14
HNO_3	624.78	O_3 (v_2)	625.32	^{17}OOO	649.14
CH_3CN	624.82	$HO^{79}Br$	625.33	^{18}OOO	649.15
OClO	624.82	HNO_3	625.34	^{17}OOO	649.27
$O^{18}OO$	624.83	O_3	625.37	^{17}OOO	649.38
$ClONO_2$	624.87	^{18}OOO	625.39	ClO	649.45
CH_3CN	624.88	^{18}OOO	625.56	$(ClO)_2$	649.51
CH_3CN	624.91	O_3 (v_2)	625.61	HO_2	649.70
CH_3CN	624.93	HO_2	625.66	$O^{17}OO$	649.79
$H^{37}Cl$	624.98	OClO	625.78	^{17}OOO	649.97
H_2O_2	625.04	O_3 (v_2)	625.79	^{17}OOO	649.98
O_3 (v_3)	625.05	O_3 (v_3)	625.80	^{17}OOO	650.01
$HO^{35}Cl$	625.07	$O^{17}OO$	625.87	^{17}OOO	650.04
^{18}OOO	625.09	$H^{35}Cl$	625.92	^{17}OOO	650.16
$HO^{81}Br$	625.18	$O^{17}OO$	626.09	^{17}OOO	650.17
O_3 (v_2)	625.28	$O^{17}OO$	626.20	^{81}BrO	650.18
O_3 (v_2+v_3)	625.30	OClO	626.22	HNO_3	650.28
O_3 (v_2)	625.32	$(ClO)_2$	626.32		
$HO^{79}Br$	625.33				
HNO_3	625.34				
O_3	625.37				

values including ones to be measured by the SMILES molecular spectroscopy team.

- Clear atmosphere with no cirrus clouds is assumed.

The simulation has revealed several characteristics of molecular spectra involved in the three frequency bands.

- The ClO spectrum is relatively isolated from other spectra in Band-C.
- The HO_2 spectrum is relatively isolated from other spectra in Band-C.
- The baseline level in the lower sideband is higher than that in the upper sideband, which is due to a strong water vapor transition at 620.701 GHz.
- Band-C is most appropriate among the three bands to observe weak spectra.
- Although the Band-C is not includes normal ozone lines, there is a possibility to acquire some ozone information from the wing emissions of its 650.733 GHz line.
- Two BrO bands are available in the SMILES bands, although the transition around 624.77 GHz in Band-A is superimposed on HNO_3 transitions, and the other around

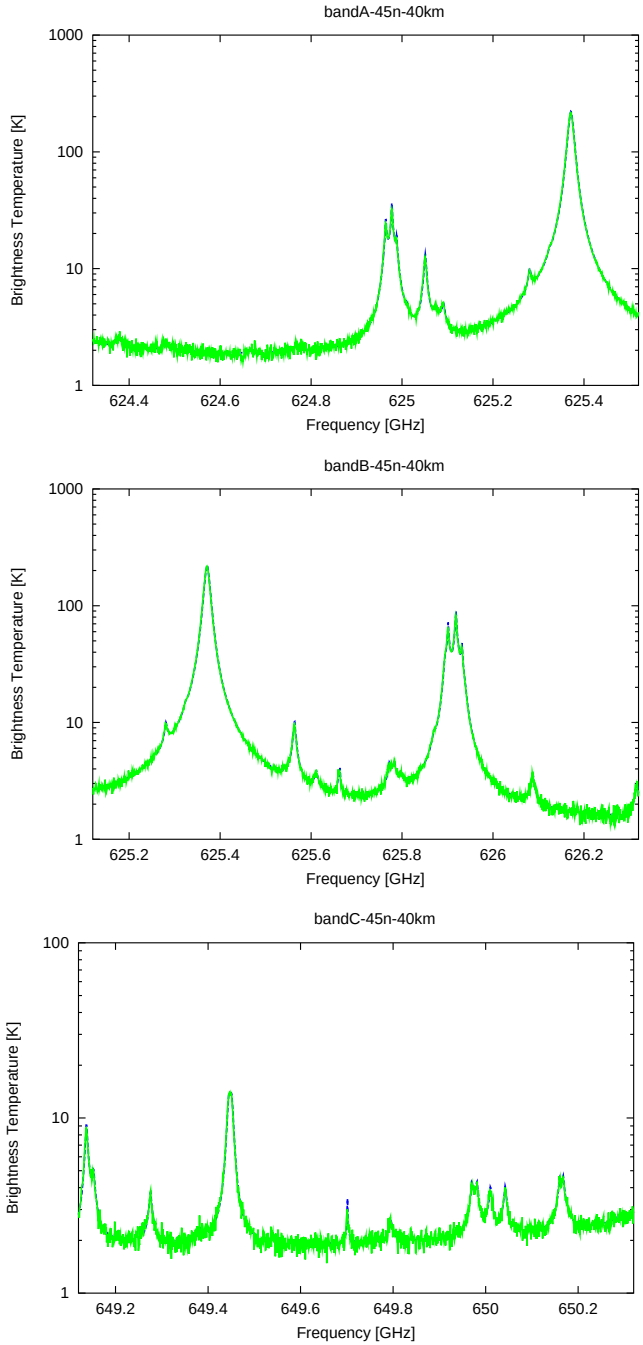

Figure 4.8 SMILES spectra for a tangent height of 40 km simulated with the 45°N model atmosphere. The figures show the quality of observation data accumulated for 30 scans in orbit.

650.18 GHz in Band-C is on isotope ozone transitions. The retrieval error of BrO from the Band-C spectrum is slightly lower than that for the Band-A case.

- Two transitions are available for HO_2, one in Band-B and the other in Band-C. The HO_2 emission in Band-C is relatively isolated from other lines. HO_2 is one of important species with few upper stratospheric and mesospheric data, and it is one

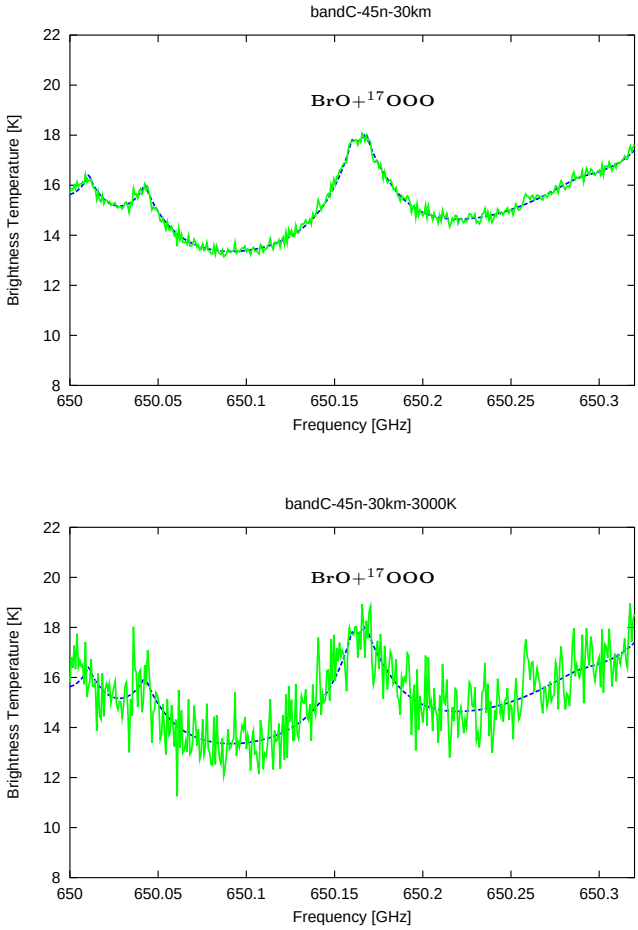

Figure 4.9 Comparison of two spectra, one expected with T_{sys} = 500 K and the other with 3000K.

of surely productive molecules for the SMILES observation.

SMILES's high sensitivity would provide new opportunities to observe stratospheric radical species such as BrO, HO_2 which have been only poorly measured so far. The BrO spectrum that would be obtained by the system with T_{sys} = 500 K (SIS mixer) with accumulations of 30 scans is compared with the same spectrum with 3000 K (Schottky diode mixers) in Figure 4.9.

4.3 Molecular Retrieval

The retrieval of molecular height profiles has been made for SMILES major species by SMOCO, and the outputs are presented in the Appendix. They include the retrieved height profiles, retrieved total errors, and averaging kernels. For the purposes of description, we divide the SMILES species into the next four groups.

- Standard products: O_3, HCl, and ClO in the stratosphere.
- Research products: HOCl, CH_3CN, HO_2, HNO_3, and BrO in the stratosphere.

- Ozone isotopes: asymmetric-18 ozone (^{18}OOO), asymmetric-17 ozone (^{17}OOO), and symmetric-17 ozone (O^{17}OO) in the stratosphere.
- Mesospheric products: O_3, HCl, and HO_2 in the mesosphere.

In the optimal estimation method, the retrieved error informs us how much new observation spectrum with the radiance uncertainty covariance is able to decrease the *a priori* uncertainty covariance, as shown in Equation (4.16). The error ratio, which is defined as the ratio of the total retrieval error to the *a priori* error covariance, is useful to evaluate the retrieval results. We used the error ratio of that sense in the Appendix. The *a priori* error covariance is not a unique value, and different from one species to the other because of its a priori information of the observations, scientific purposes, the intensity of the spectrum in each tangent height, the radiance noise, and so on. For example, in our studies in the Appendix, the diagonal component of *a priori* uncertainty covariance has been assumed to be proportional to the *a priori* height profile in the ratio of 0.5 for the standard products and HNO_3, 1.0 for the research products (except HNO_3), and 0.1 for the ozone isotopes. As the retrieval error thus depends on the *a priori* uncertainty covariance, this value is regarded as an not very good indicator of the measurement capability of an observation system for the purpose of the comparision of each molecular species. To show the instrumental capability directly in this section, the "ERROR" in the figures are presented by the ratio to the *a priori* height profile, instead of the ratio to the *a priori* error.

4.3.1 Standard Products

Three molecular species: O_3, HCl and ClO are classified as the standard products, for which SMILES is expected to give retrieved height profiles with errors less than 10 percent by the use of data available from a single atmospheric scan in orbit. The weighting functions have been calculated with a 2 km step for these species. The "ERROR" are given by their ratios to the retrieved height profiles, which are the same as the *a priori* ones, in Figure 4.11. The *a priori* height profiles used for the retrieval are given in Figure 4.10.

The volume mixing ratio of ClO in the model profile of 80°N enhanced at around 20 km due to the activation of chlorine inside the polar vortex. The single-scan error for this enhanced ClO is estimated less than 10 percent around 20 km. SMILES is also capable of observing ClO in its background abundance that is not enhanced by heterogenious reactions. These are simulated with the atmosphere model height profiles of 45°N. The single-scan error for the case is estimated less than 20 percent for 30 km to 42 km.

With respect to the normal ozone O_3, the retrieval error is estimated less than 5 percent for 20 km to 45 km, and less than 10 percent for 18 km to 52 km at any latitudes even in the case of single scan.

The retrieval error of H^{35}Cl is estimated less than 10 percent for 25 km to 45 km at any latitudes in the case of single scan. It decreases to 5 percent levels for the atmospheric model profiles at 80°N.

4.3.2 Research Products

Five molecular species of HNO_3, HOCl, HO_2, CH_3CN, BrO are classified as the research products, for which SMILES is expected to give retrieved height profiles with errors less than 50 percent by the use of 30-scan averaged data. The weighting functions have been calculated with a 4 km step for these species. The "ERROR" are given by their ratios to the retrieved height profiles, which are the same as the *a priori* ones, in Figure 4.13 and

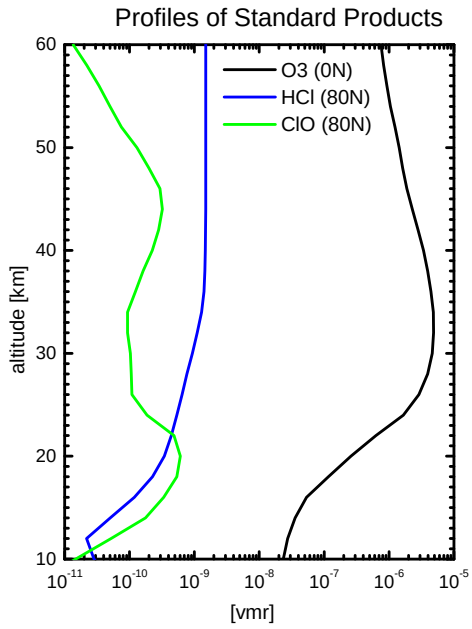

Figure 4.10 The *a priori* molecular height profiles used in the retrieval of the SMILES standard product species. The abscissa is the volume mixing ratio (VMR) of each species.

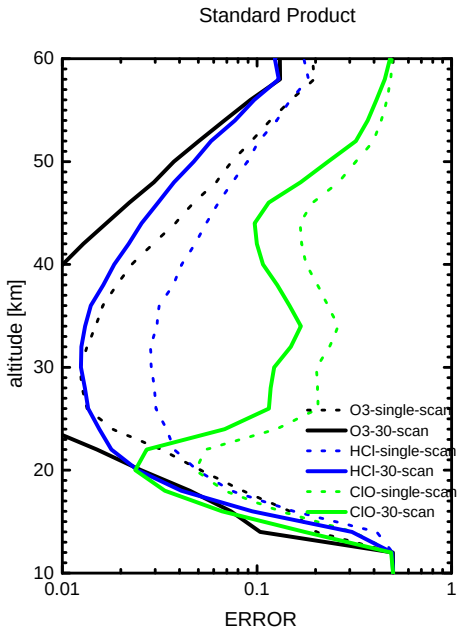

Figure 4.11 The ratio of the retrieval error to the retrieved height profile for the SMILES standard product species.

Figure 4.15. The *a priori* height profiles used for the retrieval are given in Figure 4.12 and Figure 4.14.

With respect to the five research product species, we have retrieved the height profiles from 30-scan averaged data. Among them, HOCl, CH_3CN, and HNO_3 are species that can be retrieved with errors significantly less than 20 percent. The error levels for HOCl are less than 20 percent at any latitudes for 26 km to 43 km. The profiles of CH_3CN are obtained from [*Livesey*, 2001], not model profiles. The error levels for CH_3CN in the equator are less than 20 percent for 15 km to 38 km. HNO_3 is expected to be abundant at high latitudes, and the retrieval errors are less than 20 percent at 17 km to 30 km with the atmospheric model profile at 80°N.

For other two species, i.e., HO_2 and BrO, the error levels are less than 50 percent. Since HO_2 is abundant in the upper stratosphere and mesosphere at low latitude regions, the HO_2 retrieval errors decrease to 30-40 percent levels for higher than 30 km in the equator. The BrO retrieval errors are less than 50 percent at 25 km to 37 km by the atmospheric model profile at 80°N. BrO could be detectable with errors of 50 percent levels even at mid-latitudes profile. Note that we are here talking about the retrieval errors we expect from the 30-scan averaged data, which correspond to a 5-degree latitudinal zonal mean available in half a day. Significant error reduction is therefore very hopeful when we deal with data averaged in much longer periods.

Based on the above investigations, we expect SMILES data will be useful to study the so-called HOx chemistry, including HOCl and HO_2, from aspects of its relations to the ClO chemistry.

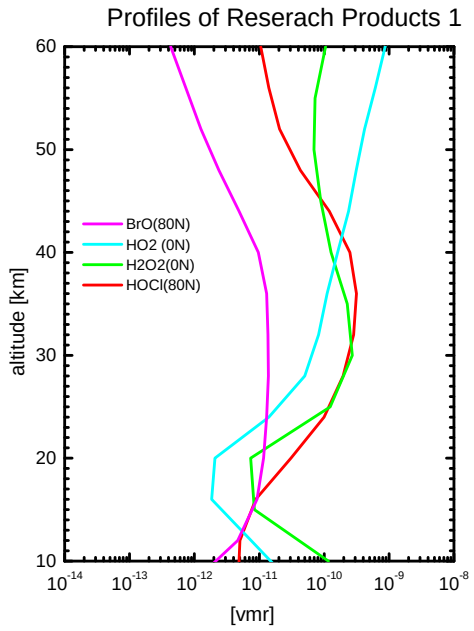

Figure 4.12 The *a priori* molecular height profiles used in the retrieval of the SMILES research product species. The abscissa is the volume mixing ratio (VMR) of each species.

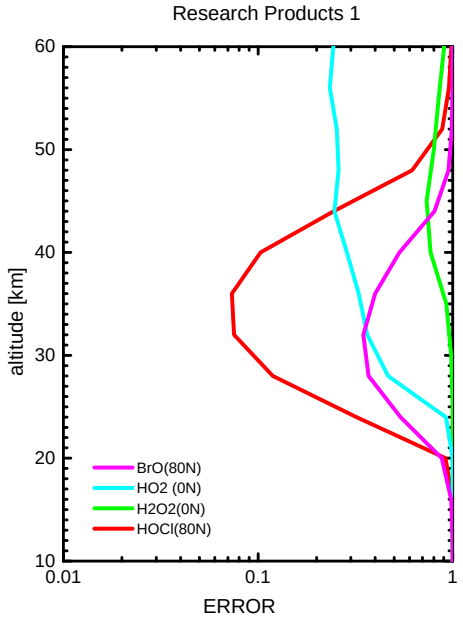

Figure 4.13 The ratio of the total retrieval error to the retrieved height profile for the SMILES research product species.

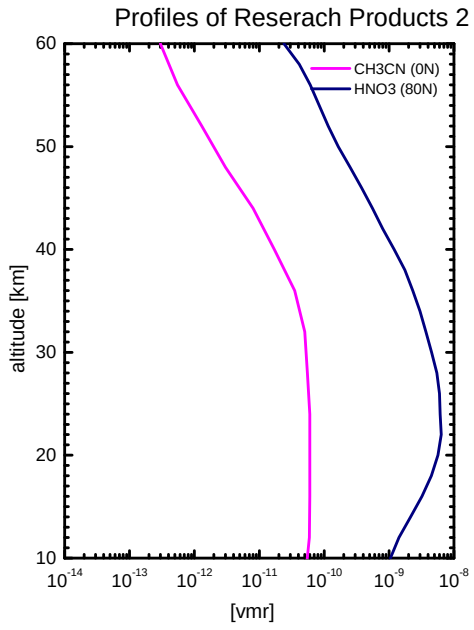

Figure 4.14 The *a priori* molecular height profiles used in the retrieval of the SMILES research product species. The abscissa is the volume mixing ratio (VMR) of each species.

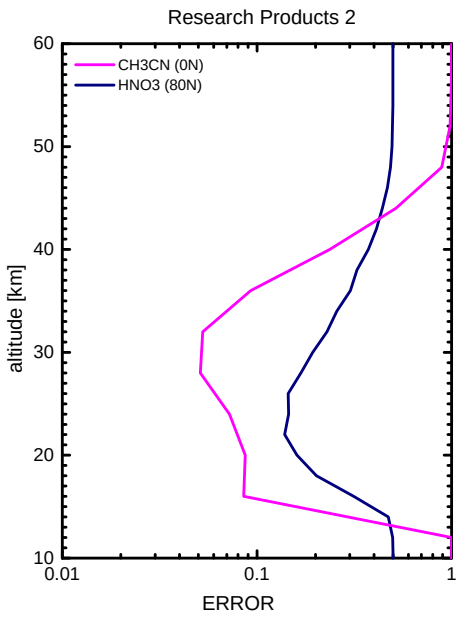

Figure 4.15 The ratio of the total retrieval error to the retrieved height profile for the SMILES research product species.

4.3.3 Ozone Isotopes

There are 73 transitions of ozone isotopes in the three frequency bands of SMILES. Among them, Band-C is most suitable to observe ozone isotopes, since it includes a lot of relatively isolated spectra for asymmetric-17 ozone (^{17}OOO), asymmetric-18 ozone (^{18}OOO), and symmetric-17 ozone (O^{17}OO). The retrieval errors with the 30-scan averaged data are summarized as follows. The "ERROR" are given by their ratios to the retrieved height profiles, which are the same as the *a priori* ones, in Figure 4.17. The *a priori* height profiles used for the retrieval are given in Figure 4.16.

- Normal ozone (O_3): The retrieval errors are less than 2 percent from 21 km to 45 km with a height resolution of 2 km.
- Asymmetric-18 ozone (^{18}OOO): The retrieval errors are less than 2 percent from 24 km to 39 km with a height resolution of 5 km.
- Asymmetric-17 ozone (^{17}OOO): The retrieval errors are less than 2 percent from 25 km to 35 km with a height resolution of 5 km.
- Symmetric-17 ozone (O^{17}OO): The retrieval errors are less than 9 percent from 25 km to 40 km with a height resolution of 5 km.

The retrieved error of isotopes are converted to the error in the isotope enrichment δ. The degree of the ozone isotope enrichment is defined as $\delta^M\mathrm{O} = ({}^M R_{obs}/{}^M R_{std} - 1) \times 1000$ [‰], where ${}^M R_{obs}$ is the observed abundance ratio of the heavy isotopomer with mass

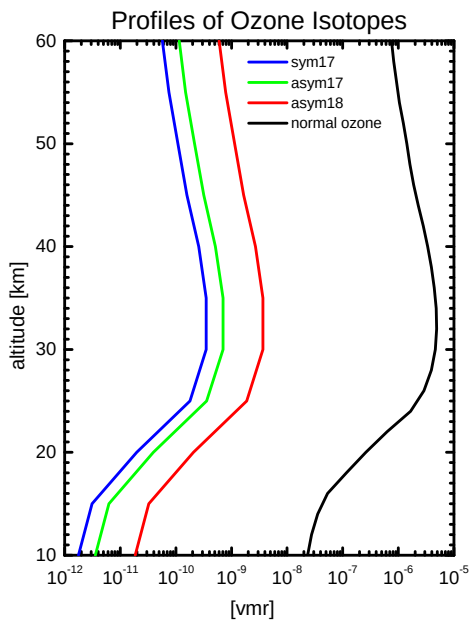

Figure 4.16 The *a priori* molecular height profiles used in the retrieval of the SMILES ozone isotopes. The abscissa is the volume mixing ratio (VMR) of each species.

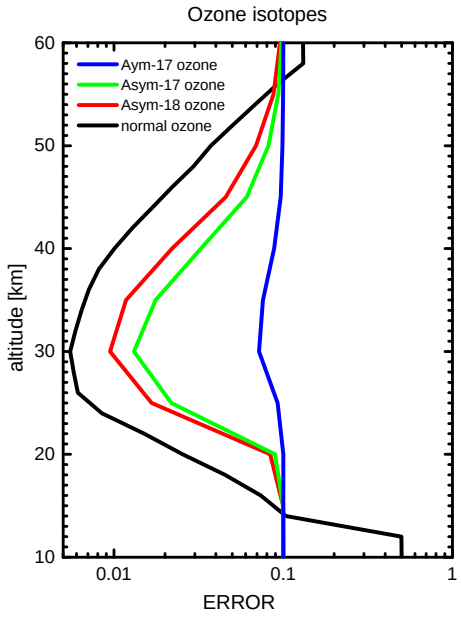

Figure 4.17 The ratio of the retrieval error to the retrieved height profile for the SMILES ozone isotopes.

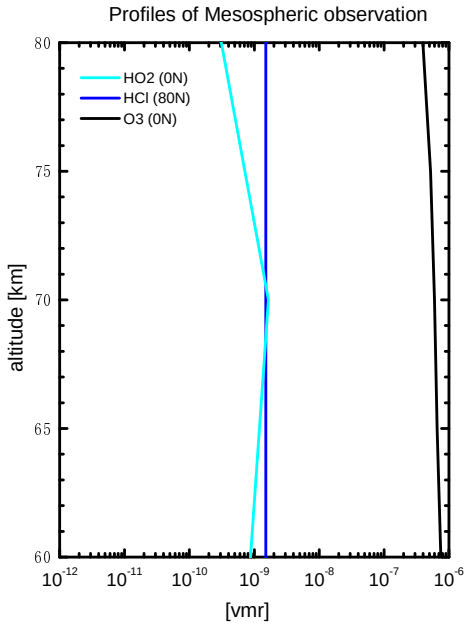

Figure 4.18 The *a priori* molecular height profiles used in the retrieval of the SMILES mesospheric species. The abscissa is the volume mixing ratio (VMR) of each species.

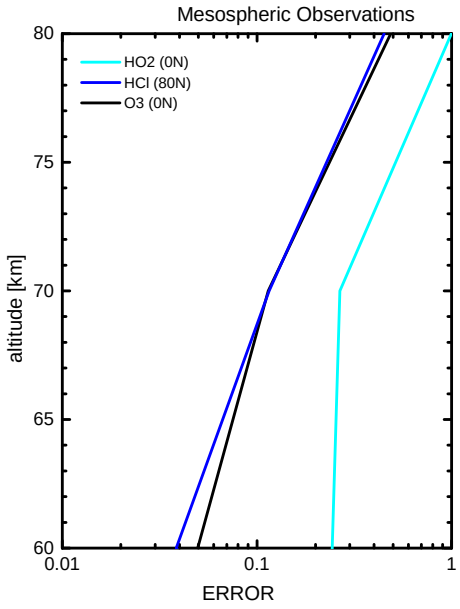

Figure 4.19 The ratio of the total retrieval error to the retrieved height profile for the SMILES mesospheric species.

number M, and ${}^{M}R_{std}$ is the standard ratio described above [*Kaye*, 1987] as described in section 2.4. The error in δ is affected by two retrieval errors: one in the retrieved normal ozone, the other in the retrieved isotope ozone. So it is given by the root-square-sum of the two errors. Since they are estimated as 2 percent for normal ozone and ^{18}OOO, the error in δ for ^{18}OOO is less than 3 percent. The error in δ for ^{17}OOO is also less than 3 percent. The absolute value of δ is expected to be 10–40 % (100–400 ‰) for ^{18}OOO, and around 10 percent (100 ‰) for ^{17}OOO, as described in Chapter 2. Therefore, SMILES will be able to provide useful data for the ozone isotope enrichment. Furthermore, the data will be available in every day and night in 5-degree latitudinal zone maps. SMILES will be the first mission to investigate the global distribution of ozone isotopes.

4.3.4 Mesospheric Products

Among the SMILES spectrum simulation, O_3, HCl and HO_2 are expected to have relative strong line intensity in the mesosphere. We therefore classified these species as the mesospheric products, and conducted the retrieval with a reduced height resolution of 10 km. With the 30-scan averaged data, the retrieval errors are estimated to be less than 50 percent at altitudes of less than 70 km for O_3 and HCl at any latitudes and for HO_2 in the equator model profiles. Although the formal observation range of SMILES is 10-60 km, it will also scan the mesosphere up to around 150 km with an increased speed. If all the spectral data available in the scan period is utilized for the retrieval, then the retrieval errors will be much reduced for the mesosphere. The ERROR are given by their ratios to the retrieved height profiles, which are the same as the *a priori* ones, in Figure 4.19. The

a priori height profiles used for the retrieval are given in Figure 4.18.

4.4 Temperature and Pointing Retrieval

The standard approach for microwave limb sounding instruments is to derive the atmospheric temperature profile and instrumental pointing information from oxygen emission lines [*Wehr*, 1998; *Engeln*, 1998; *Carlotti*, 1999; *Engeln*, 2000]. The oxygen volume mixing ratio is constant and therefore, the intensity of the emission line is only a function of the atmospheric temperature and the total pressure. Nevertheless, other emissions, e.g., ozone emissions, can also convey accurate temperature and pointing information. In that case the information originates primarily from the fact that the limb path becomes opaque for certain tangent altitudes and frequencies. In general, the limb path for the center of the spectral lines becomes opaque at higher tangent altitudes, whereas the limb path for the wings of the spectral lines becomes opaque only at lower tangent altitudes. In the opaque case there is a direct relation between the brightness temperature received by the instrument and the physical temperature of the atmosphere. The width of the spectral line conveys information on the pressure, and thus, information on pointing.

The spectral ranges which will be observed by the SMILES instrument do not include an oxygen emission line and thus information on the atmospheric temperature and instrumental pointing have to be extracted from non-uniformly mixed species emission lines. Therefore it is essential to investigate where the information on the two quantities comes from.

The atmospheric temperature profile and a first order correction of the instrumental pointing, the pointing offset, are retrieved simultaneously with the molecular species profiles. The atmospheric temperature profile is retrieved on a logarithmic pressure vertical grid corresponding to a vertical spacing in altitude of about 3 km. For this, a variance (a priori error) of 5 K was assumed, and no interchannel correlation was considered. The pointing offset is retrieved as an offset in the antenna viewing direction. For this, a standard deviation of 0.2° , corresponding to about 7 km at the tangent point, was considered.

Retrieval simulations were carried out with or without the hydrostatic equilibrium constraint. The full set of presented results refers to mid-latitude summer atmospheric conditions [*Anderson*, 1986].

4.4.1 Temperature Retrieval

4.4.1.1 Information Content

Compared with the molecular species profiles, the derivation of the atmospheric temperature profile is a more complicated process. Information on the atmospheric temperature profile is derived through different mechanisms, as outlined above. To see where the information on the atmospheric temperature comes from the information content in the measurement with respect to the atmospheric temperature is investigated. The information content is given by the $\tilde{\mathsf{K}}$ matrix which is the weighting function matrix K_x scaled by the variability of the a priori state and the measurement [*Rodgers*, 2000]:

$$\tilde{\mathsf{K}} = \mathsf{S}_\epsilon^{-\frac{1}{2}} \mathsf{K}_\mathsf{x} \mathsf{S}_\mathsf{a}^{\frac{1}{2}} \tag{4.31}$$

In the above equation S_ϵ is the measurement noise covariance matrix (in this case a diagonal matrix representing only the thermal noise), and S_a is the a priori covariance matrix (in this case a diagonal matrix with the diagonal elements equal with the variance of the atmospheric temperature profile, i.e., $(5\ \mathrm{K})^2$).

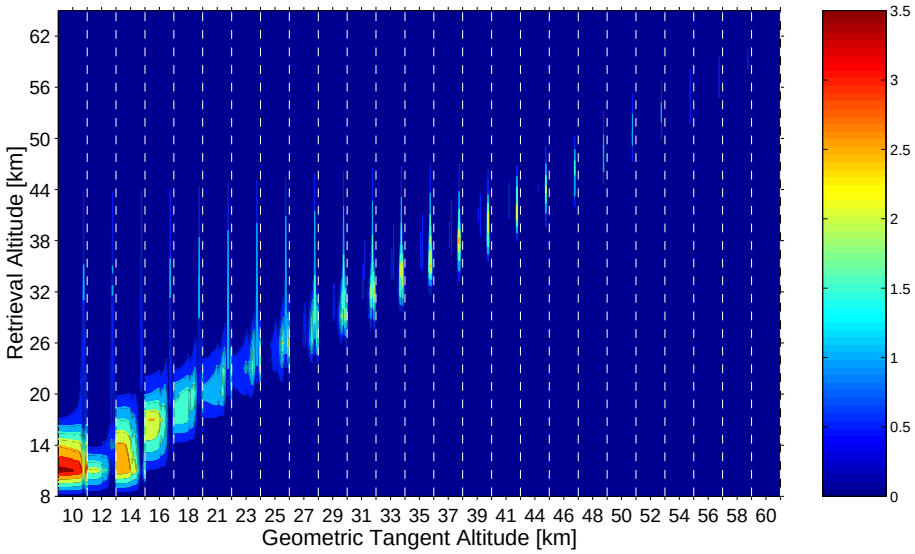

Figure 4.20 Band A: "Information content" on the atmospheric temperature. The x axis displays the measurement vector during one scan. The spectra taken at different tangent altitudes (in the altitude range of 10 – 60 km, in steps of 2.1 km) are separated by vertical dashed lines. The tangent altitudes are displayed at the middle point of the corresponding region of the measurement. The y axis displays the retrieval altitude levels. The retrieval altitudes where there is no information on the temperature (i.e., very low altitudes) are not shown.

As an example, the results for Band A are shown. Figure 4.20 ("Information content") shows the $\tilde{\mathsf{K}}$ matrix for the temperature retrieval in Band A. The x axis displays the measurement vector during one scan (i.e., 25 tangent altitudes, corresponding to altitudes between 10 and 60 km in steps of 2.1 km), while the y axis displays the retrieval altitude levels. The geometric tangent altitudes are placed on the x axis at the middle point of the corresponding part of the measurement. It is seen that the measurement has a high information content with respect to atmospheric temperature at altitudes around 11 km, altitudes where saturation effects occur. At even lower altitudes the atmosphere is totally opaque and thus no information on the temperature can be obtained from the measurement. Similar behavior has been found for the other two bands. In the first two bands, Band A and Band B (not shown), the O_3 transition at 625.37 GHz plays an important role for the temperature profile derivation at higher altitudes. Nevertheless, some information on the temperature comes from spectral features in the frequency ranges around 624.98 GHz (Band A) and 625.92 GHz (Band B), where the HCl emission lines are found. Similar analysis carried out for Band C shows that no information on the temperature is found at higher altitudes, a consequence of the lack of strong spectral features within this spectral band which could provide information on the temperature.

4.4.1.2 With Hydrostatic Equilibrium

The results for the temperature retrieval with hydrostatic equilibrium are displayed in Figures 4.21 – 4.23. The watched quantities are the retrieval precision, the measurement error, the error correlation of the temperature retrieval with the other retrieved quantities, the averaging kernel functions and the vertical resolution given by the full width at half

maximum (FWHM) of the averaging kernel functions.

Figure 4.21(a), Figure 4.22(a) and Figure 4.23(a) show that the atmospheric temperature profile can be retrieved (in all three spectral bands) with a precision better than 1 K at altitudes around 11 km, a consequence of the saturation effects. The first two bands, Band A and Band B, are almost equally suited for the temperature retrieval at most altitudes, a consequence of the fact that the same main source of information, the O_3 line at 625.37 GHz, is used in both bands. The atmospheric temperature profile can be retrieved with a precision of about 1 K up to altitudes of about 40 km in Band A (Figure 4.21(a)), and up to altitude of about 45 km in Band B (Figure 4.22(a)). In this altitude range the retrieval precision is dominated by the measurement error, the smoothing error (not shown) is rather small. The retrieval precision becomes closer to the a priori error at altitudes below 10 km, and above 50 km, a fact which shows that the information on the temperature relies more on the a priori information than on the information from the measurement. The temperature retrieval is somewhat correlated with the HCl retrieval (in Band A also with the HNO_3 retrieval) at low altitudes, and with the O_3 retrieval at high altitudes (Figure 4.21(b) and Figure 4.22(b)). A strong correlation of the temperature retrieval with the pointing offset retrieval is seen at an altitude of 11 km, the altitude where the saturation effects occur, and at 14 km, the reference altitude for the hydrostatic equilibrium. An altitude coverage (i.e., a good measurement response) up to 45 km in Band A (Figure 4.21(c)), and up to 50 km in Band B (Figure 4.22(c)) with a vertical resolution of approximately 3 km (Figure 4.21(d) and Figure 4.22(d)) is achieved. In contrast to the first two bands, the retrieval of the atmospheric temperature profile in Band C is achieved with a much poorer performance (Figure 4.23), a consequence of the fact that in this spectral range there are no strong spectral features which could give information on the atmospheric temperature. Also for this last band, a strong error correlation of the temperature retrieval with the pointing offset retrieval at 11 km (where the saturation effects occur), and at 14 km (the reference altitude for the hydrostatic equilibrium calculation) is seen (Figure 4.23(b)).

4.4.1.3 Without Hydrostatic Equilibrium

The results for the retrieved atmospheric temperature profile without hydrostatic equilibrium are displayed in Figures 4.24 – 4.26. It turns out that the retrieved temperature profile is very little affected by assuming or not assuming hydrostatic equilibrium. A slight improvement in the retrieval precision of the temperature profile at high altitudes is seen for the retrieval scenario without hydrostatic equilibrium. However, the differences are very small. Neither the shape of the averaging kernel functions or the error correlation with other retrieved quantities are changed in a significant way. A slight change in the error correlation is seen with the retrieved pointing offset, a fact which was already expected, as these two quantities are not any longer related through the hydrostatic equation. This change in error correlation is most "visible" in Band B (see for comparison Figure 4.25(b) and Figure 4.22(b)).

It has to be pointed out that the SMILES observation are not done on a vertical line. For each limb scanning, the tangent altitude travels about 100 km in horizontal direction as its altitude increases from 10 km to 60 km. That means that the hydrostatic equilibrium is not fulfilled. However, it is shown that the retrieval performance of the atmospheric temperature profile without hydrostatic equilibrium is comparable – if not better – to one obtained when the hydrostatic equilibrium is assumed.

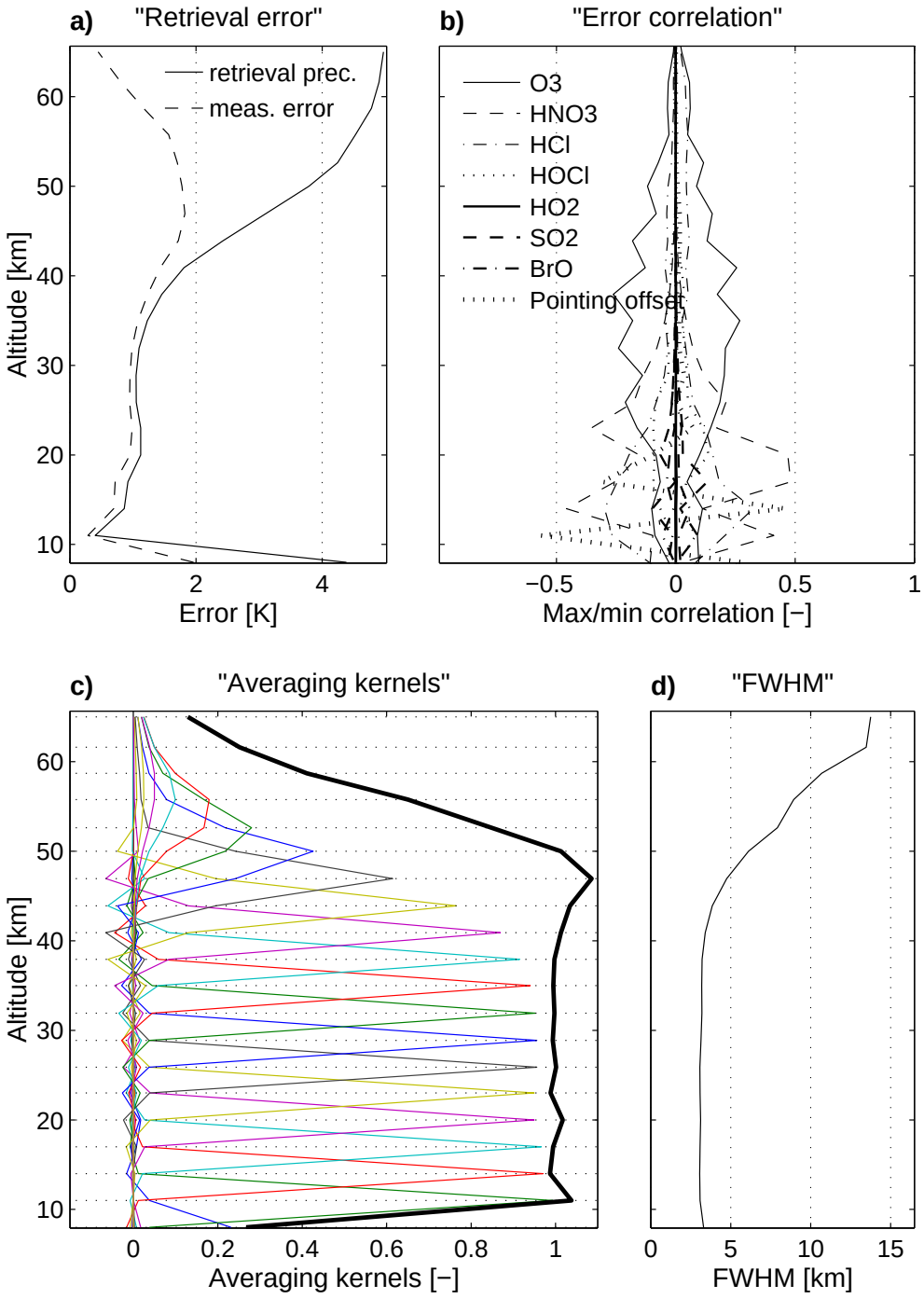

Figure 4.21 Temperature retrieval in Band A with hydrostatic equilibrium: (a) Retrieval precision and measurement error; (b) Error correlation with the other retrieved quantities; (c) Averaging kernel functions; (d) FWHM of the averaging kernel functions presented in (c). The measurement response is also displayed in the plot (c) (solid thick line). Displayed are only those altitudes where a measurement response better than 0.3 is achieved.

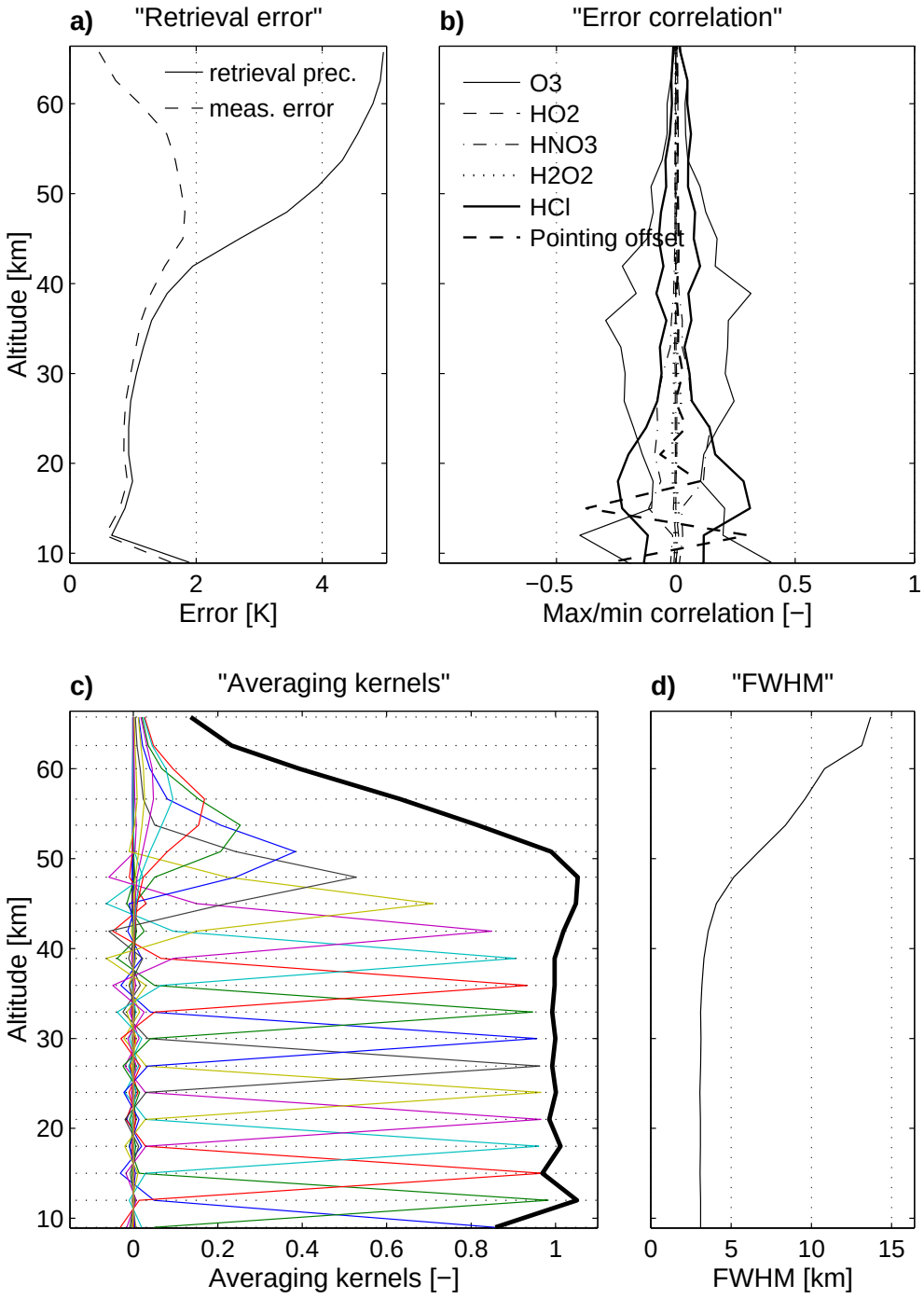

Figure 4.22 Temperature retrieval in Band B with hydrostatic equilibrium: (a) Retrieval precision and measurement error; (b) Error correlation with the other retrieved quantities; (c) Averaging kernel functions; (d) FWHM of the averaging kernel functions presented in (c). The measurement response is also displayed in the plot (c) (solid thick line). Displayed are only those altitudes where a measurement response better than 0.3 is achieved.

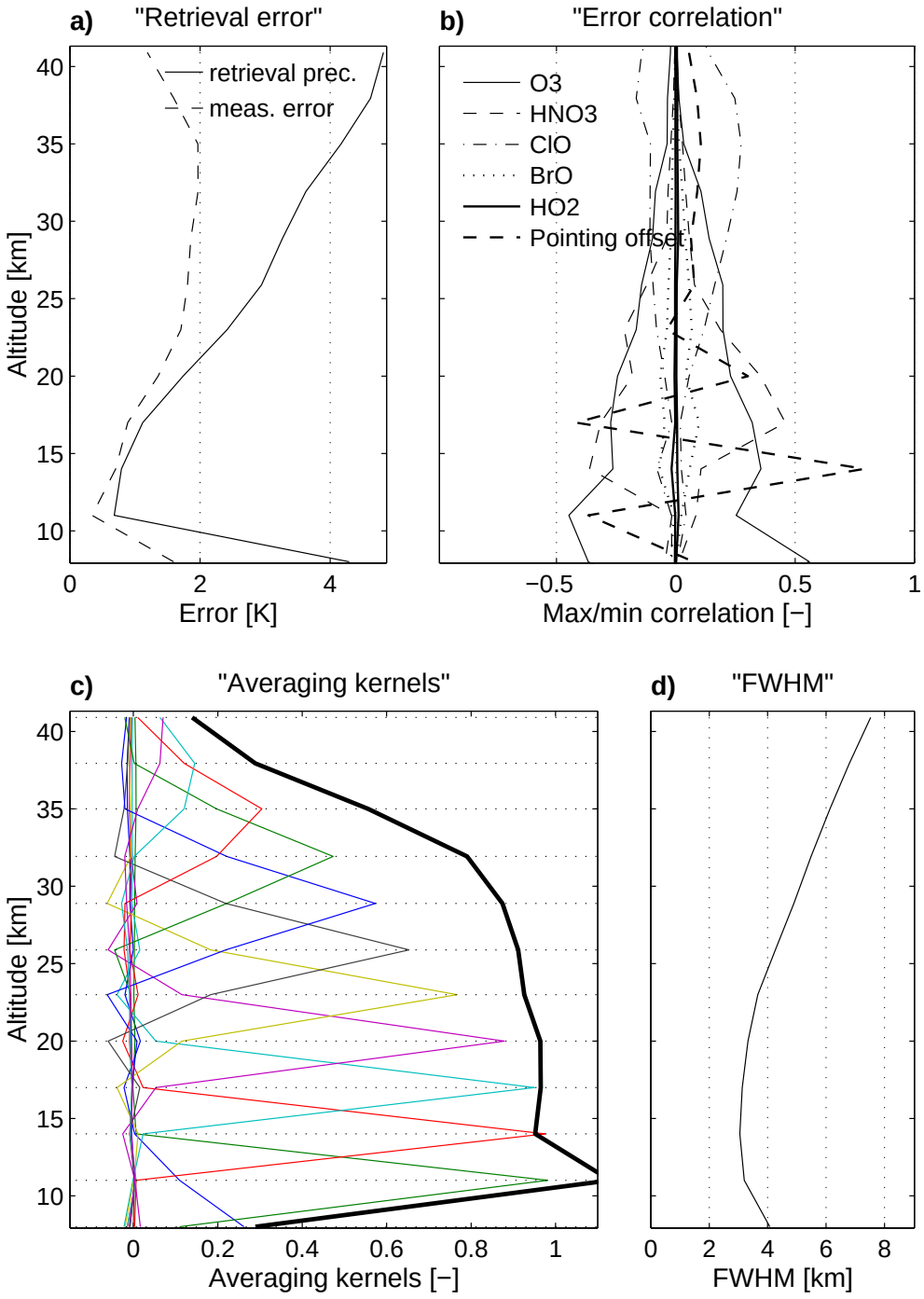

Figure 4.23 Temperature retrieval in Band C with hydrostatic equilibrium: (a) Retrieval precision and measurement error; (b) Error correlation with the other retrieved quantities; (c) Averaging kernel functions; (d) FWHM of the averaging kernel functions presented in (c). The measurement response is also displayed in the plot (c) (solid thick line). Displayed are only those altitudes where a measurement response better than 0.3 is achieved.

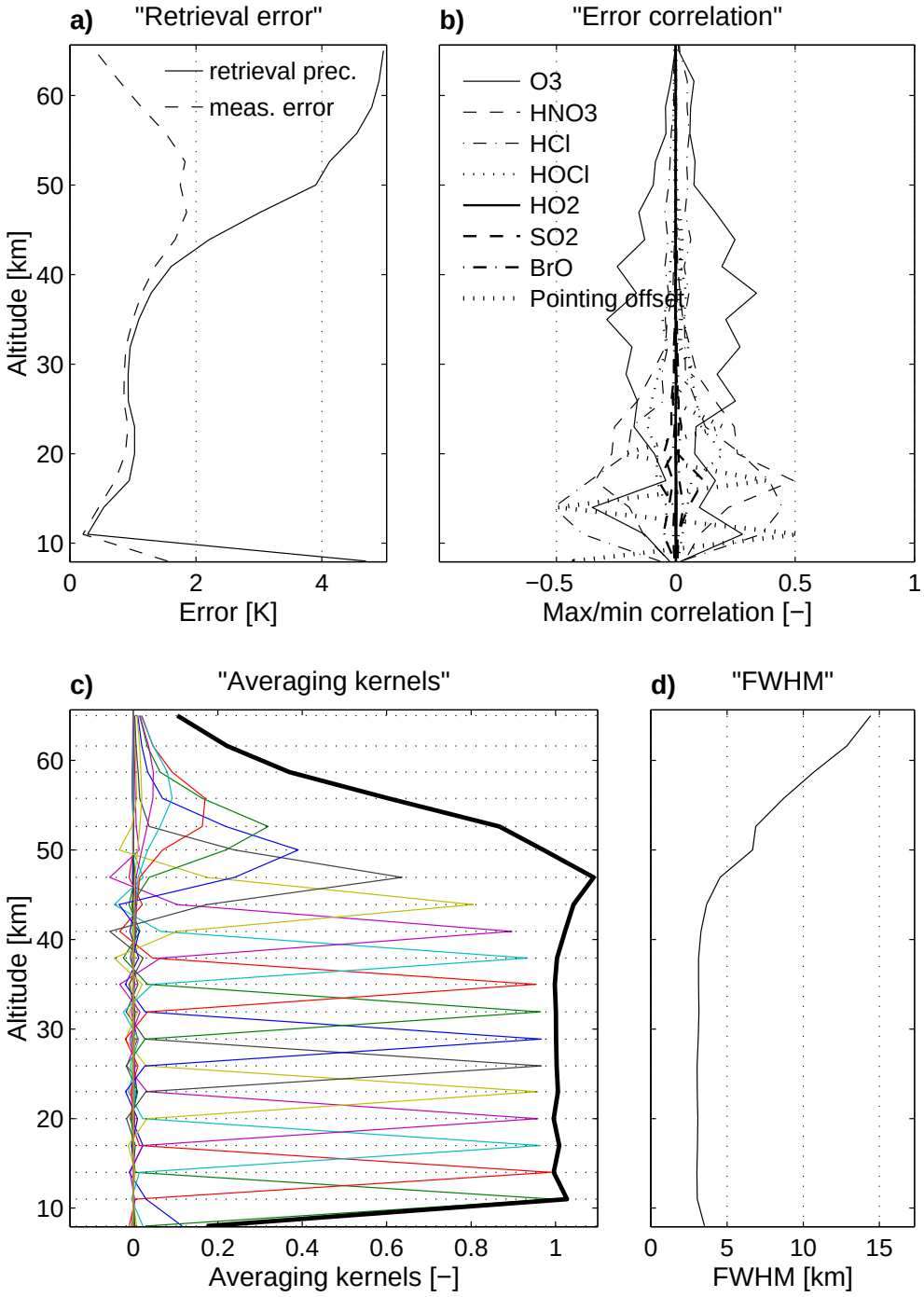

Figure 4.24 Temperature retrieval in Band A without hydrostatic equilibrium: (a) Retrieval precision and measurement error; (b) Error correlation with the other retrieved quantities; (c) Averaging kernel functions; (d) FWHM of the averaging kernel functions presented in (c). The measurement response is also displayed in the plot (c) (solid thick line). Displayed are only those altitudes where a measurement response better than 0.3 is achieved.

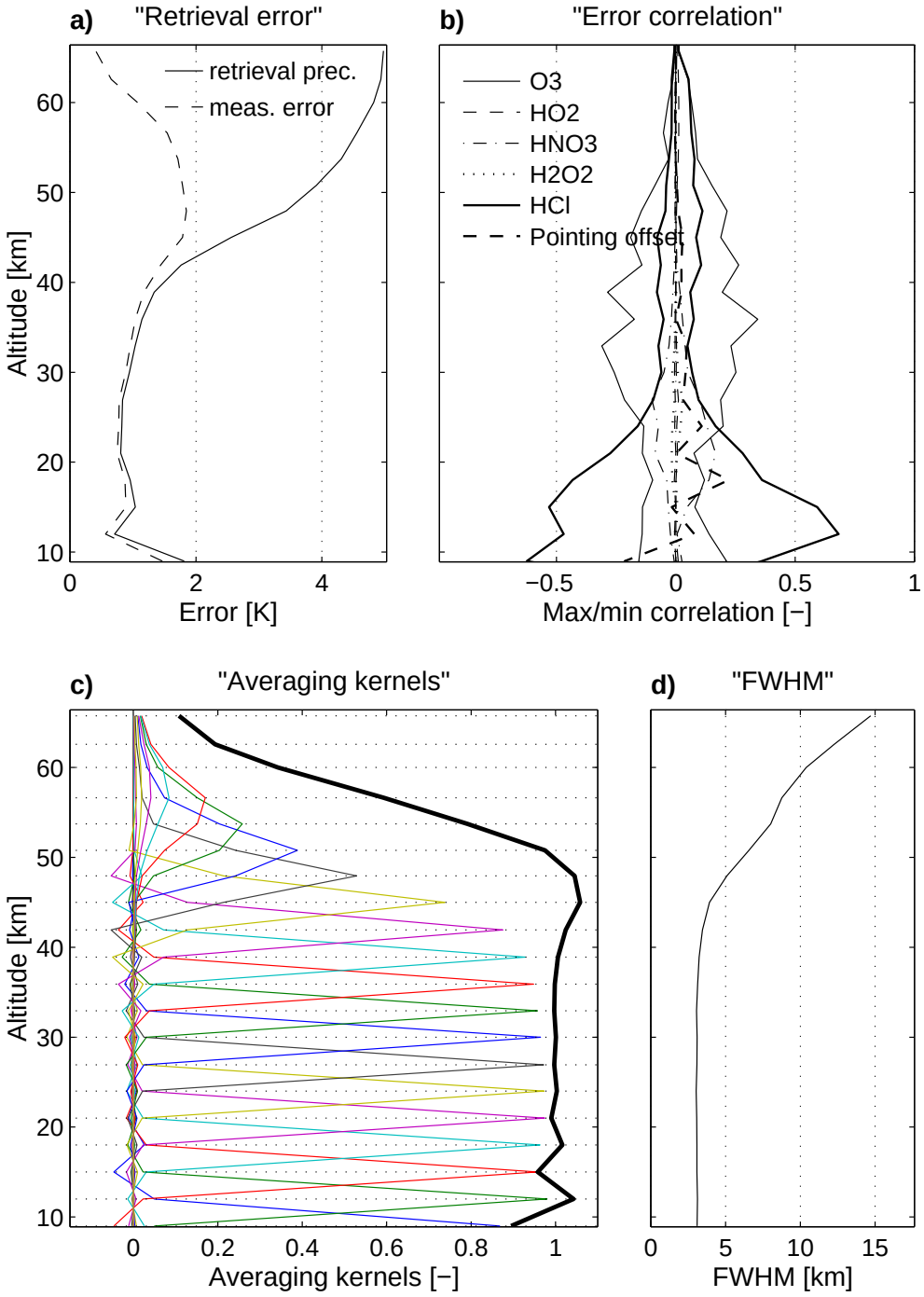

Figure 4.25 Temperature retrieval in Band B without hydrostatic equilibrium: (a) Retrieval precision and measurement error; (b) Error correlation with the other retrieved quantities; (c) Averaging kernel functions; (d) FWHM of the averaging kernel functions presented in (c). The measurement response is also displayed in the plot (c) (solid thick line). Displayed are only those altitudes where a measurement response better than 0.3 is achieved.

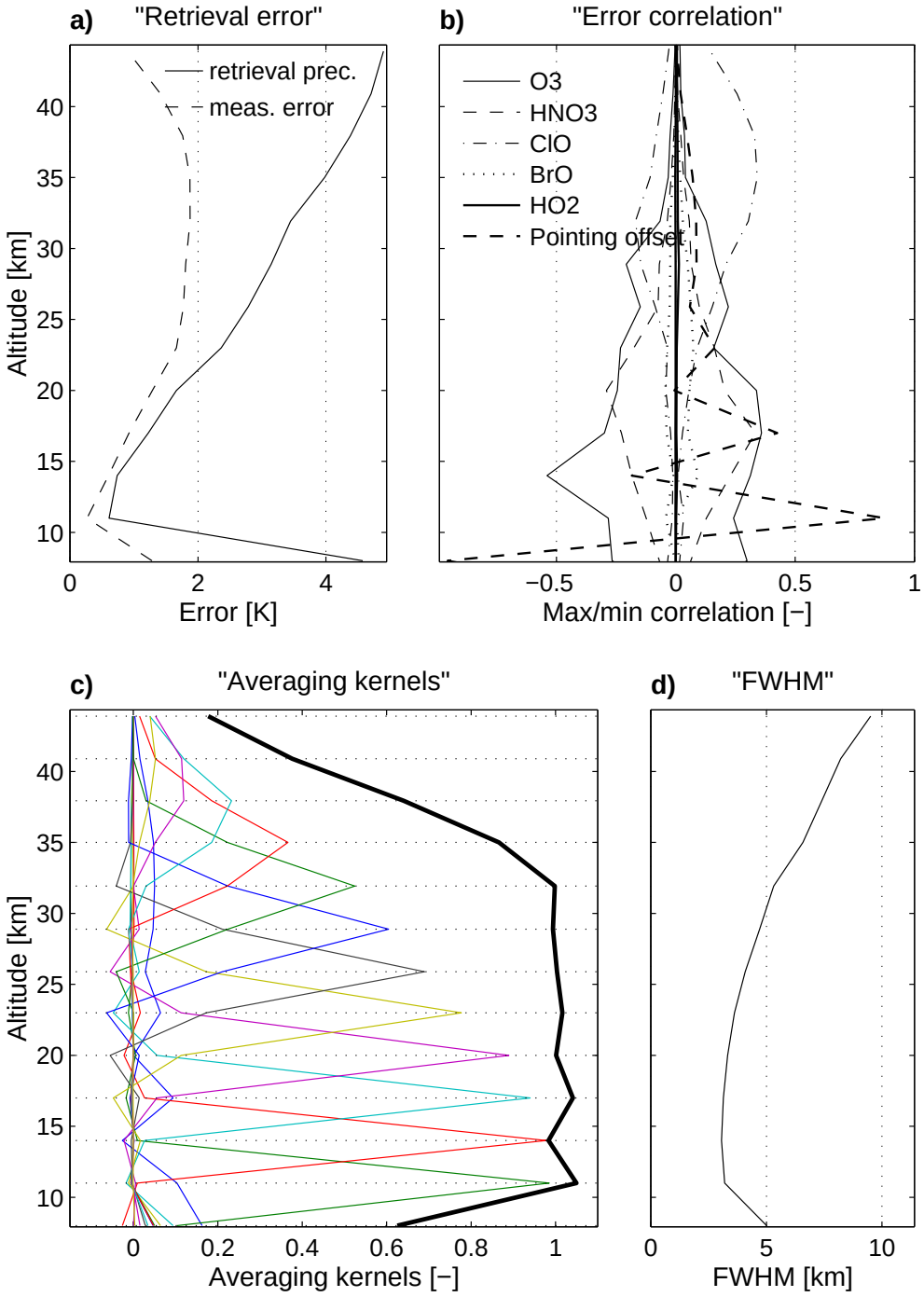

Figure 4.26 Temperature retrieval in Band C without hydrostatic equilibrium: (a) Retrieval precision and measurement error; (b) Error correlation with the other retrieved quantities; (c) Averaging kernel functions; (d) FWHM of the averaging kernel functions presented in (c). The measurement response is also displayed in the plot (c) (solid thick line). Displayed are only those altitudes where a measurement response better than 0.3 is achieved.

4.4.2 Pointing Offset Retrieval

The same steps as for the temperature retrieval were done for the pointing offset retrieval. That means that the information content in the measurement of the pointing offset is analyzed, and the retrieval performance is investigated with or without hydrostatic equilibrium constraint.

4.4.2.1 Information Content

Since no analytical expression is known to calculate the weighting function for the pointing offset, this has to be calculated numerically. The most general and also the most straightforward way to calculate the weighting function is by doing disturbance calculations by repeated use of the forward model. For example, the weighting function for the i^{th} component of the state vector can be calculated by:

$$K_{\mathsf{x_i}} = \frac{\mathbf{F}(\mathsf{x_a} + \Delta\mathsf{x_i}\mathsf{i_i}, \mathsf{b_a}) - \mathbf{F}(\mathsf{x_a}, \mathsf{b_a})}{\Delta\mathsf{x_i}} \tag{4.32}$$

where $\Delta\mathsf{x_i}$ is a small disturbance of the i^{th} component of the state vector (in this case pointing offset), and $\mathsf{i_i}$ is a vector of zeros except the i^{th} component that is unity. The weighting function of the pointing offset reflects the change of the emission for a small change in viewing angle. The magnitude of the disturbance $\Delta\mathsf{x_i}$ plays an important role. Theoretically, the smaller $\Delta\mathsf{x_i}$, the more accurate the result. However, the value applied practically must not be too small as this could lead to numerical instabilities. The value applied here to calculate the weighting function of the pointing offset is 0.001°, found to be small enough the get acceptable results. The information content of the measurement on the pointing offset is given by $\tilde{\mathsf{K}}$ (Equation 4.31). As the pointing offset is described by a single variable, the weighting function matrix has only one column, and so has the $\tilde{\mathsf{K}}$ matrix therefore.

Figure 4.27 displays the $\tilde{\mathsf{K}}$ matrix for the pointing offset, in the three SMILES bands. The presented results refer to the retrieval scenario with hydrostatic equilibrium constraint. However, retrieval simulations carried out without hydrostatic equilibrium constraint showed similar results. The $\tilde{\mathsf{K}}$ matrix is displayed for the measurement taken during one scan. The tangent altitude for each spectrum is displayed in the middle point of the corresponding region of the measurement vector.

The emission at upper tropospheric and lower stratospheric altitudes is dominated by the continuum absorption from O_2, N_2, and H_2O, but also from the line wings of the O_3 emission. Therefore the measurement is characterized by a rather flat, with respect to frequency, information content on the pointing offset. At even lower tangent altitudes the atmosphere is optically thick and the emission is fairly constant explaining the rapid decrease of the measurement information content on the pointing offset at altitudes between 9 and 12 km. These features appear in all there bands. For Band A and Band B, the optical thickness is especially high around the center frequency of the O_3 transition at 625.37 GHz (Figure 4.27, top and middle plots) and so no information on the pointing offset is obtained at this frequency. At higher altitudes the information comes mainly from the O_3 line wings. The features of the HCl lines at 624.98 GHz (Band A) and 625.92 GHz (Band B) show weakly up at high altitudes. Looking at Figure 4.27 it can be concluded that the best altitudes to derive information on the pointing offset in the spectral ranges of Band A and Band B are between 12 and 18 km, due to the continua and O_3 absorption, and between 30 and 50 km where the information on the pointing offset is mainly gained from the wings of the O_3 emission line. From these figures one can clearly see that the pressure broadening linewidth plays an important role in deriving information

on the pointing offset; the shape of the "Information content" curve for different tangent altitudes changes according to the width of the O_3 emission line. In case of Band C the information on the pointing offset is obtained only at low altitudes, due to the continuum absorption (Figure 4.27, bottom plot). For this band, the best altitudes to retrieve the pointing offset are found between 12 and 16 km.

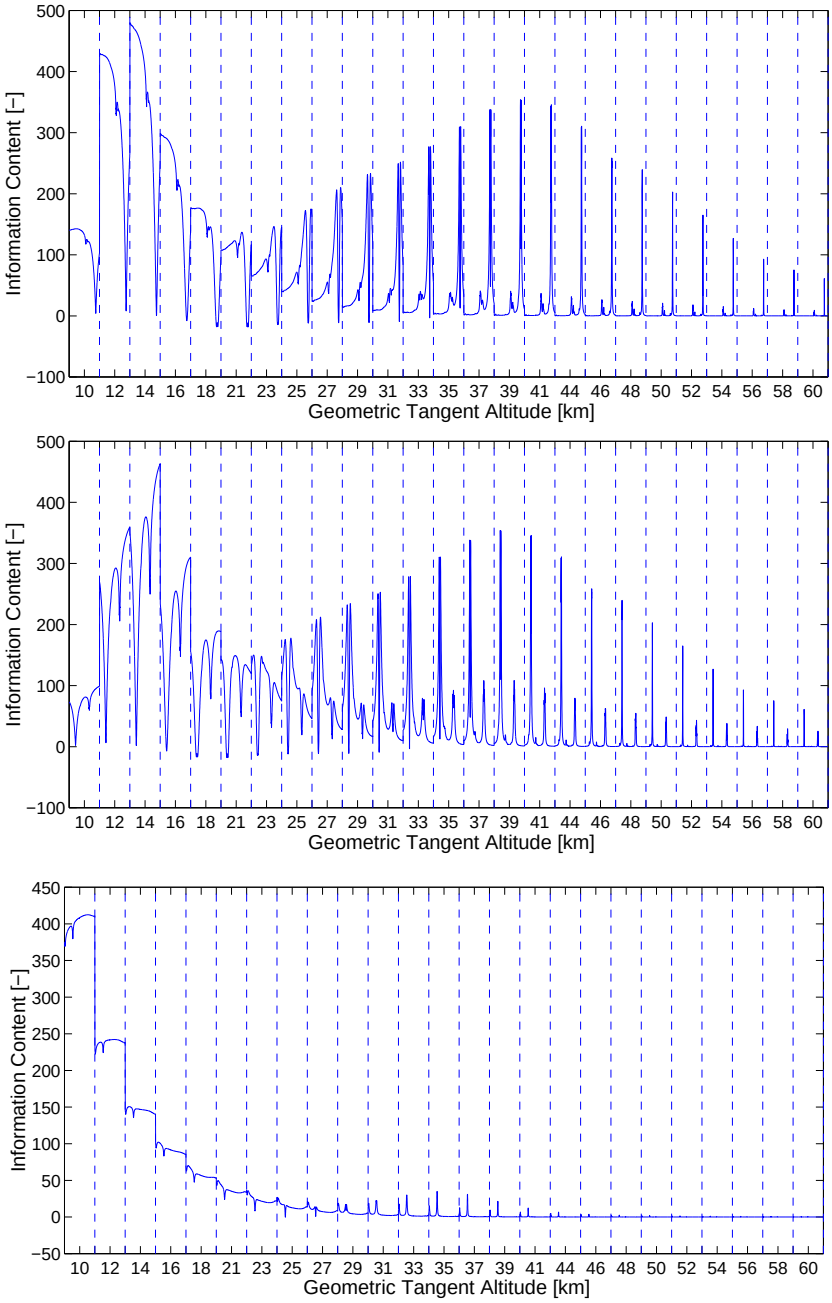

Figure 4.27 "Information content" of the measurement on the pointing offset. Top: Band A; Middle: Band B; Bottom: Band C. The x axes display the measurement vector during one scan (i.e., 25 tangent altitudes), while the y axes display the retrieval altitude levels. The geometric tangent altitudes are placed at the middle point of the corresponding part of the measurement (on the x axes). The presented calculations have been performed under the constraint of the hydrostatic equilibrium.

Table 4.3 Retrieval precision, measurement error and measurement response for the retrieved pointing offset. The retrieval precision and measurement error are given both in antenna viewing angle units [degree] and in the tangent altitude units [m]. The results refer to the retrieval scenario with hydrostatic equilibrium and for the atmospheric conditions specific to mid-latitude summer.

Term		Band A	Band B	Band C
retrieval precision	absolute [°]	$9.12\ 10^{-5}$	$9.60\ 10^{-5}$	$2.91\ 10^{-4}$
	absolute [m]	4	4	11
measurement error	absolute [°]	$7.03\ 10^{-5}$	$8.78\ 10^{-5}$	$2.72\ 10^{-4}$
	absolute [m]	3	3	10
measurement response		1	1	1

4.4.2.2 With Hydrostatic Equilibrium

Table 4.3 displays the results for the pointing offset retrieval with hydrostatic equilibrium. Listed are the retrieval precision and the measurement error (given both in antenna angle units [degrees] and in tangent altitude units [m]) and the measurement response. The pointing offset can be retrieved with an extremely good precision in all three spectral bands. A perfect measurement response is achieved in all three bands. The first two bands, Band A and Band B, are almost equally well suited for the pointing offset retrieval. This is achieved with a precision of about 0.0001° in the antenna viewing angle, corresponding to a value of few meters in the tangent altitude. For these two bands the retrieval precision is mainly dominated by the measurement error (Table 4.3). The results obtained for Band C are slightly poorer.

Generally, the pointing offset retrieval was found to be highly correlated with the temperature retrieval, and slightly weaker correlated with the O_3 retrieval. In case of Band A and Band B a correlation of the pointing offset retrieval with the HCl retrieval was also found.

4.4.2.3 Without Hydrostatic Equilibrium

Similar results for the pointing offset retrieval without hydrostatic equilibrium are given in Tables 4.4. The same as for the temperature retrieval, the results are slightly influenced by assuming or not assuming the hydrostatic equilibrium. Within one band, the pointing offset is retrieved with a similar precision for the two retrieval scenarios. Only the level of error correlation of the retrieved pointing offset with the other retrieved quantities is slightly changed. This mainly refers to the error correlations with the temperature retrieval, a fact which was already expected as the two quantities are not any longer connected through the hydrostatic equilibrium.

Table 4.4 Retrieval precision, measurement error and measurement response for the retrieved pointing offset. The retrieval precision and measurement error are given both in antenna viewing angle units [degree] and in the tangent altitude units [m]. The results refer to the retrieval scenario without hydrostatic equilibrium and for the atmospheric conditions specific to mid-latitude summer.

Term		Band A	Band B	Band C
retrieval precision	absolute [°]	$8.96\ 10^{-5}$	$1.09\ 10^{-4}$	$2.38\ 10^{-4}$
	absolute [m]	3	4	9
measurement error	absolute [°]	$7.08\ 10^{-4}$	$1.02\ 10^{-4}$	$2.82\ 10^{-4}$
	absolute [m]	2	3	3
measurement response		1	1	1

4.5 Spectroscopic Data for SMILES

4.5.1 Spectroscopic Data Required for the JEM/SMILES Experiment

The identification and monitoring of atmospheric molecules as well as interstellar molecules critically depend on the laboratory measurements of line positions, intensities, and collisional cross sections (pressure broadening parameters). The transition frequencies that fall into the submillimeter-wave region which the JEM/SMILES aims at have mostly not been directly measured. Majority of them have been extrapolated from the values measured in the lower frequency regions. As a result, it is not surprising to find discrepancies of several MHz, sometimes much larger, between the calculated and measured transition frequencies. Moreover, crucial parameters other than the center frequencies such as the pressure broadening parameters and the pressure line shifts have been, in many cases, unknown. In particular, information for minor constituents like free radicals and very reactive species are extremely incomplete, and the detection of these species themselves constitutes a great challenge for the laboratory spectroscopy.

Therefore a tremendous amount of efforts has been made to create a number of spectroscopic databases: ATMOS [*Brown et al.*, 1987], SAO [*Chance et al.*, 1994], GEISA [*Husson et al.*, 1992; *Husson et al.*, 1994], JPL [*Poynter and Pickett*, 1985; *Pickett et al.*, http://spec.jpl.nasa.gov/], HITRAN [*Rothman et al.*, 1987; *Rothman et al.*, 1992; *Rothman et al.*, 1996]. More recently the Cologne Database for Molecular Spectroscopy (CDMS) is a new addition [*Müller et al.*, http://www.ph1.uni-koeln.de/vorhersagen/]. The JPL catalog [*Poynter and Pickett*, 1985] includes line positions and line intensity parameters. Line broadening and line shift parameters are not listed in this database. Molecules that are of great importance in the JEM/SMILES mission are listed in Table 4.2. The values for these minor constituents listed in the known database may not be accurate enough. A molecular spectroscopy group has been organized to provide and to evaluate important molecular parameters, especially pressure broadening parameters for the JEM/SMILES mission. The measurements have mostly taken place at Ibaraki University.

Among the transitions listed in Table 4.2, O_3, HO_2, HOCl, HNO_3 (except for $29_{25,4} - 28_{25,3}$), other minor isotopic species, and the vibrationally excited states have not been measured. A most urgent task of the laboratory spectroscopy is to confirm and/or improve the transition frequencies and the pressure broadening parameters of the target molecules,

including common molecules such as O_3 and HCl. In particular, systematic discrepancies are often noticed among the pressure broadening parameters obtained at different locations. In this respect, it is almost imperative to check the parameters that are thought to be well established. One of the goals set by the JEM/SMILES mission is to obtain a global map of BrO. To derive reliable quantitative map by inverting the observed line features, the pressure broadening parameters accurate to a few percent are indispensable for the BrO transitions. These crucial parameters for the SMILES target molecules, BrO, HO_2, and, O_3, are now being measured by the molecular spectroscopy team.

4.5.2 Laboratory Submillimeter-wave Spectrometer System

A submillimeter-wave spectrometer system of a wide frequency coverage and high-sensitivity has been implemented. Figure 4.28 shows a schematic diagram of a system at Ibaraki University. Characteristic features of this instrument are: (1)use of backward-wave oscillators manufactured by a Russian company(ISTOK) as radiation sources and (2) double modulation detection scheme, whenever it is applicable. An oscillator tube(BWO) is housed between the pole faces of a permanent magnet of about 1 T of field strength. The free running frequency fluctuation of BWOs reaches over 10 MHz and therefore active frequency stabilization is essential for high-sensitivity and high-resolution spectroscopy. We achieved this goal by using a double phase-lock loop: the submillimeter-wave radiation is phase-locked to a harmonics of millimeter-wave radiation from a stabilized Gunn oscillator by means of a GaAs harmonic mixer fabricated in G. Winnewisser's group at Universität zu

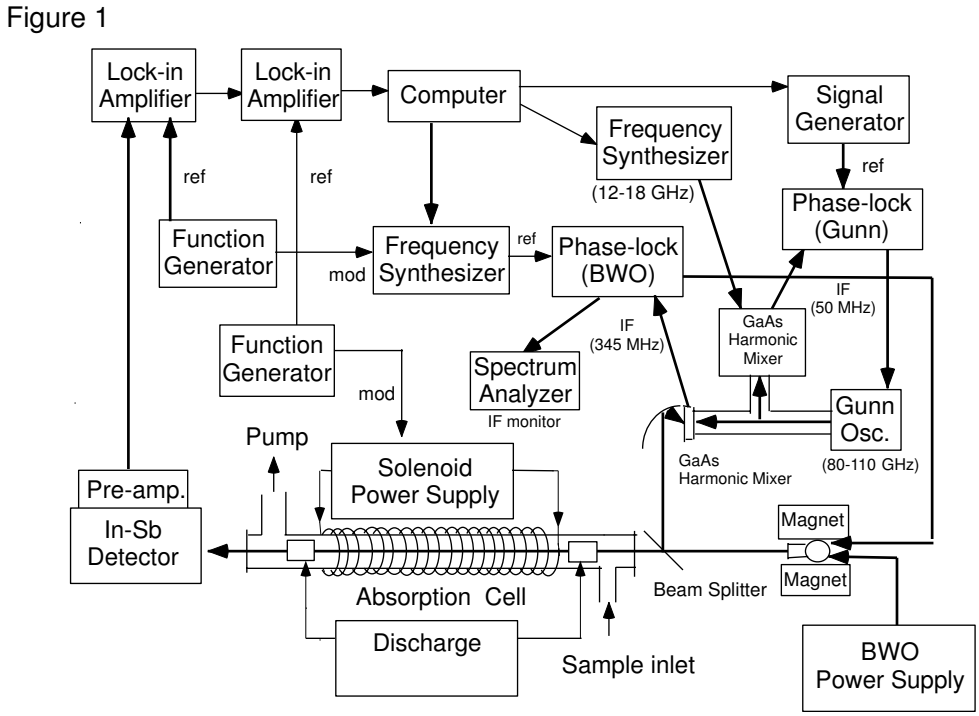

Figure 4.28 A schematic diagram of a double modulation submillimeter-wave system at Ibaraki University.

Köln. The Gunn frequency is stabilized to a harmonics of the microwave frequency(12-18 GHz) generated by a microwave synthesizer.

The submillimeter-wave output is focused by a Teflon lens to make it a parallel beam to direct through the absorption cell. A part of the power is directed to a GaAs mixer by a wire grid beam splitter. The frequency region of 380-850 GHz can be covered with three BWOs. The output power is typically a few milliwatts but it varies greatly over its frequency range. The spectrometer functions very well to the level that we initially aimed at. The submillimeter-wave lines of HO_2 was systematically measured in the range of 400-680GHz. Although the majority of transition frequencies listed in the JPL Catalog agree reasonably well with our measurements, several cases of uncomfortable discrepancy were encountered.

4.5.3 Available Molecular Parameters up to Present

Table 4.5 shows the pressure broadening parameters, γ_0, and its temperature exponent, n, defined as $\gamma(\mathrm{T}) = \gamma_0 \times (\frac{\mathrm{T}}{\mathrm{T}_0})^n$. An example of the line profile of BrO is shown in Figure 4.29. It is almost impossible to fit each hyperfine component separately to a Voigt line profile. To alleviate this difficulty a convolution method proposed by Pickett has been adopted. The pressure broadening parameters thus determined are indicated in the table in boldface. The JPL group has also been performed similar measurements. Their results are compared also in the table. The spectroscopy group of Sciences and Technologies University of Lille has recently reported the pressure broadening parameters of submillimeter-wave transitions of O_3 and BrO. We included their values also in the table. Other parameters in the table were taken from original papers, Aura reports, or HITRAN database. These values should be critically evaluated.

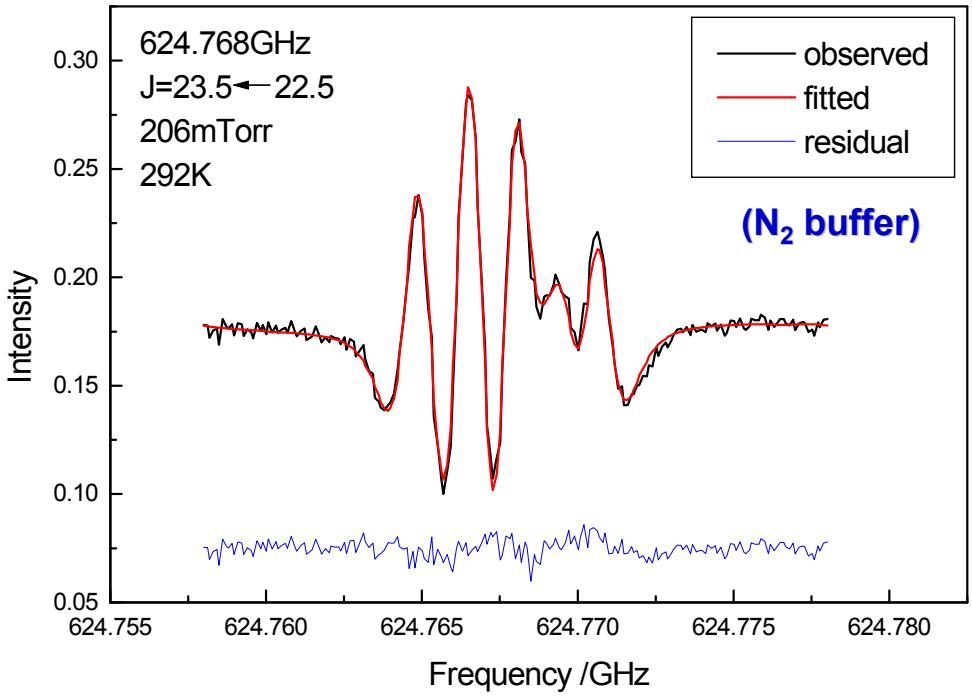

Figure 4.29 A least square fitting of the BrO spectrum to derive the pressure broadening parameter

Table 4.5 Pressure broadening parameters

molecule	frequency [GHz]	γ_0 [MHz/Torr]	n (T_0=294 K)	reference
HNO_3	181.5496	4.362	0.75	1
	369.258	4.16	0.70	2
	624.48	4.339	0.75	3
	624.78	4.339	0.75	3
	650.28	4.339	0.75	3
CH_3CN	624.8			
^{79}BrO	499.6	3.54(28)	0.45(18)	4
^{81}BrO	624.768	**3.01 (10)**		5
	624.768	3.11 (16)	0.66(3)	9
	650.179	**3.03 (10)**		5
	650.179	3.03 (15)	0.56(3)	9
$H^{37}Cl$	624.98	3.51	0.69	3
$H^{35}Cl$	625.9188	3.48	0.74	1
H_2O_2	625.04	3.944	0.50	3
	IR	3.94		6
$HO^{35}Cl$	625.075	2.37	0.5	7
HO_2	641.643	3.16	0.67	3
	641.643	**3.70 (5)**		5
	649.702	**3.37 (11)**		5
	649.702	3.71 (22)	0.2	9
ClO	649.4512	2.81(8)	0.85(9)	8
O_3	206.1320	2.890	0.75	1
	498.7	2.859(11)	0.740(24)	4
	500.4	2.798(57)	0.876(80)	4
	501.8	2.785(28)	0.784(62)	4
^{18}OOO	625.370	2.789	0.76	3
	650.011	2.777	0.76	3

[1]Aura report
[2]T. Goyette, W. Guo, F.C.Delucia, and P. Helminger,
J. Quant. Spectrosc. Radiat. Transfer **46**, 293 (1991)
[3]Hitran 96 database
[4]M. Birk, G. Wagner *et al. Study on a spectroscopic database for millimeter and submillimeter wavelength*, Final report
[5]This work, measured by M. Yamada, M. Kobayashi, H. Habara,
and T. Amano at Ibaraki Univ.
[6]V. Malathy Devi, C.P.Rinsland, M.A.H.Smith, D.Ch.Benner,
and B.Fridovitch, Appl. Opt. **25**, 1844 (1986)
[7]HITRAN default value
[8]J.J.Oh and E.A.Cohen, J. Quant. Spectrosc. Radiat. Transfer **52**, 151 (1994)
[9]E.A.Cohen et al. preliminary results, private communication

4.5.4 Plans for Further Improvement of Data

Preliminary results of the temperature dependence of the pressure broadening parameters for BrO and HO_2 molecules have been obtained. Monitoring the atmospheric abundances

of the minor isotopic species of O_3 is a major scientific objective of the SMILES mission. However, spectroscopic data of the minor isotopic species of O_3 are sparse. Therefore, systematic measurements of these species should be undertaken. The pressure broadening parameters for HCl and HOCl also seems unsatisfactory. The pressure broadening parameters are prone to systematic errors. Coordinated arrangements to critically check data obtained at different institutions are highly desirable.

A remaining problem is to experimentally establish the transition intensity. To derive the precise intensity, the dipole moment should be known. A most commonly used and best established method to obtain dipole moments is Stark effect measurements. For stable molecules such as O_3 and HCl, the dipole moments are obtained precisely. However, it is not always the case for unstable molecules. The dipole moments for HO_2 and BrO are known for quite some time. It is, however, imperative to check them again, because those Stark effect measurements had been performed at a rather early stage of microwave spectroscopy and have not been checked ever since.

References

Anderson, G. P., and S. A. Clough and F. X.Kneizys, and E. P. Shettle, AFGL atmospheric constituents (1-120 km), *Tech. Rep., Nr. TR-86-0110*, 1986.

Brown, L. R., C. B. Framer, C. P. Rinsl, and R. A. Toth., Molecular line parameters for the atmospheric molecule trace spectroscopy experiment, *Appl. Optics, 26*,5154, 1987.

Bühler, S., A. von Engeln, and K. Künzi and B.-M. Sinnhuber, J. Urban, R. Siddans, B. J. Kerridge, W. J. Reburn, R. Peter and K. Arzner The Retrieval of Data from Sub–Millimeter Limb Sounding, Final Report, *Contract No 11979/97/NL/CN*, Noordwijk, February, 1999.

Carlotti, M., B. Carli and M. Ridolfi, Derivation of temperature and pressure from submillimetric limb observations, *ESTEC, Contract No 10306/93/NL/CN*, Final Report, December, 1994.

Chance, K., K. W. Juckes, D. G. Johnson, and W. A. Traub. The Smithsonian Astrophysical Observatory Database SAO92, *J. Quant. Spectrosc. Radia. Transfer, 52*, 447, 1994.

Chandrasekhar, S., *Radiative transfer*, Dover Publications Inc., 393p, New York, 1960.

von Engeln, A., S. Bühler, J. Langen, T. Wehr, and K. Künzi, Retrieval of upper stratospheric and mesospheric temperature profiles from Millimeter-Wave Atmospheric Sounder data, *J. Geophys. Res.*, Volume *103*, pp. 31735-31748, 1998.

von Engeln, A., Satellite based Temperature Profile Determination using Microwave and Radio Occultation Instruments, *PhD. Thesis*, University of Bremen, Germany, Logos Verlag Berlin, 2000, ISBN 3-89722-453-4, ISSN 1615-6862.

Eriksson, P., F. Merino, D. Murtagh, P. Baron, and P. Richau and d. l. Noe, Studies for the Odin sub-millimetre radiometer: 1. Radiative transfer and instrument simulation, To appear in *Canadian Journal of Physics*, 2001.

Husson, N., B. Bonnet, N. A. Scott, and A. Chedin. Management and study of spectroscopic information: GEISA peogram, *J. Quant. Spectrosc. Radia. Transfer, 48*, 509, 1992.

Husson, N., B. Bonnet, N. A. Scott, A. Chedin, A. A. Churisn, V. F. Golovko, and V. G. Tyuterev. The GEISA data bank in 1993: A PC/AT compatible computers' new version, *J. Quant. Spectrosc. Radia. Transfer, 52*, 425, 1994.

Liebe, H. J, MPM - An atmospheric millimeter-wave propagation model. *Int. J. Infrared Millimeter Waves, 10*, 631-650, 1989.

Liebe, H. J, G.A.Hufford, and M.G.Cotton, Propagation modeling of moist air and suspended water/ice particles at frequencies below 1000 GHz. *in 52nd Specialists' Meeting of the Electromagnetic Wave Propagation Panel*, AGARD, Palma De Mallorca, Spain, 1993.

Livesey, N.J., J.W. Waters, R. Khosravi, G.P. Brasseur, G.S. Tyndall, W.G. Read, Stratospheric CH3CN from the UARS Microwave Limb Sounder, *Geophys. Res. Lett. 28,* 779-782, 2001.

Müller, H. S. P., S. Thorwirth, D. A. Roth, and G. Winnewiser., The Cologne Database for Molecular Spectroscopy, http://www.ph1.uni-koeln.de/vorhersagen/.

Ochiai, S., MAES, in the proceedings of the forward model workshop, Bremen, Apr., 1999.

Pickett, H. M., R. L. Poynter, and E. A. Cohen. JPL Molecular Spectroscopy,

http://spec.jpl.nasa.gov/.

Poynter, R. L. and H. M. Pickett. Submillimeter, millimeter and microwave spectral line catalog, *Appl. Opt., 24*, 2235, 1985.

Reburn, W. J., R. Siddans, B. J. Kerridge, S. Buehler, A. von Engeln, P. Eriksson, T. Kuhn, K. Kunzi, and C. Verdes, Critical Assesments in Millimetre-Wave Atmospheric Limb Sounding, *ESTEC Contract No.: 13348/98/NL/GD, Final Report, September*, 2000.

Rodgers, C. D., Retrieval of atmospheric temperature and composition from remote measurements of thermal radiation, *Rev. Geophys. and Space. Phys.,14*, 609-624, 1976.

Rodgers, C. D., Charactrization and error analysis of profiles retrieved from remote sensing measurements, *J. Geophys. Res., 95* (D5), 5587-5595, 1990.

Rodgers, C. D., *Inverse Methods for Atmospheric Sounding: Theory and Practise*, World Scientific Publ., Series on Atmospheric, Oceanic and Planetary Physics, 2000.

Rosenkranz, P. W., Water Vapor Microwave Continuum Absorption: A Comparison of Measurements and Models, *Radio Science, 33*, 919–928,1998.

Rothman, L. S., R. R. Gamache, A. Goldman, L. R. Brown, L. A. Toth, H. M. Pickett, R. L. Poynter, J-M.Flaud, and C. Camy-Peyret., The HITRAN database: 1986 edition, *Appl. Opt., 26*, 4058, 1987.

Rothman, L. S., R. R. Gamache, R. H. Tipping, M. A. H. Smith, D. Ch. Benner, V. Malathy Devi, J.-M. Flaud, C. Camy-Pyret, A. Perrin, A. Goldman, S. T. Massie, l. R. Brown, and R. A. Toth., The HITRAN molecular database: editions of 1991 and 1992, *J. Quant. Spectrosc. Radia. Transfer, 48*, 469, 1992.

Rothman, L. S., C. P. Rinsland, A. Goldman, S. T. Massie, D. P. Edwards, J.-M. Flaud, A. Perrin, V. Dana, J.-Y. Mandin, J. Schroeder, A. McCann, R. R. Gamache, R. B. Wattson, K. Yoshino, K. Chance, K. Jucks, L. R. Brown, V. Nemtchinov, and P. Varanasi., The HITRAN spectroscpic database and HAWKS (HITRAN Workstation): 1996 edition, *J. Quant. Spectrosc. Radia. Transfer*, 1996.

Verdes, C., S. Bühler, A. von Engeln, P. Eriksson, T. Kuhn, K. Künzi, The Retrieval of Data from Sub-Millimetre Limb Sounding, Part 1, *ESTEC Contract No.: 11979/97/NL/CN*, Final Report, September, 2000.

Wehr, T., S. A. Bühler, A. von Engeln, K. Künzi, and J. Langen Retrieval of Stratospheric Temperatures from Space Borne Microwave Limb Sounding Measurements *J. Geophys. Res., 103*, 25997-26006,1998.

5 Ground Data System

5.1 Objectives of JEM/SMILES Ground Data System

JEM/SMILES Ground Data System must have the following functions as similar to other ground data systems for earth observing satellites.

- Operation Planning
- Commanding
- Housekeeping Telemetry data watching
- Data processing, archiving and distribution
- Observation prediction and planning (for validation experiments)

The first two functions will have to be developed in close connection with JEM Operation System. The later two functions will be developed independently of JEM Operation System. The goal of SMILES Ground Data System is to support SMILES operation flawlessly, and to provide scientifically good SMILES data to users. Following requirements will be necessary to proceed to this goal within the limited SMILES experiment period.

- Extensive effort to improve data quality of SMILES product through data quality check, algorithm development and validation.
- Processing power enough to re-process and to improve data set quality until broad scientific acceptance.
- Seamless data distribution to potential data users.

It is assumed that the SMILES operation extends only one year (and may be extended up to two years). Thus, those efforts should be focused on at (and prior to) SMILES operation. If there will be 3 major version up during 12 months, the required processing power must be much higher than the equilibrium processing speed, which means data is processed just as much as downlinked.

SMILES data will be distributed in L1, L2, and L3 format. Table 5.1 lists characteristics and volume of these data sets. Typical scientific users will require daily gridded L3 data. Several users will compare their own observed data to SMILES L2 vertical profile data. Several higher, so-called L4, data sets, such as monthly mean data will be processed as a part of standard products. Data distribution policy of SMILES is as open as possible, similar to recent other earth observation programs of NASDA and other space agencies. Distribution of L0 and L1 data might be limited to the groups having agreement with NASDA, due to huge data volume (and limited SMILES program budget).

5.2 JEM Operation System

Figure 5.1 shows an overview of JEM Operation System and its interface to JEM experiment users. JEM Operation System will be responsible to (1) Mission Data Interface, (2) Data Management, (3) Operation Planning, (4) Commanding, and (5) House Keeping Telemetry Data Checking. These functions and its relation to JEM users, such as SMILES team, will be specified in the "Mission Operation Interface Specification (MOIS)" document.

JEM Operation System at Tsukuba Space Center (TKSC) will receive downlinked data and archive all raw data. JEM Operation System will handle mission data interface

Table 5.1 SMILES data sets

Data Type	Description	Potential Users	Volume/year	Distribution
Raw	Unedited Binary Packets	inhouse	120 kbps 1.24 GB/day 317 GB/year	NA
L0	edited engineering data file	instrument team	20 MB/file 1.24 GB/day 317 B/year	tape etc.
L1	calibrated physical data file spectral brightness temperature (K)	retrieval	2.48 GB/day 634 GB/year	tape etc.
L2	vertical profile of species ppmv or cm^{-3}	validation	2.82 MB/day/species 56.4 MB/day 14.1 GB/year	internet DVD/ROM
L3	grid data of species ppmv or cm^{-3}	general	2-3 MB/day/species 40-60 MB/day 14-20 GB/year	internet DVD/ROM

to SMILES team. SMILES house keeping telemetry data and command plan by SMILES team will be checked in detail by JEM Experiments Operation Support Client and/or user system connected to the External User Interface.

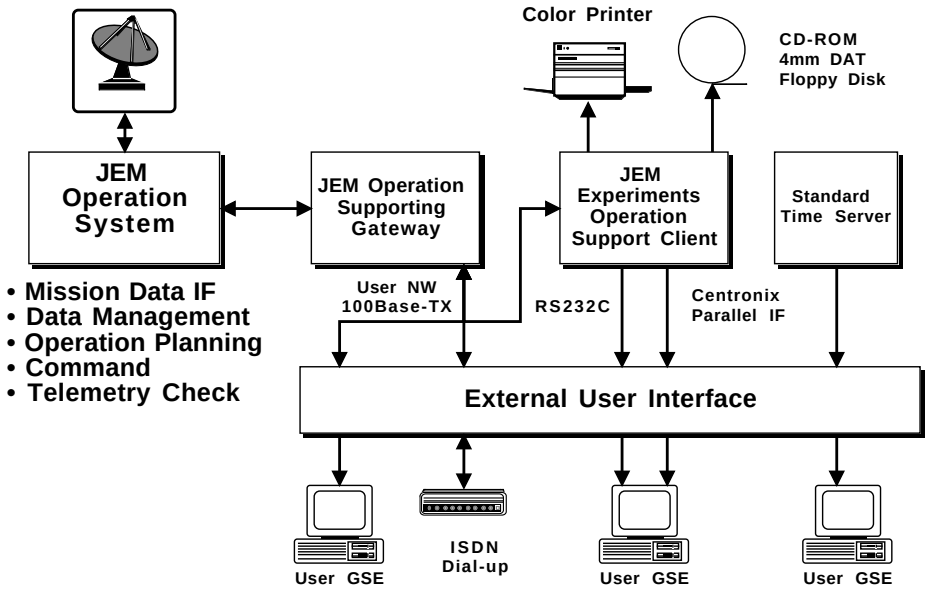

Figure 5.1 JEM Operation System and its relation to JEM Experiment users.

5.2.1 Operation Planning

JEM Operation System will arrange an operation plan of JEM and JEM experiments including SMILES, considering (1) request from experiments, (2) resource limitation, such

as power, downlink capacity, zero gravity condition, astronauts man power, etc, and (3) limitation from space station. Outline of this operation plan will be pre-determined before the launch of SMILES in the MOIS and the "Mission Operation Implementation Plan (MOIP)" document. But, details of operation will be revised monthly, weekly, and daily basis, since the operation of SMILES, JEM, and ISS will be interfered by reasons such as docking of the Space Shuttle. Figure 5.2 shows a concept of the operation planning for JEM.

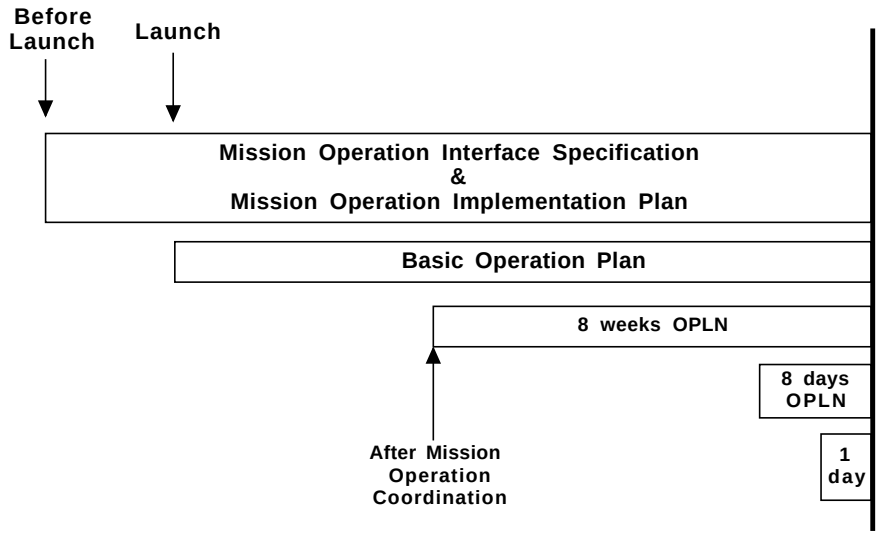

Figure 5.2 Concept of operation planning for JEM.

5.2.2 Commanding

JEM Operation System will send command sequence to JEM experiments based upon the decided JEM operation. This command sequence should be checked carefully everytime, whether it is not violating commanding rules for all other experiments on JEM, and ISS. Details of commanding will be described in the "Spacecraft Orbital Operation Handbook (SOOH)". The SOOH covers background of sensor design in addition to the details of commanding rules, housekeeping data and trouble shooting.

5.2.3 House Keeping Telemetry Data Checking

JEM Operation System will receive, archive and real-time check house keeping (HK) telemetry data, and analyze their trend. JEM Operation System will not check instrument information contained within SMILES mission data. SMILES will have a limited autonomous function, such as system abortion at cooler failure. Other anomalies will be handled by the operator at JEM Operation System based upon the SMILES SOOH.

5.3 Functions and Data Flow between ISS and SMILES ground data system

Fig 5.3 shows overall data flow of JEM/SMILES mission. Data acquired by SMILES will be multiplexed with data of other experiments of JEM. The multiplexed data will be downlinked from International Space Station (ISS) through geostationary data relay satellites to ground receiving stations. The multiplexed downlinked data are processed at JEM Operation Center at NASDA/TKSC, to RAW data of each JEM experiments. The SMILES RAW data will be provided to SMILES Ground Data System. Data transmission through these data relay system should be carried out without data loss against continuous operation of SMILES.

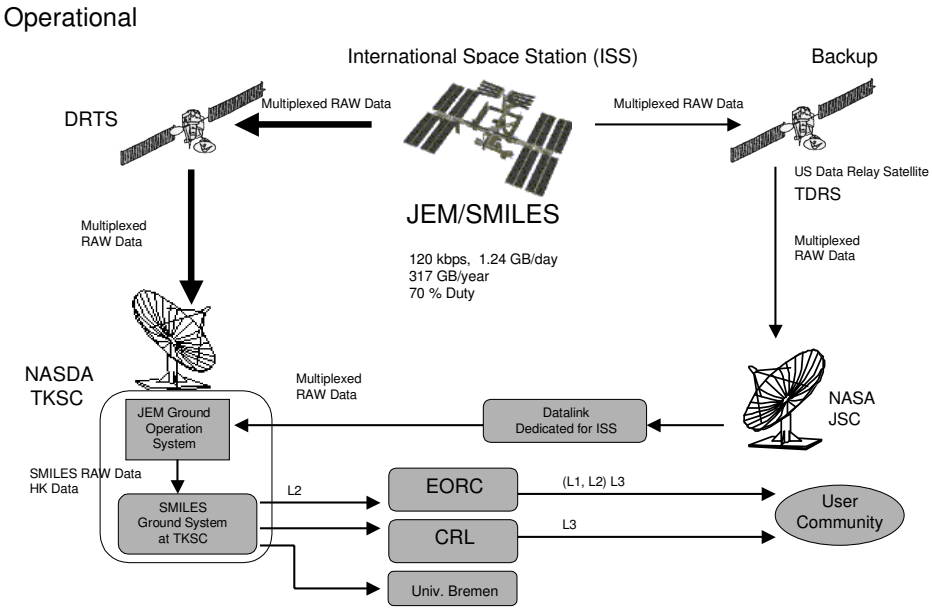

Figure 5.3 SMILES data flow.

5.3.1 JEM/SMILES to Receiving Stations

SMILES RAW data consists of HK data (House Keeping data, 16 kbps) and SMILES Mission Data (about 120 kbps). SMILES Mission Data (and HK data) will use CCSDS ver 1 packet format. The SMILES RAW data will be multiplexed with data of other instruments/experiments of JEM. The multiplexed JEM data will be downlinked immediately when data relay satellites are available. When data relay satellites are not available, the multiplexed data are stored in JEM common data storage, which can store data up to 60 minutes. Two data relay satellites are planned for downlink of JEM, primarily Japanese DRTS will be utilized, and US's TDRS will be utilized as an option. The DRTS

will then downlink to NASDA/TKSC in Tsukuba/Japan, and the TDRS will downlink to NASA/JSC in Houston/USA.

5.3.2 Receiving Stations to JEM Operation System at NASDA/TKSC

The downlinked data at JSC will be transferred to JEM Operation System through a data communication line dedicated to the JEM operation. All downlinked data will be collected and archived at JEM Operation System. Archiving of SMILES mission data (120 kbps) in JEM/OS will be tentative, and SMILES ground segment will have responsibility of archiving of SMILES data.

5.3.3 JEM Operation Center to SMILES Ground Data System

JEM RAW data collected at JEM Operation Center are processed and edited to RAW data of each JEM experiments. Following description on data handshake between the JEM Operation System and the SMILES Ground Data System (see Figure 5.4) are still TBD.

TBD number of CCSDS packets of SMILES RAW data are gathered to make a SMILES RAW data file in JEM Operation Center. The SMILES RAW data file is edited as first in and first out (FIFO) rule at JEM Operation Center, and there will be no further editing of CCSDS packets, such as sorting packets for observation time and deleting duplexed packets. The SMILES RAW data files will be stored as computer data files in a data distribution system of JEM Operation Center.

JEM Operation Center will send a data ready signal as an e-mail to SMILES Ground Data System and SMILES RAW data files are ready for data transaction. SMILES Ground Data System will make an ftp transaction to acquire a SMILES RAW data file from the data distribution system of JEM Operation Center. After successful ftp transaction, SMILES Ground Data System will send a data acquisition signal as an e-mail to JEM Operation Center. SMILES Ground Data System will check the acquired SMILES RAW data file, whether it was generated and transferred properly. SMILES Ground Data System will send a data certification signal as an e-mail to JEM Operation Center. JEM Operation Center will delete the JEM RAW data file in the data distribution system, after TBD days of the receiving of data certification signal.

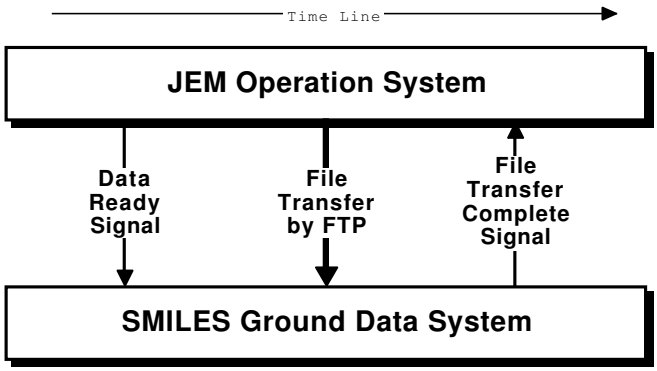

Figure 5.4 Data handshaking between JEM Operation System and SMILES Ground System.

5.4 Functions of SMILES Ground Data System

SMILES Ground Data System will be established at NASDA/TKSC (TBD). Currently three groups, NASDA/TKSC SMILES Mission Team, CRL, and NASDA/EORC are responsible for the development of SMILES Ground Data System. By considering physical contact with JEM Operation System, SMILES Ground Data System should be established at NASDA/TKSC. SMILES Ground Data System will have following functions: (1) operation planning, (2) commanding, (3) House Keeping telemetry data watching, (4) data processing, archiving, and distribution and (5) observation prediction and planning (for validation experiments).

Operation Planning and Commanding

Operation of SMILES will be categorized into the following three, (1) Initial check-out period operation, (2) Instrument Performance Check operation and (3) Normal Observation operation. Operation plan will be decided by SMILES mission team to fulfill the mission success criteria of SMILES program. Operation plans are examined by SMILES mission team members and possibly by SMILES operation simulator program (TBD). Command sequences are then decided and send to JEM Operation System, but they might be revised or interfered by conditions of SMILES, JEM, ISS and ground segment, until actual real-time operation of SMILES.

House Keeping telemetry data watching

SMILES Ground Data System will have full house keeping capability of SMILES (, JEM and ISS, if necessary). JEM Operation System will watch only alert condition of SMILES. JEM Ground Data System will make caution signal when any status of HK and/or mission data of SMILES reach caution level or show abnormal trend. SMILES Ground Data System will analyze statistical feature and trend of SMILES instrument status.

Data processing, archiving, and distribution

• SMILES RAW Data Processing

SMILES RAW data files will be acquired and processed by SMILES RAW Data Processor within SMILES TKSC Data System. SMILES RAW Data Processor will have a dedicated and isolated ethernet connection with JEM Operation Center. SMILES RAW Data Processor will make data transactions with JEM Operation Center only through this ethernet connection. SMILES RAW Data Processor temporarily stores SMILES RAW data files until TBD days after successful Level 0 (L0) data production.

If RAW Data transaction and other RAW data processing are not successful, SMILES RAW Data Processor will alarm to some of SMILES mission team members through e-mail and/or SMILES Mission Management Operation System. All log of transactions and other events of SMILES RAW Data Processor will be stored in one (or multiple) text format file(s). The log must contain at least following information; time-date of log creation, name of RAW data file, time-date of RAW data file creation, beginning and end of time-date of receiving within a RAW data file, and a status flag. The log file(s) will consist of text lines separated by a delimiter of Operating System, and a full set of records of transaction must have been written in a single text line, not in multiple text lines. The records in one text line must be organized, as any information column can be a key of sorting and/or filtering of commands of Operating System.

• L0 Data Production Processing

The RAW data in the CCSDS packet format will be depacketed and converted into the L0 data arranged in a time series after quality estimation. Continuity and flawlessness will be checked and information for data loss will be recorded. There may also be overlaps to be removed, which can be created when the data transfer via satellite is suspended. The data obtained during a quarter of an orbit operation will be edited into one file. The

content of L0 data is the SMILES observation and the instrument HK data in addition to information about time and date.
• L1 Data Production Processing
The L0 data will be converted into engineering values and processed into calibrated limb spectral radiances by using the calibration data. Anomalous data will be checked and marked before processing. The ancillary data such as the tangent altitude and the position of the observation will be created and added as a part of L1 data products.
• L2 Data Production Processing
The height profiles of geophysical quantities such as composition and temperature and their errors are retrieved from the SMILES L1 data using the optimal estimation method. The data volume is estimated to be 2.82 MB/day/species. The L2 data processing will be performed in NADA/EORC, CRL and University of Bremen, independently.
• L3 Data Production Processing
The gridded daily, weekly and monthly maps for all species will be produced in CRL, NASDA/EORC and University of Bremen, respectively. The SMILES data will be archived and distributed in L1, L2 and L3 format though the distribution of L0 and L1 data might be limited to those having agreement with NASDA or CRL due to huge data volume. There remains a security issue, but users can access SMILES L2 and L3 data products created at CRL, NASDA/EORC and University of Bremen through internet. The data stored in DVD/ROMs will also be distributed to users.
Observation prediction and planning
Since the SMILES data products must be verified through validation activities, timely and accurate announcement of near future SMILES observation is crucial for good coincidence of validation measurements. Orbit characteristics, especially attitude of ISS, will change and fluctuate even few days after the observation prediction. Thus, observation prediction must be updated frequently, perhaps daily.

5.5 Consideration on Computation in the JEM/SMILES L2 Data Processing

The task of the SMILES L2 data processing algorithm is to produce the geophysical parameters such as concentration profiles of targeted gases, temperature and pressure from measured radiance. As described in the previous chapter, the retrieval method adopted in the SMILES data simulator is Optimal Estimation Method (OEM) [*Rodgers*, 1976]. We believe this retrieval strategy for SMILES is similar to the past and the near future millimeter and sub-millimeter limb-sounding programs [*Levesey and Wu*, 1999], and it is, thus, well established already. In the following, we briefly discuss the performance requirements for the SMILES L2 data processing.

The computational efficiency is determined by both the number of matrix operations and the numerical cost for updating an expected measurement and a weighting function. In the forward model, an efficient method for calculating the Voigt function is required. For this purpose we use Hui 's rational approximation [*Hui et al.*, 1978][*Suzuki*, 1994]. The test result of forward model calculation (brightness temperature) for 61 rays is currently 77 sec (10 to 60 km, 1 km tangent height interval, using 400 MHz Pentium-III). It looks easy to improve computation speed to achieve requirements for operational condition, such as better than 10 sec, by using faster CPU. If these methods for fast computation of Voigt function are not acceptable in speed, table interpolation using such B-spline method in pressure and temperature will be applied as similar to the systems of ADEOS/ILAS or ADEOS/IMG.

Let us turn our attention to the matrix operations. Let the size of the state vector be

$n \sim 150$ which may be typical for the simplest retrieval including the baseline parameters. The measurement vector is a set of observed radiance at scanned tangent altitudes. Since the SMILES limb scan will be done by taking spectral data from 10 to 60 km in the interval of ~ 2 km, the size of the measurement vector m becomes 26 times the number of selected frequency data from AOS's 1500 channels for a 1.2 GHz band. If $30 \sim 1500$ frequency data are used in retrieval, the dimension of the weighting function matrix becomes $(7.8 \times 10^2) \times 150 \sim (3.9 \times 10^4) \times 150$. As is easily seen from (4.14) in Chapter 4, the number of floating point operations per iteration in the case of $m > n$ is estimated as $\sim (mn^2 + n^3)$, where it is assumed that the error covariance matrix is diagonal and $\mathbf{S}_a^{-1}$ is prepared in advance. Note that mn^2 corresponds to the operation $\mathbf{K}^T\mathbf{S}_\epsilon^{-1}\mathbf{K}$ while n^3 comes from the inversion of the Hessian. Then the number of operations needed to perform a retrieval turns out to be $2.1 \times 10^7 - 8.8 \times 10^8$, which corresponds to execution time, $0.02 - 0.88$ sec, on a 1 Gflops/sec computer in an ideal situation. If a couple of species or more have to be solved together, the execution time increases mainly according to $\sim mn^2$. For example, for an extreme case $n = 1000$ and $m = 1500$, the execution time becomes 40 sec times the number of iteration and the weighting function occupies 0.3 GB. Nevertheless OEM still seems to work as an efficient retrieval algorithm.

Table 5.2 Estimated performance requirements (GFlops and memory size) for SMILES Data System compared to those of EOS/MLS program.

	JEM/SMILES	EOS/MLS
L0 Processing	Desktop WS Performance 8 GB Disk and network I/O limited	Desktop WS Performance 8 GB Disk and network I/O limited
L1 Processing	Desktop WS Performance 8 GB Disk and network I/O limited	Desktop WS Performance 8 GB Disk and network I/O limited
L2 Processing	4 GFlops (peak performance) 20 GFlops (with a margin for reprocessing) > 32 GB Computation limited	1 GFlops (true performance) > 16 GB Computation limited

The detail design of SMILES Data Processing is not specified yet. As described above, the most computing intensive part of SMILES retrieval will require 1 GFlops, 'net' performance. Actual data processing will require 5-6 times performance for re-processing after version ups etc. One GFlops net performance should be measured by Linpack 100 benchmark since the nature of SMILES retrieval scheme. One GFlops net performance is usually equal to 3-4 GFlops peak performance. See Table 5.2. Overall computation requirement is very feasible even from today's standard, and it will not be expensive at the time of SMILES operation. Data archiving and distribution look quite feasible, since the data volume of SMILES is moderate. Data retrieval scheme for the sub-millimeter limb sounder has been already established for other space programs, and thus we see no difficulty on development of SMILES data retrieval system.

References

Hui, A. K., B. H. Armstrong, and A. A. Wray, *J. Quant. Spectrosc. Radia. Transfer, 19*, 509, 1978.
Levesey N. J., and D. L. Wu, EOS MLS Retrieval Processes Algorithm Theoretical Basis, *Jet*

Propulsion Laboratory Document D-16159, Version 1.1, 15 October 1999.

Rodgers, C. D., Retrieval of atmospheric temperature and composition from remote measurements of thermal radiation, *Rev. Geophys. and Space. Phys., 14*, 609-624, 1976.

Suzuki, M., Comparison of the fast calculation codes for Voigt function, *CGER'S Supercomputer Activity Report 1992*, 71-75, 1994.

6 Validation Plan

6.1 Introduction

It is well known that satellite borne observation is very useful for getting information in global scale. The data products derived from these measurements might have literally the same quality over the globe because they are obtained with one, the same, instrument. But also well known is the importance of continuous validation of the satellite borne instrument for maintaining the quality of data through the mission lifetime.

The validation of JEM/SMILES data products should be strictly controlled following the standardized handling procedures. These procedures will be discussed and determined in their details by scientists in JEM/SMILES validation team, which is not yet officially established, and then will be approved later by the members of science team. Another important point of validation is the responsibility for each data product. A scientist on the science team who knows well of its scientific use and meanings must be responsible for the validation of each data product.

As the standardized procedure is not established, the concepts of JEM/SMILES validation as well as those of the correlative measurements are described in this section.

6.2 The Basic Concepts of Validation for JEM/SMILES Data Products

The following items should be included in the standardized procedures:

1. Sensitivity studies including the simulation study to determine the expected precision and accuracy of each data product
2. Inspection of all incoming data, and checking the reasonableness and unexpected phenomena through the examination of routine analyses products
3. Close examination of the characteristics of 'radiance residuals' as functions of many parameters for checking the artifacts
4. Comparison of the same parameter measured in more than one spectral region as possible as we can
5. Comparison with other correlative measurements from ground-based, aircraft, and balloon measurements
6. Comparison of JEM/SMILES data with data obtained by other space-borne instruments such as Aura(formerly EOS-Chem)/MLS

Each item is essential to maintain the quality of data product and will need a responsible scientist as well.

6.3 Correlative Measurement

6.3.1 The Needs of Correlative Measurements

The correlative measurements are inevitable to validate the JEM/SMILES data products. JEM/SMILES is capable of measuring many atmospheric species, exact identifications of whose species are dependent on a final specification of the instrument, though. At present, standard products for JEM/SMILES are not finally determined. Then the needs of correlative measurement are listed below for only major targeted (probable) data products, respectively.

- O_3
  Total and vertical profiles of O_3 are needed. Correlative measurements such as aircraft and balloon measurements of the vertical profile coincident with JEM/SMILES observation are very valuable.

- ClO
  Ground-based measurements of vertical profiles are needed at a various site using the millimeter-wave radiometer. Coincident measurements with JEM/SMILES should be organized. Aircraft measurements, coincident with JEM/SMILES observations are also important. Balloon-borne measurement is very useful to compare the vertical profile. Satellite-borne measurements will be comparable with JEM/SMILES product. at the JEM/SMILES era.

- HNO_3, HCl, HO_2
  Balloon measurements of the vertical profile with IR spectrometers are needed, especially coincident with JEM/SMILES observations.

- BrO
  Ground-based measurements of total column are needed. Aircraft measurements, coincident with JEM/SMILES observations, in situ, and column amount measurements are particularly valuable. Balloon-borne measurement is useful to compare the vertical profile. Satellite instruments will also be usable for validation purpose at the JEM/SMILES era.

- H_2O_2
  Any kind of measurement of atmospheric H_2O_2 is valuable.

The followings are not for data products of JEM/SMILES, but these data will also be valuable for improving the quality of data products.

1. More accurate spectral parameters for target species and H_2O in frequency region of 600 - 700 GHz: Linewidth, center frequency, line strength, air broadening coefficients, etc.

2. Atmospheric water vapor profiles in the upper troposphere and in the stratosphere

3. Temperature and pressure profiles along the JEM/SMILES observation

6.3.2 Plan of Correlative Measurements

The use of existing data (measurement network), conducting a field validation campaign, and setting a new ground-based instrument to an observation site should be considered in the planning of validation.

6.3.2.1 The Use of Existing Data

As for O_3, WMO-GAW ozonesonde stations and ground-based Dobson stations routinely make measurements of vertical profile and total column O_3. These data are available via WMO. The climatology of ozone distribution field can also be constructed based upon these data.

There is no measurement site (network) that provides the profile of other species than O_3 routinely without any special contract. However, NDSC primary and complementary

sites can provide very accurate data of some species, their total and vertical profiles including ClO. Close collaboration with NDSC sites is very valuable for getting accurate validation data.

6.3.2.2 Field Campaign

Even for the O_3, it will be hard to get coincident data with JEM/SMILES observation from routine observation. Therefore several validation (field) campaigns will be planned during the JEM/SMILES mission.

CAMPAIGN Site

In order to select the campaign site we must consider the geographical coverage of JEM/SMILES observation and the availability of balloon launching facility. In north polar region one of the candidate site will be Fairbanks in Alaska or Lynn Lake in Canada. In Fairbanks there exist ground-based instruments: Millimeter wave radiometer, FTIR, and lidar at Poker Flat (http://www.crl.go.jp /team5/index.html). These instruments are maintained with both CRL and Geophysical Institute of University of Alaska Fairbanks. So ground-based and balloon measurements can both be carried out coincident with JEM/SMILES observation. But the geographical position of Fairbanks, about 65°N, is located nearly the northern limit of observable region by JEM/SMILES. On the other hand Lynn Lake is located at around 52°N, where balloon observations were carried out by NSBF, the balloon launching team of the USA. Anyway collaboration with USA or USA/Canada must be necessary.

In mid-latitude regions several balloon observation sites will be found as a candidate site such as France, Japan, United States of America, and Australia. All of these countries have at least one balloon observation site within their home countries. The validation campaign in tropical region is also important and valuable. Christmas Island, where NASDA operates a tracking station, is one of the candidate site as well as Watukosek, Indonesia, where NASDA and LAPAN of Indonesia are conducting the ozonesonde measurement and some ground-based observations.

Balloon borne Instrument

The candidate instruments for balloon observations will be a submillimeter radiometer, FTIR, and UV-Visible spectrometer. Measurements by more than one instrument will be valuable for validation purpose. So international collaborations must be made. Daily ozonesonde measurements at campaign site during the campaign period will be the minimum requirement.

Ground-based Instrument

Millimeter radiometer, FTIR, and UV-Visible spectrometer can provide good validation data, total column amounts and profiles for some species. In Poker Flat, Alaska CRL operates, with GI/UAF, some ground-based instruments usable for validation purpose. This site is important for supplying validation data continuously. As mentioned before, close collaboration with NDSC will also play a key role to achieve a good validation result. Also important point is that NASDA should operate at least one ground-based instrument by itself for checking the quality of JEM/SMILES data constantly.

Candidate period of field campaign

In high latitude summer is good season for validation considering the stability of at-

mospheric condition. However the enhancement of ClO occurs in winter to spring season. Ozone depletion event will also be expected in winter season. As for the validation purpose, validation campaign in high latitude will be recommended to be conducted both in winter and summer seasons. In middle and low latitudes, exception of special ozonesonde campaign, one field campaign will be planned at anytime in a year.

6.3.3 Activities in JEM/SMILES Team for Validation

6.3.3.1 Development of a Balloon Borne Submillimeter Spectrometer

JEM/SMILES is one of the most advanced instrument, whose signal to noise ratio is the best among other submillimeter spectrometers of not only space borne but also ground- or air- borne ones. Therefore JEM/SMILES will show the best performance to measure some species such as ClO and BrO. This means that there is no good instrument at present to provide validation data for these species. CRL team is developing a balloon borne submillimeter spectrometer of using super conductor (SIS mixer) as a detector. This balloon borne spectrometer will demonstrate the same performance as JEM/SMILES and will be used for validation purpose for JEM/SMILES. This project of developing the balloon borne SMILES (BSMILES) will play an important role in conducting correlative measurements, because vertical profiles of ClO and other species can be measured by BSMILES with the same or better accuracy than JEM/SMILES. Key components of the BSMILES system were constructed. Performances of those are checked, and good results have been demonstrated as expected. The BSMILES is in integration phase and will be scheduled to complete its development by the end of 2002. The first balloon borne measurement of BSMILES will be carried out in 2003 from SBC (Sanriku Balloon Center of ISAS, Japan).

6.3.3.2 Laboratory Measurement of Spectroscopic Parameters

As mentioned above, spectroscopic parameters for many atmospheric species are not accurately determined or measured in the frequency range of around 600GHz. In particular an air pressure broadening parameter is one of key parameters to derive the vertical profiles of atmospheric species from limb sounding. CRL and Ibaraki University are jointly planning the laboratory measurements of spectroscopic parameters for some species. They already measured some parameters as described in section 4.4. This project of laboratory measurement will also be one of key projects in validation plan for the success of deriving good data products from JEM/SMILES observation.

6.3.3.3 Use of Observation Sites in Japan

Within Japan there exist several good observation sites maintained by University and National Institute. So not only the international collaborations but also the collaborations within Japan are also very important. NIES's group operates microwave radiometer, FTIR, and lidar at Tsukuba, Ibaraki and Rikubetu, Hokkaido. STEL of Nagoya University also maintains FTIR , UV-Visible spectrometer and ozonsonde stations at Rikubetu and Moshiri, Hokkaido. These observation sites are very suitable for validation of JEM/SMILES observation. During the mission lifetime of JEM/SMILES these sites are considered as main sites for steadily providing validation data.

6.4 Summary

Validation campaign as well as the use of existing database for O_3 will become the key for validating JEM/SMILES data. In order to get coincident data with JEM/SMILES observation, international collaborations play the key role; for example, close collaboration with NDSC. The use of observation sites in Japan maintained by the National Institute and the University will also be inevitable for getting validation data constantly. Even for getting good validation data of O_3, a kind of special ozonesonde campaign must be planned.

Ground-based instruments of CRL at Poker Flat, Alaska will provide good validation data constantly. NASDA/EORC will operate at least one ground-based instrument for checking the performance of JEM/SMILES. Balloon observation is also essential to get validation data. Close collaboration with foreign research bodies as well as with Japanese researchers must be key point to succeed the balloon campaign.

Cross validation with other space-borne instrument such as Aura/MLS would be useful.

Appendix: Estimation of Retrieval Errors for SMILES Major Species

In this Appendix, the results of error estimations are shown in detail for all the 9 molecular species to be observed by SMILES, for ozone isotopes, and for ozone, $H^{35}Cl$, and HO_2 in the mesosphere, using standard atmospheric profiles in the polar, mid-latitude, and equatorial regions.

A.1 Radical Observation

Simulations are set up as follows. The spectroscopic line parameters, such as line position and line strength, are taken from the JPL catalog, and pressure broadening parameters are given by the HITRAN catalog. The height profiles of molecular volume mixing ratios, temperature, and pressure used in the simulations are the standard profiles for the mid-latitude, equatorial, and polar regions given by the Rutherford Appleton Laboratory.

For the instrumental parameters, representative values of the SMILES instrument are used. The retrieval error in the volume mixing ratio, the error ratio defined as the ratio of the retrieval error to the *a priori* error, and the averaging kernels are calculated for each molecules in the three SMILES observation bands. The frequency grid for the forward model is 0.8 MHz, and no frequency binning is applied for the retrieval. The molecules considered in the forward model and retrieval are normal O_3, ozone isotopes, vibrationally-excited O_3, HCl, ClO, HOCl, H_2O_2, HO_2, HNO_3, BrO, and CH_3CN, as well as H_2O, N_2, and O_2. The *a priori* profiles are assumed to coincide with the true profiles for all the molecular species except ozone isotopes. The *a priori* standard deviations are assumed to be 100 percent of the *a priori* profiles for the research products and 50 percent for the standard products. The measurement error covariance matrix $\mathbf{S}_\epsilon$ is given from the measurement noise, $\sigma = (T_{sys} + T_{atm})/\sqrt{B\tau}$, where T_{sys} is the receiver system noise temperature assumed to be 500 K, and T_{atm} is the antenna temperature from the spectrum, B is the equivalent noise bandwidth assumed to be 0.8 MHz, τ is the integration time. The integration time τ is assumed to be 0.5 s for each tangent height for single-scan data, and is assumed to be 15 s for data averaged over 30 scans, which corresponds to a (day-time) half-daily zonal mean for mid-latitude regions. The limb scan step is 2 km for tangent altitudes from 8 to 60 km. The retrieval height grid is set to be 2 km and 4 km for the standard products and the research products, respectively, in the 8-60 km region.

The results are shown in the figures shown below. The single scan profiles are shown for the standard products, and the 30-scan averaged profiles, which consist of the 5°-averaged zonal mean profiles, are shown for the research products.

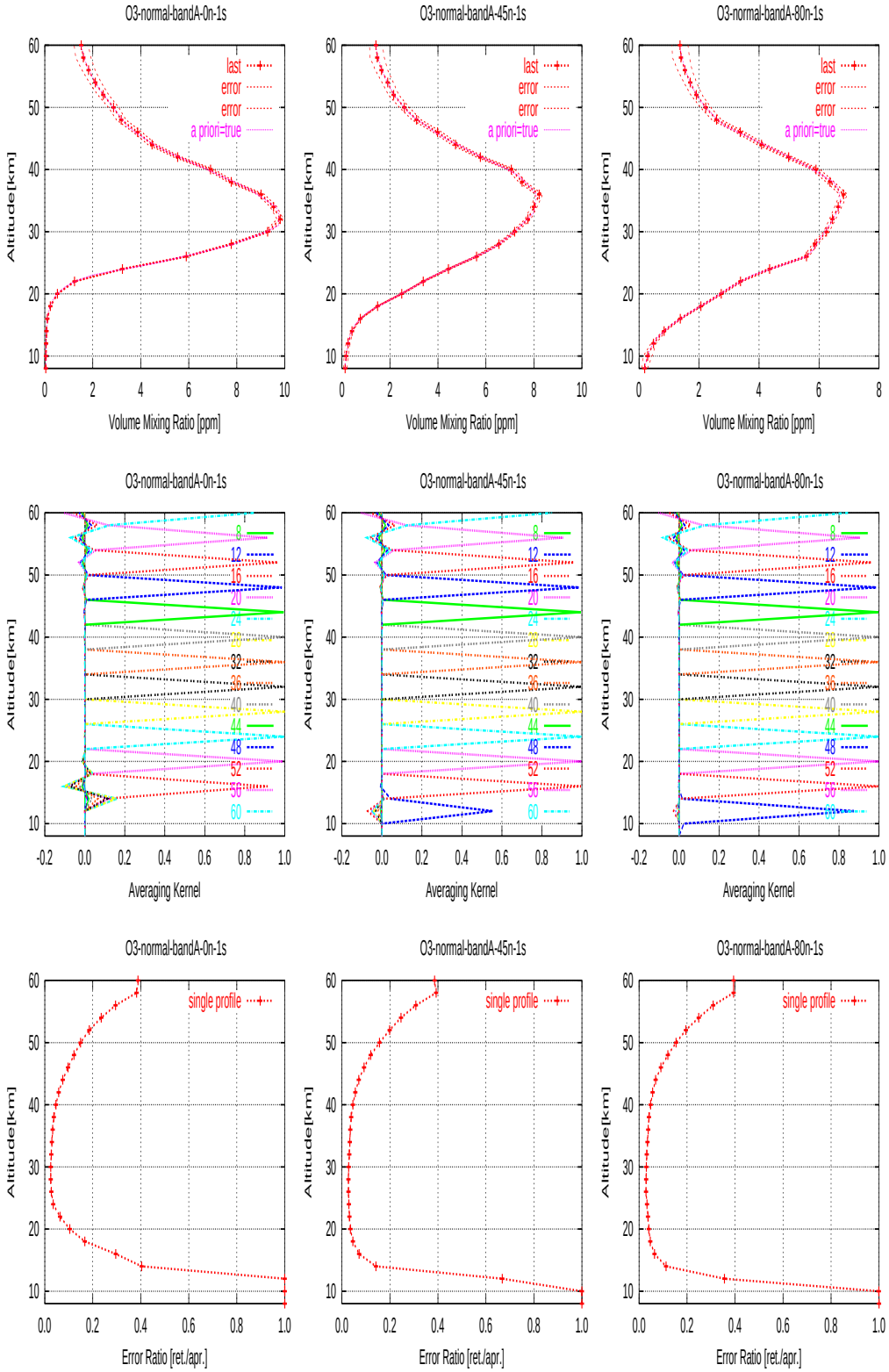

Figure A.1 Retrieval simulation results for single-scan data in BAND-A for standard profiles of normal O_3 at latitudes of 0°N (*left*), 45°N (*center*), and 80°N (*right*). *Top*: Retrieved volume mixing ratios are shown with *rms* retrieval error bounds and *a priori* profiles which are assumed to coincide with true profiles; *Middle* Averaging kernels; *Bottom*: Retrieval error ratios defined as the ratio of the retrieval errors to the *a priori* errors which are assumed to be 50 % of the *a priori* volume mixing ratios.

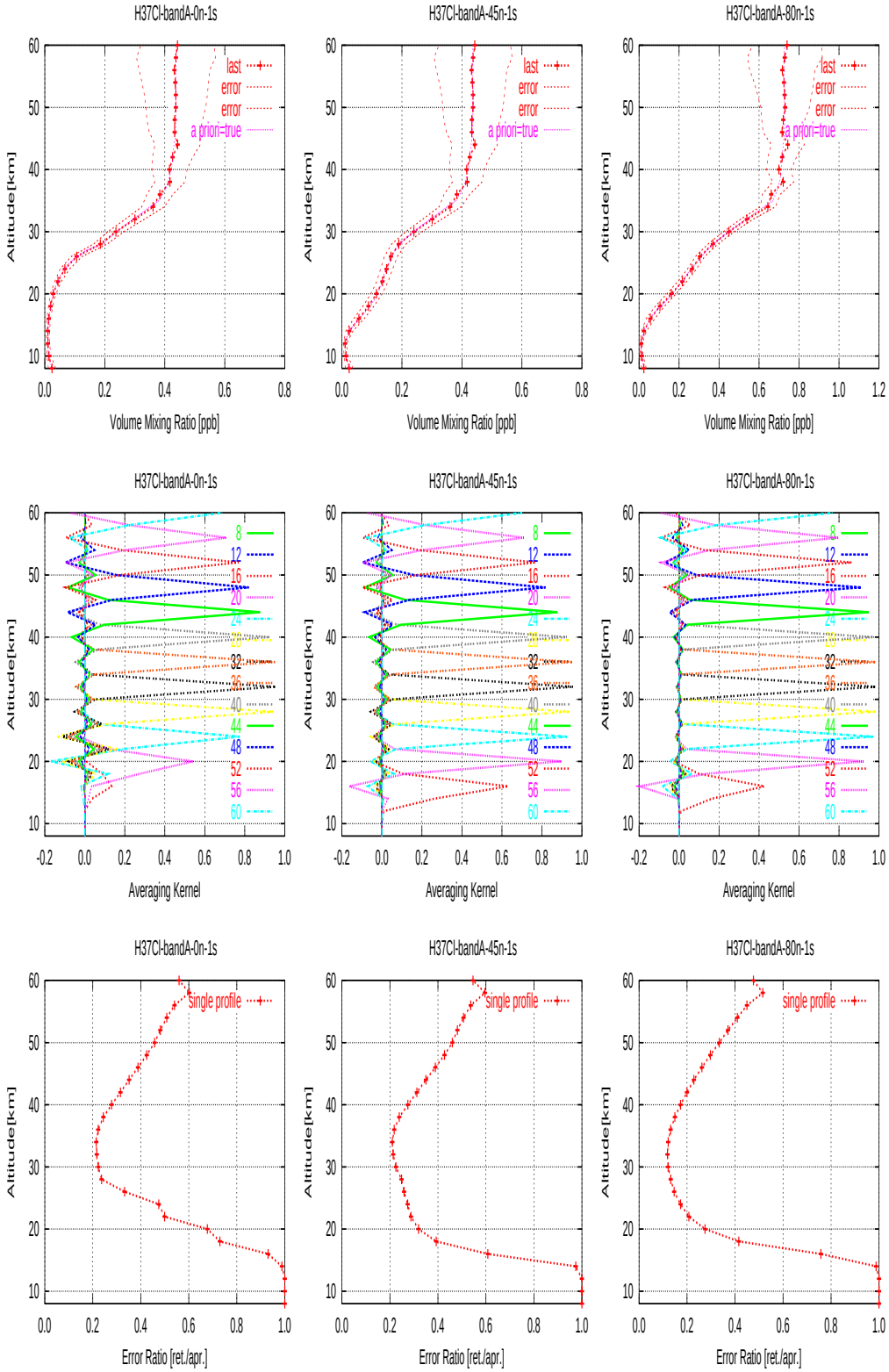

Figure A.2 Retrieval simulation results for single-scan data in BAND-A for standard profiles of $H^{37}Cl$ at latitudes of 0°N (*left*), 45°N (*center*), and 80°N (*right*). *Top*: Retrieved volume mixing ratios are shown with *rms* retrieval error bounds and *a priori* profiles which are assumed to coincide with true profiles; *Middle* Averaging kernels; *Bottom*: Retrieval error ratios defined as the ratio of the retrieval errors to the *a priori* errors which are assumed to be 50 % of the *a priori* volume mixing ratios.

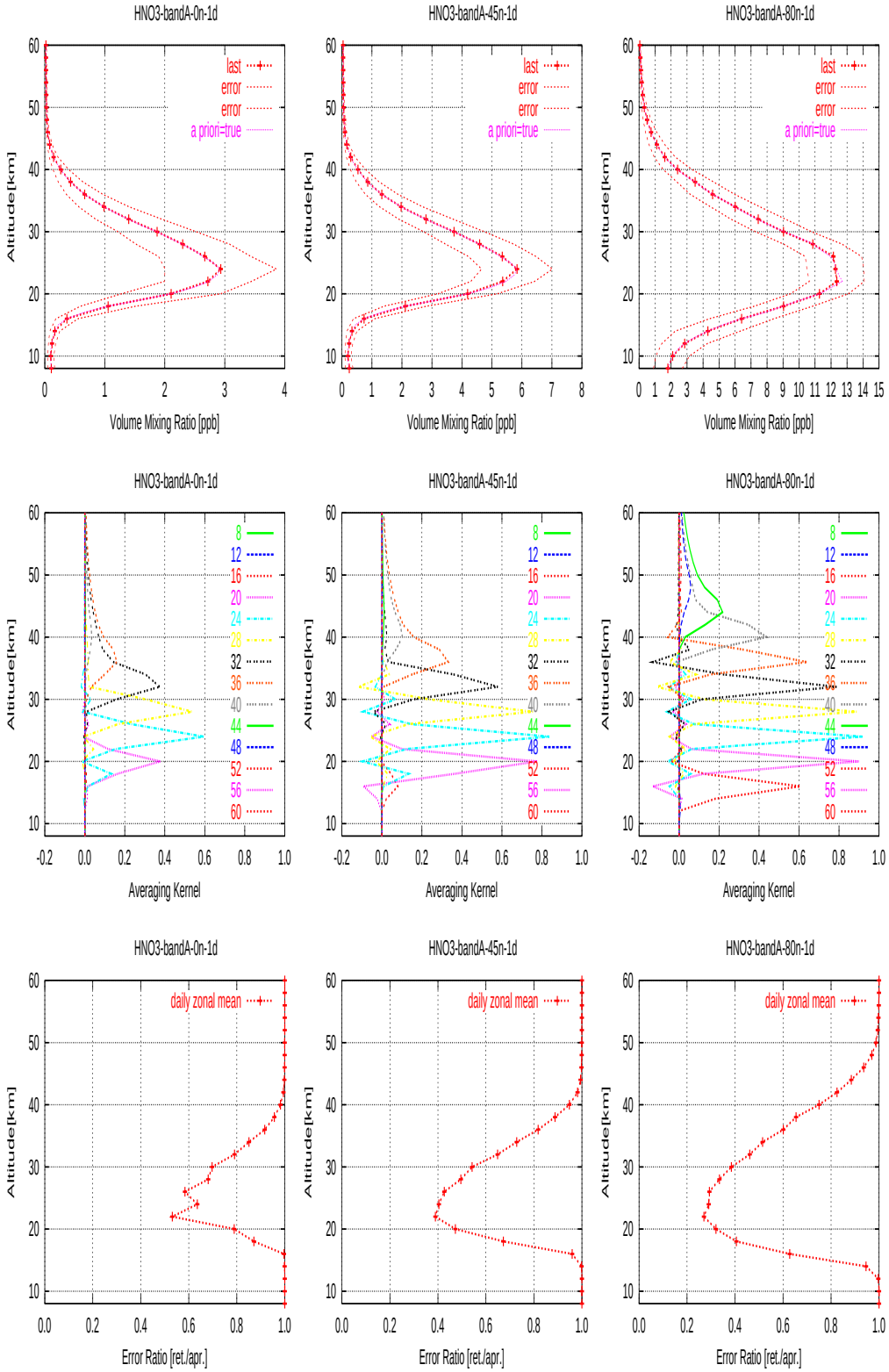

Figure A.3 Retrieval simulation results for 30-scan averaged data in BAND-A for standard profiles of HNO_3 at latitudes of 0°N (*left*), 45°N (*center*), and 80°N (*right*). *Top*: Retrieved volume mixing ratios are shown with *rms* retrieval error bounds and *a priori* profiles which are assumed to coincide with true profiles; *Middle* Averaging kernels; *Bottom*: Retrieval error ratios defined as the ratio of the retrieval errors to the *a priori* errors which are assumed to be 50 % of the *a priori* volume mixing ratios.

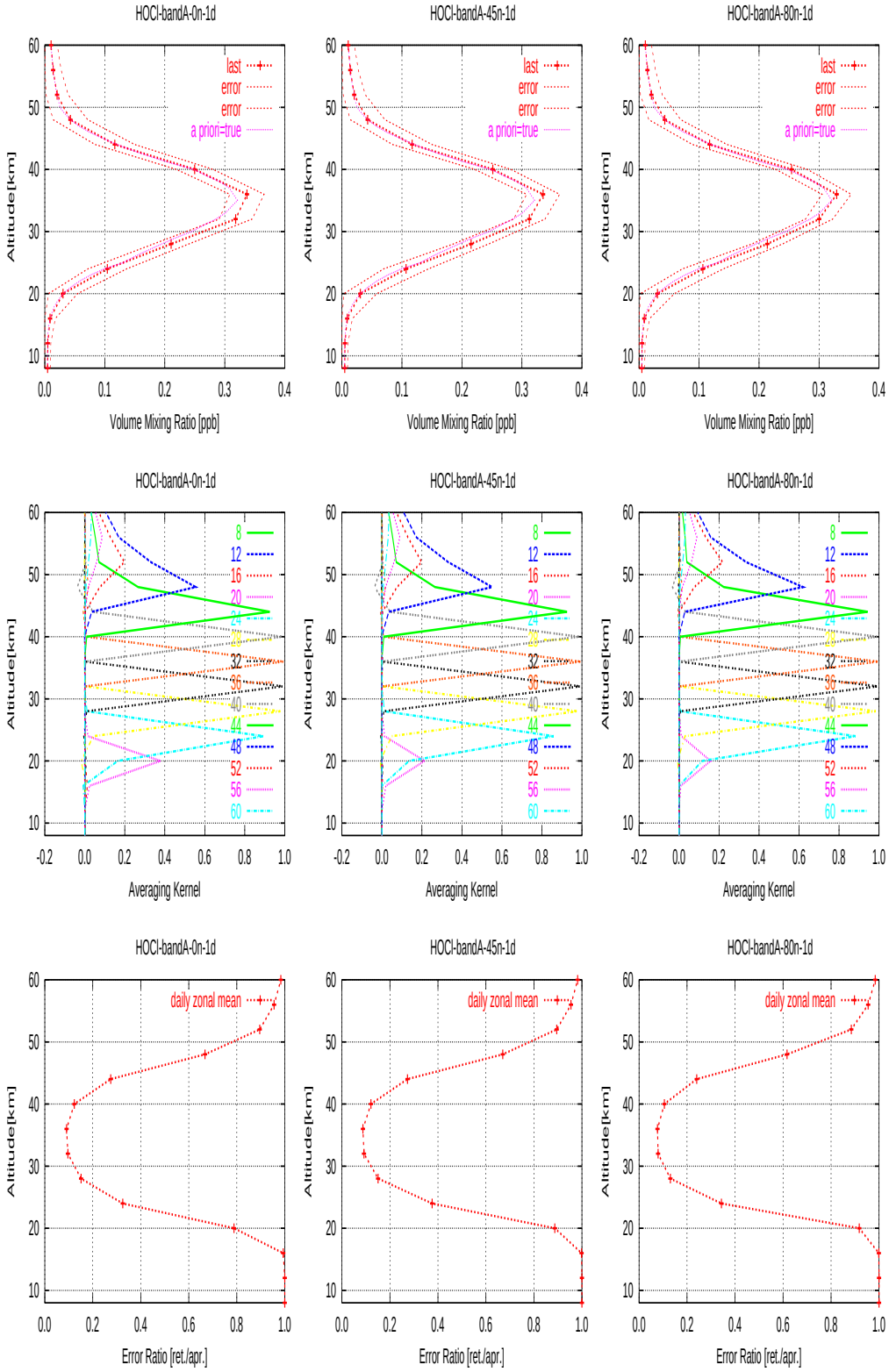

Figure A.4 Retrieval simulation results for 30-scan averaged data in BAND-A for standard profiles of HOCl at latitudes of 0°N (*left*), 45°N (*center*), and 80°N (*right*). *Top*: Retrieved volume mixing ratios are shown with *rms* retrieval error bounds and *a priori* profiles which are assumed to coincide with true profiles; *Middle* Averaging kernels; *Bottom*: Retrieval error ratios defined as the ratio of the retrieval errors to the *a priori* errors which are assumed to be 100 % of the *a priori* volume mixing ratios.

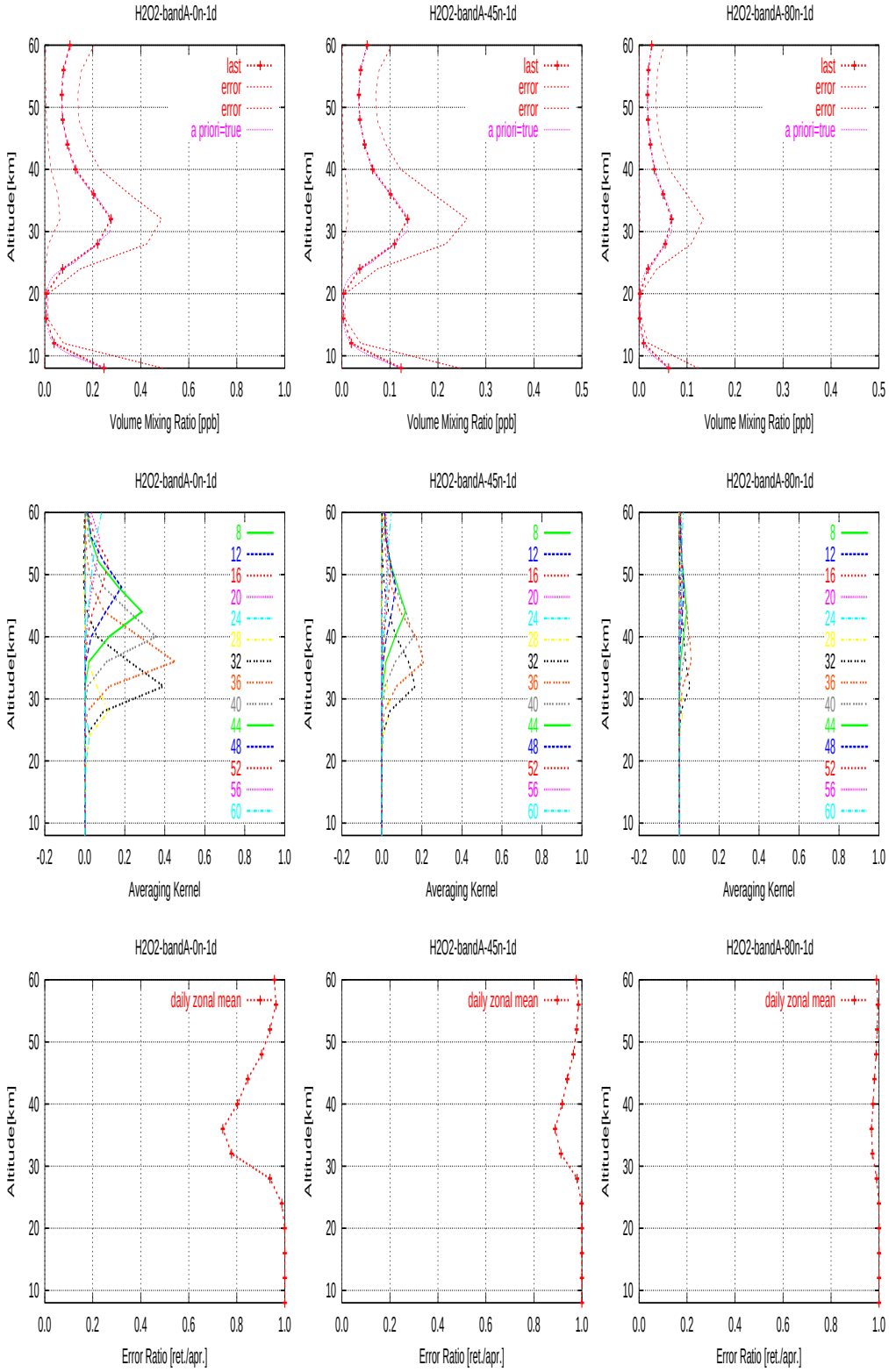

Figure A.5 Retrieval simulation results for 30-scan averaged data in BAND-A for standard profiles of H_2O_2 at latitudes of 0°N (*left*), 45°N (*center*), and 80°N (*right*). *Top*: Retrieved volume mixing ratios are shown with *rms* retrieval error bounds and *a priori* profiles which are assumed to coincide with true profiles; *Middle* Averaging kernels; *Bottom*: Retrieval error ratios defined as the ratio of the retrieval errors to the *a priori* errors which are assumed to be 100 % of the *a priori* volume mixing ratios.

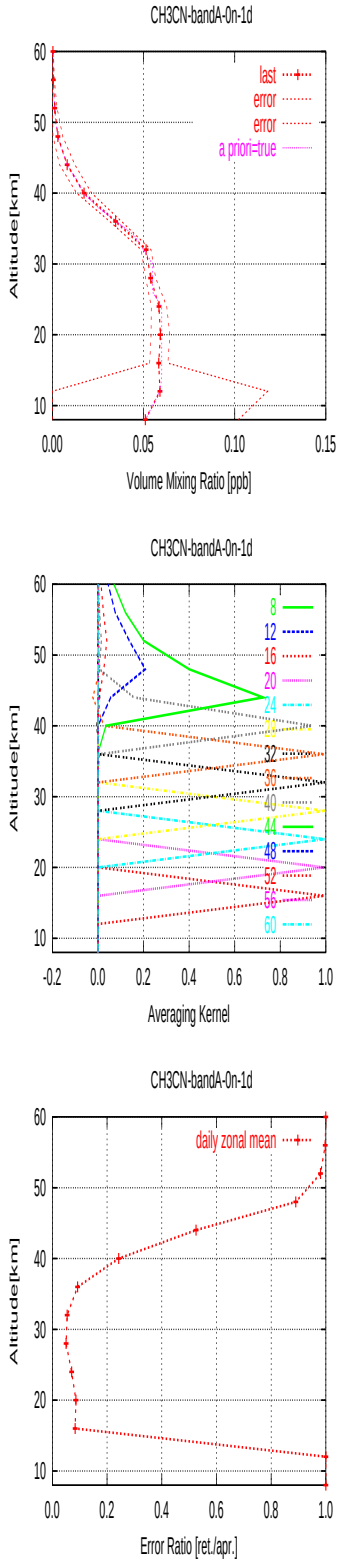

Figure A.6 Retrieval simulation results for 30-scan averaged data in BAND-A for the standard profile of CH_3CN at a latitude of 0°N. *Top*: Retrieved volume mixing ratios are shown with *rms* retrieval error bounds and *a priori* profiles which are assumed to coincide with true profiles; *Middle* Averaging kernels; *Bottom*: Retrieval error ratios defined as the ratio of the retrieval errors to the *a priori* errors which are assumed to be 100 % of the *a priori* volume mixing ratios.

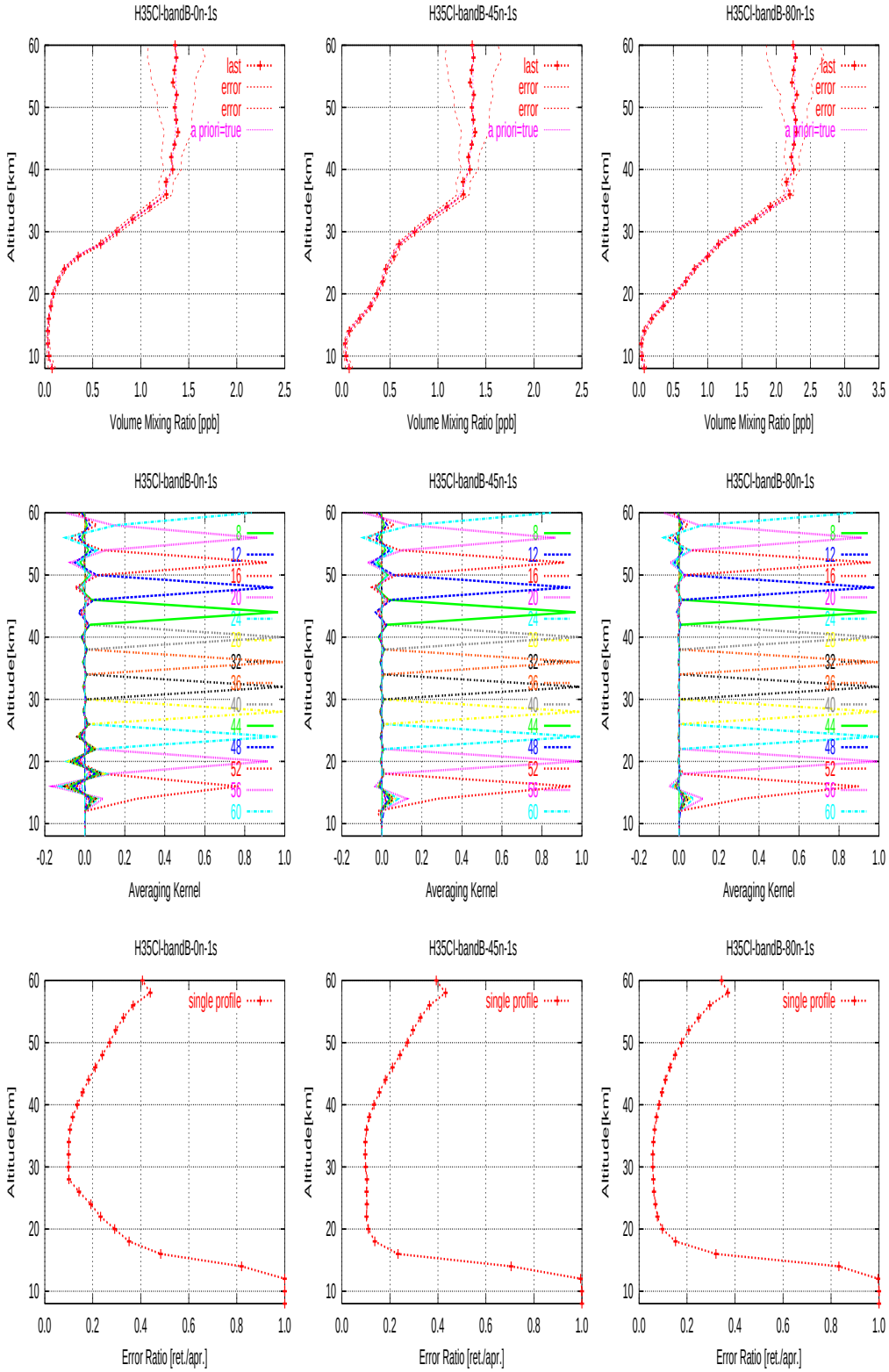

Figure A.7 Retrieval simulation results for single-scan data in BAND-B for standard profiles of $H^{35}Cl$ at latitudes of 0°N (*left*), 45°N (*center*), and 80°N (*right*). *Top*: Retrieved volume mixing ratios are shown with *rms* retrieval error bounds and *a priori* profiles which are assumed to coincide with true profiles; *Middle* Averaging kernels; *Bottom*: Retrieval error ratios defined as the ratio of the retrieval errors to the *a priori* errors which are assumed to be 50 % of the *a priori* volume mixing ratios.

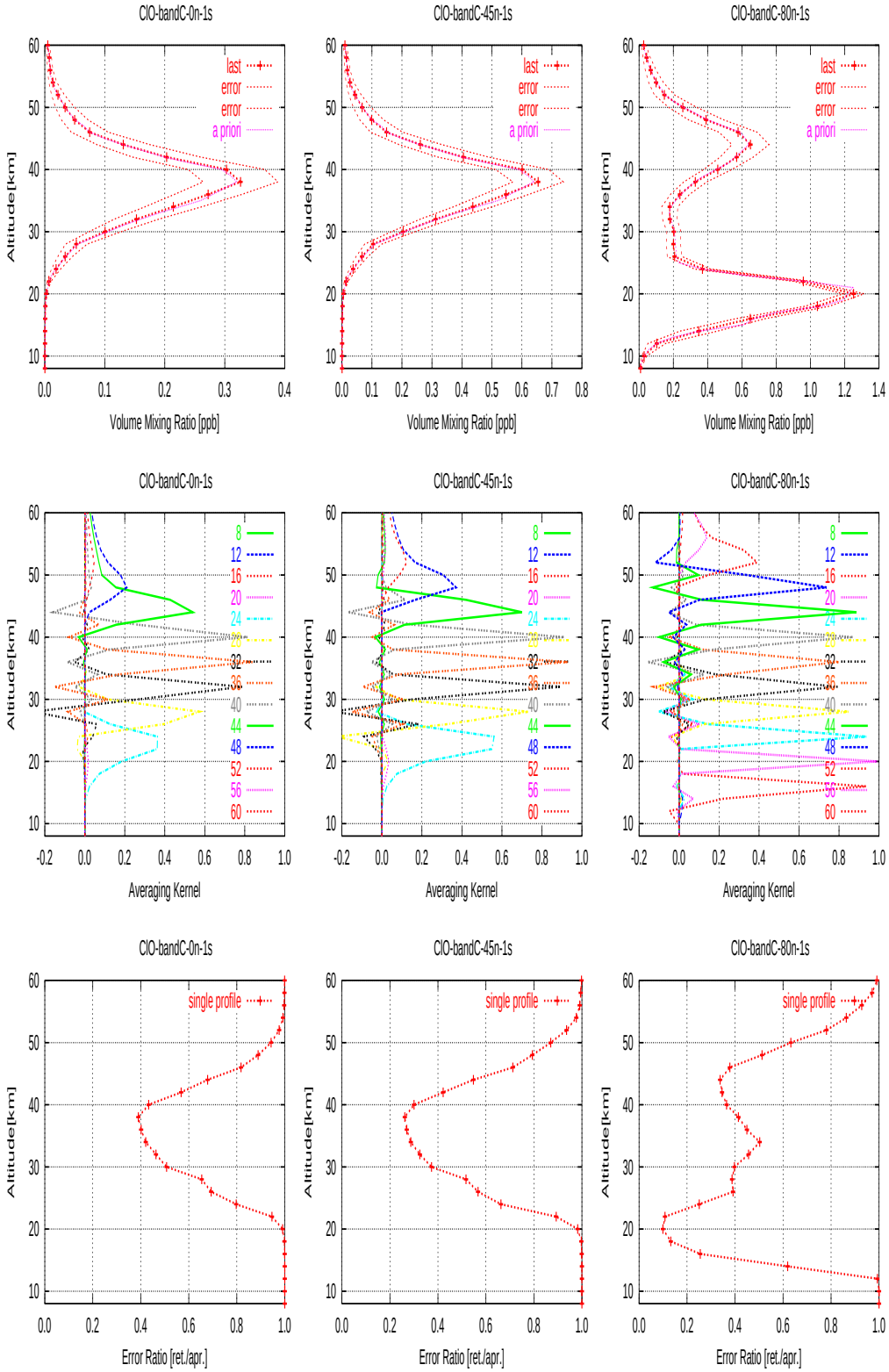

Figure A.8 Retrieval simulation results for single-scan data in BAND-C for standard profiles of ClO at latitudes of 0°N (*left*), 45°N (*center*), and 80°N (*right*). *Top*: Retrieved volume mixing ratios are shown with *rms* retrieval error bounds and *a priori* profiles which are assumed to coincide with true profiles; *Middle* Averaging kernels; *Bottom*: Retrieval error ratios defined as the ratio of the retrieval errors to the *a priori* errors which are assumed to be 50 % of the *a priori* volume mixing ratios.

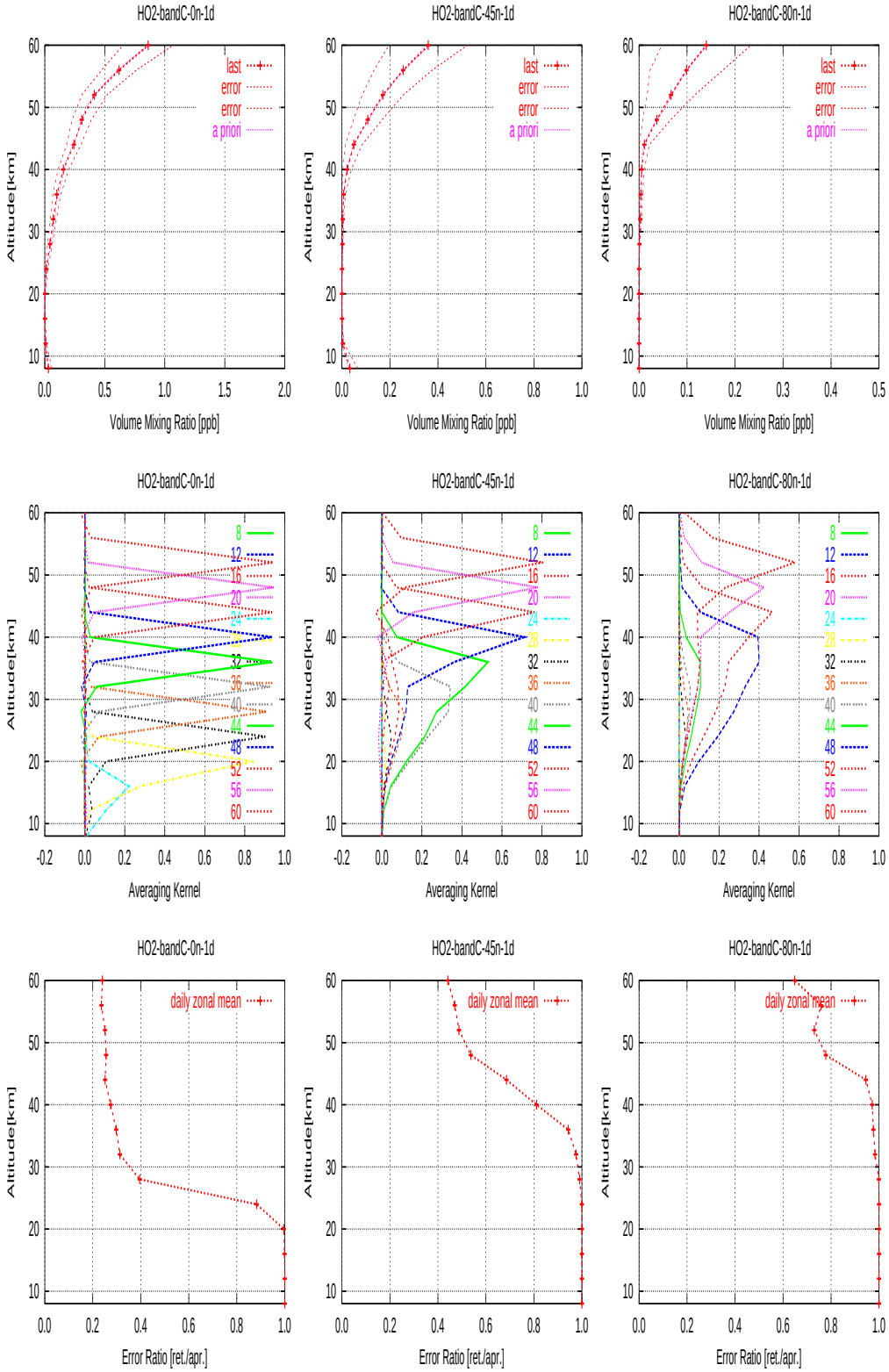

Figure A.9 Retrieval simulation results for 30-scan averaged data in BAND-C for standard profiles of HO_2 at latitudes of 0°N (*left*), 45°N (*center*), and 80°N (*right*). *Top*: Retrieved volume mixing ratios are shown with *rms* retrieval error bounds and *a priori* profiles which are assumed to coincide with true profiles; *Middle* Averaging kernels; *Bottom*: Retrieval error ratios defined as the ratio of the retrieval errors to the *a priori* errors which are assumed to be 100 % of the *a priori* volume mixing ratios.

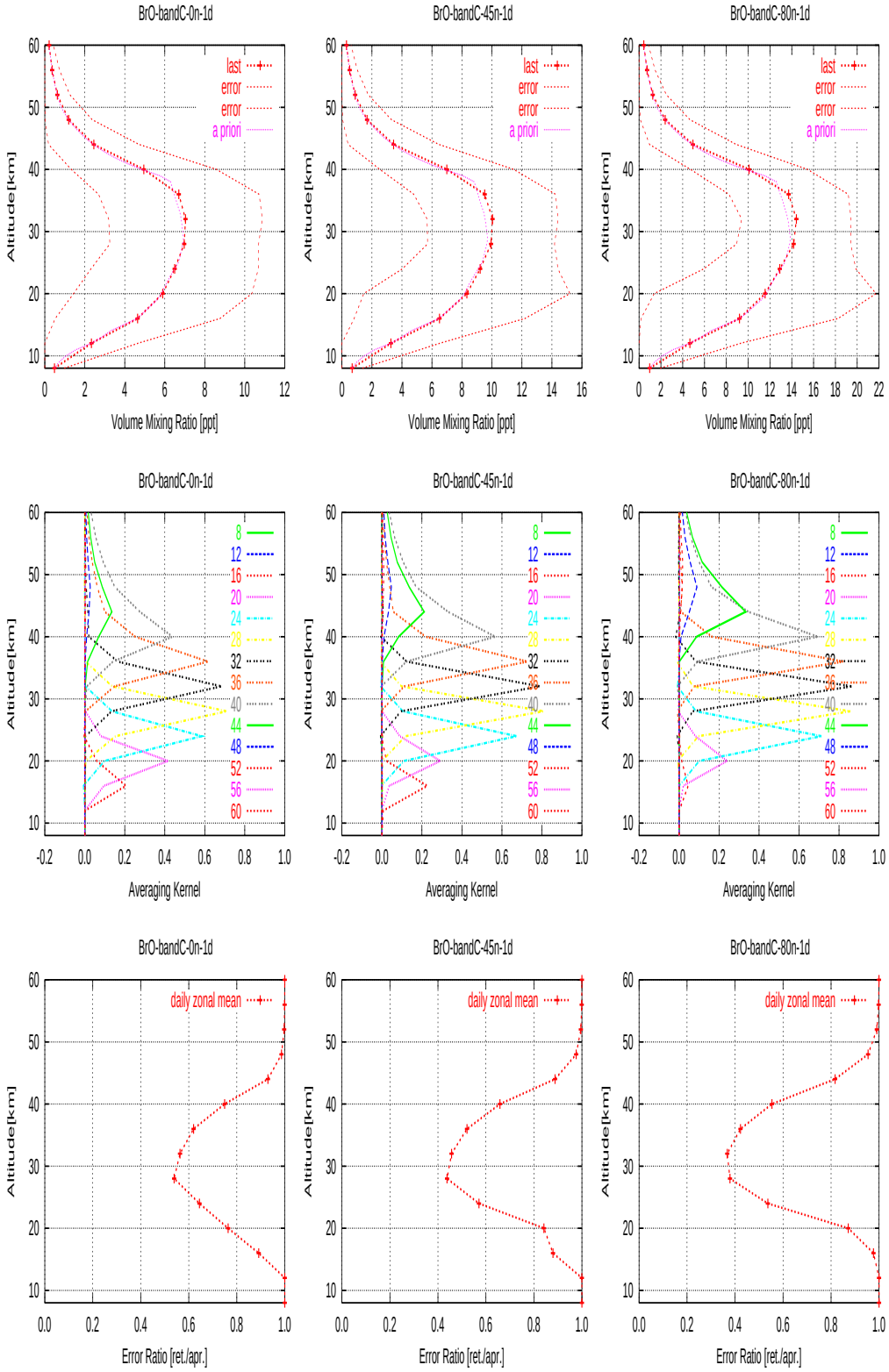

Figure A.10 Retrieval simulation results for 30-scan averaged data in BAND-C for standard profiles of $H^{35}Cl$ at latitudes of 0°N (*left*), 45°N (*center*), and 80°N (*right*). *Top*: Retrieved volume mixing ratios are shown with *rms* retrieval error bounds and *a priori* profiles which are assumed to coincide with true profiles; *Middle* Averaging kernels; *Bottom*: Retrieval error ratios defined as the ratio of the retrieval errors to the *a priori* errors which are assumed to be 100 % of the *a priori* volume mixing ratios.

A.2 Isotope Observations

Simulation setup is the same as that for the radical observations for forward model calculations.

The *a priori* profiles of ozone isotopes are assumed those derived for the standard mid-latitude profile of ozone by applying the atomic-oxygen isotope abundances estimated from the SMOW (Standard Mean Ocean Water) isotope ratio. The true profiles are assumed to be enriched profiles in the simulation. The 11-percent enriched profiles are given at 8-60 km. The *a priori* standard deviations are assumed to be 10 percent of the corresponding *a priori* profiles. The measurement error covariance matrix $\mathbf{S}_\epsilon$ is given from the measurement noise, $\sigma = (T_{sys} + T_{atm})/\sqrt{B\tau}$, where T_{sys} is the receiver system noise temperature assumed to be 500 K, and T_{atm} is the antenna temperature, B is the equivalent noise bandwidth assumed to be 0.8 MHz, τ is the integration time. The limb scan step is 2 km for tangent altitudes from 8 to 60 km, and the retrieval height grid and the weighting function step are 5 km. The averaging kernels are plotted every 5 km.

From initial retrieval simulations, it is found that for the here investigated 4 ozone isotopes excluding normal ozone, single-scan spectra of nominal integration time 0.5 s per tangent height have to be averaged over 30 spectra, which correspond to half-daily (day time) zonal means at mid-latitudes from the SMILES observation.

There are 73 transitions of the ozone isotopes in the SMILES observation frequency bands. As relatively isolated spectra of asymmetric-17 O_3 (^{17}OOO) and asymmetric-18 O_3 (^{18}OOO), and symmetric-17 O_3 (O^{17}OO) are found in the Band-C, this upper sideband is therefore better to observe ozone isotopes. The spectral intensity at each transition frequency of the asymmetric ozone isotopes is less than 20 K both substituted of ^{18}O and ^{17}O at the tangent height range 10- 60 km at Band-C. Symmetric-17 O_3, has transitions in all three Bands. As symmetric-18 O_3 (O^{18}OO) has three transitions with very weak intensity in Band-A and B, it should be difficult to observe and to obtain the enrichment in the daily zonal means. If the monthly mean profiles are obtained with stable instrumental conditions, the discussion of the symmetric-18 O_3 height profiles will be possible.

The retrievals were performed for the 30-scan averaged data, which correspond to half-daily (12 hour day time) zonal means. The retrieval results and averaging kernels, absolute error, and relative error are shown for 4 ozone isotopes including normal ozone.

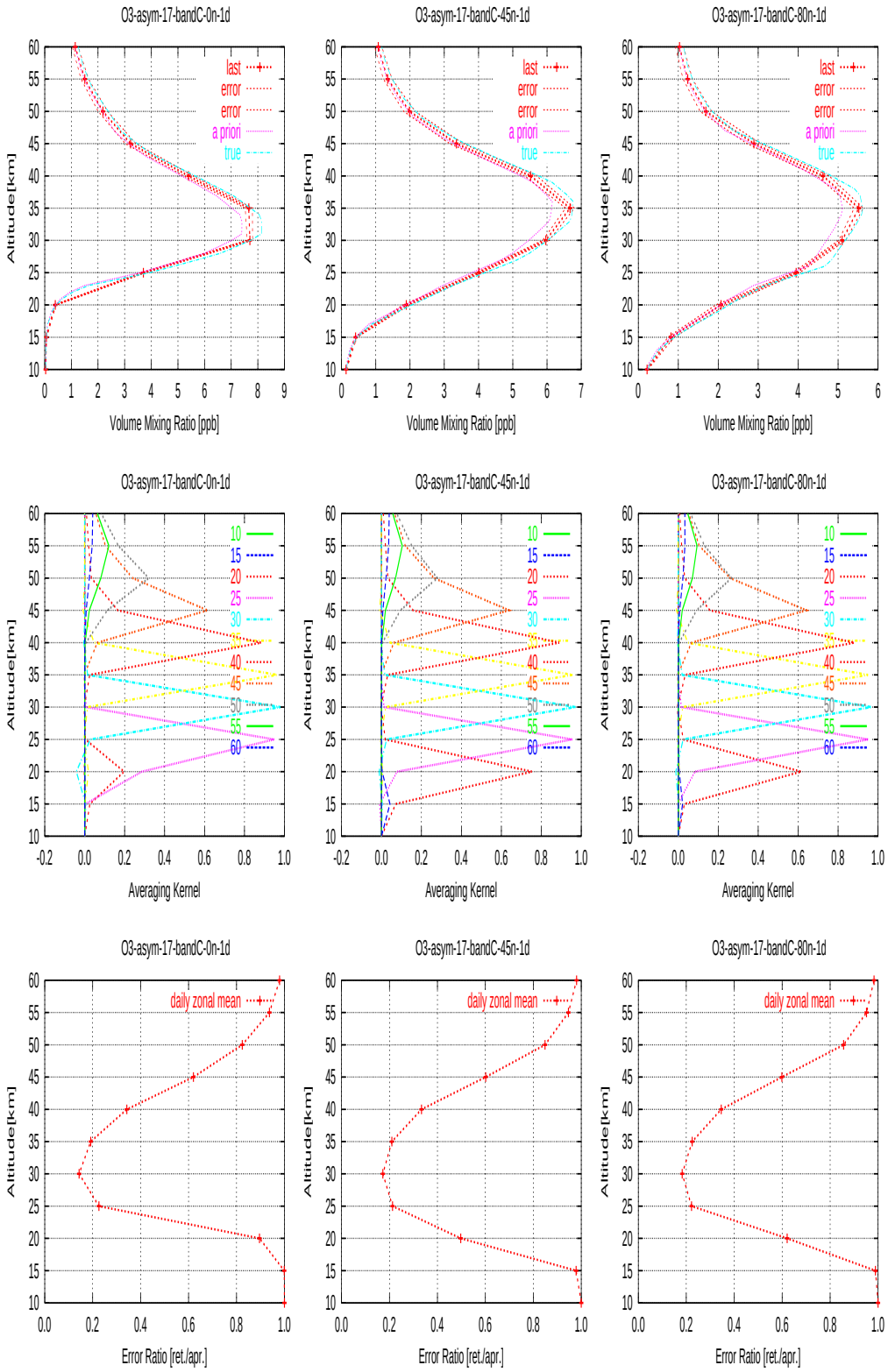

Figure A.11 Retrieval simulation results for 30-scan averaged data in BAND-C for asymmetric-17 O_3 at latitudes of 0°N (*left*), 45°N (*center*), and 80°N (*right*). *Top*: Retrieved volume mixing ratios are shown with *rms* retrieval error bounds and *a priori* profiles which are here assumed to be 90% of true profiles; *Middle* Averaging kernels; *Bottom*: Retrieval error ratios defined as the ratio of the retrieval errors to the *a priori* errors which are assumed to be 10 % of the *a priori* volume mixing ratios.

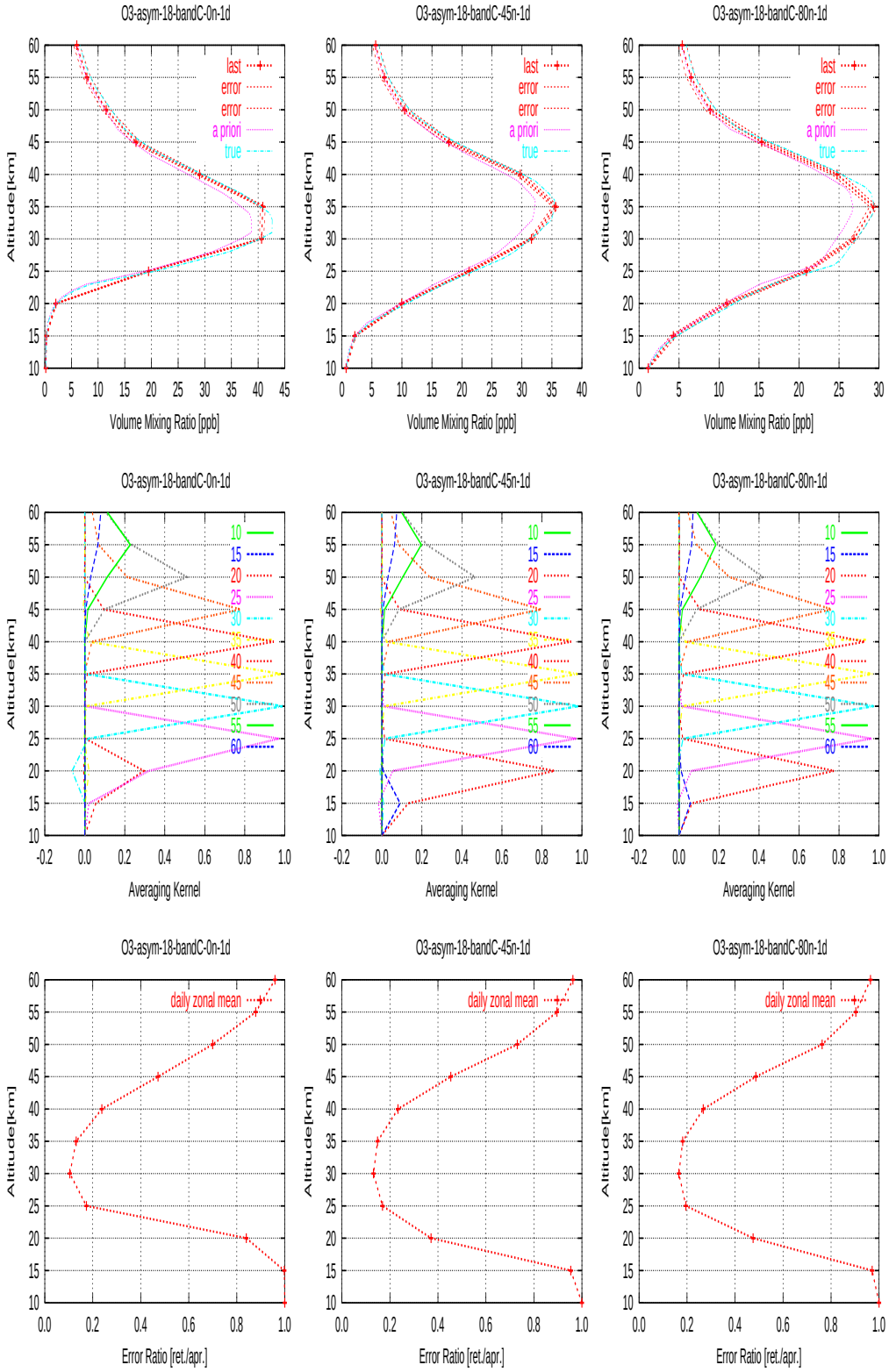

Figure A.12 Retrieval simulation results for 30-scan averaged data in BAND-C for asymmetric-18 ozone at latitudes of 0°N (*left*), 45°N (*center*), and 80°N (*right*). *Top*: Retrieved volume mixing ratios are shown with *rms* retrieval error bounds and *a priori* profiles which are here assumed to be 90% of the true profile; *Middle* Averaging kernels; *Bottom*: Retrieval error ratios defined as the ratio of the retrieval errors to the *a priori* errors which are assumed to be 10 % of the *a priori* volume mixing ratios.

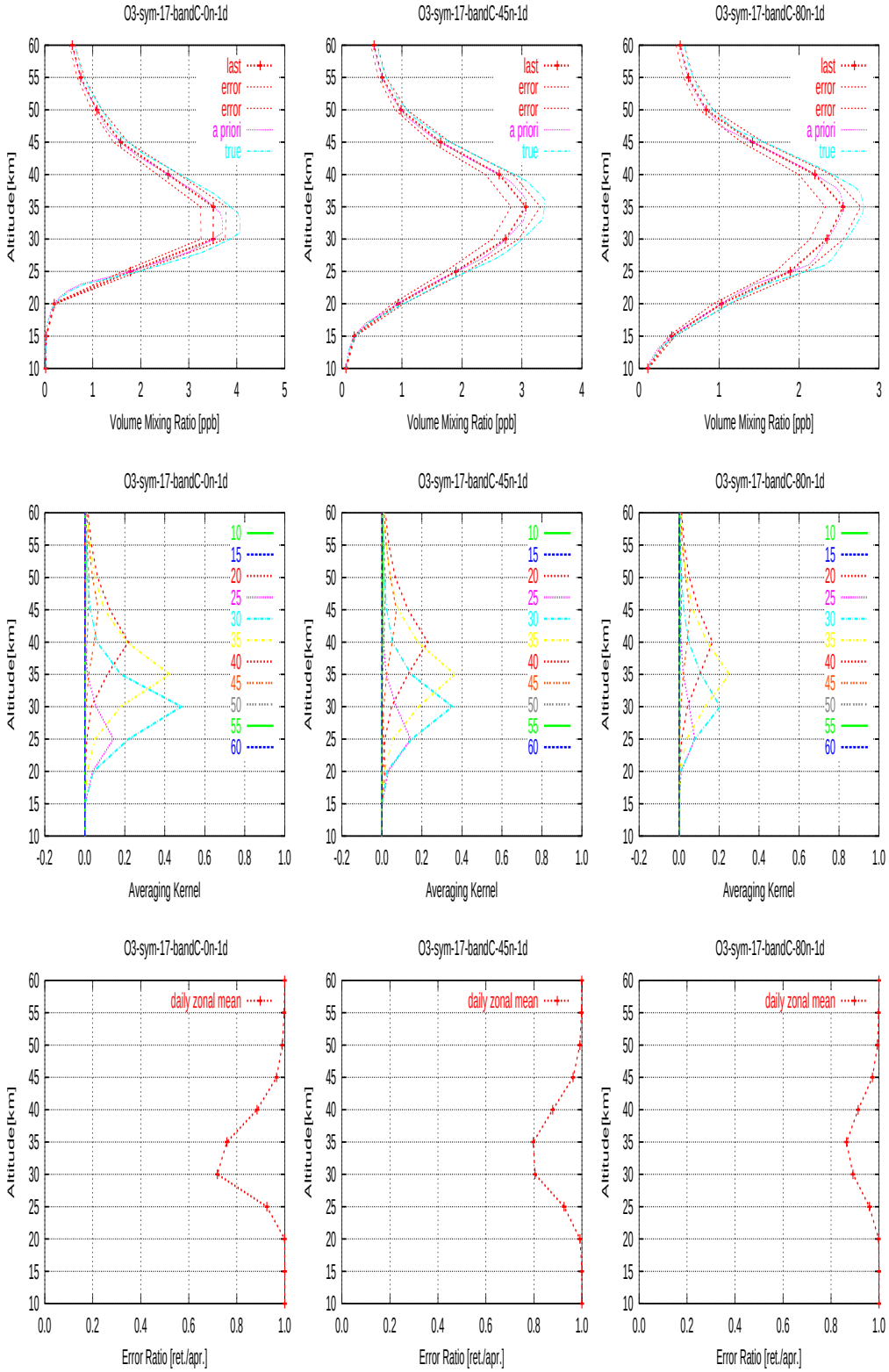

Figure A.13 Retrieval simulation results for 30-scan averaged data in BAND-C for symmetric-17 ozone at latitudes of 0°N (*left*), 45°N (*center*), and 80°N (*right*). *Top*: Retrieved volume mixing ratios are shown with *rms* retrieval error bounds and *a priori* profiles which are here assumed to be 90% of the true profiles; *Middle* Averaging kernels; *Bottom*: Retrieval error ratios defined as the ratio of the retrieval errors to the *a priori* errors which are assumed to be 10 % of the *a priori* volume mixing ratios.

A.3 Mesospheric Observation

We performed the error estimation for ozone, HCl, and HO_2 in the mesosphere, using the model atmosphere for the polar, mid-latitude, and equatorial regions, using the same conditions as those used for the radical analysis except for weighting function height step and observation height step. The errors for each 10 km partial column is obtained.

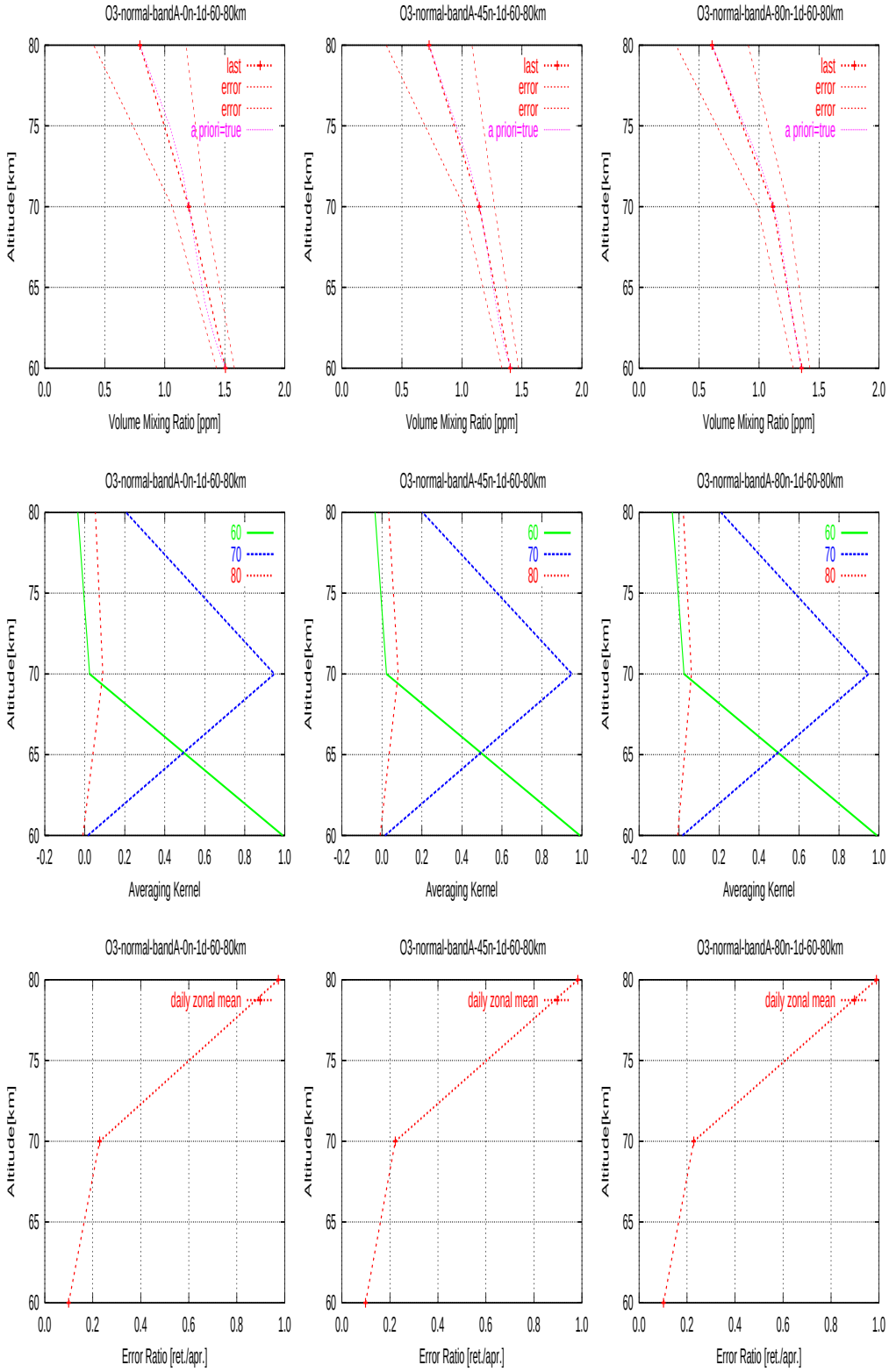

Figure A.14 Retrieval simulation results for 30-scan averaged data in BAND-A for the standard profiles of normal O_3 in the mesosphere at latitudes of 0°N (*left*), 45°N (*center*), and 80°N (*right*). *Top*: Retrieved volume mixing ratios are shown with *rms* retrieval error bounds and *a priori* profiles which are assumed to coincide with true profiles; *Middle* Averaging kernels; *Bottom*: Retrieval error ratios defined as the ratio of the retrieval errors to the *a priori* errors which are assumed to be 50 % of the *a priori* volume mixing ratios.

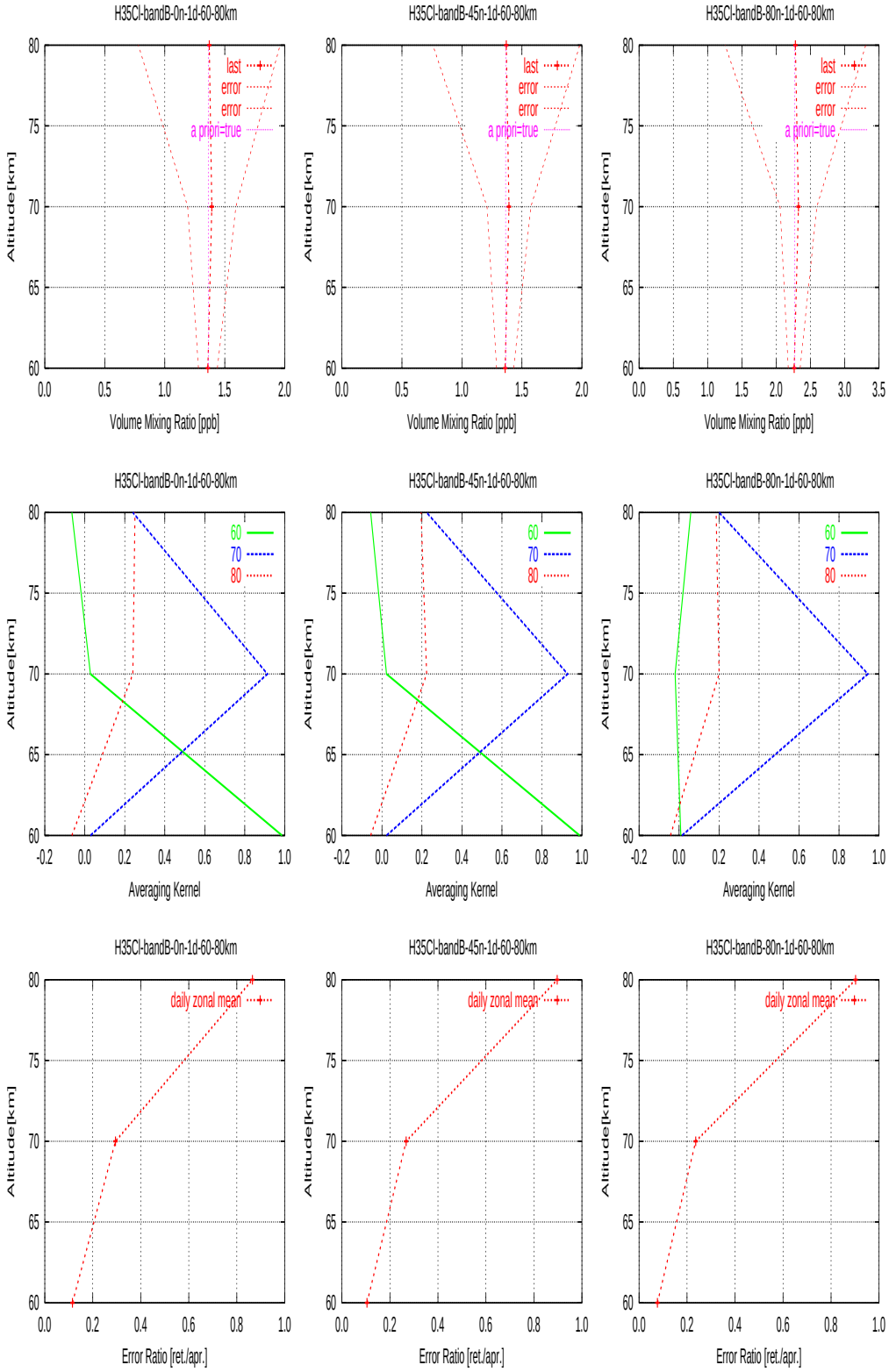

Figure A.15 Retrieval simulation results for 30-scan averaged data in BAND-B for the standard profiles of $H^{35}Cl$ in the mesosphere at latitudes of 0°N (*left*), 45°N (*center*), and 80°N (*right*). *Top*: Retrieved volume mixing ratios are shown with *rms* retrieval error bounds and *a priori* profiles which are assumed to coincide with true profiles; *Middle* Averaging kernels; *Bottom*: Retrieval error ratios defined as the ratio of the retrieval errors to the *a priori* errors which are assumed to be 50 % of the *a priori* volume mixing ratios.

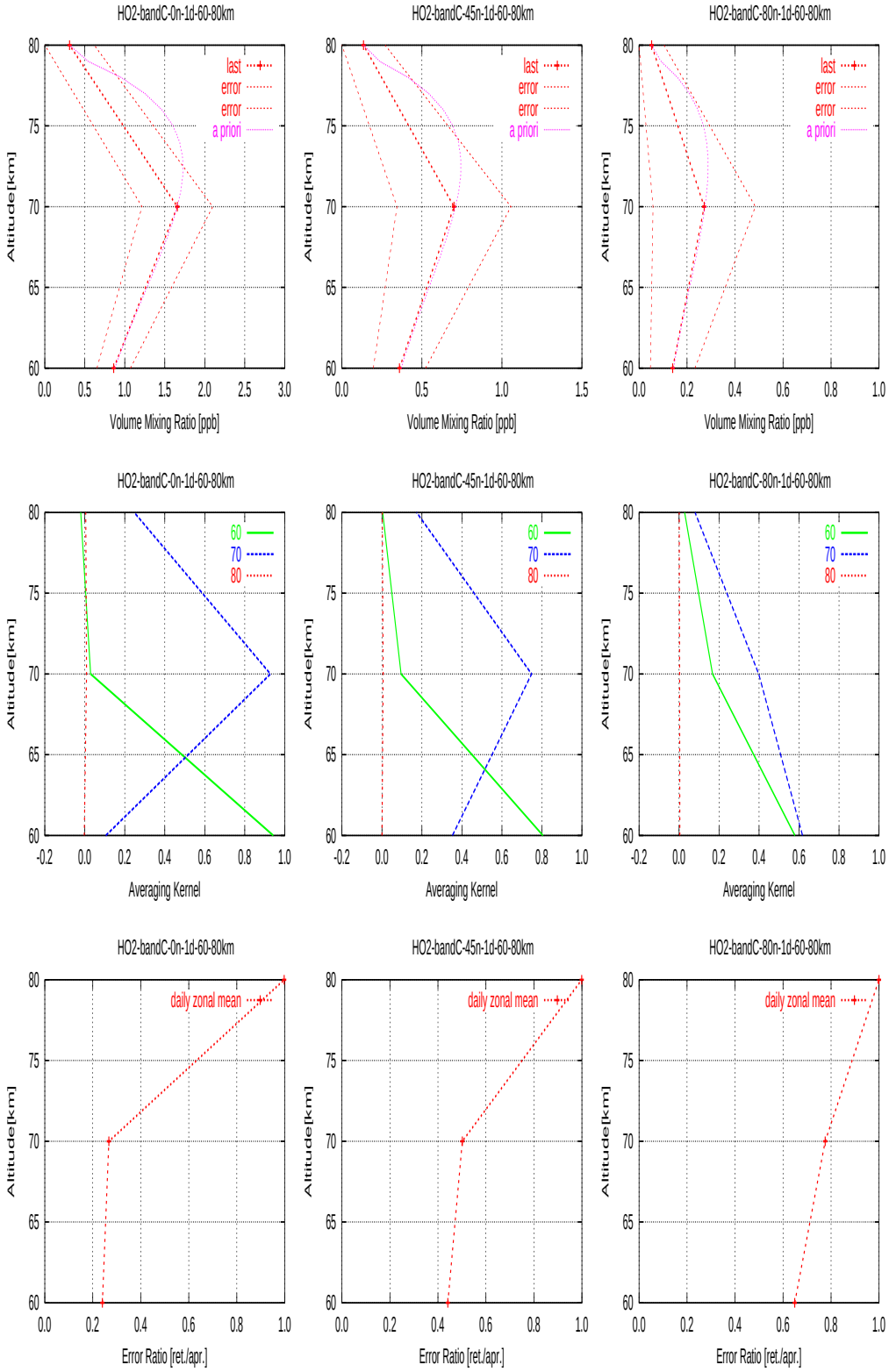

Figure A.16 Retrieval simulation results for 30-scan averaged data in BAND-C for the standard profiles of HO_2 in the mesosphere at latitudes of 0°N (*left*), 45°N (*center*), and 80°N (*right*). *Top*: Retrieved volume mixing ratios are shown with *rms* retrieval error bounds and *a priori* profiles which are assumed to coincide with true profiles; *Middle* Averaging kernels; *Bottom*: Retrieval error ratios defined as the ratio of the retrieval errors to the *a priori* errors which are assumed to be 100 % of the *a priori* volume mixing ratios.

List of Acronyms

A/D	analogue to digital
AAMP	Ambient Temperature Amplifiers
ADE	Antenna Drive Electronics
AMS	Airborne Mass Spectrometer
ANT	Submillimeter Antenna
ANT-RCS	antenna reference coordinate system
AO	announcement of opportunity
AOPT	Ambient Temperature Optics
AOS	Radio Spectrometer
AOS	acousto-optic (*or* acousto-optical) spectrometer
ATLAS	Atmospheric Laboratory for Applications and Science
ATMOS	Atmospheric Trace Molecule Spectroscopy
AU	AOS Analyzer Unit
BBM	breadboard model
BDR	basic design review
bps	bit per second
BSMILES	Balloon-borne SMILES
BUS	Payload Bus
BWO	backward-wave oscillator
CAM	STT Camera Units
CAMC	STT Camera Controller
CCD	charge coupled device
CCSDS	Consultative Committee for Space Data System
CD-ROM	compact disc - read-only memory
CDMS	Cologne Database for Molecular Spectroscopy
CDR	critical design review
CFC	chlorofluorocarbon
CHL	Calibration Hot Load
CMG	Control Moment Gyro
CPU	Central Processing Unit
CRE	Cryo-electronics Unit
CREC	CRE Control Electronics
CRL	Communications Research Laboratory
CS	cryogenic sampling
CST	Cold Sky Terminator
CVU	Video Unit
DNL	differential non-linearity
DPC	Data Processing and Control Section
DRTS	Data Relay Test Satellite
DRTS-W	Data Relay Test Satellite-West
DRTSS	Data Relay Test Satellite System
DSB	double sideband
DVD/ROM	digital versatile (*or* video) disc / read-only memory

EF	Exposed Facility
EFM	engineering flight model
EFU	Exposed Facility Unit
ELM-ES	Experiment Logistics Module - Exposed Section
ELM-PS	Experiment Logistic Module - Pressurized Section
EM	engineering model
EOPD	Earth Observation Program Department
EORC	Earth Observation Research Center
EOS	Earth Observing System
EOS-CHEM	Earth Observing System Chemistry Mission
EPS	Electric Power System
ESA	European Space Agency
ESTO	Earth Science & Technology Organization
FIFO	first in and first out
FIP	FACOM Information Processing
FIRS	Far Infra-Red Survey
FM	flight model
FM1	forward model I
FM2	forward model II
FOV	field of view
FTIR	Fourier transform infrared spectrometer
FWHM	full-width at half-maximum
GAW	Global Atmospheric Watch
GB	gigabytes
GCS	geocentric inertial equatorial coordinate system
GEISA	Gestion et Êtude des Informations Spectroscopiques Atmosphériques
Gflops	giga floating operations per second
GI/UAF	Geophysical Institute, University of Alaska Fairbanks
GIE-CS	geocentric inertial equatorial coordinate system
GN&C	Guidance, Navigation and Control
GSE	ground support equipment
H	height
HCS	heliocentric inertial equatorial reference coordinate system
HECP	Helium Gas Compressors
HEMT	high electron mobility transistor
HITRAN	High-resolution Transmission Molecular Absorption Database
HK	house keeping
HPBW	half-power beamwidths
HRDL	High-Rate Data Link
HRDR	High Rate Data Recorder
HTV	H-II Transfer Vehicle
ICS	Interorbit Communication System
IF	intermediate frequency
IFA	IF Amplification Section
ILAS	Improved Limb Atmospheric Spectrometer
IMG	Interferometric Monitor for Greenhouse Gases
I/O	input/output
IR	infrared
ISDN	integrated services digital network
ISS	International Space Station

IUP	Institut für Umweltphysik (Institute for Enviromnental Physics)
JCP	JEM Control Processor
JEM	Japanese Experiment Module
JEM/OS	JEM Operation System
JEMRMS	JEM Remote Manipulator System
JIF	JEM Interface Mechanism
JPL	Jet Propulsion Laboratory
JSC	Johnson Space Center
L	length
L1	level 1
L2	level 2
L3	level 3
LAPAN	Lembaga Penerbangan dan Antariksa Nasional (National Institute of Aeronautics and Space)
LO	local oscillator
LS	lower stratosphere
LSB	lower sideband
LVLH	local vertical local horizontal
MAES	Millimeter Wave Atmospheric Emission Simulator
MAS	Millimeter-wave Atmospheric Sounder
MASTER	Millimeter-wave Acquisitions of Stratosphere/Troposphere Exchanges Research
MB	megabytes
MFS	Mainframe Structure
MIL-STD	Military Standard
MLS	Microwave Limb Sounder
MNT	Antenna Mounting Structure
MOIP	Mission Operation Implementation Plan
MOIS	Mission Operation Interface Specification
MPI	Martin-Puplett interferometer
MPM	Millimeter-Wave Propagation Model
N	north
NA	not applicable
NAO	National Astronomical Observatory
NASA	National Aeronautics and Space Administration
NASDA	National Space Development Agency of Japan
NDSC	Network for the Detection of Stratospheric Change
NIES	National Institute of Environment Study
NRO	Nobeyama Radio Observatory
NSBF	National Scientific Balloon Facility
NW	network
OEM	optimal estimation method
OPLN	operation plan
PDH	Payload Data Handling Unit
PDR	preliminary design review
PM	JEM Pressurized Module
PSC	polar stratospheric cloud
REF	Antenna Reflectors
RF	radio frequency
rms	root-mean-squares
RMS	root-mean-squares

RSS	root-sum-squares
S	south
SAO	Smithsonian Astrophysical Observatory Line Database
SBUV	solar backscatter ultraviolet
SIKIE	symmetry induced kinetic effect
SIS	superconductor-insulator-superconductor
SJTD	Stirling & JT Drive Electronics
SLO	submillimeter-wave local oscillator
SLOC	Submillimeter LO Controller
SMILES	Superconducting Submillimeter-Wave Limb-Emission Sounder
SOOH	Spacecraft Orbital Operation Handbook
SOPRANO	Sub-millimetre Observation of Process in the Absorption, Noteworthy for Ozone
SRX	Submillimeter Receiver
SSB	single sideband
SSC	Swedish Space Corporation
STE	stratosphere-troposphere exchange
STEL	Solar-Terrestrial Environment Laboratory
STT	Star Tracker
STT-RCS	Star-Tracker reference coordinate system
SYNC	synchronization
TBD	to be determined
TCS	Thermal Control System
TDRSS	Tracking and Data Relay Satellite System
TEA	Torque Equilibrium Attitude
TKSC	Tsukuba Space Center
TOMS	Total Ozone Mapping Spectrometer
TRN	Beam Transfer Section
UARS	Upper Atmosphere Research Satellite
US	United States
USA	United States of America
USB	upper sideband
UT	Universal Time
UT	upper troposphere
UTC	Coordinated Universal Time
UV	ultraviolet
W	width
WGS84	World Geodetic System 1984
WMO	World Meteorological Organization
ZOE	Zone of Exclusion

COMMUNICATIONS RESEARCH LABORATORY

NASDA 宇宙開発事業団

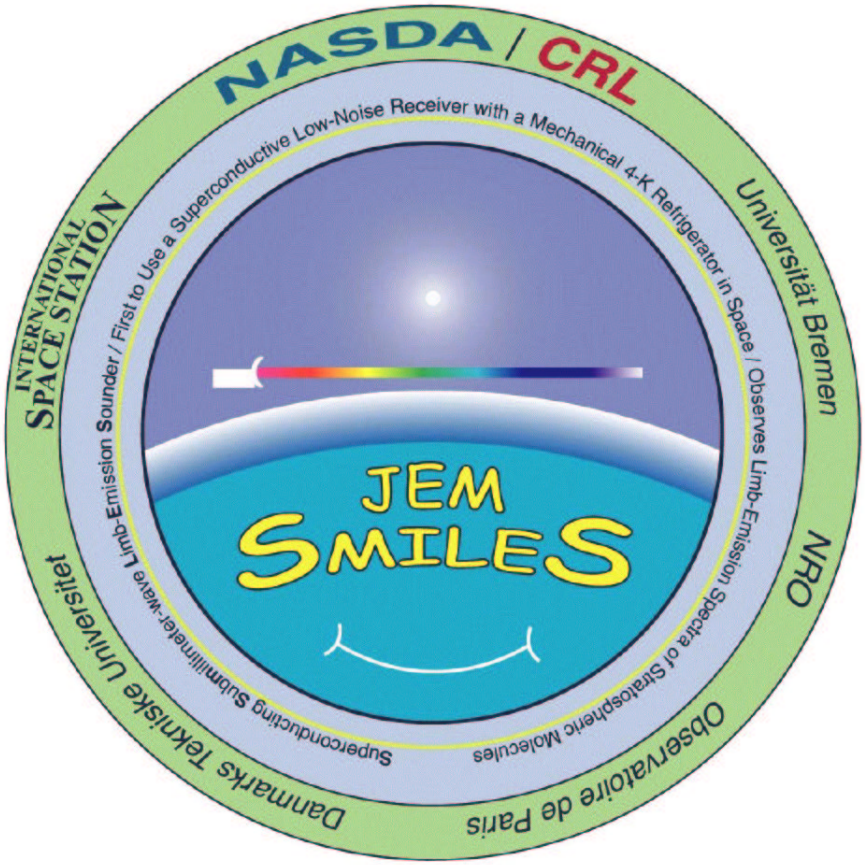

NASDA JEM/SMILES:
http://smiles.tksc.nasda.go.jp/

CRL JEM/SMILES:
http://www.crl.go.jp/dk/c214/smiles/